Optical Feshbach Resonances in a Bose-Einstein Condensate

Dissertation

zur Erlangung des Doktorgrades an der
Fakultät für Mathematik, Informatik und Physik
der Leopold-Franzens-Universität Innsbruck

vorgelegt von

Matthias Theis

durchgeführt am Institut für Experimentalphysik
unter der Leitung von
Univ.-Prof. Dr. Rudolf Grimm

April 2005

Abstract

This thesis reports on the first observation of optical tuning of interactions in an ultracold atomic gas. To control the elastic interactions, we use optically induced scattering resonances. They are realized by coupling pairs of atoms to a bound molecular state with the help of laser light. In comparison to the well-known magnetic Feshbach resonances, these optical Feshbach resonances allow a very fast switching of interactions in a spatially resolved way. This is because laser light can be switched on and off much faster than magnetic fields and because the light intensity can be spatially structured.

Our experiments are performed with a Bose-Einstein condensate (BEC) of ^{87}Rb atoms, which we produce in our new BEC setup. This apparatus has been constructed in the framework of this thesis and offers excellent optical access to the ultracold atom cloud.

To investigate the tunability of atomic interactions with single-frequency laser light, we optically couple pairs of free atoms to an electronically excited molecular state. The coupling is achieved with a laser that is tuned close to the respective free-bound photoassociation transition. By changing the laser detuning we are able to adjust the atomic scattering length to any value between $10\,a_0$ and $190\,a_0$, where a_0 denotes the Bohr radius. The atomic scattering length is a single quantity that fully describes ultracold elastic interactions. Since laser induced atom losses restrict the duration of our experiments, Bragg spectroscopy is employed as a fast method to measure the scattering length.

We also demonstrate that optical Feshbach resonances can be realized with a two-color Raman coupling scheme. To implement this scheme, a second laser is added that couples the excited molecular state to a weakly bound molecular level in a ground state potential. Tuning the second laser results in a modification of the atomic scattering length similar to the one observed with a single laser. In addition, this scheme allows to control the width of the resonance via the detuning of the first laser.

For the one-color and two-color coupling schemes, we investigate how the elastic scattering properties depend on the different available parameters, i.e. the laser detunings and intensities. Our experimental findings can successfully be described with an available theoretical model, which treats ultracold collisions in the presence of laser light.

Optical Feshbach resonances have the possibility of becoming a valuable tool for fast switching of interactions. This is of special interest in quantum computation schemes with neutral atoms, where interactions between different atomic qubits need to be controlled.

Zusammenfassung

Diese Arbeit berichtet über die erste Beobachtung einer rein optischen Kontrolle der Wechselwirkung ultrakalter Atome. Um die Wechselwirkung zwischen den Atomen einzustellen, benutzen wir optisch induzierte Streuresonanzen. Diese basieren auf der optischen Kopplung von Paaren kollidierender Atome an einen gebundenen Molekülzustand. Anders als die bekannten magnetischen Feshbach-Resonanzen ermöglichen solche optische Feshbach-Resonanzen ein sehr schnelles Verändern der Wechselwirkung und deren räumliche Strukturierung. Denn Laserlicht kann viel schneller an- und ausgeschaltet werden als ein Magnetfeld, und es ermöglicht räumlich strukturierte Intensitätsmuster.

Ausgangspunkt unserer Experimente ist ein Bose-Einstein-Kondensat (BEC) aus ^{87}Rb Atomen, das wir in unserer neuen BEC Apparatur erzeugen. Der Aufbau wurde im Rahmen dieser Arbeit konstruiert und ermöglicht einen ausgezeichneten optischen Zugang zu den gespeicherten ultrakalten Atomen.

Um zu untersuchen wie atomare Wechselwirkungen mit einem einzelnen Laserstrahl kontrolliert werden können, koppeln wir Paare freier Atome an einen elektronisch angeregten Molekülzustand. Die optische Kopplung wird mit Laserlicht erreicht, dessen Frequenz in der Nähe des entsprechenden Photoassoziationsübergangs liegt. Indem wir die Laserfrequenz verstimmen, ist es möglich die atomare Streulänge über einen Bereich von $10\,a_0$ bis $190\,a_0$ zu variieren, wobei a_0 den Bohr-Radius bezeichnet. Die Streulänge ist ein Parameter, der die elastische Wechselwirkung ultrakalter Atome vollständig beschreibt. Weil laserinduzierte Atomverluste die Zeitdauer unserer Experimente einschränken, benutzen wir die Methode der Bragg-Spektroskopie, die eine schnelle Messung der Streulänge erlaubt.

In einem weiteren Experiment zeigen wir, dass optische Feshbach-Resonanzen auch mit einem Zwei-Photonen Raman-Prozess induziert werden können. Dazu wird ein weiterer Laser verwendet, der den angeregten Molekülzustand an ein molekulares Niveau in einem Grundzustandspotential koppelt. Wenn dieser zweite Laser durchgestimmt wird, beobachten wir wieder eine Variation der Streulänge, ähnlich wie zuvor.

Sowohl für die optische Kopplung mit einem einzelnen Laser als auch mit einem Raman Schema untersuchen wir, wie die elastischen Streueigenschaften von den verfügbaren Parametern, also den Laserverstimmungen und Intensitäten, abhängen. Die experimentellen Ergebnisse können wir erfolgreich mit einem vorhandenen theoretischen Modell beschreiben, das ultrakalte Stöße in der Gegenwart von Laserlicht behandelt.

Optische Feshbach-Resonanzen können sich zu einem wertvollen Werkzeug entwickeln, um Wechselwirkungen schnell zu verändern. Das ist besonders interessant für Konzepte zur Quanten-Informationsverarbeitung mit neutralen Atomen, wo Wechselwirkungen zwischen verschiedenen atomaren Qubits kontrolliert werden müssen.

Contents

1 Introduction **9**

2 Ultracold Collisions and Feshbach Resonances **11**
2.1 Elastic Collisions 12
2.2 Inelastic Processes 15
2.3 Scattering Length and Feshbach Resonances 18
2.3.1 Scattering Length in Ultracold Gases 18
2.3.2 Feshbach Resonances 19
2.4 Optical Collisions and Photoassociation 22
2.5 Optically Induced Feshbach Resonances 25
2.5.1 One-Color Optical Feshbach Resonance 25
2.5.2 Raman Scheme for Optical Feshbach Tuning 28

3 Bose-Einstein Condensates **31**
3.1 BEC of Interacting Atoms 33
3.2 Thomas-Fermi Approximation 34

4 Setup of the Experiment **37**
4.1 Vacuum System 38
4.1.1 MOT Section 39
4.1.2 Differential Pumping 41
4.1.3 XUHV Section and Glass Cell 43
4.2 Magnetic Fields 45
4.2.1 Magnetic Trapping of Neutral Atoms 45
4.2.2 Magnetic Transfer Line 47
4.2.3 QUIC Trap 53
4.2.4 Power Supplies and Magnetic Field Control 55
4.3 Magneto-Optical Trap 57
4.4 Detection and Imaging System 60
4.5 Lasers for Experiments 62

5 General Procedures and BEC Production 65
5.1 Measurement Cycle and Experimental Control 65
5.2 Detection and Diagnosis 68
5.3 Magnetic Transfer and QUIC Trap 70
5.4 Evaporative Cooling and BEC 73

6 Optical Tuning of the Scattering Length 77
6.1 Photoassociation Spectroscopy 78
6.1.1 One-Color Photoassociation: Excited Molecular States . 78
6.1.2 Two-Color Photoassociation: Molecules in the Ground State 84
6.2 Measuring the Scattering Length 86
6.2.1 Methods to Quantify Ultracold Interactions 86
6.2.2 Bragg Spectroscopy Measurements 87
6.3 One-Color Optical Feshbach Resonances 91
6.3.1 Observation of Optical Feshbach Tuning 91
6.3.2 Theoretical Description and Discussion 95
6.4 Optical Feshbach Tuning with Raman Transitions 97
6.4.1 Raman Scheme for Optical Feshbach Resonances 97
6.4.2 Experimental Realization of Two-Color Optical Feshbach Resonances 102
6.4.3 Comparison to Theoretical Models, Discussion 106
6.5 Details of the Theoretical Model 111

7 Summary and Outlook 115

A Rubidium-87 Properties 119

B Index to Important Data Files 121

C Publications 123

Bibliography 137

Chapter 1

Introduction

In the last few years the study of ultracold atomic gases has led to a wealth of phenomena, which reflect the peculiar nature of quantum physics. In particular, experimental access to various interesting quantum systems was achieved. After the advent of laser cooling in the 1980s [Chu98, CT98, Phi98], dilute gases of alkali atoms at millikelvin or microkelvin temperatures could be produced. A further substantial reduction of temperature and the occupied volume in phase space was achieved with evaporative cooling. This technique led to temperatures in the nanokelvin regime and allowed the first successful production of atomic Bose-Einstein condensates in 1995 [And95, Bra95, Dav95].

These ultracold gases are strongly affected by the quantum-wave nature of matter and the scattering properties no longer conform to classical physics but are determined by the laws of quantum mechanics [Wei99, Dal99b, Bur02]. In this ultracold regime atom-atom interactions can be controlled with the help of external electro-magnetic fields. This was demonstrated for the first time in 1998, when Feshbach resonances were observed in atomic gases and their influence on the interactions studied [Ino98, Cou98, Rob98].

The strength of atomic interactions and their repulsive or attractive character govern many properties of ultracold gases and, in particular, of Bose-Einstein condensates. This concerns the stability of a condensate, its density distribution and the nature of condensate excitations, to name a few. As a consequence, the possibility to control atomic interactions with Feshbach resonances has been a very important achievement and has lead to many important experiments. They comprise, for example, the realization of bright matter wave solitons [Kha02, Str02] as well as Bose-Einstein condensation of new atomic species [Cor00, Web03] and of molecules [Joc03, Gre03, Zwi03, Bou04].

Up to now, all experiments that applied Feshbach resonances used external magnetic fields to tune interactions. However, other schemes are possible as well. Even before the first experimental realization of Feshbach resonances in atomic gases, an optical scheme to induce scattering resonances was proposed [Fed96a, Boh97]. Laser light tuned close to a photoassociation transition al-

lows for the modification of atomic interactions just as in the case of magnetic Feshbach resonances (see section 2.5.1). Such optical resonances permit fast switching and a local tuning of interactions, since one can rapidly switch the laser intensity and produce spatially varying intensity patterns. Furthermore, optically induced resonances are always available. This distinguishes them from magnetic ones, which occur only for certain atomic spin states. Optical Feshbach resonances have been observed by Fatemi *et al.* [Fat00] in photoassociation spectroscopy and in the experiments described in this work. Fatemi *et al.* observed that the photoassociative production of molecules can be influenced by an additional laser, but the direct effect of the laser on atomic interactions and scattering properties was not studied.

This thesis reports on the realization of optical Feshbach resonances and their implementation to tune ultracold atomic interactions. We have used laser light at a single frequency as well as a two-color Raman scheme to induce optical scattering resonances. In our measurements we have directly investigated the effect of these resonances on the atomic s-wave scattering length in a ^{87}Rb Bose-Einstein condensate (BEC). The scattering length is a single parameter which describes the ultracold interactions. Our results show that we can optically control interactions and collision properties to a very high precision. All experiments have been performed with our new BEC apparatus, which has been constructed in the framework of this thesis.

The following chapter starts with a short summary of fundamental results from scattering theory before giving a first introduction to optical Feshbach resonances. In chapter 3 the essential properties of Bose-Einstein condensates and relevant equations are briefly outlined. To introduce the technical basis of our experiments, chapter 4 describes the experimental setup. Chapter 5 reports on the general experimental procedures we use and gives details on our production of ^{87}Rb BECs. In chapter 6 our measurements on optical Feshbach resonances are presented. Furthermore, a theoretical description of optical scattering resonances is given in this chapter, according to a model by Bohn and Julienne [Boh99]. This allows for more detailed discussions of our findings before chapter 7 summarizes our results and gives a short outlook.

Chapter 2

Ultracold Collisions and Feshbach Resonances

Many properties of ultracold quantum gases are determined by the particle-particle interactions and consequently these interactions are subject of broad physical interest. In the majority of experiments the gases are so dilute that interactions only manifest themselves in two-body collisions. Elastic two-body interactions are crucial for the thermalization of the atomic cloud and thus for evaporative cooling. They determine the stability and the shape of Bose-Einstein condensates as well as many other properties. Due to the great significance there is a strong interest not only to understand the nature of these two-particle interactions but also to be able to control them. Experimentally this control can be achieved with the help of Feshbach resonances, which have become an important topic in ultracold atom collisions. The presence of laser light can also strongly modify the collision process as is demonstrated by photoassociation of colliding atoms, to give a dramatic example. This raises the question if optical fields can be applied to modify elastic scattering as well.

The first sections of this chapter give a summary of basic results from ultracold elastic scattering theory and a short overview of inelastic processes. The next section describes fundamental aspects of Feshbach resonances and is followed by a section that deals with collisions in light fields and photoassociation. Finally an introductory discussion of optically induced scattering resonances lays the foundations of the experiments reported in this thesis. More detailed treatments of most topics presented here can be found in literature, e.g. [Sak94, Joa75, Dal99b, Wei99, Bur02], ranging from elementary introductions to reviews of important developments in the field of ultracold collisions.

2.1 Elastic Collisions

The scattering properties for binary collisions of two atoms with mass m and momenta p_1, p_2 depend on the interaction potential $V(\boldsymbol{r})$, where $\boldsymbol{r} = \boldsymbol{r}_1 - \boldsymbol{r}_2$ is the relative position of the atoms. Introducing the relative momentum $\boldsymbol{p} = 1/2(\boldsymbol{p_1} - \boldsymbol{p_2})$ and the reduced mass $m_r = m/2$ we only consider the relative motion. For an elastic scattering event with collision energy $E_k = \hbar^2 k^2/(2m_r)$ the Schrödinger equation to be solved is

$$\left(\frac{\hat{\boldsymbol{p}}^2}{2m_r} + V(\boldsymbol{r})\right)\psi_k(\boldsymbol{r}) = E_k\psi_k(\boldsymbol{r}). \tag{2.1}$$

All relevant collision processes happen in the presence of an interatomic potential $V(\boldsymbol{r})$ that is virtually zero for large distances. Under this condition and for an incident plane wave the solution of the scattering problem can asymptotically be written as a superposition of the incident wave and a scattered spherical wave:

$$\psi_k(\boldsymbol{r}) \sim e^{i\boldsymbol{k}\cdot\boldsymbol{r}} + f(k,\phi,\theta)\frac{e^{ikr}}{r}. \tag{2.2}$$

Here ϕ is the azimuthal angle around the direction of incidence $\boldsymbol{k}/k$ and θ is the angle between $\boldsymbol{k}/k$ and the direction of observation $\boldsymbol{r}/r$. The scattering amplitude $f(k,\phi,\theta)$ introduced in (2.2) depends on the potential V and describes all the scattering physics. One of the most important observables, the total scattering cross section σ, is obtained from f by integrating over the full solid angle

$$\sigma(k) = \int |f(k,\phi,\theta)|^2 d\Omega. \tag{2.3}$$

Partial Waves for Spherical Potentials

For a spherically symmetric scattering potential $V(\boldsymbol{r}) = V(r)$ the relative angular momentum is conserved and it is helpful to expand the scattering wave function in terms of angular momentum eigenfunctions. Due to symmetry the problem is independent of ϕ, and by using the so-called partial wave expansion ψ_k can be written as

$$\psi_k(\boldsymbol{r}) = \sum_{l=0}^{\infty} P_l(cos\theta)\frac{u_{k,l}(r)}{r}, \tag{2.4}$$

where $P_l(cos\theta)$ are the Legendre polynomials and the $u_{k,l}(r)$ are the radial wave functions. Inserting this expansion into the Schrödinger equation (2.1) yields separate one dimensional Schrödinger equations for the radial wave functions:

$$\frac{\hbar^2}{2m_r}\frac{\partial^2 u_{k,l}(r)}{\partial r^2} + \left(E_k - V(r) - \frac{\hbar^2 l(l+1)}{2m_r r^2}\right)u_{k,l}(r) = 0. \tag{2.5}$$

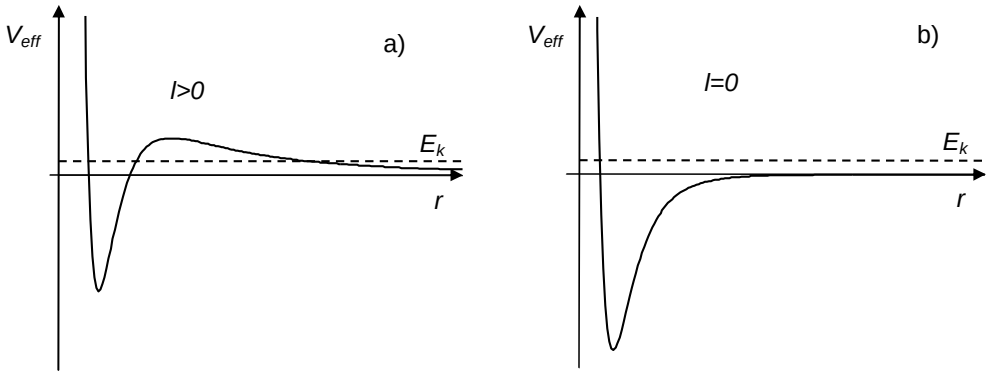

Figure 2.1: Effective potential V_{eff} for the radial parts of the partial waves. a) Partial waves with $l > 0$ experience a centrifugal barrier that inhibits collisions for low collision energies E_k. In b) V_{eff} is shown for s-waves (that is $l = 0$) where collisions can still occur.

This equation contains an effective potential $V(r) + \hbar^2 l(l+1)/(2m_r r^2)$, which is the sum of $V(r)$ and a centrifugal term. For partial waves with angular momentum $l > 0$ this adds a centrifugal barrier to the potential V and has prominent consequences in the limit of very low temperatures. In this ultracold regime the collision energy is so small that the centrifugal barrier effectively blocks all partial waves with $l > 0$ from the region where the potential $V(r)$ differs considerably from zero, see figure 2.1. Therefore only s-waves ($l = 0$) contribute to the scattering of ultracold atoms. For ground state collisions of most alkali atoms, including ^{87}Rb, the pure s-wave regime has typically been reached at temperatures below 0.1 mK to 1 mK [Wei03].

As a consequence of the spherical symmetry and the conservation of flux for each partial wave[1] the partial waves can be written as the sum of an incident and an outgoing spherical wave, which differ only by a relative phase shift $\delta_l(k)$. These scattering phases fully characterize the scattering process and one can express the total cross section as [Sak94]

$$\sigma(k) = \sum_{l=0}^{\infty} \frac{4\pi}{k^2}(2l+1)\sin^2(\delta_l(k)). \tag{2.6}$$

Identical Particles

So far it was assumed that the particles can be distinguished and that one could discriminate between the two scattering events shown in figure 2.2. In a sample of identical particles this is not the case and a modification of scattering amplitude and cross section is to be expected. For identical bosons, e.g.

[1]The total flux is conserved as the collisions are elastic. Due to angular momentum conservation this is true for each partial wave separately.

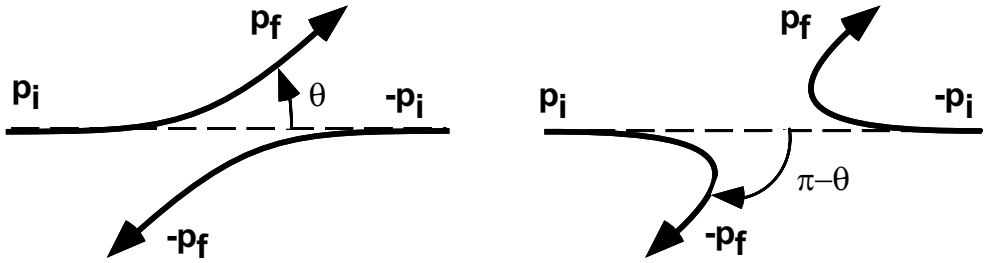

Figure 2.2: Two scattering events that can not be distinguished for identical particles. Adopted from [Dal99b].

for ^{87}Rb atoms, the wave function has to be symmetric with respect to the interchange of particles. This symmetrization procedure yields the scattering wave function $\psi_{k,sym}(\boldsymbol{r}) = 1/\sqrt{2}(\psi_k(\boldsymbol{r}) + \psi_k(-\boldsymbol{r}))$. Using the parity $(-1)^l$ of the Legendre polynomials one sees from (2.4) that for bosons only the even partial waves $l = 0, 2, 4, ..$ contribute to the scattering process but now with twice their weight. The symmetrization principle therefore results in an elastic cross section that reads for identical bosons

$$\sigma(k) = \sum_{l\,even} \frac{8\pi}{k^2}(2l+1)\sin^2(\delta_l(k)). \tag{2.7}$$

Rewriting $\sin^2(\delta_l(k))$ as $1/4\,|1 - \exp(2i\delta_l)|^2$ and introducing the scattering matrix element $S_{0,0}(l) = \exp(2i\delta_l)$ for elastic collisions of a given partial wave, equation 2.7 can be rewritten in terms of these S-matrix elements

$$\sigma(k) = \sum_{l\,even} \frac{2\pi}{k^2}(2l+1)|1 - S_{0,0}(l)|^2. \tag{2.8}$$

Note that here $|S_{0,0}(l)| = 1$, which only holds if no inelastic collisions are allowed. The S-matrix formalism is used in general collision theory and can also describe scattering events where inelastic processes are possible as well, see section 6.5. In this case the unitarity condition only applies to the total S-matrix and we have $|S_{0,0}(l)| \leq 1$ in general[2].

Collisions of Ultracold Atoms and Zero Energy Limit

As already seen from the effective potential for $u_{k,l}(r)$, higher partial waves with $l > 0$ play no role in the scattering process if the energy E_k is low enough. This can be deduced more rigorously form the so called Wigner threshold law

[2]To express the scattering matrix element by a phase shift, one has to use complex scattering phases δ_l in this general case (cf. section 6.5).

describing quantum scattering for $E_k \to 0$. According to this threshold law the phases δ_l vary as[3] [Mot65, Lan77, Wei99]

$$\delta_l \propto k^{2l+1} \quad \text{for} \quad k \to 0. \tag{2.9}$$

This scaling of the scattering phase has the important consequence that in the low energy limit only s-wave scattering takes place and the cross section approaches a constant value:

$$\sigma \to 8\pi a^2. \tag{2.10}$$

Here the s-wave scattering length

$$a = -\lim_{k\to 0} \tan(\delta_0(k))/k \tag{2.11}$$

has been introduced. The scattering length a is a single number which completely characterizes the interactions at very low temperatures. It is the essential parameter to describe Feshbach resonances (see section 2.3) and it is also important in the context of Bose-Einstein condensation. This is because a determines the mean-field interaction energy, which constitutes the dominant energy scale for a condensate in the Thomas-Fermi regime (see chapter 3). In consequence the scattering length governs many properties of the BEC and there is a strong interest to be able to control the value of a. Experimentally this control can be achieved by using Feshbach resonances (section 2.3).

2.2 Inelastic Processes

Besides the elastic interaction processes described in section 2.1 atoms can also encounter inelastic collisions. This class of collisions changes the internal state of the colliding atoms and releases the corresponding energy, which is carried away in the form of increased kinetic energy. These inelastic processes lead to atom loss from the BEC. In many cases the atoms gain enough energy to overcome the trapping potential and are lost from the trap.

In the context of Feshbach resonances loss processes are of special interest. One reason is that Feshbach resonances can be found and localized by monitoring losses, see for example [Ino98, Ste99a, Rob00, Chi00, Mar02, Ino04]. In the case of optically induced Feshbach resonances the strong inherent losses via excited molecular states will have to be considered in every application and they influence the possible tuning range of the scattering length a. Due to their experimental importance this section shortly summarizes the most relevant loss processes.

[3] To be more precise, the asymptotic behavior of δ_l depends on the potential $V(r)$. If the potential varies as $1/r^n$ the stated behavior is true only for $2l+3 < n$, e.g. for $l \leq 1$ and the ground state Van der Waals potential $\propto 1/r^6$. For $2l+3 \geq n$ we have $\delta_l \propto k^{n-2}$, see [Dal99b] for example.

Two-Body Decay

Inelastic two-body collisions change the internal state of the colliding atoms. Except for samples in the absolute ground state such collisions can set free a considerable amount of energy and lead to substantial loss rates. In addition, trapping neutral atoms in a magnetic trap is always sensitive to the spin state $|F, m_F\rangle$ of the atoms[4]. A change in sign of the magnetic quantum number m_F switches from repulsion to attraction and ejects the atom from the trap. As the absolute ground state cannot be stored magnetically, inelastic two-body collisions are always present in magnetic traps. Any two-body losses of the atom number N are described by the differential equation

$$\frac{\dot{N}}{N} = -K_2 \langle n(\boldsymbol{r}) \rangle = -K_2 \int \frac{n^2(\boldsymbol{r})}{N} \, d^3r, \tag{2.12}$$

where K_2 is the two-body loss rate coefficient and $\langle n(\boldsymbol{r}) \rangle$ is the average of the atomic density distribution weighted by $n(\boldsymbol{r})$.

For ^{87}Rb atoms in the doubly polarized state $|F = 2, m_F = \pm 2\rangle$ there is only one relevant inelastic two-body loss mechanism, the so-called dipolar spin relaxation, see for example [Met99]. The same applies to the stretched states $|F = 1, m_F = \pm 1\rangle$ in a laser cooled ^{87}Rb gas, because the energy < 1 mK is too low to populate the upper hyperfine states. The rate coefficient for dipolar relaxation in a $|F = 2, m_F = +2\rangle$ sample is about $1 \cdot 10^{-15}\,\mathrm{cm}^3/\mathrm{s}$ for a B-field of 2 G [Mar03, Boe96a, Jul97]. If the atoms are in the $|F = 1, m_F = -1\rangle$ state, the loss rate constant is even less: $K_2 \leq 10^{-17}\,\mathrm{cm}^3/\mathrm{s}$ [Mar03, Bur97].

The values given above are valid for thermal atoms. In a condensate the two-body inelastic rates are suppressed by a factor of 2 [Kag85, Bur97, Ket97]. This results from the different nature of density fluctuations. For a thermal gas (gaussian) density fluctuations occur and enhance the probability to find two atoms at the same position by a factor of two. In a condensate all atoms occupy the same quantum state and thermal fluctuations are absent. Thus the coherence properties of a condensate are reflected in a reduced collision rate[5].

Three-Body Recombination

Another loss process is the formation of Rb_2 molecules where the binding energy is released in the form of kinetic energy. To fulfill energy and momentum conservation at the same time, molecule formation can only take place in a tree-body collision. In such a recombination process the atom carries away 2/3 of the released binding energy and the molecule the remaining third. For ^{87}Rb

[4] To avoid confusion of atomic quantum numbers and those of the dimer atom-atom pair capitals will always refer to atomic quantum numbers and lower case letters to the dimer molecule.

[5] This also applies to elastic collisions, see for example [Ket97].

ground state atoms the highest lying molecular state has a binding energy $E_b \approx h \cdot 24\,\mathrm{MHz}$ [Wyn00b], which corresponds to a temperature of 1.2 mK. Therefore three-body recombination removes the three involved atoms from the BEC and transfers a considerable amount of kinetic energy to the reaction partners.

As three particles are involved the atom loss is now described by

$$\frac{\dot{N}}{N} = -K_3 \left\langle n^2(\boldsymbol{r}) \right\rangle = -K_3 \int \frac{n^3(\boldsymbol{r})}{N}\, d^3r. \tag{2.13}$$

For ^{87}Rb condensates in the $|F = 2, m_F = +2\rangle$ and $|F = 1, m_F = -1\rangle$ state, loss rate constants of $K_3 \approx 2 \cdot 10^{-29}\mathrm{cm}^6/\mathrm{s}$ [Söd99] and $K_3 \approx 6 \cdot 10^{-30}\mathrm{cm}^6/\mathrm{s}$ [Bur97] have been measured. Note that for thermal atoms the rates are larger by a factor of $6 = 3!$ [Kag85, Bur97, Ket97], again due to the coherence properties of a BEC[6]. Comparing these numbers with the two-body rate coefficients one finds that molecular recombination becomes important for atom densities above $10^{13}\,\mathrm{cm}^{-3}$ which are achieved in BEC experiments.

Inelastic Collisions in Light Fields

The presence of light fields can introduce additional inelastic loss channels via the release of internal energy after absorbing a photon. In the experiments presented in this thesis we use laser light, which has a detuning from the atomic transition that is much larger than the natural line width. Under this condition photoassociation is responsible for the only relevant light induced loss processes. Photoassociation is based on optically coupling the collisional state to an electronically excited molecular potential and is described in more detail in section 2.4. It only happens at a sizeable rate, if the laser is tuned close to the transition to a bound state in the excited potential. Then a photon from the laser field can photoassociate two colliding atoms to form an excited molecule. The created molecule decays again by spontaneous emission of a photon on a typical timescale of 10 ns. This decay most likely yields a pair of ground state atoms in non-trappable spin states or at substantially increased kinetic energy. With a probability of a few percent, vibrationally excited ground state molecules can be the outcome of the decay as well. In either case the process constitutes a loss channel from the cold atomic sample. As two atoms are involved this loss process is described by equation (2.12).

[6] Actually the factor of 3! is derived for non-interacting atoms and is modified slightly by atomic interactions [Kag85].

2.3 Scattering Length and Feshbach Resonances

Scattering resonances in collisions of ultracold atoms have become a very important and versatile tool to control atomic scattering properties in the last few years. After the first observation of a so-called Feshbach resonance in gases of ultracold atoms [Ino98, Cou98, Rob98] they have been applied in many experiments to tune interactions or to create ultracold molecules.

Feshbach resonances have been used to perform ultra-high resolution molecular spectroscopy [Chi00, Mar02], to coherently couple atoms in a BEC to molecular states [Don02] and to create bright matter wave solitons [Kha02, Str02]. By exploiting such Feshbach resonances to change the character of inter-particle interactions from attraction to repulsion (and to choose favorable collision rates) Bose-Einstein condensation of new atomic species has been achieved [Cor00, Web03]. In addition, molecules have been produced from ultracold atoms by ramping over a Feshbach resonance starting either from an atomic Fermi gas [Reg03, Str03, Xu03] or from an atomic BEC [Her03, Dür04]. Finally, it has been possible to achieve BEC of molecules created from pairs of fermionic atoms [Joc03, Gre03, Zwi03, Bou04]. Feshbach resonances are also very important in recent studies of (strongly interacting) Fermi gases, where they are used to tune from a molecular BEC state to the BCS regime, see [Bar04b, Bou04, Reg04, Zwi04, Bar04a, Kin04, Chi04a]. Recently Feshbach resonances have been observed in scattering between different atomic species [Sta04, Ino04]. Furthermore, magnetically tunable collision resonances have also been observed in collisions between ultracold molecules [Chi04b].

The basis of this wealth of experiments is the application of threshold scattering resonances to tune interactions in binary ultracold collisions and the connection of these resonances to the appearance of (weakly bound) molecular states. These topics shall be briefly discussed in this section.

2.3.1 Scattering Length in Ultracold Gases

Elastic scattering at very low temperatures is fully described by the s-wave scattering length a. Clearly a must depend on the interatomic potential $V(r)$ as it is the only parameter entering the cross section (see equation 2.10) and the potential needs to be reflected in the collision properties. The actual value of the scattering length is very sensitive to the van der Waals potential $V(r) = -C_6/r^6$ at long-range and the position of the short range repulsive part of the potential, which is often modelled by hard-core repulsion [Dal99b]. This sensitivity is reflected in the relation between scattering length and the position of the last bound molecular state. When the molecular potential is modified, e.g. by increasing the C_6-coefficient of a ground state potential, new bound

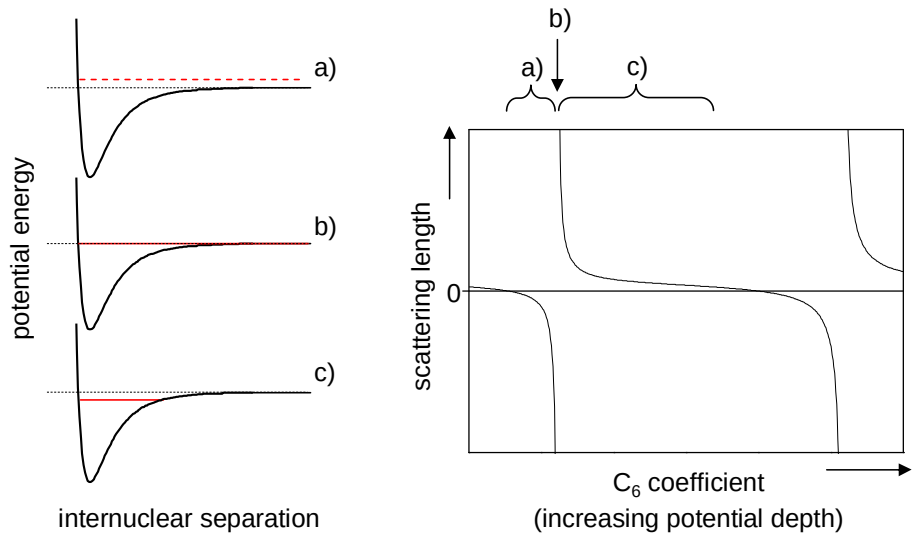

Figure 2.3: Dependence of the scattering length on the position of the last bound state. Increasing the potential depth, e.g. by increasing the C_6 coefficient, results in a divergence of a whenever a new bound state appears: A virtual bound state close above threshold corresponds to a negative scattering length a), which diverges if a real bound state appears b), and becomes positive for a weakly bound state just below threshold c).

state can appear. In this situation one finds a divergence of the scattering length whenever a new bound state occurs at the dissociation threshold, which is a consequence of the general Levinson theorem [Lev49]. If the new state is just below threshold, the scattering length is large and positive, while it is large and negative shortly before a virtual bound state crosses threshold from above to become a bound level [Dal99b, Gri93], see figure 2.3. This relation between a (positive) scattering length a and the position of the last bound state can be expressed quantitatively. For a scattering length significantly larger than the effective range of the potential, the binding energy E_B of the last bound state is given by $E_\mathrm{B} = \hbar^2/(2m_r a^2)$ [Sak94, Lan77].

2.3.2 Feshbach Resonances

Feshbach resonances have originally been a phenomenon in the field of nuclear reactions and have been described theoretically by Herman Feshbach [Fes58, Fes62]. When laser cooling allowed the realization of dilute atomic gases at very low temperatures s-wave scattering resonances became an issue in the physics of ultracold atomic collisions as well. Such resonances have been predicted in collisions of alkali atoms for the first time by Tiesinga et al. [Tie92, Tie93] and are now studied and applied in many experiments.

A Feshbach resonance in ultracold collisions occurs when a pair of colliding atoms is coupled to a bound state in a higher-lying molecular potential[7]. This situation is depicted in figure 2.4. Two incident atoms approach each other along their interaction potential V_o which is usually called the open or collisional channel. The figure also shows another potential V_c. For large internuclear distances it connects to a continuum at an increased energy. This continuum corresponds to atom pairs with internal states that have a higher energy, e.g. atoms in higher hyperfine state. The second potential V_c repre-

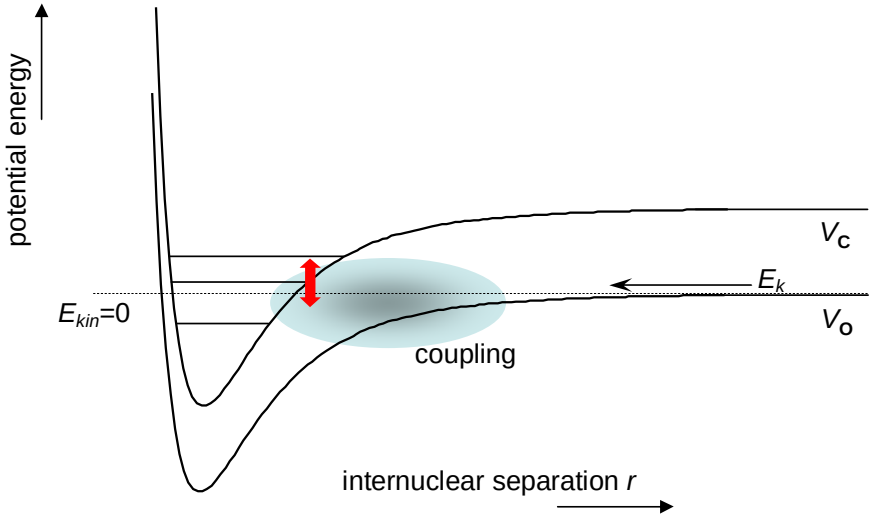

Figure 2.4: Occurrence of a Feshbach resonance in an atomic collision. The scattering state of the open channel V_o is coupled to a bound level in the closed channel V_o. The resonance can be tuned by modifying the relative position of scattering and bound state (indicated by the red arrow).

sents a so-called closed channel if the scattering energy of the incident atoms lies below the dissociation threshold of V_c. If there is a coupling between the two channels the effective collision potential is modified due to a mixing of the potentials V_o and V_c. As described in the last section a modification of the collision potential results in a variation of the scattering length a that is correlated to the varying position of the last bound state. The influence on a can also been deduced by looking at the collision wave function, which depends on the shape of the scattering potential. If the potential is modified the scattering wave function is modified as well. In consequence the scattering phase δ_0 changes (see section 2.1) and this is reflected in a varying scattering length according to the definition (2.11).

[7] As all other interatomic potentials in this thesis, the potential is understood to be an interaction potential in the Born-Oppenheimer approximation, see for example [Hak98].

In the case of a Feshbach resonance the energy where the scattering process becomes resonant is linked to the position of the bound state[8] in the closed channel. The Feshbach resonance appears when this bound state coincides energetically with the incident collisional state[9]. Here the situation is very much as in the previous section: if the bound state of the closed channel approaches the resonance from below, the scattering length increases, while it is decreased for a bound states located just above the resonance energy.

Tuning the Scattering Length with Feshbach Resonances

There have been different proposals how to couple the collisional state to a bound level so that the scattering length can be modified at will. These proposals comprise coupling schemes exploiting external radio-frequency fields [Moe96], static electric fields [Mar98] and optical fields [Fed96a, Boh97]. However, the first proposals suggested the use of magnetic fields to tune the scattering properties of alkali atoms [Tie92, Tie93, Moe95, Vog97, Boe96b]. Such magnetically tunable Feshbach resonances occur when the open and the close channel have different magnetic moments and the relative position of the two potentials can be shifted by varying an external magnetic field. Obviously, this allows to control the energy difference of a given bound state in the closed channel and the incident continuum state. Thus the scattering length can be tuned if there is some coupling between V_o and V_c which can arise from Coulomb (or so-called "chemical") interactions and from spin-spin or spin-orbit interactions.

Up to now all experiments applying Feshbach resonances to tune the scattering properties have used the last type of resonances. For these magnetically induced resonances a variation of the scattering length according to

$$a = a_{\mathrm{bg}} \left(1 - \frac{\Delta_B}{B - B_{\mathrm{res}}}\right) \tag{2.14}$$

has been predicted [Moe95] and observed experimentally [Ino98]. Here a_{bg} is the off-resonant background scattering length, Δ_B is the width and B_{res} the position of the resonance. The resonance width Δ_B is determined by the coupling between open and closed channel and by the shift of the two potentials as a function of the B-field [Moe95, Tim99]. Equation (2.14) shows that very large positive and negative values of the scattering length can be realized with magnetic Feshbach resonances. However, around a (magnetic) Feshbach resonance inelastic losses are typically enhanced as well as elastic scattering. In general this applies to two- and three-body processes [Tie92,

[8] Often such a state is rather called a "quasi-bound" than a "bound" state as it is coupled to the continuum of the open channel, but this distinction will not be made here.

[9] To be more precise, the actual resonance position is shifted from the energy of the unperturbed bound state due to the coupling between the open and closed channel. However the coupling is usually weak and the offset can be neglected [Moe95, Tim99].

Tie93, Fed96b, Ste99a, Rob00] except for samples in the absolute ground state where only three-body losses are possible. If two-body losses are present, the scattering length no longer diverges at resonance, as stated by (2.14), but shows a dispersive behavior. While for many atomic species Feshbach resonances have been found and applied where losses are no problem at all, they can be so severe for certain species and spin states that they effectively limit the tuning range of the scattering length, as has been observed in a ^{23}Na BEC [Ino98, Ste99a] for instance. On the other hand, resonant enhancement of losses can come in handy to find and localize a Feshbach resonance, see for example [Chi00, Mar02, Ino04].

2.4 Optical Collisions and Photoassociation

Following the proposal in [Fed96a] scattering resonances can also be in induced with laser light. The proposed scheme involves collisions in a light field and is closely related to photoassociation [Boh97]. Therefore, this type of optical collisions, to use a common term, is described in this section.

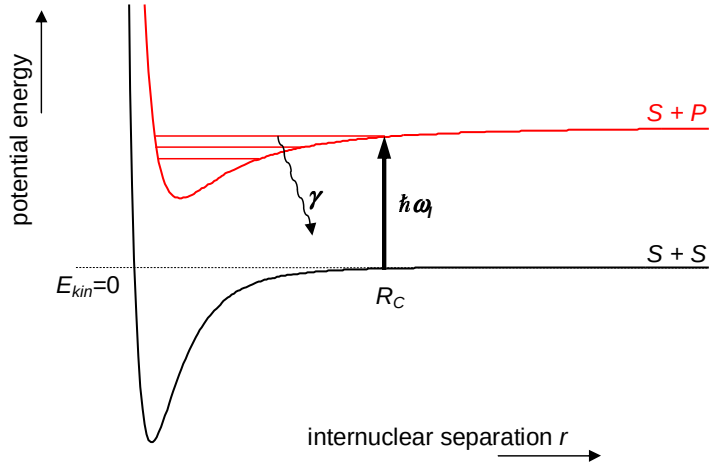

Figure 2.5: Schematic diagram of the molecular potential for two ground-state atoms $(S + S)$ and an attractive excited potential connecting to an $S + P$ asymptote. An optical free-bound transition and the subsequent decay are indicated.

Figure 2.5 shows the two potentials that are involved in an optical collision. At very short distances the coulomb interaction of the two nuclei gives rise to a strong repulsion while at large distances the interaction is described by either a van der Waals term $V(r) = -C_6/r^6$ for the electronic ground state or a dipole potential $V(r) = \mp C_3/r^3$ for the excited $S + P$ states[10], see figure

[10] As usual, the angular momentum state of the atomic electron shell is denoted by capital

2.5). If atoms collide in the presence of a light field with frequency ω_l they can be excited to a dipole potential. The outcome of such an optical collision depends on the laser detuning from the single-atom transition frequency and the involved potentials. For the experiments in chapter 6 only photoassociation is important. Thus the following discussion is limited to this process. In ultracold gases photoassociation typically takes place at rather large atom separation and therefore the term "potential" normally refers to the long-range part only.

Photoassociation requires laser light that is red detuned relative to a single-atom (D-line) transition. Then an optically driven free-bound transition can couple the pair of colliding ground state atoms to a bound state in an excited potential. This happens around the Condon point R_C [Wei99], which is the internuclear separation where the laser frequency ω_l matches the energy difference between the ground state potential $V_\mathrm{G}(r)$ and excited state potential $V_\mathrm{E}(r)$: $\hbar\omega_l = V_\mathrm{E}(R_C) - V_\mathrm{G}(R_C)$. For a collisional state described by the wave function $\psi_\mathrm{G}(r,k)$ and an excited molecular level $\psi_\mathrm{E}(r)$ the strength of the optical free-bound coupling is characterized by

$$\Gamma_\mathrm{stim} = \frac{4\pi^2 I_\mathrm{laser} {d_\mathrm{E}}^2}{c} |\langle\psi_E(r)|\psi_G(r,k)\rangle|^2. \tag{2.15}$$

Here I_laser is the laser intensity and d_E the molecular dipole transition element, see [Boh97, Wei99]. This parameter can be determined from Fermi's golden rule and represents the stimulated transition rate from the excited molecular level back to the ground state continuum [Boh96]. In equation 2.15 the bound state wave function is normalized to unity, $\langle\psi_\mathrm{E}|\psi_\mathrm{E}\rangle = 1$, while the collisional wave function $\psi_\mathrm{G}(r,k)$ is assumed to be energy normalized, i.e. the solutions of (2.4) and (2.5) are multiplied by a factor $\sqrt{mk/(\pi\hbar^2)}$ to obtain $\langle\psi_\mathrm{G}(r,E)|\psi_\mathrm{G}(r,E')\rangle = \delta(E-E')$ [Jul01, Wei99]. In consequence, the parameter Γ_stim is proportional to the collision wave vector k.

Equation (2.15) shows that for efficient photoassociation a good Franck-Condon overlap $\langle\psi_\mathrm{E}(r)|\psi_\mathrm{G}(r,k)\rangle$ between ground and excited state is very important. Starting from a continuum state of ultracold colliding atoms with large de Broglie wavelength $2\pi/k$ sizable Franck-Condon factors are obtained mainly for bound states close to the dissociation limit and for states in so-called long-range potentials. In consequence, only these states are accessible in photoassociation experiments. Typical Condon points range from tens to hundreds of Bohr radii, which means that essentially the long-range part of the molecular potentials $V_\mathrm{G}(r)$ and $V_\mathrm{E}(r)$ is probed.

If the frequency ω_l of the photoassociation laser is scanned, atom losses from the sample can be observed whenever the light field resonantly couples

letters S, P, D, .. while lower case letters are used for the angular momentum of the atom pair's relative motion.

$\psi_G(k)$ to a bound states in an excited potential. Observing these losses as a function of the laser frequency thus allows to obtain a spectrum of molecular states in the excited potential[11]. An important feature that distinguishes ultracold photoassociation from "normal" molecular spectroscopy is the very high resolution limited only by the natural molecular line widths on the order of 10 MHz. The high resolution is a consequence of the extremely low kinetic energies in ultracold samples. Even more narrow features can be observed in two-color photoassociation.

Figure 2.6 schematically depicts such a two-color or Raman photoassociation process. Two lasers are used to couple a pair of colliding atoms to a molecular level in the ground state potential. The two lasers allow a coherent two-color Raman transition that corresponds to the absorption of a photon with energy $\hbar\omega_1$ from the first laser field and subsequent stimulated emission of another photon with a frequency ω_2 given by the second light field. In this way the scattering state of two free atoms is connected to a rovibrational level in the ground state potential. The strength of the coupling is again restricted by the Franck-Condon overlap of the involved states and therefore only highly vibrationally excited molecular states are accessible. Employing Raman photoassociation to measure the energies of the last bound states in the molecular ground state potential is a precise method to determine properties of this potential, such as the C_6 coefficient and the scattering length a (see [Bur02, Wyn00b, Wei99] and references therein). Starting from a BEC such Raman processes have been used to achieve very high spectroscopic resolutions on the order of 1 kHz and to produce ^{87}Rb dimers at rest [Ger00, Wyn00a].

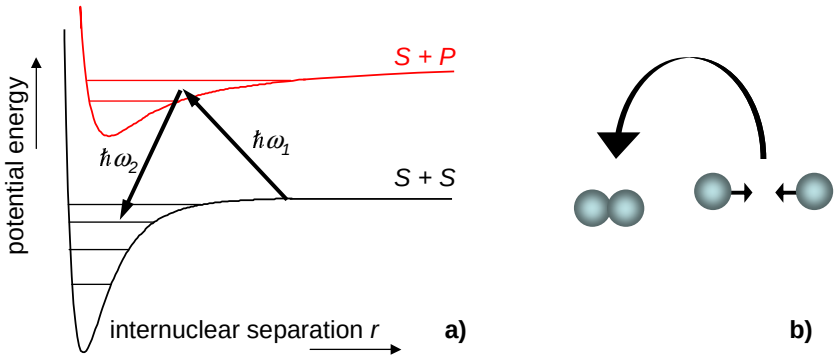

Figure 2.6: Schematic depiction of a Raman process in photoassociation. a) Involved molecular states and lasers. b) Ground state atoms are photoassociated to a ground state molecule.

[11] Instead of monitoring losses one can also add further lasers to photoionize the excited molecules and detect the ions. Both techniques have delivered precise spectroscopic data, see for example [Wyn00b, Wei99] and references therein.

2.5 Optically Induced Feshbach Resonances

Feshbach resonances are an important tool in the physics of ultracold atoms and magnetically tunable Feshbach resonances are in common use. However, other schemes to realize a scattering resonance may turn out to have advantages in certain applications. Especially when it comes to fast switching of the scattering length or to addressing only a part of the atom cloud, optical coupling schemes offer excellent control. This is because laser beams can be switched very fast and allow spatially resolved intensity patterns. The use of optical fields to modify the scattering length in atomic collisions has been proposed by Fedichev *et al.* [Fed96a] and has been further discussed by Bohn and Julienne [Boh97, Boh99]. Optical s-wave scattering resonances have been observed in one-color photoassociation spectroscopy by Fatemi *et al.* [Fat00] and in the experiments reported in this thesis [The04, Tha05b]. Fatemi *et al.* have identified the resonance via a modification of the photo-ionization signal. In our experiments we induce optical Feshbach resonances with one-color and two-color laser schemes and we analyze the tuning of the scattering length by means of a direct measurement, see chapter 6. To discuss the experimental data we use the convenient theoretical model by Bohn and Julienne.

This section serves as an introduction to the most essential aspects of optical Feshbach resonances and it presents basic results from the theoretical model in [Boh99]. A more detailed treatment can be found in sections 6.3.2, 6.4.1 and 6.5 of chapter 6.

2.5.1 One-Color Optical Feshbach Resonance

Optically induced scattering resonances use laser light to couple two colliding atoms to a bound molecular level. In a single-photon scheme, as discussed in this section, the bound state belongs to an excited molecular potential $V_e \propto C_3/r^3$, which constitutes the closed channel for the Feshbach resonance. Changing the detuning Δ_1 of the laser from the photoassociation transition allows to tune over the resonance and modify the scattering properties.

Here a note concerning the term "optical Feshbach resonance" should be added. Some physicists prefer to make a distinction between scattering resonances due to intrinsic coupling, e.g. by Coulomb or spin interactions, and such resonances where the coupling is due to external fields. Then the name "Feshbach resonance" is only applied to the first case and not to optically induced resonances [Bur02]. However, from a general point of view both are realizations of the same phenomenon, a scattering resonance, and they are described by the same theoretical formalism. To stress the close relation to the well-known magnetically tunable resonances the term "optical Feshbach resonance" will be used in this thesis.

The close analogy to the discussion of Feshbach resonances in section 2.3 is most apparent in the dressed state picture shown in figure 2.7. Within this picture the excited molecular potential V_e is shifted by the energy $\hbar\omega_1$ of a laser photon towards the ground state potential V_g. Then the bound molecular state deviates from the threshold of the open channel V_g by the laser detuning Δ_1 and we recover the situation depicted in figure 2.4.

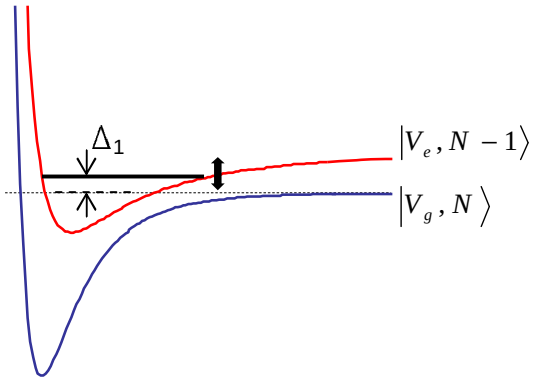

Figure 2.7: Optical scattering resonance depicted in a dressed state picture. The excited potential $|V_\mathrm{e}, N-1\rangle$ is separated from the ground state potential $|V_\mathrm{g}, N\rangle$ by the laser detuning Δ_1. Here N denotes the number of photons in the light field.

Quantitative Description of Optical Feshbach Resonances

For a quantitative description of optical Feshbach resonances, we need to introduce the parameters and terms shown in the left part of figure 2.8. A pair of ultracold atoms in the scattering state $|0\rangle$ collides along the ground state potential. Due to the low temperature the collision energy $E = \hbar^2k^2/(2m_\mathrm{r})$ of the continuum state $|0\rangle$ is very close to the threshold of the open channel potential. Laser light with intensity I_1 and frequency ω_1 couples this state to an excited molecular level $|1\rangle$. This free-bound coupling is described by the resonant stimulated transition rate Γ_stim introduced in equation (2.15). Experimentally we can control the coupling via the laser intensity and its detuning $\Delta_1 = E_1/\hbar - \omega_1$ from the photoassociation resonance. Here E_1 is the energy of state $|1\rangle$ relative to the threshold of the collision potential. The decay of the excited molecular level, which is described by a spontaneous decay rate γ_1, is also indicated in the figure. This constitutes an inelastic channel for the collision process, because atoms can be lost from the sample by a stimulated transition to the molecular state $|1\rangle$ and its subsequent decay.

Bohn and Julienne [Boh97, Boh99] give analytic expressions for the scattering length a and the inelastic loss rate coefficient K_inel as a function of the laser detuning Δ_1, see section 6.3.2 and section 6.5. If we assume that $\Gamma_\mathrm{stim} \ll \gamma_1$,

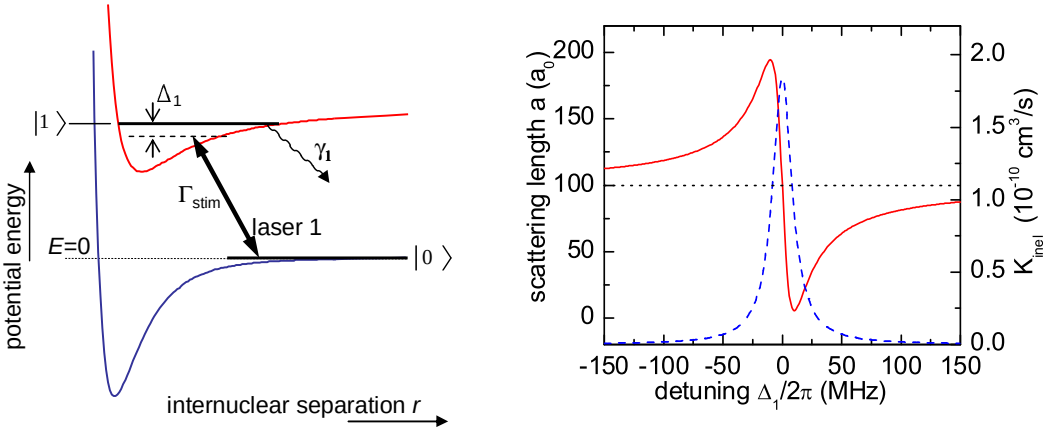

Figure 2.8: Optical Feshbach Resonance. Left: Schematic diagram of the optical coupling between collisional and molecular state due to a single laser (not to scale). Right: Scattering length a (solid line) and inelastic collision rate coefficient $K_{\rm inel}$ (broken line) as a function of Δ_1 for typical parameters: $\Gamma_{\rm stim}/2\pi = 50\,$kHz, $\gamma_1/2\pi = 20\,$MHz, $k = 2.5\times10^5\,$m^{-1}, $a_{\rm bg} = 100a_0$ (indicated by dotted line, a_0 is the Bohr radius).

which turns out to be the case in our experiments, and if we consider atoms in a BEC [12] these expressions read

$$a = a_{\rm bg} - \frac{1}{2k}\,\frac{\Gamma_{\rm stim}\;\Delta_1}{\Delta_1^2 + (\gamma_1/2)^2} \tag{2.16}$$

$$K_{\rm inel} = \frac{2\pi\hbar}{m}\,\frac{1}{k}\,\frac{\Gamma_{\rm stim}\;\gamma_1}{\Delta_1^2 + (\gamma_1/2)^2}\;. \tag{2.17}$$

Here a_{bg} is the non-resonant background value of the scattering length for the case where no optical coupling is present. According to section 2.4 the parameter $\Gamma_{\rm stim}$ is proportional to the collision wave vector k. In consequence a and $K_{\rm inel}$ have well defined values independent of the collision momentum. In particular, equation (2.16) is consistent with the Wigner threshold law, which requires a constant scattering length in the limit of small k, see section 2.1. Equation (2.17) relates the parameter $\Gamma_{\rm stim}$ to the quantity $K_{\rm inel}$, which can be observed experimentally and allows a measurement of $\Gamma_{\rm stim}$.

To depict the content of equations (2.16) and (2.17), a and $K_{\rm inel}$ are plotted versus the detuning Δ_1 in figure 2.8 for typical experimental parameters. While the losses exhibit a Lorentzian profile, the scattering length shows a dispersive variation when Δ_1 is tuned. If we rewrite (2.16) as

$$a = a_{\rm bg}\left(1 - \frac{\Delta_{\rm Fesh}\Delta_1}{\Delta_1^2 + (\gamma_1/2)^2}\right)\,, \tag{2.18}$$

[12] Note that, according to the discussion in section 2.2, $K_{\rm inel}$ would be larger by a factor of two for non-condensed atoms.

with $\Delta_{\mathrm{Fesh}} = \Gamma_{\mathrm{stim}}/(2ka_{\mathrm{bg}})$, we see that we only obtain a divergence of the scattering length for a vanishing decay rate γ_1. This shows that the presence of (strong) two-body losses constitutes the essential difference to the magnetic Feshbach resonances between atoms in the absolute ground state, cf. equation (2.14).

As can be seen from the denominator in equations (2.16) and (2.17), the resonance width is simply given by the loss rate γ_1. It should be noted that besides Δ_1 also the laser intensity I_1 enters the equations for a and K_{inel} because $\Gamma_{\mathrm{stim}} \propto I_1$. This yields two experimental parameters that control elastic and inelastic scattering.

2.5.2 Raman Scheme for Optical Feshbach Tuning

By adding a second laser, as shown in figure 2.9, it is possible to employ a coherent Raman scheme for coupling the pair of colliding atoms (state $|0\rangle$) to a high-lying molecular level $|2\rangle$ in the ground state potential. Again it can be expected that this allows to realize an optical scattering resonance if the stimulated Raman transition is tuned to match the molecular state $|2\rangle$.

In this situation there are four parameters that influence the coupling: the intensities I_1 and I_2 of the lasers 1 and 2 and the detunings $\Delta_1 = E_1/\hbar - \omega_1$

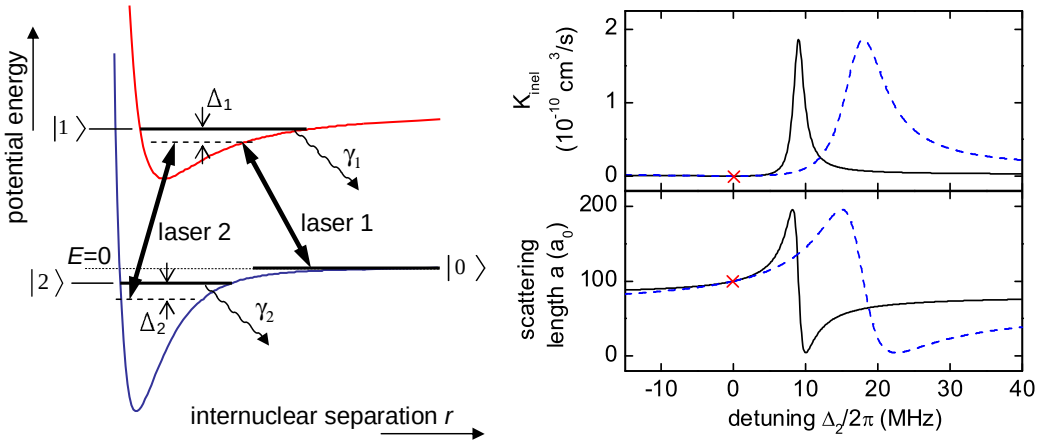

Figure 2.9: Raman scheme for inducing an optical Feshbach resonance. Left: Diagram showing the relevant states and transitions. Right: Scattering length and inelastic collision rate K_{inel} according to equations (2.19) and (2.20). Both are plotted versus the detuning Δ_2 for the case of a molecular state $|2\rangle$ with negligible decay rate γ_2. The solid line corresponds to $\Delta_1/2\pi = 100\,\mathrm{MHz}$ and the broken line to $\Delta_1/2\pi = 50\,\mathrm{MHz}$. Other parameters: $\Gamma_{\mathrm{stim}}/2\pi = 50$ kHz, $\Omega_{12}/2\pi = 30\,\mathrm{MHz}$, $\gamma_1/2\pi = 20$ MHz, $k = 2.5 \times 10^5$ m^{-1}, $a_{\mathrm{bg}} = 100\,a_0$. The cross marks the positions where $\Delta_2 = 0$.

and $\Delta_2 = E_2/\hbar - (\omega_1 - \omega_2)$. Here E_1 and E_2 are the energies of state $|1\rangle$ and $|2\rangle$ relative to the threshold of the collision potential. Note that Δ_2, as defined here, is a two-photon detuning while Δ_1 refers to a one-photon process. According to their definitions both detunings are positive if the relevant transition is tuned below the molecular level. The strengths of the two optical transitions are represented by $\Gamma_{\text{stim}} \propto I_1$ for the free-bound coupling of laser 1 and by a Rabi frequency $\Omega_{12} \propto \sqrt{I_2}$, which describes the bound-bound coupling due to laser 2, see section 6.4.1.

From the general theory in [Boh99] we can extract equations that describe the scattering length and the inelastic collision rate coefficient for this Raman coupling scheme (cf. section 6.4.1 and section 6.5):

$$a = a_{\text{bg}} - \frac{1}{2k} \frac{\Gamma_{\text{stim}} \, (\Delta_1 - \Omega_{12}^2/\Delta_2)}{(\Delta_1 - \Omega_{12}^2/\Delta_2)^2 + (\gamma_1/2)^2} \tag{2.19}$$

$$K_{\text{inel}} = \frac{2\pi\hbar}{m} \frac{1}{k} \frac{\Gamma_{\text{stim}} \, \gamma_1}{(\Delta_1 - \Omega_{12}^2/\Delta_2)^2 + (\gamma_1/2)^2} \, . \tag{2.20}$$

These simplified equations assume that the decay of state $|2\rangle$ can be neglected, i.e. the spontaneous decay rate of state $|2\rangle$ is $\gamma_2 = 0$, and that $\Gamma_{\text{stim}} \ll \gamma_1$. As before, the inelastic rate K_{inel} is given for atoms in a BEC. Setting $\Omega_{12} = 0$, which corresponds to switching off laser 2, reproduces equations (2.16) and (2.17). To investigate the new tuning possibilities Δ_1 is held constant and a and K_{inel} are studied as functions of the Raman detuning Δ_2. Again we obtain resonant losses and a dispersive variation of the scattering length as shown in figure 2.9. When Δ_1 is decreased, we observe an increasing asymmetry of the graphs for a and K_{inel}, as well as an enlarged width of the resonance features. Further the position of the resonance $\Delta_{2,\text{res}}$ shifts when the detuning Δ_1 is modified and is determined by $\Delta_{2,\text{res}} = \Omega_{12}^2/\Delta_1$.

Properties of Two-Color Feshbach Resonances

It is well known that a coherent Raman scheme extinguishes losses via the upper state $|1\rangle$ when the Raman detuning Δ_2 is set to zero. This effect can be understood as a quantum interference between two paths leading to the same decay channel: $|0\rangle \rightarrow |1\rangle \rightarrow$ loss γ_1 and $|0\rangle \rightarrow |1\rangle \rightarrow |2\rangle \rightarrow |1\rangle \rightarrow$ loss γ_1 [Boh96]. But this suppression of loss cannot be exploited to tune the elastic collision properties while keeping the loss rate close to zero. Equation (2.19) shows that for $\Delta_2 = 0$ we always have $a = a_{\text{bg}}$. However, measuring the losses for $\Delta_2 = 0$ can be used to obtain information on the coherence of the coupling between states $|0\rangle$ and $|2\rangle$.

Equations (2.19) and (2.20) have the same general form as those for the one-photon case. Thus the maximum tuning range of scattering length can not be increased by employing a Raman scheme. Also, for a given change in scattering length $a - a_{\text{bg}}$ the loss rate coefficient is not reduced compared to

a one-photon optical resonance. Clearly this is only true if one sticks to the same excited molecular state $|1\rangle$, i.e. the same parameters $\Gamma_{\rm stim}$ and γ_1.

By expanding (2.19) and (2.20) about the resonance position Ω_{12}^2/Δ_1, we can rewrite these equations in a form which allows a convenient comparison with the one-color Feshbach resonance. Neglecting terms of second order in $(\Delta_2 - \Omega_{12}^2/\Delta_1)$ we obtain

$$a = a_{\rm bg} - \frac{1}{2k}\,\frac{\widetilde{\Gamma}\,(\Delta_2 - \Omega_{12}^2/\Delta_1)}{(\Delta_2 - \Omega_{12}^2/\Delta_1)^2 + (\widetilde{\gamma}/2)^2} \tag{2.21}$$

$$K_{\rm inel} = \frac{2\pi\hbar}{m}\,\frac{1}{k}\,\frac{\widetilde{\Gamma}\,\widetilde{\gamma}}{(\Delta_2 - \Omega_{12}^2/\Delta_1)^2 + (\widetilde{\gamma}/2)^2}\ , \tag{2.22}$$

where $\widetilde{\Gamma} = \Gamma_{\rm stim}\left(\frac{\Omega_{12}}{\Delta_1}\right)^2$ is the effective resonant transition rate and $\widetilde{\gamma} = \gamma_1\left(\frac{\Omega_{12}}{\Delta_1}\right)^2$ the resonance width. These expressions exhibit a strong analogy to the one-color Feshbach resonance. The detuning Δ_2 has effectively taken the place of Δ_1, while the equations have the same shape as for the single-laser scheme. Merely the resonance position has shifted by Ω_{12}^2/Δ_1.

Chapter 3

Bose-Einstein Condensates

The quantum nature of atoms results in several fascinating phenomena that cannot be explained by classical physics. One manifestation of quantum behavior are the peculiar scattering properties at ultracold temperatures, which have been introduced in chapter 2 already. When the temperature T is so low that the de Broglie wavelength

$$\lambda_{\mathrm{dB}} = \sqrt{\frac{2\pi\hbar^2}{m k_{\mathrm{B}} T}} \tag{3.1}$$

becomes comparable to the effective range of the interaction potential, the collision processes are determined by quantum mechanics and can no longer be described by classical or semiclassical models[1].

Another very prominent consequence of quantum physics concerns the statistics of bosonic gases. At temperatures even lower than those required for quantum scattering a regime is reached where the wave packets of individual particles begin to overlap, see figure 3.1. In this situation Bosons, such as ^{87}Rb atoms for instance, begin to macroscopically populate the ground state and can be described by a single condensate wave function. This transition from thermally distributed atoms to a large occupation of the ground state, constitutes the phase transition connected to Bose-Einstein condensation.

Quantitatively the increasing overlap of the atomic wave functions can be expressed by the phase-space density $D = n\lambda_{\mathrm{dB}}^3$, which is defined as the product of spacial atom density n and λ_{dB}^3. Then the onset of BEC corresponds to D reaching unity. This simple consideration turns out to be close to the result from a quantum statistical treatment of a non-interacting Bose gas. In the limit of large particle number $N \to \infty$ and weak (harmonic) trapping, theory yields a critical peak phase space density $D_{\mathrm{c}} = \zeta(3/2) \approx 2.612$ for the BEC

[1] To determine the onset of quantum scattering behavior more rigorous definitions can be made. One possibility is to compare the scattering energy with the height of the centrifugal barrier for states with $l > 0$ [Met99]. A more elaborate distinction is made in [Jul89, Jul92] by observing when the WKB approximation for the scattering wave function breaks down.

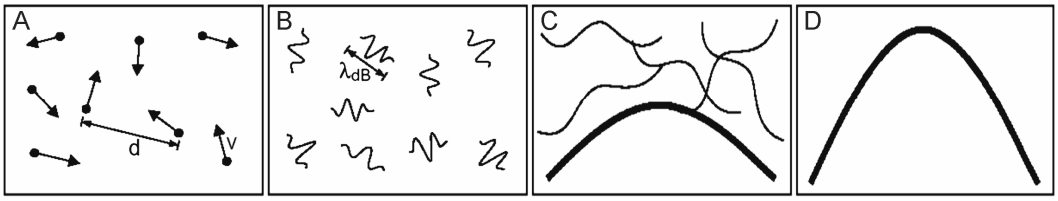

Figure 3.1: Illustrative description of BEC. A thermal gas at high temperatures can be viewed as a system of classical "billiard balls" (A). Reducing temperature increases the de Broglie wavelength and yields a system of atomic wave packets that exhibits quantum scattering (B). At even lower temperatures the wave functions start to overlap and a BEC component appears (C). For $T = 0$ all atoms share the same macroscopic wave function and form a pure condensate (D). Figure adapted from [Ket99].

transition. Here ζ denotes the Riemann zeta function $\zeta(x) = \sum_{n=1}^{\infty} n^{-x}$. Corrections due to atomic interactions and the finite particle number are typically as small as a few percent [Dal99a, Bon02, Pit03].

The theoretical derivation of D_c and other thermodynamical quantities starts from the bosonic distribution function

$$N_\nu = \frac{1}{e^{(\epsilon_\nu - \mu)/(k_B T)} - 1} \tag{3.2}$$

for a trapped ideal gas with single particle states ν of energy ϵ_ν. Here the chemical potential μ appears, which is determined by the condition that $\sum_{\nu \geq 0} N_\nu$ equals the total atom number. A statistical treatment of the thermal, non-condensed component in a 3-dim harmonic trap, i.e. the atoms in the excites states ($\nu > 0$), yields a critical temperature

$$T_c = \frac{\hbar \bar{\omega}}{k_B} \left(\frac{N}{\zeta(3)} \right)^{1/3} \approx 0.94 \frac{\hbar \bar{\omega}}{k_B} N^{1/3} \tag{3.3}$$

for the BEC transition, see for example [Dal99a, Pit03]. In equation (3.3) $\bar{\omega} = (\omega_x \omega_y \omega_z)^{1/3}$ is the geometric average of the trapping frequencies and $\zeta(3) \approx 1.202$. By evaluating the density distribution of the Bosons [Nar98, Dal99a] at the trap center and inserting the expression for T_c into equation (3.1) one also obtains the critical phase-space density stated above.

There exist several review articles and textbooks on the topic of Bose-Einstein condensation, e.g. [Dal99a, Ket99, Bon02] and [Pet02, Pit03]. Due to the extensive coverage in literature this chapter only provides a very short summary of the basics of BEC and introduces some of the most relevant results.

3.1 BEC of Interacting Atoms

To describe a BEC of trapped interacting atoms, one usually starts from the many-body Hamiltonian in second quantization, as it is done in [Pit03] for example. Rather than solving the full many-body Hamiltonian numerically the Bogoliubov approximation [Bog47] can be used to describes the interactions by a mean-field method. The Bogoliubov ansatz consists in writing the bosonic field operators $\hat{\Psi}(\boldsymbol{r},t)$ and $\hat{\Psi}^\dagger(\boldsymbol{r},t)$ that annihilate and create a particle at position $\boldsymbol{r}$ as a sum $\hat{\Psi}(\boldsymbol{r},t) = \Phi(\boldsymbol{r},t) + \hat{\Psi}'(\boldsymbol{r},t)$ of the complex function $\Phi(\boldsymbol{r},t)$ and a first order perturbation term $\hat{\Psi}'(\boldsymbol{r},t)$. While the latter represents excitations of the system, the complex field $\Phi(\boldsymbol{r},t) = \langle\hat{\Psi}(\boldsymbol{r},t)\rangle$ describes the Bose-condensed atoms. The function $\Phi(\boldsymbol{r},t)$ determines the condensate density via $n = |\Phi(\boldsymbol{r},t)|^2$ and is often called the "condensate wave function".

For the Bogoliubov approximation to be valid the majority of the atoms need to be in the BEC and consequently the number of condensed atoms must be large, $N \gg 1$, see [Pit03][2]. In most experiments the quantum gases are very dilute in the sense that the scattering length a is much smaller than the particle separation, $n|a|^3 \ll 1$. Under this condition only two-body interactions are relevant and ultracold interactions are fully characterized by the value of a. As a consequence, the potential $V_{\text{int}}(\boldsymbol{r},\boldsymbol{r}')$ can be replaced by an effective contact interaction $g\delta(\boldsymbol{r},\boldsymbol{r}')$, where the coupling constant

$$g = \frac{4\pi\hbar^2 a}{m} \tag{3.4}$$

describes the inter-particle interactions [Pit03].

These approximations allow to derive an important equation for the condensate wave function Φ, which is called the Gross-Pitaevskii equation [Gro61, Pit61]

$$i\hbar\frac{\partial}{\partial t}\Phi(\boldsymbol{r},t) = \left(-\frac{\hbar^2}{2m}\nabla^2 + V_{\text{ext}}(\boldsymbol{r}) + g|\Phi(\boldsymbol{r},t)|^2\right)\Phi(\boldsymbol{r},t). \tag{3.5}$$

Writing $\Phi(\boldsymbol{r},t)$ as $\phi(\boldsymbol{r})\exp(-i\mu t/\hbar)$ finally yields the time-independent equation

$$\mu\phi(\boldsymbol{r}) = \left(-\frac{\hbar^2}{2m}\nabla^2 + V_{\text{ext}}(\boldsymbol{r}) + g\phi^2(\boldsymbol{r})\right)\phi(\boldsymbol{r}). \tag{3.6}$$

This nonlinear equation contains the kinetic energy term, the trapping potential V_{ext} and the mean-field energy term $g\phi^2(\boldsymbol{r})$, which represents the interactions and is proportional to the density $n(\boldsymbol{r}) = \phi^2(\boldsymbol{r})$.

[2]The Bogoliubov approximation actually amounts to replacing the annihilation and creation operators a and $a^\dagger$ by the real number $\sqrt{N}$ and in ignoring the commutator relation $[a^\dagger, a] = 1$. This obviously requires $N \gg 1$.

3.2 Thomas-Fermi Approximation

In general it is a very involved task to solve the Gross-Pitaevskii equation due to its nonlinearity. For repulsive interactions, i.e. positive scattering length a, the situation simplifies, if the kinetic energy E_{kin} can be neglected with respect to the interaction energy E_{int}. Because we use a harmonic potential to trap the atoms, as done in most BEC experiments, the external potential V_{ext} is assumed to be harmonic from now on. Under this condition the ratio of the two energies varies as [Dal99a]

$$\frac{E_{\text{int}}}{E_{\text{kin}}} \propto \frac{Na}{a_{\text{ho}}}, \tag{3.7}$$

where $a_{\text{ho}} = \sqrt{\hbar/(m\bar{\omega})}$ is the harmonic oscillator length, which contains the geometric average $\bar{\omega} = (\omega_x\omega_y\omega_z)^{1/3}$ of the trap frequencies. Usually, the condition $Na/a_{\text{ho}} \gg 1$ is fulfilled and we can make the so called Thomas-Fermi approximation by omitting the kinetic energy term in equations (3.5) and (3.6). From equation (3.6) follows the simple relation $\mu = V_{\text{ext}}(\boldsymbol{r}) + gn(\boldsymbol{r})$, which determines the density distribution to be

$$n(\boldsymbol{r}) = \frac{\mu - V_{\text{ext}}(\boldsymbol{r})}{g} \qquad \text{for} \quad \mu - V_{\text{ext}} > 0 \tag{3.8}$$

and $n = 0$ otherwise. Thus the spacial distribution of the condensate reflects the parabolic shape of the harmonic trap.

Using equation (3.8) and the normalization $\int d\boldsymbol{r}\; n(\boldsymbol{r}) = N$ the chemical potential in a harmonic potential can be related to the atom number

$$\mu = \frac{\hbar\bar{\omega}}{2}\left(\frac{15Na}{a_{\text{ho}}}\right)^{2/5}. \tag{3.9}$$

Together with the condition $V_{\text{ext}}(R_{\text{TF},i}) = \mu$ this expression yields the Thomas-Fermi radii of the BEC along the axes ($i = x, y, z$) of the trap

$$R_{\text{TF},i} = \sqrt{\frac{2\mu}{m\omega_i^2}} = a_{\text{ho}}\frac{\bar{\omega}}{\omega_i}\left(\frac{15Na}{a_{\text{ho}}}\right)^{1/5}. \tag{3.10}$$

Further the peak atom density n_0 is immediately obtained from equation (3.9) as

$$n_0 = \frac{\mu}{g} = \frac{1}{8\pi}\left(\frac{15N}{a_{\text{ho}}^6 a^{3/2}}\right)^{2/5}. \tag{3.11}$$

Typical atom traps exhibit an anisotropic cigar shape, and according to equation (3.8) the trapped BEC reflects this anisotropy in its shape. In many experiments the density distribution is not directly observed in the trap.

Rather the condensed gas is imaged after switching off the trap and allowing the condensate to expand freely for some time. During this process the density dependent interaction energy is transferred to kinetic energy. Yet the parabolic density distribution is preserved during the expansion as a consequence of the parabolic variation of the mean-field interaction energy $E_{\text{int}} \propto n$, see [Cas96, Kag96, Hol96, Dal99a]. In contrast, a thermal cloud exhibits an isotropic expansion resulting in a Gaussian shape. This allows to distinguish a thermal component from the parabolically distributed BEC, see section 5.2.

Chapter 4

Setup of the Experiment

To create ultracold quantum gases and to perform experiments with Bose-Einstein condensates, there are several technical requirements to be met. Optical and magnetic forces are used to capture ^{87}Rb atoms at a temperature of 300 K and cool them over nine orders of magnitude to below 300 nK while storing them in a trap. This requires laser light at different well defined frequencies as well as properly designed magnetic fields. At all stages of the experiment the atoms need to be protected from collisions with background gas atoms, which demands ultrahigh vacuum (UHV) conditions.

Producing ultracold quantum gases of alkali atoms involves laser cooling and usually the first cooling stage is realized by a magneto-optical trap (MOT). Operating a MOT involves laser beams from six directions. Together with an imaging system, ports for a vacuum pump and the atom source they consume quite some space. This restricts the optical access to the trapped atoms when it comes to set up tools for performing experiments with the atomic sample. To circumvent these restrictions, one can move the atoms to another position after trapping and pre-cooling them in the MOT. A spatial separation also helps to solve another task, which consists in providing enough atoms when the MOT is loaded while ensuring low pressure and long trap lifetimes at the later stages of the experiment. Implementing a differential pumping stage between the MOT and the separated experimental region allows to obtain the required pressure difference.

In our new setup ^{87}Rb atoms are loaded into the MOT in a special vacuum chamber and are then transferred magnetically [Gre01] to a glass cell at a pressure below 10^{-11} mbar. During the transport we move the atoms over a distance of 48.6 cm and around a corner of 120°, see figure 4.1. In the glass cell the atom cloud is magnetically trapped and evaporatively cooled to form a BEC. The spatial separation between MOT and final trap position allows excellent optical access to perform a multitude of experiments.

This chapter describes the components needed for realizing this experimental scheme. Section 4.1 introduces the vacuum system and section 4.2 deals

with the magnetic fields needed for trapping and transferring the atoms. The remaining sections are dedicated to the MOT (4.3), the imaging system (4.4) and the lasers used for our experiments on optical Feshbach resonances (4.5).

4.1 Vacuum System

Our vacuum setup consists of two main sections. In the MOT section ^{87}Rb atoms are captured, pre-cooled and loaded to a magnetic trap. The second section is a vacuum chamber at extreme ultrahigh vacuum (XUHV) conditions and comprises the glass cell. These two sections are separated by a differential pumping stage and a gate valve. Figure 4.1 gives an overview of the complete vacuum system and shows the installed components also including the vacuum pumps, the pressure gauges and the Rubidium source.

One aim in designing the vacuum components was to keep the setup very compact. As can be seen from figure 4.1 it requires an area of only 1.4 m $\times$ 1.0 m while the centers of the vacuum chambers are 25 cm above the optical table. In view of the magnetic fields used for transporting the atoms from the MOT chamber to the glass cell, the central vacuum components are constructed to be as flat as possible. A flat design allows to mount the magnetic coils close to the atoms, which is important to minimize the dissipated power and the currents needed for operating the coils (see section 4.2.2). The overall height of the chambers in our setup has been chosen to be 50 mm, because the installed gate valve doesn't allow a smaller separation of the coils anyway. Figure 4.3 shows the central vacuum components in more detail and gives an impression of the dimensions.

The glass cell is oriented at an angle of 120° relative to the axis between MOT and XUHV chamber. This allows free optical access along the long glass cell axis and leaves ample space on the left-hand side of the cell to set up optics for our experiments, see figure 4.1. It is this geometry that ultimately defines the route of the atom transfer described in section 4.2.2.

Besides excellent optical access to the final trap position along three orthogonal axes, the magnetic transfer scheme offers large flexibility to modify the setup. Our setup is designed to allow easy future extensions by connecting an additional science chamber to the system. To this end the installed glass cell can be replaced by a cell with adaptor flanges at both ends and the science chamber can be connected to the second end of the glass cell. The additional chamber could serve as a vacuum lock to bring diagnosis tools to the sample (e.g. an ion detector for detecting photoionized molecules), or the condensate could be transported into the chamber for further experiments with surface traps or optical resonators.

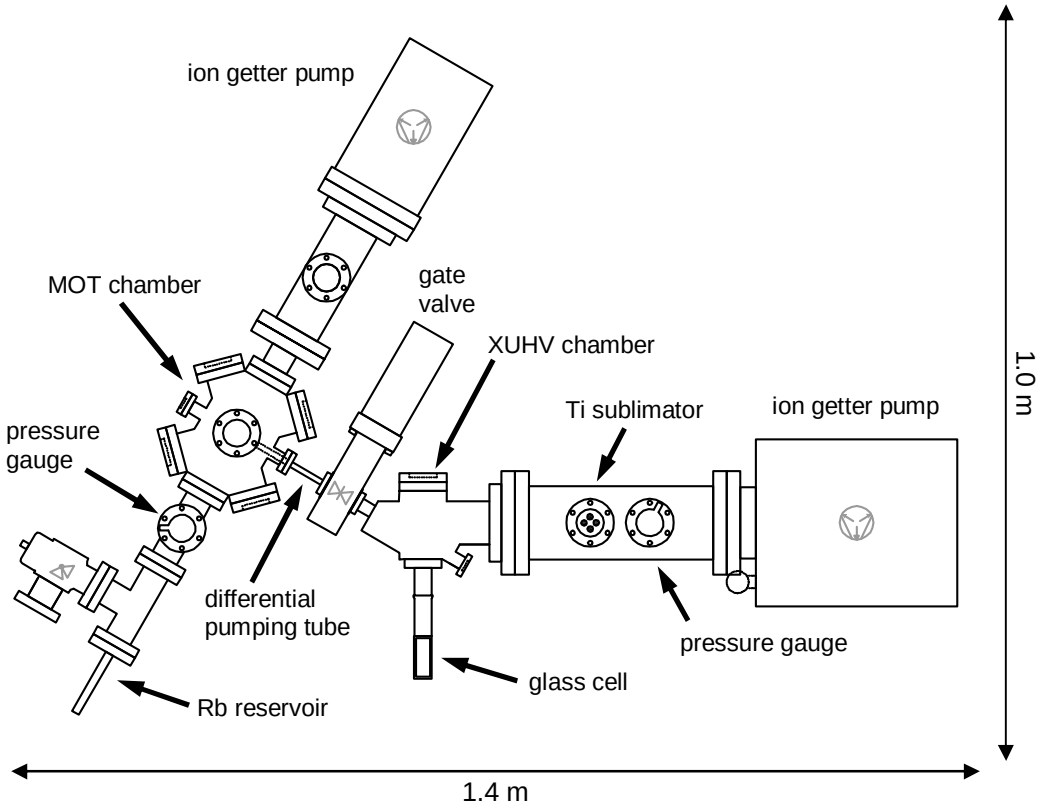

Figure 4.1: Overview of the vacuum system (top view). The left part is the MOT section. It is separated by a differential pumping tube and an all-metal gate valve from the XUHV section, which includes the glass cell.

4.1.1 MOT Section

The central part of the first vacuum section is the MOT chamber which was produced in our institute workshop from stainless steel. To avoid magnetization of the vacuum setup, only steel of grades ANSI 316LN and ANSI 316L (corresponding to the DIN specification 1.4429 and 1.4435) has been used. For these grades the magnetic permeability is less than 1.005. In the horizontal plane the MOT chamber has six ports with CF40 flanges and two with CF16 flanges, see figures 4.1 and 4.3. The latter two ports define the axis along which the atoms are transported to the second vacuum section. This axis is also used for absorption imaging of the atoms in the MOT. The CF40 ports orthogonal to this direction connect to an ion getter pump (Varian Vacion Plus 75 StarCell) and to a four way CF40 cross. This cross leads to a viewport (straight direction), to a Rb reservoir (downwards) and to an ionization pressure gauge (Varian UHV-24p), see figure 4.2. To allow an exchange of the Rb source without venting the system, the source is separated from the main

chamber by an all-metal valve (VAT, Series 54 DN40). In vertical direction the MOT chamber has two CF40 viewports which are used together with the remaining four horizontal ports for the MOT laser beams. All viewports in our vacuum system have an anti-reflection coating (Laseroptik GmbH, Germany, AR 780nm 0°) on both sides of the windows reducing unwanted reflections to well below 0.5% for wavelengths between 690 nm and 850 nm.

To be able to load the MOT we permanently maintain an "atmosphere" of Rb atoms in the MOT chamber. At the beginning, we used Rb dispensers from SAES Getters as a source of Rubidium atoms. Two arrays of five dispenser sticks (SAES Getters, Rb/NF/7/25/FT10+10), containing 94 mg of Rb altogether, were installed in the Rb source section and operated at a current of typically 2 A to 4 A. This resulted in a pressure reading of about 5×10^{-8} mbar. After about one year of operation we observed a less efficient loading of the trap at constant MOT laser power and constant pressure reading. This indicated that less ^{87}Rb and more other components were contained in the vapor. As we could not determine a clear reason for our observation we decided to replace the dispenser sticks by bulk Rubidium (Sigma-Aldrich Part-No 276332-1G), which we now use instead of the dispenser sticks. The vapor pressure of ^{87}Rb

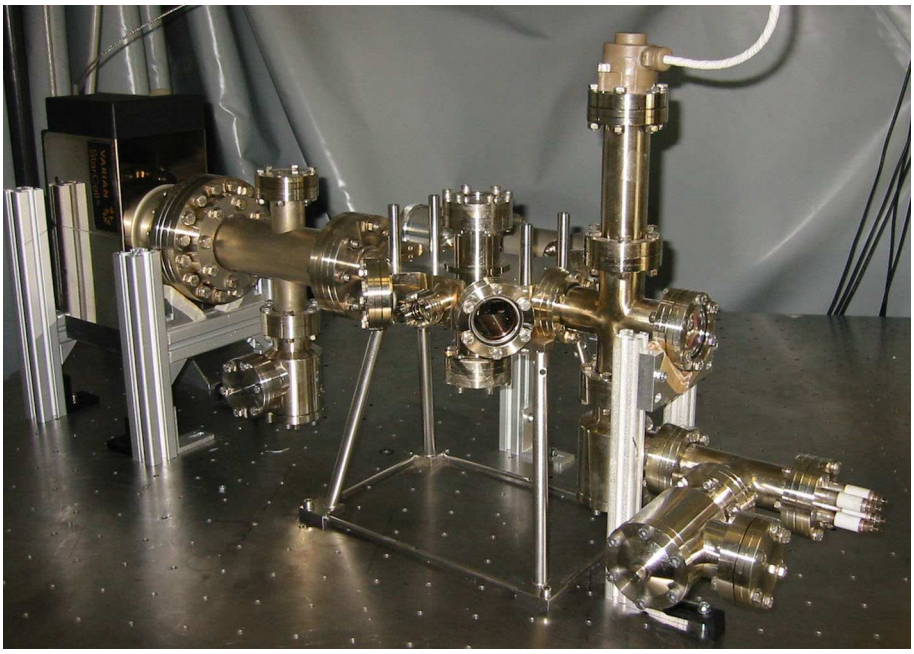

Figure 4.2: MOT section. From left to right: ion getter pump and connection tube, MOT chamber, four way cross with ionization pressure gauge (upwards) and Rb source (downwards). The Rb source is placed in the tubing with the electrical feedthroughs at the right-most end of the apparatus. .

is about 4×10^{-7} mbar at room temperature [Nes63], which is why we do not need to heat the source section. Nevertheless, the Rubidium is placed in a stainless steel tube that can be heated from the outside if required. To control the Rubidium flux we adjust the conductance of the valve between source and main chamber, at a given pumping speed of the ion getter pump.

4.1.2 Differential Pumping

To achieve a pressure difference of at least three orders of magnitude between the MOT chamber and the XUHV part of the setup, these sections are connected by a stainless steel tube with an inner diameter of 6.2 mm and a total length of 115 mm. When transferring the atoms it is desirable to bring them into a region at lower pressure as fast as possible, in order to reduce trap losses. For this reason, the differential pumping tube extends 49 mm into the MOT chamber just to the edge of the MOT laser beams, defined by the clear view of the viewports[1]. Between this tube and the XUHV chamber an all-metal gate valve (VAT, Series 48.1 DN16) is installed and allows a vacuum proof separation of the two sections. How the described elements connect the two vacuum sections can be seen from figure 4.3.

As no bellow is used to compensate for a displacement between the two chambers, care has to be taken when baking the system. After the first bakeout of the complete system we found a vacuum leak at the CF16 flange connecting the XUHV chamber to the gate valve. Because both chambers had been fixed to the optical table, the bakeout caused too much strain due to thermal expansion. After re-tightening the flange we unscrewed the feet of one of the chambers so that it was free to move in horizontal direction during the second bakeout.

Under high vacuum conditions the mean free path λ is much larger than the dimensions of our vacuum setup (at a pressure $p < 10^{-6}$ mbar and for air at room temperature $\lambda > 50$ m [Moo89]). Thus gas molecules or atoms do not interact with each other and collide only with the walls of the vacuum system. In this so called 'molecular flow regime' the relevant parameters like pressure and gas flow are described by simple formulas analogous to those known from electrical circuits, see [Wut89, O'H89] for example. Tubes and other vacuum components, characterized by their conductance C, define the gas flow $Q = dV/dt$ between one end of the component and the other. Here V denotes the gas volume that passes the vacuum element. For a given conductance the flow between two points at pressure p_1 and p_2 is given by $Q = C(p_1 - p_2)$. A vacuum pump acts as a drain and the gas flow is determined by the pumping speed S of the pump and the pressure p at the pump inlet: $Q = pS$.

[1] The part of the tube penetrating into the MOT chamber is indicated in figure 4.1 by a dotted line.

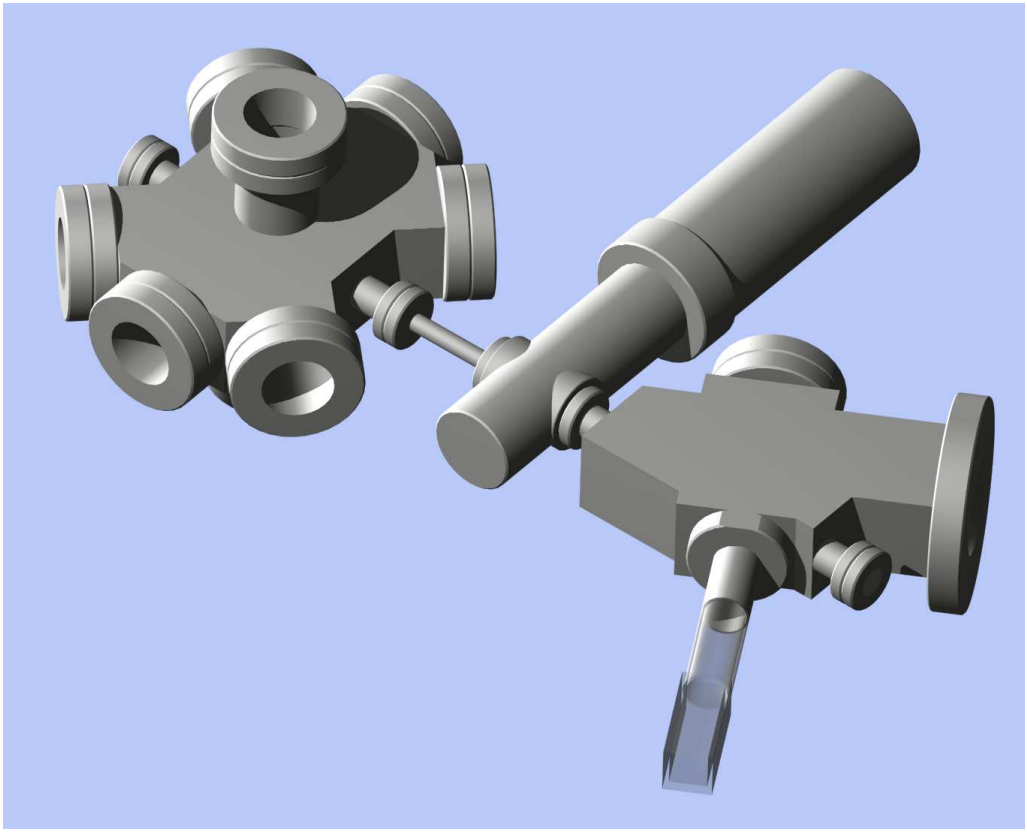

Figure 4.3: The central vacuum components. From left to right: MOT chamber, differential pumping tube, all-metal gate valve and XUHV chamber with the glass cell. The height of the chambers is 50 mm and the distance between MOT chamber and glass cell amounts to 486 mm (along the transport route of the atoms). To obtain a scale for the height, note that the viewports at the MOT chamber have an outer (inner) diameter of 70 mm (38 mm).

A basic parameter to determine the pressure p_2 in the XUHV section is the effective pumping speed of the pumps installed in this part of the setup. An ion getter pump and a titanium sublimation pump (see section 4.1.3) provide together an effective pumping speed of more than 1100 ℓ/s for air. The value for Rb may be larger or smaller by a factor of 2 or 3. However, it is safe to assume a total effective pumping speed $S > 350\,\ell$/s at the center of the XUHV chamber. With the help of well established equations [Wut89] the conductance of the used vacuum components can be calculated from their dimensions. This yields a conductance of $C \approx 0.2$ ℓ/s between the centers of the MOT and the XUHV chamber. For a pressure of $p_1 \approx 1 \times 10^{-8}$ mbar in the MOT region this design of the vacuum system ensures a pressure p_2 below 10^{-11} mbar, according to $p_2 S = C(p_1 - p_2)$.

4.1.3 XUHV Section and Glass Cell

A glass cell is an ideal device to provide the vacuum conditions needed for experiments with ultracold quantum gases. It combines very small outer dimensions with an optimum of optical access to the trapped atoms. In our setup a glass cell constitutes the most important component of the XUHV section, which further comprises a steel vacuum chamber and a pumping section, cf. figure 4.1. While the glass cell represents the environment for producing the BEC and for performing experiments, the XUHV chamber serves as a link between the cell and the other vacuum components.

Just like the MOT chamber the XUHV chamber was built in our workshop from stainless steel of a grade with low magnetic permeability. The height of the chamber is again chosen to be 50 mm. As can be seen from figures 4.3 and 4.4 it has two CF16 ports which share a common axis. One connects the chamber to the gate valve while a viewport mounted at the other port permits a view into the MOT chamber. Opposite a CF25 port, to which the glass cell is attached, a CF40 viewport enables optical access along the glass cell axis.

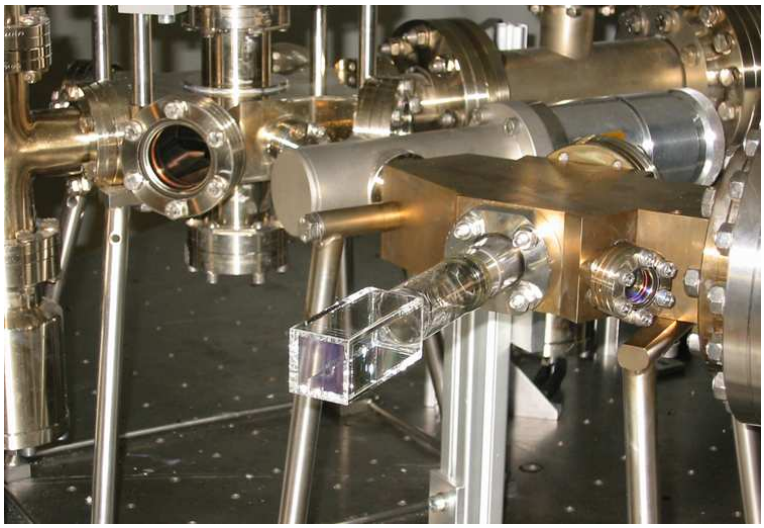

Figure 4.4: XUHV chamber with glass cell. On the left a part of the MOT chamber and the gate valve can be seen. The flange at the right edge of the photo connects to the ion getter pump and the sublimation pump.

The installed glass cell was manufactured from Spectrosil quartz glass by OptiGlass Ltd. in England. It has outer dimensions of 26 mm × 26 mm × 62 mm and a wall thickness of 3 mm, which is sufficient to guarantee stability and low diffusion leak rates. To attach it to the steel chamber a graded seal quartz-to-metal adaptor (Larson Electronic Glass Inc. USA, model SQ-100-T-SPCL) was fused to the glass cell. This tubular adaptor has an inner diameter of

22 mm and results in an overall distance of 112.7 mm from the edge of the cell to the CF25 flange. To reduce reflections from the glass windows the outside of the cell is coated with an anti-reflection coating optimized at wavelengths of 532 nm, 730-900 nm and 1064 nm (Laseroptik GmbH, Germany, MAR AR 532nm, 730-900nm, 1064nm, 0°). For technical reasons the coating had been done before the quartz-to-metal adaptor was fused to the cell. Due to the high temperatures the fusing process led to a visible degradation of the coating at the cell edge connecting to the adaptor. However, a measurement at Laseroptik GmbH indicated that the coating still functions in that region. In addition, the laser beams pass the glass cell only at the central region and the quality of the coating close to the edge has been of no relevance so far.

A CF100 tube connects the XUHV chamber to an ion getter pump (Varian VacIon 150 StarCell), a Titanium sublimation pump (Varian Series 916-0061) and an ionization pressure gauge (Varian UHV-24p) as shown in the overview drawing figure 4.1. The Titanium sublimation pump consists of three filaments made from an Ti-Mo alloy. By applying a current of 47 A to one filament for about one minute we have heated the filament and evaporated enough material to coat the surrounding walls with a Ti film. In our setup the film covers an area of 250 cm^2 to 300 cm^2. Titanium is a surface getter and at room temperature it pumps most chemically active gases with a pumping speed per surface area between $2\,\ell\,\mathrm{s}^{-1}\mathrm{cm}^{-2}$ and $9\,\ell\,\mathrm{s}^{-1}\mathrm{cm}^{-2}$. From this we estimate the resulting pumping speed to be larger than 500 ℓ/s. The Ti sublimation pump is complemented by an ion pump to ensure sufficient pumping of inert gases as well. With these pumps in operation we observe a pressure in the CF100 tube below the range of the ionization gauge, i.e. below 1×10^{-11} mbar. At this pressure the trap lifetime due to collisions of trapped atoms with the background gas is on the order of minutes, which is much longer than the time required for our experiments.

4.2 Magnetic Fields

Magnetic fields play a prominent role in our experiment. They are needed to operate the MOT, they are used for the atom transfer and they confine the atoms in a magnetic trap while the BEC is produced. Our setup includes 17 sets of magnetic coils that are controlled independently and dynamically during the experimental cycle. Further, we operate six pairs of coils at fixed currents to compensate magnetic background fields. This section describes the design and setup of the employed magnetic coils after shortly summarizing the basics of magnetic trapping.

4.2.1 Magnetic Trapping of Neutral Atoms

Magnetic trapping of neutral atoms exploits the magnetic moment $\boldsymbol{\mu}$ of the atom and its interaction with an external magnetic field $\boldsymbol{B}$ [Mig85]. This interaction results in a potential energy $V_{mag} = -\boldsymbol{\mu}\cdot\boldsymbol{B}$ with energy eigenvalues

$$E_{mag} = \mu_{\mathrm{B}} g_F m_F B. \tag{4.1}$$

Here $\mu_{\mathrm{B}} = e\hbar/2m_e$ is Bohr's magneton, g_F the Landé g-factor and m_F the magnetic quantum number for the z-component of the total spin $\boldsymbol{F}$. As usually, the z-axis is chosen to be oriented along $\boldsymbol{B}$.

If the atom moves at a velocity $\boldsymbol{v}$ through an inhomogeneous magnetic field, the local direction of $\boldsymbol{B}$ varies at a certain speed. To avoid a change of the m_F state the change of direction of $\boldsymbol{B}$ has to be slow compared to the Larmor precession frequency $\omega_L = \mu_{\mathrm{B}} g_F B/\hbar$ of the atomic spin:

$$|\partial/\partial t(\boldsymbol{B}/B)| = |\boldsymbol{v}\cdot\nabla(\boldsymbol{B}/B)| \ll \omega_L. \tag{4.2}$$

In this case the spin follows the magnetic field vector adiabatically and equation (4.1) yields the position dependence of the potential energy $E_{mag}(\boldsymbol{r}) \propto B(\boldsymbol{r})$.

Due to Maxwell's laws it is impossible to create a static magnetic field maximum in free space [Win84] and thus a local minimum of B has to be used for the trapping potential. Whether a given spin state $|F, m_F\rangle$ can be trapped at the minimum depends on the sign of $g_F m_F$. For the hyperfine states $F = 2$ and $F = 1$ in the electronic ground state of ^{87}Rb the Landé g-factor can be calculated [Ste02, Hak00] to be $g_F = 1/2$ and $g_F = -1/2$, respectively. Therefore only the low-field seeking states $|F = 2, m_F = 2\rangle$, $|F = 2, m_F = 1\rangle$ and $|F = 1, m_F = -1\rangle$ can be trapped magnetically, see figure 4.5.

The simplest magnetic trap is realized by a pair of magnetic coils in the so-called anti-Helmholtz configuration, i.e. a pair of coils separated by a distance d with aligned coil axes and opposite current directions. In a multipole expansion [Ber87] the field $\boldsymbol{B}(\boldsymbol{r})$ close to the center of this arrangement is well described

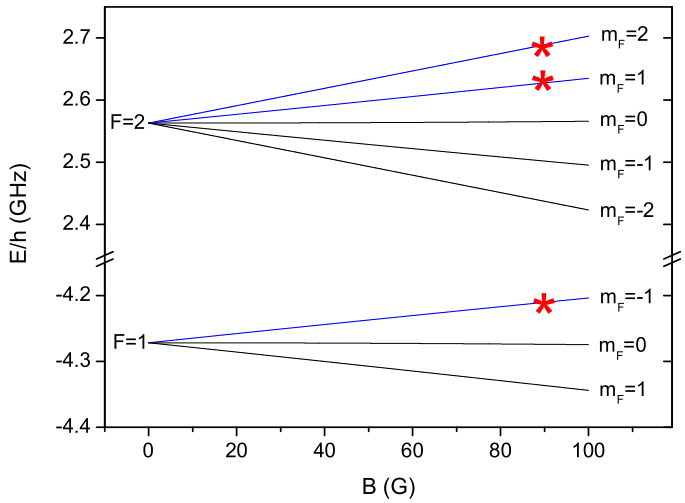

Figure 4.5: Zeeman diagram of the ^{87}Rb ground state. The energies of the hyperfine states $|F, m_F\rangle$ are plotted versus the magnetic field (linear Zeeman regime for low B-fields). Only the states marked by an asterisk can be trapped magnetically.

as a quadrupole field

$$\boldsymbol{B}(\boldsymbol{r}) = \left(\frac{\partial B_x}{\partial x} x, \frac{\partial B_y}{\partial y} y, \frac{\partial B_z}{\partial z} z \right), \tag{4.3}$$

where the coordinate system has its origin in the center of the assembly and its z-axis is chosen to be parallel to the axis of the coils. From $\mathrm{div}(\boldsymbol{B}) = 0$ it follows that the gradients along the different axes are related by

$$\frac{\partial B_z}{\partial z} = -\left(\frac{\partial B_x}{\partial x} + \frac{\partial B_y}{\partial y} \right). \tag{4.4}$$

Thus a magnetic quadrupole trap can be characterized by only two parameters: the steep gradient $\partial B_z/\partial z$ and the aspect ratio $A = (\partial B_x/\partial x) \,/\, (\partial B_y/\partial y)$, which is the ratio of the gradients along the remaining axes. If the quadrupole field is created by a pair of circular coils, the rotational symmetry results in A=1 and $\partial B_z/\partial z = 2\,\partial B_x/\partial x$.

As the magnetic field vanishes at the center of a magnetic quadrupole trap, the atom's Larmor frequency becomes arbitrarily small while $\boldsymbol{B}$ inverses its direction. Therefore the criterion of adiabaticity (4.2) is not fulfilled at the center and atoms are lost due to Majorana spin transitions [Maj33] to non-trappable states. This loss channel is unimportant for atomic samples at temperatures above 50 μK, e.g. after MOT and molasses cooling, because the atom density at the trap center is low. However, to achieve BEC the cloud is cooled to the ground state of atomic motion in the trap and a different geometry with a non-zero offset field has to be used, see section 4.2.3.

4.2.2 Magnetic Transfer Line

The spatial separation between MOT and glass cell in our setup requires to transfer the atoms over a distance of 48.6 cm. We realize this transport with a magnetic transfer line composed of pairs of quadrupole coils. This concept for transporting atoms over large distances has been developed in Munich [Gre01] and has established a new generation of BEC experiments.

At the heart of the magnetic transfer line is the observation that two neighboring (partially overlapping) pairs of quadrupole coils create a quadrupole field again if they carry currents with the same direction. Such a configuration can be compared to a pair of stretched elliptical coils and results in an elongated trapping potential with an aspect ratio $A > 1$. When the current is decreased in one coil and increased in the other one, the center of the magnetic trap moves. In consequence, a series of mutually overlapping coils allows to transfer magnetically trapped atoms over a given distance. If we require the geometry of the trapping potential to stay constant, three parameters need to be controlled during the transfer: the position x_t of the trap center, the vertical gradient $\partial B_z/\partial z$ and the aspect ratio A. To avoid parametric heating [Geh98] of the atoms by a periodic modulation of the trap geometry, full control of all three parameters is necessary. This can be achieved by using three pairs of quadrupole coils at a time. Then adequate time sequences for the currents allow to move an elongated quadrupole trap in space while maintaining a fixed geometry as shown in figure 4.6.

Geometry and Components of the Transfer Line

Our atom transfer starts from the position of the MOT, where the atom cloud is held in a magnetic quadrupole trap created by the MOT coils. Thirteen pairs of transport coils connect this starting point with the final trap position at the glass cell, see figure 4.7. After a distance of 31.5 cm the transfer route leads around a corner of 120° to allow unperturbed optical access to the glass cell. The second transfer section, from the corner to the glass cell, covers an overall separation of 17.1 cm. It delivers the atoms to a magnetic quadrupole trap formed by a pair of coils aligned to the center of the cell. Together with a third coil this pair constitutes a so-called quadrupole-Ioffe-configuration trap (QUIC trap) [Ess98], which we use as the final trap to produce the BEC, see section 4.2.3.

In total, this amounts to 15 separate quadrupole traps, which principally suffice to realize the magnetic transport. But as the MOT coils have a much larger diameter than the transfer coils (see below) this would initially stretch the trap to an extreme extend or require too large and negative currents. To avoid this problem a correction or "push" coil is mounted opposite to the first transfer coils. Its symmetry axis is oriented along the direction of transport,

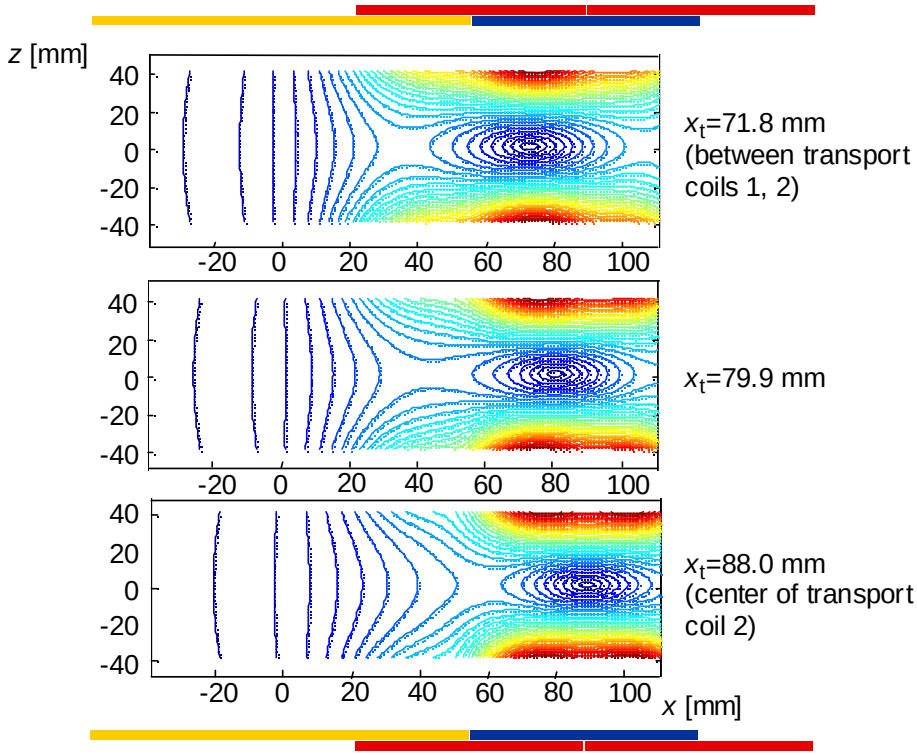

Figure 4.6: Contour plots of the magnetic field B in the xz-plane during the transfer (x is the direction of transfer and z is along the symmetry axes of the MOT coils). While the center of the trap x_t is moved by 16.2 mm the geometry stays the same. The bars above and below the diagrams indicate the positions of the magnetic coils (yellow: MOT coils, red: transfer coils 1,3, blue: transfer coils 2).

see the green coil on the left in figure 4.7. The effect of this coil is to "push" the trapping potential towards the transfer section. This allows to overcome the separation between the center of the MOT and the first pair of transfer coils at a moderate elongation of the trap.

The transfer line is composed of identical coils that are mounted in two layers above and below the vacuum chambers, always overlapping with the next neighbors, see figures 4.7 and 4.8. Due to the height of the vacuum chambers the inner coils are separated by 50 mm. However, there is an exception to this arrangement, which concerns the second to last pair of coils before the corner is reached (green colored coils in figure 4.7). These coils are placed in a third layer because at their original position they would have to partially penetrate other coils due to the bend of the transfer route.

Each transport coil dissipates electric power, which is transformed to thermal energy. Depending on the coil and its position, this power averages to

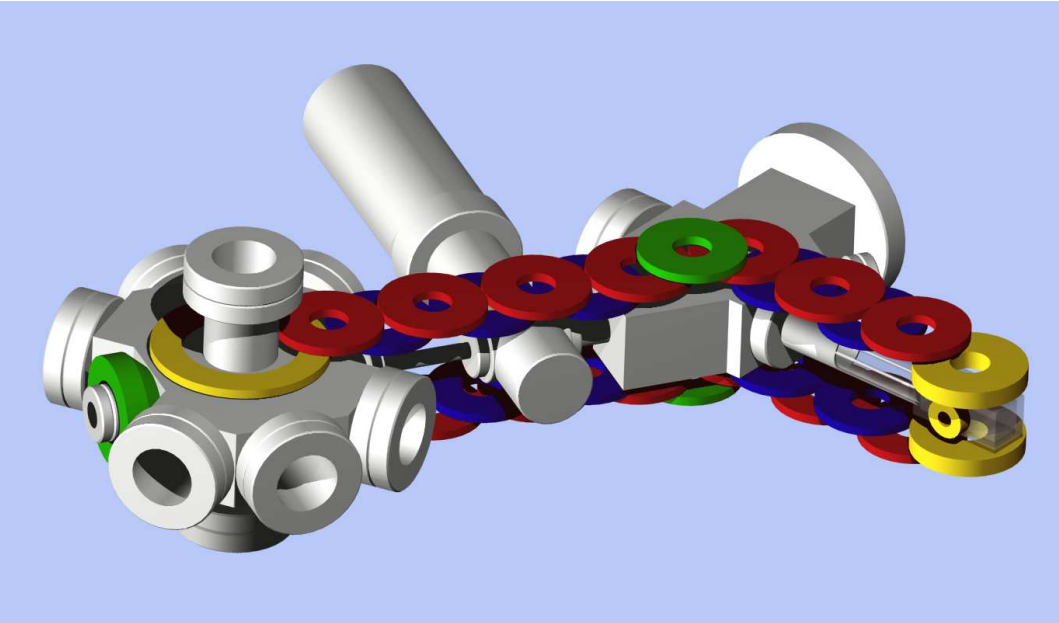

Figure 4.7: Magnetic transfer line. The drawing shows how the 13 pairs of transfer coils (red, blue and green), the MOT coils (yellow), the push coil (green, left-hand side) and the three coils for the final QUIC trap (yellow, right-hand side) are arranged around the vacuum chambers.

a value between 3 W and 6 W during one experimental cycle. Therefore the coils need to be in good thermal contact with a heat sink. To remove the heat and to allow convenient mounting, the coils are placed in aluminum housings and are encapsulated with a thermally conductive epoxy resin with a heat conductivity of $\approx 1\,\mathrm{W/(Km)}$. The housings conduct the produced heat to water cooled aluminum plates. These plates also serve as base bars to which the transfer coils are mounted (see figure 4.8). All coils and the heat sink bars are slit to suppress eddy currents, which limit the speed at which the magnetic fields can be switched. A 0.2 mm thin thermally conductive foil isolates the housings from each other to prevent a shortage of the slits.

Magnetic Coils

The most important aspect concerning the design of the magnetic coils is to minimize the dissipated power $P = RI^2$, which is given by the resistance R of the coil and the current I. For a pair of circular windings the magnetic field on the symmetry axis $B(z) = B_z(z)$ can be easily calculated. Also the steep magnetic gradient $\partial B_z/\partial z$ of the magnetic quadrupole field is readily

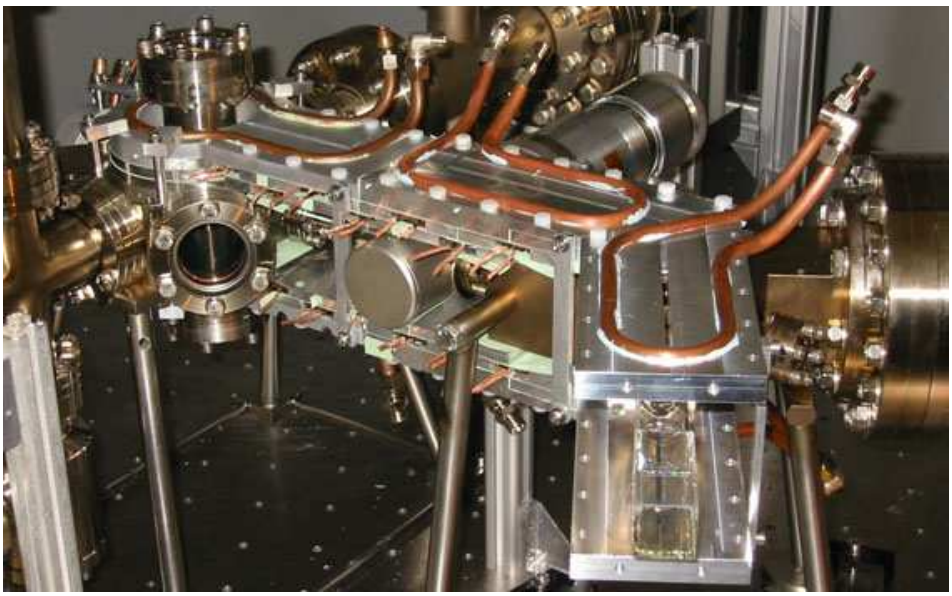

Figure 4.8: Magnetic coils and cooling bars of the transfer line. In this photo the last transfer section is not mounted except for the cooling bars above and below the glass cell.

obtained:

$$\partial B_z/\partial z = 3\mu_0 \frac{r^2 d}{(r^2+d^2)^{5/2}} I \ . \tag{4.5}$$

Here d denotes the separation between the two coils and r is the radius of the windings. Scaling d and r synchronously while maintaining a constant gradient $\partial B_z/\partial z$ requires an increase in the current proportional to d^2. Then the dissipated power rises by a factor of d^4, or even more if we regard the increasing resistance of the coil. It is due to this strong dependence that the vacuum chambers have a flat design and allow a separation between the (inner) coils as small as 50 mm (cf. section 4.1). In addition, equation (4.5) shows that for a given separation of the coils the radius r can be optimized to yield a certain gradient with a minimum of current I.

All coils used in our setup are made from copper wire with a rectangular cross-section of $1 \times 2.5\,\mathrm{mm}^2$. The transport line is composed of 26 identical *transfer coils* in rectangular housings of $80\,\mathrm{mm} \times 65\,\mathrm{mm} \times 6.5\,\mathrm{mm}$. For the transport we have chosen a magnetic field gradient $\partial B_z/\partial z = 130\,\mathrm{G/cm}$, which guarantees a steep enough trap[2], even if ^{87}Rb atoms in the $|F=1, m_F=-1\rangle$ state are transported at temperatures up to 1 mK. To achieve this gradient with "moderate" currents below 100 A and to keep the aspect ratio reasonably small, we found the optimum transfer coils to have two layers of 17 windings each

[2]Here a typical aspect ratio of $A = 1.69$ is assumed, see below.

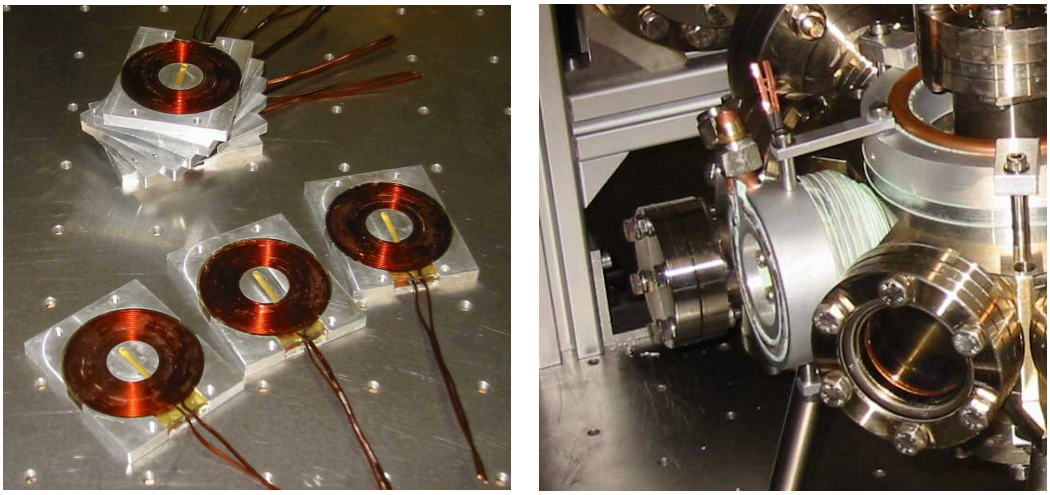

Figure 4.9: Left: Transfer Coils. Right: Push coil mounted to the MOT chamber. The inner diameter leaves exactly the space needed for the CF16 viewport that holds the coil (not visible here).

and an inner and outer diameter of 23.6 mm and 65 mm, respectively. Corresponding to the two layers the height is 2×2.5 mm plus a production tolerance of 0.5 mm. This geometry takes into account optimized inner and outer radii r_i, r_o such that the coils dissipate a minimum of power $P = R(r_i, r_o)I(r_i, r_o)^2$. Due to the large quantity of transfer coils required, they have been produced by an external company (OSWALD Magnetik, Germany) using housings provided by the workshop of our institute.

The starting point for the transport is a quadrupole trap created by the *MOT coils*. As these coils have to fit over the viewport of the MOT chamber, the inner diameter has been set to 70 mm. Our MOT coils consist of 2×15 windings arranged in two layers and have an outer diameter of 106.6 mm. There is one more coil used for the magnetic transfer: the *"push" coil*. It has a conical shape to fit between two CF40 viewports of the MOT chamber, which minimizes the distance to the center of the MOT. A total of 80 windings with a core diameter of 38 mm and a maximum outer diameter of 67 mm allows to realize the necessary magnetic fields with currents below 100 A. This coil has water cooling included in its housing while the MOT coils are thermally contacted to the cooling plates shown in figure 4.8. To ensure sufficient heat conduction, we have encapsulated these coils with a thermally conductive epoxy resin (Stycast 2850MT from Emerson & Cuming). Again, the Push coil and the MOT coils have one slit to suppress eddy-currents and are isolated from other metals by a heat conductive foil.

Controlling the Transfer

In order to transport the atoms to the glass cell, time sequences need to be calculated for the current in every single pair of transfer coils. We obtain these sequences from numerical simulations realized with Matlab scripts, see appendix B. First, we use the geometry of the coils to separately determine the field created by each pair of coils for a unit current $I = 1\,\mathrm{A}$. In a second step the results are used to calculate the required currents $I(x)$ as a function of the trap position x. This step requires the steep trap gradient $\partial B_z/\partial z$ and the aspect ratio A as input parameters. As mentioned before, the gradient $\partial B_z/\partial z$ is set to a value of $130\,\mathrm{G/cm}$. During the transport we use an aspect ratio of $A = 1.69$. Starting with $A = 1$ it is smoothly increased during the first 43 mm of the transfer and is then kept at a constant value. An aspect ratio $A > 1$ corresponds to a trap that is elongated in the direction x of motion. Because

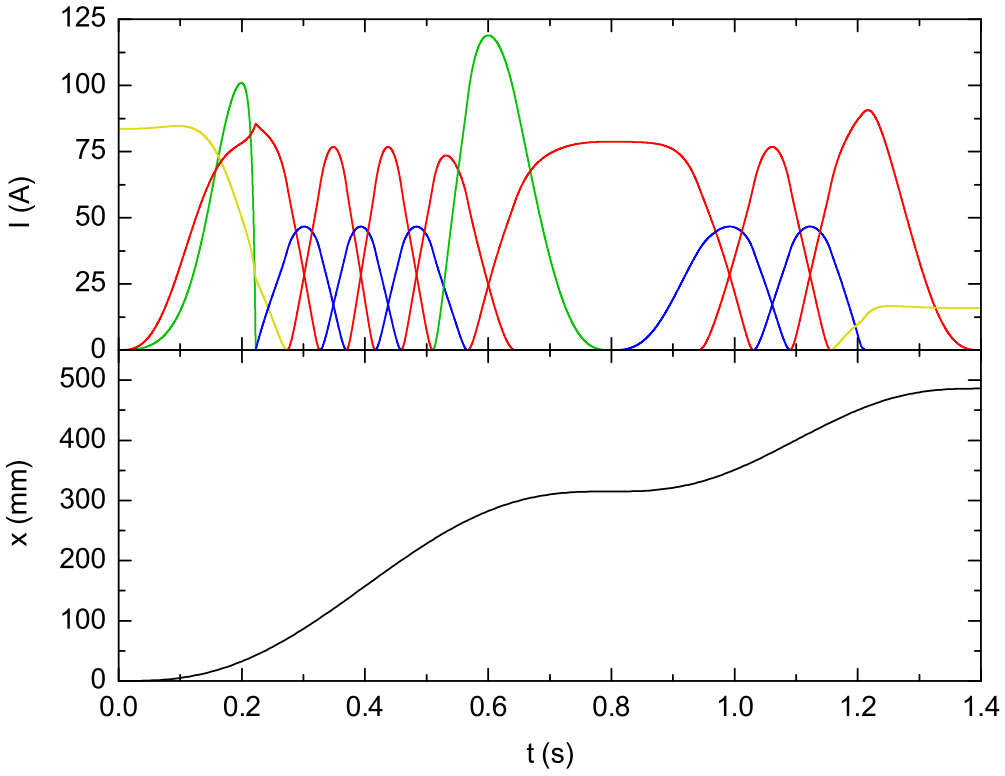

Figure 4.10: Transfer sequence. In the lower graph the position x is plotted versus the time t. The upper diagram shows the currents through the transfer coils as a function of time. Here the same color code is used as in figure 4.7 (push coil: green, MOT and QUIC coils: yellow, first and second layer of transfer coils: blue and red). At the corner ($x = 315\,\mathrm{mm}$, $t = 0.8\,\mathrm{s}$) the atoms are stopped and are then re-accelerated.

we transport the atoms around a 120° bend, the stretched trap needs to rotate in space by 120° as well. To realize this in a controlled way, the atoms are stopped in the corner and the aspect ratio is reduced to $A = 1$ before the trap is accelerated in the new direction and stretched again. At the final position we want to have good optical access along the vertical glass cell axis, i.e. the symmetry axis z of the QUIC quadrupole coils. Therefore, the center of the latter coils is shifted away from the last transfer coils by 8 mm (cf. figure 4.7). This spacing requires the aspect ratio to be raised temporarily to $A = 3.29$ before it is finally reduced to 1 again. Here we do not use a compensation coil like the push at the beginning of the transfer, because it would reduce the optical access to the cell.

To completely define the transport sequence, we need to choose the acceleration $a(t)$ of the trap and to determine the position $x(t)$ as a function of time. With respect to a heating of the atom cloud the sample should be accelerated and decelerated smoothly. We restrict the maximum acceleration to $2.8\,\mathrm{m/s^2}$ and use a transfer sequence that requires 1.4 s to cover the total transfer distance. Figure 4.10 shows in the lower diagram the function $x(t)$ implemented in our transfer. Combining $x(t)$ with the current curves $I(x)$ calculated in the previous step, we obtain the complete transfer sequence as a function of time, see upper diagram in figure 4.10. The bend of the transfer route (x=315 mm) is reached after 0.8 s and the trap is brought to rest before starting the second section. The figure shows that, indeed, three currents are used at a time to achieve full control of the three relevant transfer parameters.

4.2.3 QUIC Trap

A magnetic trap suitable for storing atoms and cooling them towards the BEC transition must have a non-zero magnetic field at the trap center. Otherwise atoms are lost due to spin transitions to non-trappable states (cf. section 4.2.1). This problem is solved in most BEC experiments by using a magnetic trap of the Ioffe type [Got62], which was originally developed in the field of plasma physics. After the proposal to use this kind of trap for storing neutral atoms [Pri83] Ioffe traps have been applied in several variations to store laser cooled atoms and to achieve Bose-Einstein condensation [Bra95, Mew96, Mya97, Hau98, Ess98, Hän01, Ott01]. All Ioffe traps produce a non-vanishing offset field B_0 and exhibit a harmonic variation of the potential close to the trap minimum.

In our setup we use a quadrupole-Ioffe-configuration (QUIC) trap [Ess98]. This trap consists of a pair of quadrupole coils and an additional so-called "Ioffe" coil, see figure 4.11. The symmetry axis of the latter coil is oriented perpendicular to the one of the quadrupole coils and defines the axial x-direction. There are two major advantages of a QUIC trap compared to the "classical" four bar Ioffe-Pritchard trap [Ber87, Pri83, Got62]. First, this trap dissipates

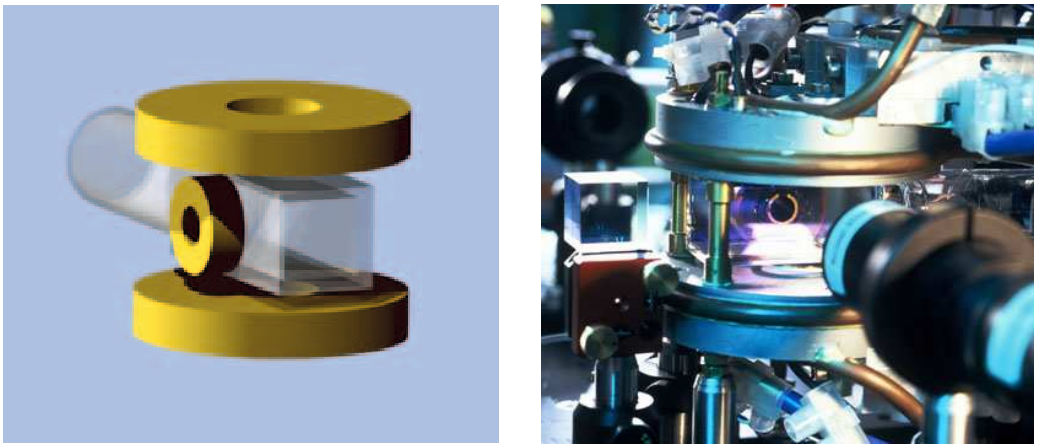

Figure 4.11: Left: The QUIC trap coils and their arrangement around the glass cell. Right: The glass cell with the installed QUIC trap (and parts of the imaging optics). Above and below the cell the round aluminum housings of the quadrupole coils can be seen. Behind the cell the Ioffe coil is visible (best discernible is the inner copper tube surrounded by blue epoxy that fixes the windings).

less power, which simplifies the heat removal. In our setup the total dissipated power is about 350 W at a current of 40 A. This allows to cool the coils with normal tap-pressurized water. The second advantage is very important for loading this trap from the transfer line. If the current through the Ioffe coil is ramped from zero to its final value, the trapping potential smoothly changes from a quadrupole to a Ioffe potential[3]. Obviously, this trap is well suited to connect to the quadrupole potential used for the transport.

The quadrupole coils used in our QUIC trap consist of 70 windings and have an inner diameter of 11.8 mm, an outer diameter of 32.5 mm and a height of 11.4 mm. They are mounted above and below the glass cell and are 35 mm apart from each other. Both coils are molded in water cooled aluminium housings, see the right picture in figure 4.11. Also shown in the figure is the Ioffe coil, which is made of 16 windings wound around a copper tube (inner coil diameter: 10 mm, outer diameter 24.6 mm). The tube is connected to a water cooled copper heat sink and allows a clear view along the x-axis of the QUIC trap with a diameter of 8 mm.

We operate the QUIC trap with the pair of quadrupole coils and the Ioffe coil connected in series. This ensures maximum relative stability of the fields produced by the Ioffe coil and the quadrupole coils, respectively. To improve the absolute stability of the current, a capacitor of 10 mF is switched in parallel

[3]Actually, the transfer is not reversible. During the transformation a second trap minimum occurs that finally merges with the first one to form the QUIC potential. A spilling of atoms to the second minimum then makes the process irreversible [Ess98].

to the outputs of the power supply whenever the QUIC trap is operated. As a result, the relative current noise was reduced by an order of magnitude to a value of approximately 3×10^{-4} (peak to peak), which we found to be sufficient for producing stable BEC's. A measurement of the current induced in a pick-up coil indicates that we can switch off the magnetic field produced by the QUIC trap within $300\,\mu$s.

Due to the magnetic field of the earth, the ion getter pumps and other laboratory equipment a background B-field is always present. To be able to control the background field three pairs of rectangular compensation coils are installed around the glass cell. At the moment we only use the coils along the axial direction of the QUIC to create a constant field $B_x \approx 1.5\,\mathrm{G}$. This is because the offset field created by the QUIC coils is very sensitive to the relative position of the Ioffe and the quadrupole coils. We preferred to use the external coils rather than readjusting the QUIC to achieve a 2 G bias field, large enough for producing stable condensates.

By applying a current of 40 A to the QUIC we obtain a cigar shaped magnetic trap with an axial B-field curvature of $\partial^2 B_x/\partial x^2 = 320\,\mathrm{G/cm^2}$ and a radial gradient $\partial B_z/\partial z = 235\,\mathrm{G/cm}$. For ^{87}Rb atoms in the $|F = 2, m_F = 2\rangle$ state this results in a trap with trap frequencies of $\omega_x = 23\,\mathrm{Hz}$ in axial direction and $\omega_{y,z} = 212\,\mathrm{Hz}$ in the radial directions.

To allow forced evaporation in the QUIC trap, two rf-antennas are installed, which produce the radio-frequency (rf) fields we use to induce spin transitions to non-trapped states. These antennas are placed directly above and below the glass cell and are centered at the vertical axis of the two quadrupole coils. Each antenna consists of three windings with a diameter of 25 mm. The rf-signal is generated by a synthesized function generator from Stanford Research Systems (model DS345, up to 30 MHz).

4.2.4 Power Supplies and Magnetic Field Control

To realize the magnetic fields and the current sequences required for the transfer, we use four power supplies from Delta Elektronika (Netherlands). Two different types of power supplies, models SM 15-200DS91 P031 (0-17V, 0-200A) and SM 30-100D P031 (0-30V, 0-100A), allow to obtain either high currents or high voltage. We operate these supplies in the current control mode and control the currents via four analog ports with a computer control system (see section 5.1). To avoid problems with different ground potentials, the analog inputs are galvanically isolated from the control system with the help of analog optocouplers.

The combinations of power supply and transport coils allow only limited rise and fall times (typically $\approx 3\,\mathrm{ms}$) according to the effective resistance, capacitance and inductance. At a given time, at most three power supplies are active (see section 4.2.2). Nevertheless it is advisable to use four separate sup-

plies. While the current through one supply is still going down exponentially, one can employ the fourth to energize the next transfer coils. Thus sudden jumps of the trapping potential due to reminiscent currents can be avoided when switching to the next pair of transfer coils.

A specially designed MOSFET switch box [Win02] switches the outputs of the four power supplies to the different magnetic coils according to a three-bit signal used by the computer control system to address the individual coils. An additional control box ensures that no coil is energized at high currents for an extended period. This is vital because the cooling system is not designed to remove the heat created by the coils in a 100% duty cycle. In addition, the control box acts as an interlock circuit to guarantee that the cooling water is circulating and that the temperature of the coils is not too high (see [Win02]).

For an optimum transfer the real currents through the coils should follow the intended curves (see figure 4.10) as closely as possible. The power supplies exhibit a low-pass characteristic and this would distort the current sequences if no further measures are taken. For this reason we have measured the transfer function for each combination of power supply and magnetic coil. These data are then used to compensate the frequency response by amending the programmed current curve appropriately. Details on this procedure can be found in [Win02]. As a result, the obtained currents $I(t)$ are in good agreement with the target functions except for an exponential decay, which can not be eliminated without inverting the output voltage.

4.3 Magneto-Optical Trap

In our experiment the first step to create a ^{87}Rb BEC is to capture and precool atoms in a MOT. This type of trap is a very efficient and well established tool to collect a large number of atoms from the background gas (or a decelerated atomic beam) and to cool them from room-temperature to a few ten μK [Raa87, Phi98, Met99]. This happens with the help of strong radiative forces, which are position-depended due to the presence of a magnetic quadrupole field. The lasers, the optics and the further technical setup used to realize the MOT in our experiment are described in this section.

Lasers

Operating a MOT requires light laser at the MOT or cycling transition. In addition some repumping light is needed to recover atoms that have been lost from the cycling transition via non-resonant excitation of neighboring excited levels. For our ^{87}Rb MOT we use the $|5s\ S_{1/2}, F = 2\rangle \rightarrow |5p\ P_{3/2}, F' = 3\rangle$ transition of the D_2 line together with a repump laser which is tuned to the $|5s\ S_{1/2}, F = 1\rangle \rightarrow |5p\ P_{3/2}, F' = 2\rangle$ transition, cf. figure A.1. To abbreviate the notation F will be used from now on to designate a hyperfine level in the electronic ground state while F' will refer to the excited state.

The laser light for the MOT transition is obtained from a Coherent 899 Titanium:Sapphire laser (Ti:Sa). This laser is optically pumped by a Coherent Verdi-V10 laser with a pump power of typically 5 W to 6 W. To select only one cavity mode of the Ti:Sa laser and to be able to tune the wavelength, a set of two etalons (Coherent 895), a galvanometer-driven Brewster plate and a piezo-mounted cavity mirror (tweeter assembly 899-21 from Coherent) are installed. With the help of a heating resistor the temperature of the thick etalon in the 895 etalon set is controlled (precision 10 mK). This allows to tune the frequency of the Ti:Sa laser by varying the etalon temperature and thus the separation of its surfaces. Typically the etalon temperature is set to a value around 30°C. A linear dependence between the laser wavelength and the temperature with a slope of $\Delta\lambda/\Delta T = 0.0039\,\mathrm{nm/K}$ allows convenient tuning over the free spectral range of the thick etalon (which is 10 GHz or 0.0203 nm). To stabilize the laser frequency on slow time scales (on the order of 100 Hz) the galvanometer drive rotates the Brewster glass plate to change the optical path length in the Ti:Sa ring resonator. Faster adjustments (up to about 2 kHz) can be made by translating the piezo-mounted cavity mirror, but with a reduced range compared to the Brewster plate.

In order to set the Ti:Sa laser to the appropriate frequency a reference is needed to which the laser can be locked. This reference frequency is obtained from a diode laser, which will be called the "master laser" in the following. The master laser consists of a temperature stabilized Sanyo DL-7140-001 laser

diode with an external resonator setup that uses a grating in the Littrow configuration, see for example [Wie91, Ric94]. A piezo-electric actuator allows to change the angle of the grating and in consequence the length of the external resonator. Using this piezo element we can tune the frequency of the laser to localize the intended lock point. Frequency stabilization is realized by varying the diode current, which permits tuning on a faster time scale. The absolute frequency reference to lock this laser is obtained from modulation transfer spectroscopy [Raj79, Shi82, Ber01] in a rubidium vapor cell. This scheme provides a Doppler-free and robust error signal with a capture range of about $\pm 10\,\mathrm{MHz}$. We use this error signal to lock our master laser directly to the MOT transition $F = 2 \rightarrow F' = 3$.

When operating a MOT it is desirable to be able to vary the MOT laser detuning in a controlled way, cf. section 5.1. We obtain this tunability by using a beat-lock scheme [Sch99] to stabilize the Ti:Sa frequency relative to the master laser. To this end a beam is extracted from the master laser and is frequency shifted by $+95\,\mathrm{MHz}$ with an acousto-optical modulator (AOM). With a fast photodiode we detect the beat signal between the Ti:Sa laser and the beam from the master laser. This beat note and the rf-signal from a voltage controlled oscillator (VCO) are fed into a rf-mixer. Then the difference frequency is selected with a low-pass filter and converted to a voltage. Finally, the obtained signal serves as the error-signal to lock the Ti:Sa laser. Varying the frequency of the VCO allows to tune the Ti:Sa light delivered to the MOT from -110 MHz to +40MHz with respect to the $F = 2 \rightarrow F' = 3$ transition.

The repumping process on the $F = 1 \rightarrow F' = 2$ transition is realized with light obtained from a second grating stabilized diode laser, called the repumper. As this transition is about $7\,\mathrm{GHz}$ away from the MOT transition the repumper is separately stabilized to a ^{87}Rb vapor cell. For this frequency lock we use the technique of frequency modulation spectroscopy [Bjo80] as described in [Joc00]. Here the cross-over signal between the $F' = 1$ state and the $F' = 2$ state is used as the lock point. Thus the frequency of the repumper lies $78\,\mathrm{MHz}$ below the $F = 1 \rightarrow F' = 2$ transition (cf. figure A.1) and the frequency is shifted with an AOM to match this transition. In general, we employ AOM's in all laser beams before they are led to the experiment. This allows fast switching of the laser light within $\sim 1\,\mu\mathrm{s}$. Additional mechanical shutters guarantee a complete shut-off of the lasers but only react on a much longer time-scale ($\sim 1\,\mathrm{ms}$).

MOT Geometry and Details

To realize a MOT containing a large number of atoms, which are loaded from the ^{87}Rb background gas, it is advisable to use large laser beam diameters. This follows from the fact that the loading rate R_{load} of a vapor cell MOT increases with the beam diameter [Mon90, Lin92, Sch02] and that the maximum number

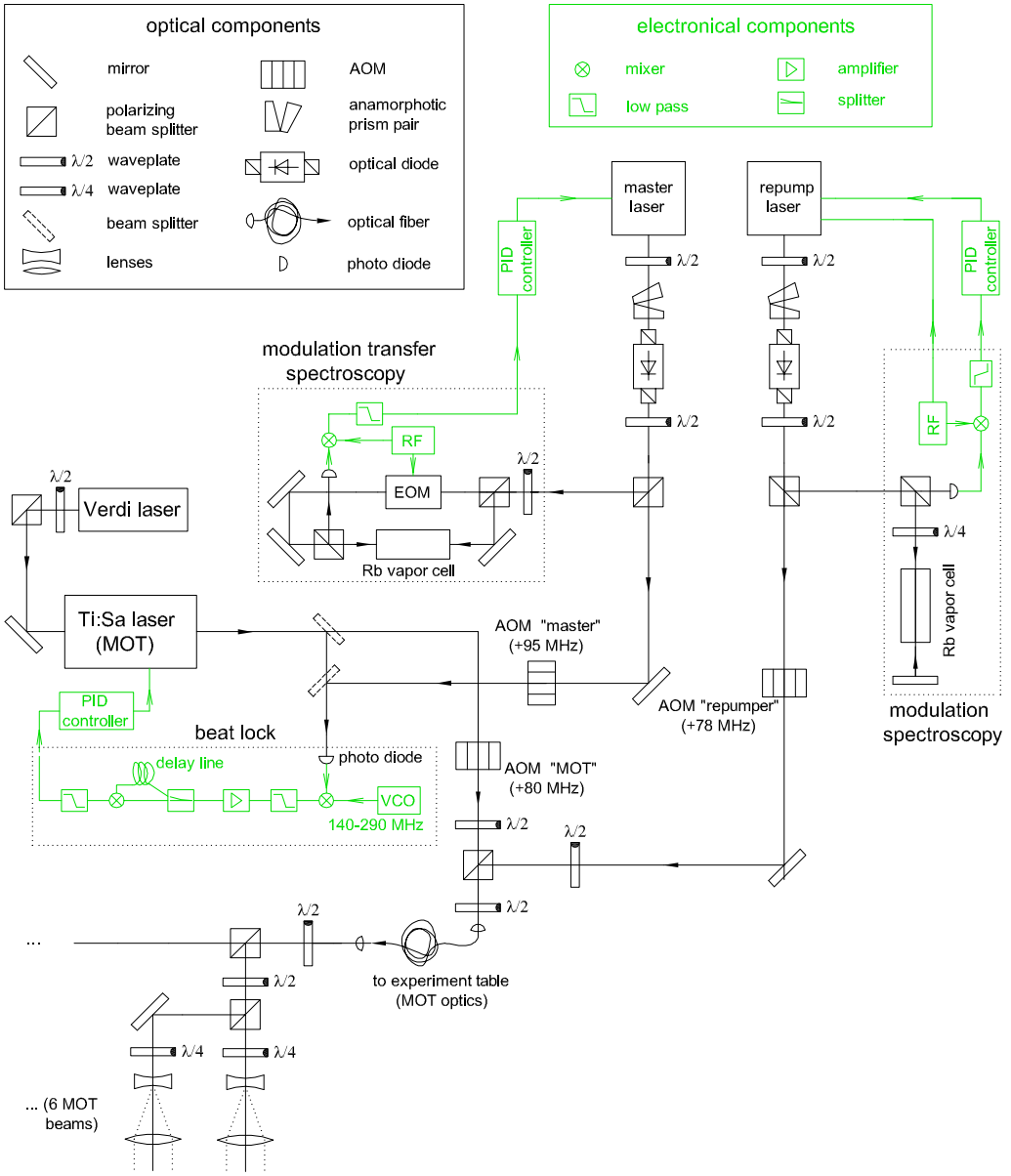

Figure 4.12: Schematic outline of the MOT lasers and optics (in this overview several standard components, such as lenses for example, are omitted). Optical components are drawn in black, while electronic devices are shown in green.

of atoms in the MOT is given by $N_{\max} = R_{\text{load}}/\gamma_{\text{loss}}$. Here γ_{loss} is the loss rate from the trap. The relation for $N_{\max}$ follows directly from the differential equation $\dot{N}(t) = R_{\text{load}} - \gamma_{\text{loss}} N(t)$ for the number N of atoms in a vapor cell MOT[4]. In our setup we take the dependance of $N_{\max}$ on the beam diameter into

[4]This equation neglects density dependent losses due to (light assisted) collisions between trapped atoms, which reduce the atom number at large atom densities. However the general argument stays correct.

account and use large laser beams with a diameter of 35 mm ($1/e^2$ diameter for the intensity). This value is matched to the 38 mm clear view of the installed viewports.

The lasers used to create the light needed for our MOT are located on a special optical table reserved for the laser system. To transfer the light to the experiment, we employ polarization-maintaining single-mode optical fibers. We couple the MOT cooling light and the repumper light into a common optical fiber and guide it to the experiment table. After extracting a collimated beam from the optical fiber, six single beams are formed and circularly polarized. Before the beams enter the vacuum chamber they are enlarged to the final diameter with Galilei telescopes, see figure 4.12.

Directly after the optical fiber 250 mW of laser light are typically available at the MOT transition. As the power is almost equally distributed among the six MOT beams, each beam has a peak intensity of about $2.2\,\mathrm{mW/cm^2}$. This corresponds to 1.3 times the saturation intensity of the $F = 2 \rightarrow F' = 3$ cycling transition. To create the magnetic field required for the MOT a current of 9 A is run through the MOT quadrupole coils. According to the coil geometry this results in a magnetic field gradient of $\partial B_z/\partial z = 14\,\mathrm{G/cm}$ along the steep z-direction of the quadrupole field. To obtain optimum performance of the MOT, the vacuum chamber is surrounded by three pairs of compensation coils that are used to suppress magnetic background fields and to ensure a maximum perfection of the employed quadrupole field.

After cooling the atoms in the MOT and an additional molasses cooling stage (see chapter 5) the atoms are optically pumped into a single spin state and are then loaded into a magnetic trap. During the spin-polarization procedure we prepare the sample either in the $|F = 2, m_F = 2\rangle$ state or in the $|F = 1, m_F = -1\rangle$ state. The required laser light for this process is derived from the master laser and from the repumper with the help of AOM's, see section 5.3.

4.4 Detection and Imaging System

All quantities measured in our experiments are extracted from absorption imaging of the atom cloud in the glass cell. This technique [Ket99] allows to obtain all relevant parameters such as atom number, temperature or spatial distribution (see section 5.2). In addition to the absorption technique we use the fluorescence of the MOT atoms to obtain some information on the system when optimizing the first experimental stages. This section describes the technical tools installed for diagnostic purposes.

To allow adjustment of the MOT, two CCD cameras record the shape of the atomic fluorescence signal from two orthogonal directions. One camera

(COHU model 4912 CCD camera) is oriented along the direction of transfer and views into the MOT chamber through a CF16 viewport, see camera 1 in figure 4.13. A CF16 viewport at the XUHV chamber is used to shine in the absorption light. While this camera is also employed for absorption imaging, a video CCD camera is used only to observe the MOT fluorescence. The latter camera is mounted at an angle of 90° with respect to the first one and is also shown in figure 4.13. Besides the two cameras a photodiode provides a signal proportional to the total fluorescence. This constitutes a simple monitor of the atom number in the MOT that is permanently available. The photodiode is installed at the same viewport as the COHU camera, where a polarizing beam splitter cube divides the light between camera and photodiode.

The second position where we need to analyze the atomic cloud is the glass cell. At this location all experiments are performed and high quality imaging is needed. As the main detection system a low noise and high resolution CCD camera from THETA SYSTEM (model SIS1-S285) is installed, see camera number 2 in figure 4.13. The required absorption laser beam is directed along the axis of the Ioffe coil and then passes the cell before it enters the imaging optics of the THETA camera, cf. figure 4.11. To obtain images of the BEC with good resolution, we use imaging optics consisting of achromatic doublet lenses. These optics yield a magnification of 3.75 and in consequence one pixel on the camera corresponds to an area of $1.74 \times 1.74\,\mu\text{m}^2$ in the plane of observation. Another imaging system is installed at an angle of 90° to obtain pictures of the atoms that show the long axis of the cigar shaped cloud. Here again a COHU 4912 camera is used equipped with either of two imaging optics, which provide a magnification of 2.5 or 1.

For the absorption imaging laser light is needed at or close to an atomic resonance. We use light that is split from the master laser beam used for the beat-lock of the MOT Ti:Sa. With an AOM the light is shifted to the desired frequency close to the $F = 2 \rightarrow F' = 3$ transition. Typically, we use a detuning from the resonance of -10 MHz to -20 MHz. To pump atoms that are in the $F = 1$ states into $F = 2$, we use repumping light on the $F = 1 \rightarrow F' = 2$ transition. Light at this frequency is already employed during the operation of the MOT. Thus in the MOT chamber we can use the MOT optics to deliver it to the atom cloud for imaging purposes as well. At the glass cell an additional laser beam is directed along the vertical axis of the cell to shine in the repumping light.

4.5 Lasers for Experiments

The setup described so far comprises all necessary components to produce BEC's and to detect the (condensed) atom cloud. For photoassociating atoms and for experiments on optically induced Feshbach resonances additional lasers are needed, which will be introduced in this section.

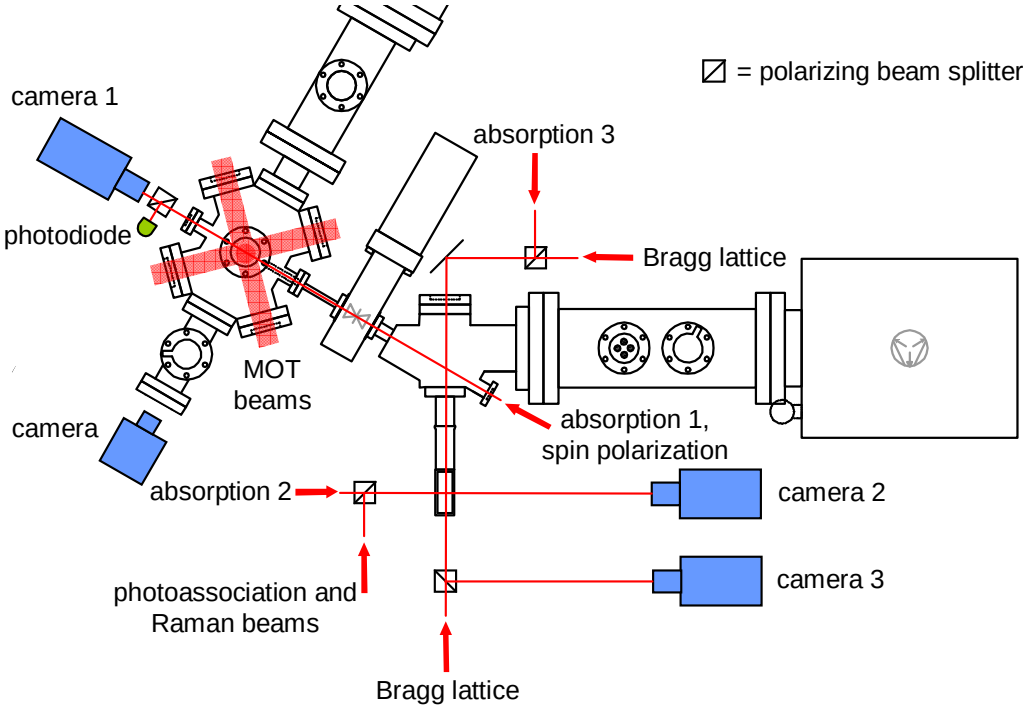

Figure 4.13: Arrangement of the laser beams and imaging system. The figure shows the installed cameras together with the paths and directions of the most important laser beams. The numbers of the cameras can be used to identify the corresponding absorption beams. Information on the Bragg lattice laser beams also shown in this figure can be found in section 6.2.2.

Photoassociation and Raman Laser Light

Photoassociation experiments and measurements on optical Feshbach tuning require laser light that can be scanned over a wide range to locate photoassociation resonances. Once the resonance is found we need to be able to set the laser to any desired frequency in the neighborhood of the molecular transition. The tuning range which needs to be accessible in our experiments spans from the ^{87}Rb D_1 and D_2 line transition to wavelengths that are about 2 nm above the respective line. This allows to address several weakly bound excited molecular states that connect asymptotically to excited pairs of atoms in the

$S + P_{1/2}$ or $S + P_{3/2}$ states. We achieve this flexibility by using a second Ti:Sa laser whose frequency is stabilized with the help of an optical transfer lock. In the following this laser will be called the photoassociation Ti:Sa (PA Ti:Sa) to distinguish it from the MOT Ti:Sa. To realize the frequency lock for the PA Ti:Sa a beam derived from this laser is coupled into a scanning Fabry-Perot cavity. In addition a reference beam derived from the master laser is also coupled into the cavity. Then the scanning optical cavity system (Melles Griot, 2 GHz free spectral range) delivers a frequency spectrum with two peaks corresponding to the two lasers. The distance between the peaks is converted to a voltage and, after subtracting a voltage to define the set point, it is used as the error signal [Hel05]. Because the master laser is frequency locked, we can use this signal to keep the PA Ti:Sa at a fixed frequency.

Again, the Ti:Sa laser is from Coherent (model 899, short wavelength optics, 720 nm to 825 nm) and features the 895 etalon set including a heating system [Hel05] for the thick etalon. Together with a galvanometer-driven Brewster glass plate this allows tunable single frequency operation. The error signal obtained from the Fabry-Perot cavity is sent to a PID controller that regulates the Ti:Sa frequency via the rotatable Brewster plate. By controlling the set point it is possible to tune the PA Ti:Sa frequency over a range of typically 100 MHz without changing the etalon temperature. For larger detuning the etalon temperature needs to be adjusted as well. The linewidth of the Ti:Sa laser is between 3 MHz and 4 MHz and the implemented scanning cavity lock yields an absolute accuracy of better than 10 MHz. Via an optical fiber this Ti:Sa setup delivers a maximum optical power of about 200 mW to the experiment table. As the intensity of the PA light needs to be stable during the experiments a photodiode is used to measure the power incident on the atoms and to provide an error signal for stabilizing the intensity via an acousto-optical modulator.

Finding a certain molecular transition involves scanning the Ti:Sa and observing the photoassociation losses from the atomic sample. In order to find a starting point sufficiently close to a given molecular resonance, we use a wavemeter to tune the Ti:Sa laser to the approximate frequency. The wavemeter [Bla00] has been built in our institute and has a resolution of about $\pm 5 \times 10^{-4}$ nm, which corresponds to ± 250 MHz. Using this wavemeter in a first step we can locate molecular states by scanning only a relatively narrow frequency range of up to 500 MHz.

To realize Raman transitions between colliding atoms and ground state molecules, coherent laser light is needed at two frequencies. We realize the coherent pair of Raman laser beams by sending some of the light from the PA Ti:Sa through an AOM in a double-pass configuration. Then the AOM frequency (set at about 318 MHz) is used to precisely control the difference frequency of the two laser beams over a range of several tens of MHz.

Chapter 5

General Procedures and BEC Production

To obtain a ^{87}Rb BEC we apply several experimental techniques and a sequence of successive experimental stages is performed. The first sections of this chapter describe the general experimental procedures which we employ in all experiments. Finally, this chapter is concluded by a section on the production of ^{87}Rb condensates in our setup.

5.1 Measurement Cycle and Experimental Control

In order to produce a cloud of ultracold alkali atoms, we start with a magneto-optical trap, which is a powerful tool to trap a large number of atoms and cool them from room temperature to temperatures below 100 µK. Before we achieve Bose-Einstein condensation several other experimental stages follow. They consist of further cooling stages and the transport to the glass cell.

A typical experimental cycle is depicted in figure 5.1. We always begin with a MOT loading phase of an overall duration of typically 4 s to 5 s. This phase is started already at the end of the preceding cycle, so that we can begin loading the MOT while the computer still calculates the data for the next cycle. In the subsequent optical molasses stage the detuning of the MOT cooling lasers is increased and the magnetic quadrupole field is switched off for polarization gradient cooling.

Before the atomic cloud is transferred to a purely magnetic trap we optically pump the atoms into the spin state chosen for condensation, which is either $|F = 2, m_F = 2\rangle$ or $|F = 1, m_F = -1\rangle$. This spin polarization stage takes 450 μs. To load the atoms into a magnetic trap, we switch on the MOT coils again and store the atoms in the obtained quadrupole trap for about 20 ms before the transport to the glass cell starts. If we want to produce a

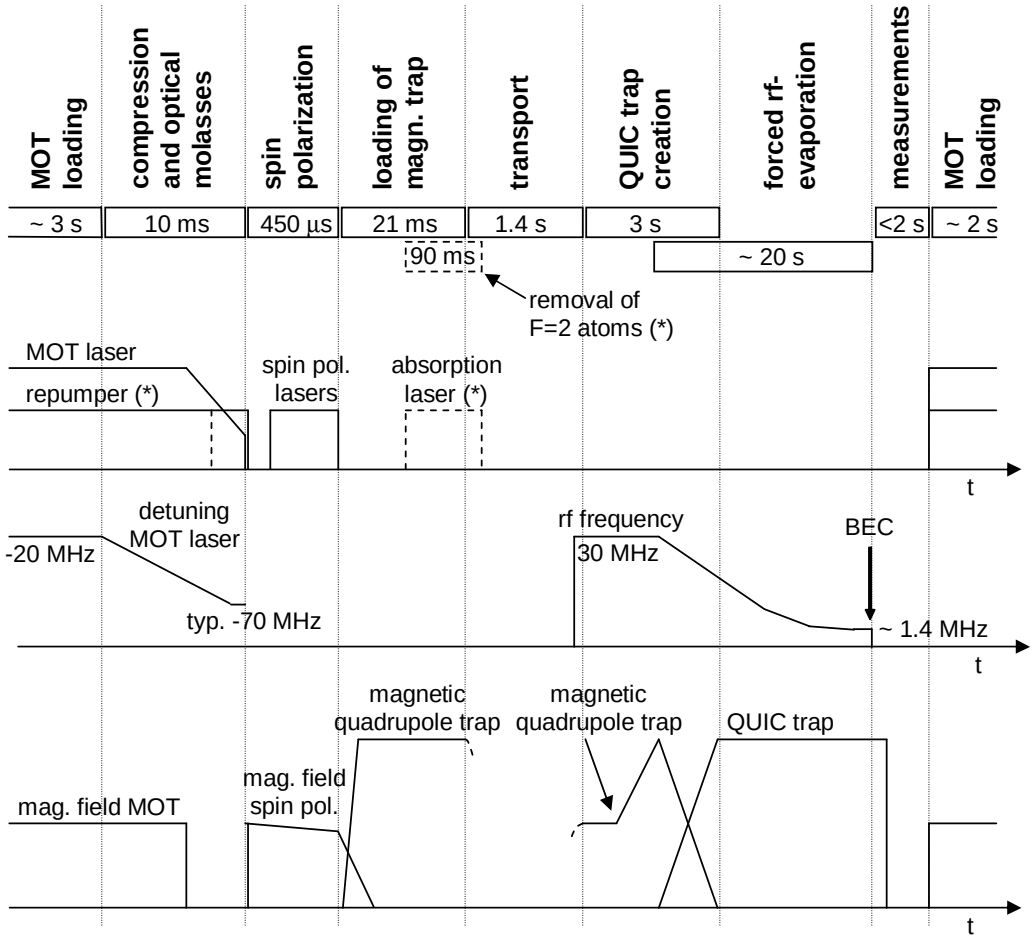

Figure 5.1: Timing diagram for a typical experimental cycle. The time axis is not to scale. For each stage the approximate duration is stated in the bar at the top. Special procedures that are used only for producing a BEC in the $|F = 1, m_F = -1\rangle$ are marked by dashed lines and a (*) behind the corresponding labels. In this case the repuming laser is switched off 1.5 ms earlier than in the procedure to create a $|F = 2, m_F = 2\rangle$ condensate.

$|F = 1, m_F = -1\rangle$ BEC, the remaining atoms in the $F = 2$ states are removed by shining in resonant absorption light on the $F = 2 \rightarrow F' = 3$ transition for 90 ms. In the next step a transfer sequence moves the magnetically trapped atom cloud from the MOT position to the glass cell within 1.4 s. At the cell we increase the gradient of the quadrupole trap and finally we convert the trap into a QUIC trap, which is completed 3 s after the arrival of the atoms.

Producing a BEC of ^{87}Rb requires further cooling to increase the phase-space density to the critical value, which is on the order of one, cf. chapter 3.

This is achieved by forced evaporative cooling with the help of rf fields. When the atoms are close to the final position, and still before the transformation of the quadrupole trap to a QUIC trap has started, we begin the rf sweep for forced evaporation. The rf frequency ramp cools the sample within about 20 s to quantum degeneracy. At the end we obtain a BEC, which is then used to perform the experiments. Finally the cycle is completed by starting the MOT loading phase again.

During the experimental sequence many processes have to be controlled with a precision down to the millisecond or even microsecond time scale. On the other hand, one whole experimental cycle to produce a BEC takes typically 30 seconds. To achieve accurate timing over this time interval with a precision below one microsecond we use a separate real-time control system (ADwin Gold from Jäger Messtechnik, Germany) and a high speed digital I/O card from National Instruments (model PCI-6534). The ADwin Gold system allows precise timing over a full experimental cycle with minimum time steps of 50 μs. These steps are determined by the time the ADwin system requires to calculate the values for the analog output channels. Faster processes are controlled by the National Instruments interface card, which has a time resolution of 100 ns but can only produce cycles shorter than about one second. Here the overall cycle duration is limited by the on-board memory of 64 MB. This card is triggered by the ADwin system to obtain stable relative timing of pulses originating from the two systems.

The front end for the experimental control is realized by a graphical LabVIEW user interface. In the LabVIEW interface all parameters are entered and, if needed, dynamic loops are generated for automatical variation of certain variables from one cycle to the other. A Matlab script then calculates timing tables for the digital channels and parameter tables to create the analog signals. The latter include the current sequences for the transport, which are composed of cubic polynomials (splines). Finally, the ADwin system and the National Instruments card use these tables to create the required output signals, see [Tha05a]. In order to increase the number of digital output channels a port expander is used to multiply the output ports of the ADwin system [Tha05a]. At the time being it provides 64 digital channels from 16 initial output ports.

In a laboratory there are many electrical devices present that create electromagnetic noise, predominantly at the power line frequency of 50 Hz and its higher harmonics. Thus it is advisable to synchronize the experiment to the line frequency in order to increase the stability of experimental conditions. In our setup the ADwin control system is synchronized to the AC line [Tha05a] with the help of externally generated 20 kHz clock pulses that are in phase with the line frequency.

5.2 Detection and Diagnosis

To obtain quantitative information about the atomic cloud such as atom number and momentum distribution, we use the well-established technique of absorption imaging [Ket99] in combination with a time-of-flight expansion. We employ absorption imaging at two locations: the MOT chamber and the position of the BEC in our glass cell. This destructive means of measuring atom numbers or temperatures always takes place at the end of an experimental cycle.

For absorption measurements we switch off the trapping potential and let the atomic cloud expand for a certain time t_e before we illuminate the atoms with absorption light on the $F = 2 \rightarrow F' = 3$ transition for typically 100 µs. At the same time we shine in laser light from the $F = 1 \rightarrow F' = 2$ repumper. When working with an atom cloud in the $|F = 1, m_F = -1\rangle$ state we turn on the repumper already 100 µs before the absorption light pulse in order to transfer the atoms to the F=2 hyperfine state. For technical convenience we use absorption light with a σ^+ polarization in the MOT chamber and linear polarized light to image the atoms in the glass cell. Therefore we have to take into account different absorption cross sections σ for the two cases, which are given by the Clebsch-Gordan coefficients of the transitions between different m_F substates [Met99, Ste02]. As the value for the absorption cross section σ is sensitive to the details of the experimental conditions, such as laser polarization, external B-field and population of the different magnetic substates, absorption imaging is subject to a systematic error on the order of 30 %. Usually we have to image BEC's of about 10^6 atoms where in the central region of maximum atom density the cloud completely absorbs resonant light. To avoid an error in our measurements due to this saturation effect, we normally work with light that is detuned from the atomic resonance by 20 MHz. In this way some light is transmitted even at the center of the cloud.

Measuring Atom Numbers

Absorption imaging investigates the shadow an atom cloud casts onto our CCD camera. This means we have to integrate the local optical density $\sigma\, n(\boldsymbol{r})$ along the direction z of the absorption laser beam to determine the light transmission through a cloud with density distribution $n(\boldsymbol{r})$. From this operation the two-dimensional optical density $\mathcal{D}(x, y) = \sigma \int n(\boldsymbol{r})\, dz$ is obtained, which enters the transmission function $T(x, y)$ of the sample

$$T(x, y) = e^{-\mathcal{D}(x,y)}. \tag{5.1}$$

Experimentally we determine the transmission function by taking two subsequent images. The first image records the shadow of the atomic cloud and the second one is a reference image of the absorption laser beam without

any atoms present. We take the reference picture 1 s after the first one, because of the time required for the read-out of the CCD chip. Dividing the first by the second image yields $T(x, y)$ and thus the column density profile $\eta(x, y) = \int n(\boldsymbol{r})\, dz = -ln(T(x, y))/\sigma$. From a fit of theoretical curves for $\eta(x, y)$ to the experimental column density we finally can determine the atom number N. In the case of a thermal cloud well above the BEC transition temperature one can assume a Maxwell-Boltzmann distribution and $\eta(x, y)$ has a Gaussian shape

$$\eta_{\mathrm{th}}(x, y) = \frac{N}{2\pi w_x w_y} \exp\left(-\frac{x^2}{2w_x^2} - \frac{y^2}{2w_y^2}\right). \tag{5.2}$$

For a pure BEC $\eta(x, y)$ results from integrating the parabolic density profile along z

$$\eta_{\mathrm{BEC}}(x, y) = \frac{5N}{2\pi R_x R_y}\left(1 - \frac{x^2}{R_x^2} - \frac{y^2}{R_y^2}\right)^{2/3}. \tag{5.3}$$

Here $w_{x,y}$ are the Gaussian widths of the expanded thermal cloud and $R_{x,y}$ the radii of the expanded BEC. During our experiments we typically work with a bimodal distribution containing a dominant BEC component and about 20% of thermal atoms. To determine the numbers of thermal and condensed atoms, we fit the sum of η_{th} and η_{BEC} to the experimentally obtained column density[1] (see appendix B). Usually, we measure the atom number after a time-of-flight expansion of $t_{\mathrm{e}} = 12\,\mathrm{ms}$.

Temperature Measurement

The temperature of a thermal atom cloud is measured in our experiments by the time-of-flight expansion technique. For a trapped thermal sample the velocity distribution and the spatial distribution have a Gaussian shape. Because the Gaussian width $\sigma_v = \sqrt{k_{\mathrm{B}}T/m}$ of the initial velocity distribution is related to the temperature T, we measure this quantity to obtain T. When we switch off the trap a thermal cloud with initial spatial widths $w_{x,y,z}(0)$ expands according to

$$w_{x,y,z}(t_{\mathrm{e}}) = \sqrt{w_{x,y,z}^2(0) + \sigma_v^2 t_{\mathrm{e}}^2}\,. \tag{5.4}$$

We determine the width of the cloud for different expansion times t_{e} and fit equation (5.4) to the data (see B.1). From the fit parameter σ_v we can then calculate the desired temperature of the sample.

[1] This method neglects the fact that the real distribution of thermal atoms is determined by the Bose distribution function (3.2) and that the thermal component is pushed outwards due to interaction with the BEC atoms. However, the error caused by this effect is smaller than the general error related to absorption imaging and for our measurements the exact number of thermal atoms is not important.

5.3 Magnetic Transfer and QUIC Trap

Every experimental cycle starts with the loading of the magneto-optical trap, which we operate at a total MOT laser power of 210 mW and a detuning from the $F = 2 \rightarrow F' = 3$ transition of about 20 MHz. The intensity of the repump laser (see section 4.3) is set to a total power of ~ 10 mW during the operation of the MOT. At the end of the loading stage we increase the MOT laser detuning to typically 60 MHz to 70 MHz and reduce the laser intensity to compress the atom cloud. Finally we switch of the magnetic field to allow for a molasses cooling stage (see the timing diagram in figure 5.1). After this step we usually end up with about 2×10^9 to 3×10^9 atoms at a temperature of about 50 µK.

Spin Polarization

Before we load the atoms into the magnetic trap we optically pump them into the desired spin-substate. During this spin polarization stage a homogeneous magnetic field is required, which splits the F state into its different m_F levels and determines the axis of quantization. For this purpose we use the push coil (see section 4.2.2) although it has not been designed for this purpose originally. But as the direction of the B-field deviates by less than 1° over the size of the atom cloud, we find our spin polarization procedure to work out reasonably well. A current of 10 A produces a magnetic field of about 10 G at the position of the atoms. We switch on the magnetic field and begin to ramp it back to zero over a time of 3 ms. The spin-polarization laser pulse is applied for 250 µs and propagates along the axis of the B-field.

To obtain a polarized cloud in the $|F = 2, m_F = +2\rangle$ state we use σ^+ light on the $F = 2 \rightarrow F' = 2$ transition. The laser light is derived from the MOT master laser (see section 4.3), which we shift to the required frequency with an acousto-optical modulator operated at 267 MHz. Simultaneously we shine in the repump laser to transfer atoms from the $F = 1$ ground state to the $F = 2$ level. With this pumping scheme the atoms gather in the desired state $|F = 2, m_F = +2\rangle$ after a few absorption-emission cycles.

A polarized sample in the spin state $|F = 1, m_F = -1\rangle$ requires a different preparation. Because we want to have the atoms in the $F = 1$ ground state, we switch off the repumper already 1.5 ms before the end of the optical molasses. The atoms are optically pumped into the spin state $|F = 1, m_F = -1\rangle$ with σ^- light on the $F = 1 \rightarrow F' = 1$ transition, which we extract from the repumping laser. As opposed to the polarization scheme before, we now have to depopulate the $F = 2$ state. We achieve this by optically exciting atoms to $F' = 2$ from where they can decay to the $F = 1$ state. For this process we use σ^- light tuned to $F = 2 \rightarrow F' = 2$ transition. The σ^- polarization is helpful because it pumps the atoms towards states with smaller m_F quantum number. However, this configuration would result in another dark state $|F = 2, m_F = -2\rangle$.

Therefore we switch on the MOT cooling laser at a very low intensity during the optical pumping. The MOT light on the $F = 2 \rightarrow F' = 3$ transition originates from six different directions (corresponding to the six MOT beams) and has no defined global polarization. Therefore it removes atoms from the $|F = 2, m_F = -2\rangle$ dark state and returns them to the optical cycle without significantly disturbing the pumping towards magnetic substates with minimal m_F values.

For a quantitative analysis we store the spin polarized atom cloud in a magnetic trap for 200 ms and then switch on the MOT again. We compare the obtained fluorescence of the atoms to the fluorescence after loading the MOT. In this way we find an overall efficiency of 50% to 60% for spin polarization and transfer to the magnetic trap. This value increases to about 70% if we reduce the MOT intensity and thus its size.

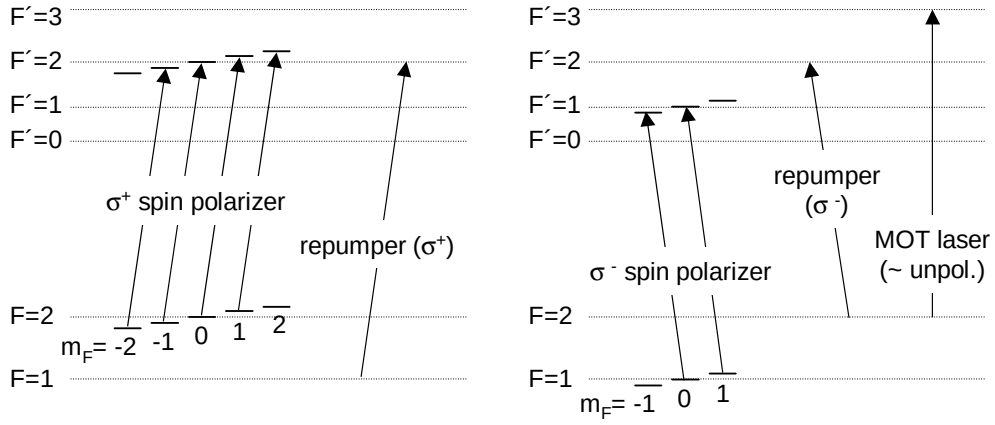

Figure 5.2: Laser transitions involved in spin polarization. Left: Preparation of state $|F = 2, m_f = 2\rangle$. Right: Preparation of state $|F = 1, m_f = -1\rangle$.

Transfer to the Glass Cell and QUIC Trap

After the spin polarization procedure we switch on the magnetic MOT coils and ramp up the current to 83.57 A within 0.5 ms. This results in a magnetic quadrupole trap with a steep gradient of $\partial B_z/\partial z = 130\,\mathrm{G/cm}$. In this trap we typically collect about 1×10^9 to 1.5×10^9 atoms at a temperature of roughly 150 µK to 200 µK. The heating is mainly due to the loading of the magnetic trap as we observe only little heating ($< 25\,\mu\mathrm{K}$) during the optical pumping.

If we are working with atoms in the $|F = 1, m_F = -1\rangle$ state we shine in a 90 ms pulse of $F = 2 \rightarrow F' = 3$ absorption light after the atoms have been transferred to the magnetic trap. In this way we can remove any atoms in the magnetically trappable $F = 2$ states and obtain a very pure spin-polarized sample. This pulse overlaps with the beginning of the magnetic transport

sequence, which starts 20 ms after the atoms are loaded to the magnetic trap. During the transfer we translate the trap by a total distance of 48.6 cm within 1.4 s. Over the whole distance the steep gradient of the trap is kept fixed at 130 G/cm and the geometry of the trap is fully controlled. Details on the magnetic transport are given in figure 4.10 and in section 4.2.2.

When the atom cloud has reached the glass cell the atoms are still contained in a quadrupole trap, whose (strong) gradient is increased to $\partial B_z/\partial z = 330\,\mathrm{G/cm}$ by ramping the current to 40 A within 1 s. Once this is completed we gradually raise the current of the Ioffe coil from 0 A to 40 A to transform the trap into a QUIC trap. The second step also takes 1 s. Finally we end up with about 4×10^8 atoms in the QUIC trap and a temperature around 300 µK. In the QUIC trap we find trap lifetimes on the order of a minute, which is by far sufficient for evaporative cooling.

From the simulations used to design the QUIC trap we find trapping frequencies of $\omega_{y,z}/2\pi = 150\,\mathrm{Hz}$ in the radial directions and $\omega_x/2\pi = 16\,\mathrm{Hz}$ in the axial direction, if the trap is operated at 40 A and if the ^{87}Rb sample is in the $|F = 1, m_F = -1\rangle$ state. For $|F = 2, m_F = 2\rangle$ atoms the trap frequencies are larger by a factor of $\sqrt{2}$, i.e. they are 212 Hz and 23 Hz, respectively. We have verified the trap frequencies experimentally for a BEC in the $|F = 1, m_F = -1\rangle$ spin state, which we use for most experiments. For the frequency measurements an additional external coil is pulsed on for 1 ms to displace the atoms from their rest position. After the displacement we observe the center-of-mass oscillation in the unperturbed trapping potential. From the experimental data we obtain oscillation frequencies of $(150.4 \pm 1.5)\,\mathrm{Hz}$ and $(16.3 \pm 0.5)\,\mathrm{Hz}$ which agrees very well with the values expected from the simulation of the trapping potential.

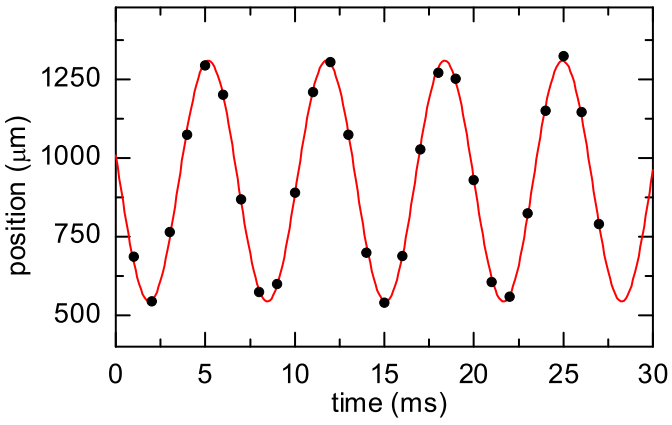

Figure 5.3: Trap frequency in radial direction for ^{87}Rb $|F = 1, m_F = -1\rangle$ atoms in the QUIC trap at a current of 40 A. The measured oscillation of the atoms in the trap is shown together with a sine-curve fitted to the data.

5.4 Evaporative Cooling and BEC

The last step before our measurements are performed is the production of a BEC. We achieve the transition to the condensate phase with the help of evaporative cooling. In this context it should be stressed that the term cooling is always used in the sense of reducing temperature and increasing phase-space density at the same time.

Evaporative Cooling

Evaporative cooling of atomic gases has been proposed in 1986 [Hes86] and is an essential step to reach the transition to the Bose-Einstein condensed phase in all BEC experiments so far. It allows to increase the phase-space density by six to seven orders of magnitude and bridges the gap between the laser cooled atom cloud and quantum degeneracy. This well-established cooling technique has been described comprehensively in literature, see for example [Lui96], [Met99] and the review article [Ket96].

We used forced evaporation that is based on rf-induced spin transitions in our magnetic trap. Depending on the magnetic field B and the corresponding splitting $|g_F|\mu_B/h \times B = 1.4\,\mathrm{MHz/G} \times B$ between neighboring magnetic sublevels m_F, an rf field of frequency $f_{\mathrm{rf}} = |g_F|\mu_B/h \times B$ induces transitions to non-trappable m_F states. Atoms with above-average kinetic energy can access regions with higher trapping potential $V_{\mathrm{trap}}(\boldsymbol{r}) \propto B(\boldsymbol{r})$ and higher magnetic field. Therefore a rf field of high frequency f_{rf} selectively removes atoms with high kinetic energy. A ramp of the rf frequency from high to low continuously takes out the high energy tail of the thermal energy distribution. This allows evaporative cooling if elastic collisions are fast enough to ensure thermalization of the atom cloud and dominate over inelastic processes. Fortunately, for $T > 100\,\mathrm{nK}$ and a ^{87}Rb scattering length of $a = 5.3\,\mathrm{nm}$ the elastic collision rate coefficient $K_{el} = (16\pi\hbar/m)\,k\,a^2$ [Ket96] exceeds the inelastic collision rate coefficients $K_{inel} = K_2/2$ (see section 2.2) by more than three orders of magnitude.

In our experiments we switch on the rf field at a frequency of 30 MHz when the atom cloud reaches the final glass cell position. Once the transformation of the quadrupole trap into a QUIC trap begins, we start to ramp down the rf frequency to a final value of typically 1.44 MHz. The 17.7 s frequency ramp consists of piecewise linear curves and is shown in figure 5.4. At the end of the frequency ramp we also lower the amplitude of the rf field as shown by the dotted line in the same plot. This ramp has been obtained by gradual improvements during the first months, in which our experiment has been producing BEC's.

If we consider the moment when the QUIC trap has formed as a starting point, the initial atom cloud is characterized by a peak phase-space den-

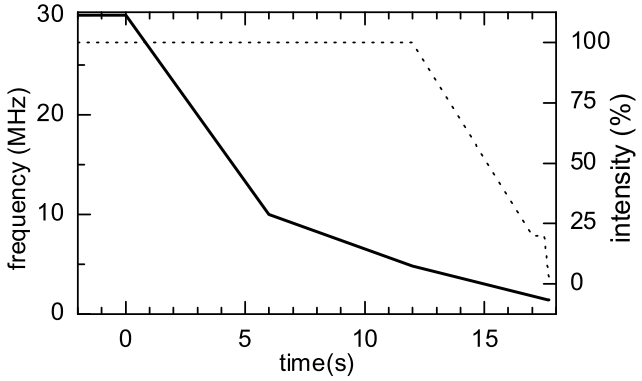

Figure 5.4: Evaporation ramp used in the experiments. The frequency of the rf field (solid line, left axis) and the rf amplitude (dotted line, right axis) are plotted versus time.

sity of $D = n\lambda_{\mathrm{dB}}^3 \approx 0.6 \times 10^{-6}$. This value corresponds to $N = 4 \times 10^8$ thermal atoms and a temperature of 300 µK, see section 5.3. At the end of the evaporation ramp and at the onset of condensation we typically have $N' = 3 \times 10^6 ... 5 \times 10^6$ atoms and the critical phase-space density is reached ($D' = D_{\mathrm{c}}$). From these values we obtain an estimate for the overall efficiency $\alpha = -\log(D'/D)/\log(N'/N)$ [Ket96] of the evaporation ramp of $\alpha > 2.7$. This value states how much the phase-space density increases for a certain loss of atoms and typically ranges between 1 and 3 in experiments with alkali atoms [Ket96, Met99]. The estimate for α gives only a lower limit, because we start the evaporation already before the QUIC trap is formed. In conclusion we find our evaporation procedure to have a good efficiency while it reliably produces large condensates as described below.

Bose-Einstein Condensation

After applying the appropriate sequence for spin polarization we can use the evaporation ramp described above to produce BEC's of up to 2×10^6 atoms in either of the states $|F = 2, m_F = 2\rangle$ or $|F = 1, m_F = -1\rangle$. However, we have performed most experiments with condensates of 1.0×10^6 to 1.5×10^6 atoms and an thermal component of typically 1×10^5 to 2×10^5 atoms by stopping the rf evaporation ramp at a slightly higher frequency. We find the atom number in the BEC to be more stable under these conditions while we still achieve condensates of more than a million atoms.

For atoms in the $|F = 2, m_F = 2\rangle$ state we observe the appearance of a BEC component at a critical temperature of about 500 nK and about 5×10^6 atoms. This is in agreement with the value obtained from the expression (3.3) for the same atom number. Due to the reduction of the trapping frequencies

by a factor of $1/\sqrt{2}$ the critical temperature is reduced by the same factor for a sample in the $|F = 1, m_F = -1\rangle$ state (cf. the linear dependence on $\bar{\omega}$ in equation (3.3)). The transition from a thermal atom cloud to a pure BEC is depicted in figure 5.5, which shows the atom density distribution for different final frequencies of the evaporation ramp.

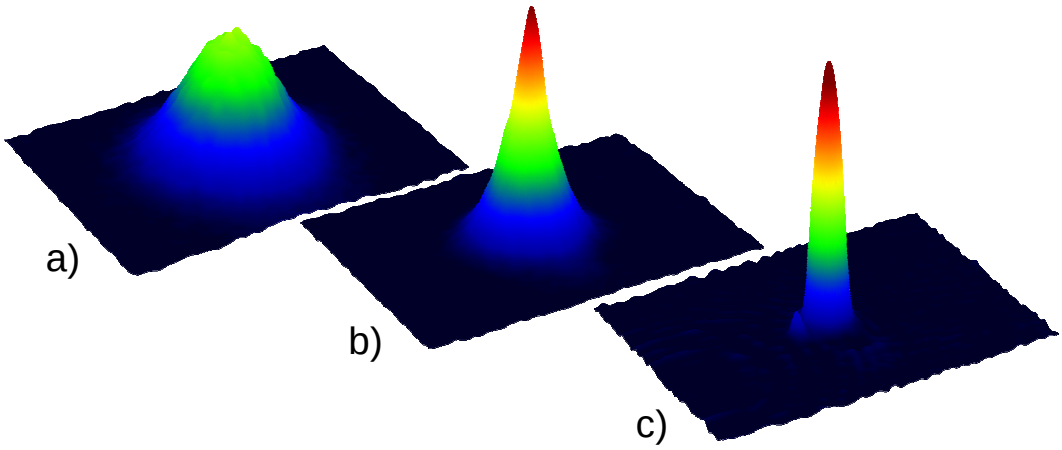

Figure 5.5: Occurrence of Bose-Einstein condensation. From left to right the final frequency of the rf ramp is decreased. a) Thermal atom cloud. b) Bimodal distribution of a BEC component and a thermal component. c) Pure BEC of about 1.5×10^6 atoms. (In this figure the atomic column density is represented by the peak hight and the color.)

In the measurements presented in the next chapter we switch off the rf field after the condensate has been produced and before the actual measurement is performed. Under this conditions we observe a lifetime of only about 300 ms for a $|F = 1, m_F = -1\rangle$ BEC with an initial peak density of $n_0 \approx 4 \times 10^{14}\,1/\mathrm{cm}^3$. As the thermal component rises at the same time and the total atom number is roughly constant, the loss from the BEC is mainly due to a heating effect. From the three-body loss rate coefficient K_3 and for the given density one expects a BEC lifetime of more than a second, see section 2.2. We attribute the reduced lifetime to a 150 Hz noise from the power line, which unfortunately matches the trap frequency and excites atoms to states with increased kinetic energy. However, the observed lifetime is much longer than the millisecond time scale of the experiments in this thesis and it does not affect our measurements. The lifetime increases to several seconds if the rf field is kept switched on to compensate for the heating and shield the condensate from thermal atoms.

The extension of the condensate is an important parameter to compare to the beam diameters used for photoassociation measurements and optical Feshbach tuning (see chapter 6). In the case of a $|F = 2, m_F = 2\rangle$ BEC the

Thomas-Fermi radii according to equation (3.10) are $R_x = 44.4\,\mu\text{m}$ in the axial direction and $R_{y,z} = 4.8\,\mu\text{m}$ in the radial directions. These values are given for a typical BEC of 1×10^6 atoms and for the trapping frequencies stated in section 5.3. For a condensate in state $|F = 1, m_F = -1\rangle$ with the same atom number the radii are $R_x = 51.7\,\mu\text{m}$ and $R_{y,z} = 5.5\,\mu\text{m}$, respectively.

Chapter 6

Optical Tuning of the Scattering Length

The concept of optical Feshbach resonances exploits laser light to couple a pair of colliding ground state atoms to a bound molecular state. As a consequence, the high degree of control one has over optical fields is carried forward to the control of atomic scattering properties. We demonstrate optical Feshbach tuning of the atom-atom interactions in our ^{87}Rb BEC with the help of a one-photon coupling scheme and of stimulated two-photon Raman transitions. In order to see in which way these processes can be controlled, we study the effect of the available parameters, i.e. laser frequency and intensity, on scattering length and atom loss. This chapter describes our experiments [The04, Tha05b], in which we implement these optical techniques to tune interactions. Furthermore, the results are discussed and related to the theoretical description of optical scattering resonances by Bohn and Julienne [Boh97, Boh99].

The effect of the applied light field on atom-atom interactions depends on the optical coupling strength. To identify a molecular state with a suitably strong coupling to the collisional state, we use photoassociation spectroscopy, as described in section 6.1. After choosing an optical transition for inducing scattering resonances, we need a technique to measure the effect of optical Feshbach resonances on the atomic scattering length. Section 6.2 discusses this aspect and describes the method of Bragg spectroscopy, which we implement in our measurements. In the following sections the central experimental results on optical Feshbach tuning are presented, first for a one-photon scheme (section 6.3) and afterwards for a two-photon Raman transition (section 6.4). The findings from the theoretical description of these processes are discussed in the respective sections as well.

6.1 Photoassociation Spectroscopy

Applying laser light to optically couple the collisional state of two atoms to a molecular level is the basis of optical Feshbach resonances. This process is also used in photoassociation spectroscopy to localize molecular states. We employ this technique with one-color laser light to identify an excited molecular state suitable for optical Feshbach tuning. Using a two-color Raman transition allows to connect to molecular levels in the ground state potential. Photoassociation with such a Raman scheme is investigated as well, because it is the basis of two-color optical scattering resonances.

6.1.1 One-Color Photoassociation: Excited Molecular States

To realize optical Feshbach tuning of ultracold interactions, an appropriate excited molecular level is needed for the optically coupling the collisional channel to a closed channel. This level should feature a reasonable strong optical transition in order to increase the effect of the optical resonance on the scattering length. From equation (2.15) we know that the strength of the coupling is strongly influenced by the Franck-Condon overlap of the two involved states. As we start from a continuum state of ultracold atoms, the Franck-Condon factor is, in general, maximized at large interatomic distances, see section 2.4. Thus the most promising molecular states are located in long-range potentials. We have investigated several states, for which a good Franck-Condon factor was expected, and compared the transition strengths, see table 6.1. These states are in the 1_g and O_g^- long-range potentials and connect asymptotically to two free ^{87}Rb atoms either in the states $5\,S_{1/2} + 5\,P_{1/2}$ or $5\,S_{1/2} + 5\,P_{3/2}$.

For our experiments on optical Feshbach resonances, we are interested in excited molecular states which fulfill one more requirement. This concerns the rovibrational substructure. The different levels should be sufficiently far apart from each other, because then we can tune the laser over the optical resonance with little disturbance due to the presence of other molecular states.

Recording Photoassociation Spectra

In order to find a certain molecular state, we first use the known binding energy of the vibrational level to set the photoassociation Ti:Sa laser (see section 4.5) to the approximate transition frequency. With the help of our wave meter the required frequency can be adjusted with an accuracy better than 500 MHz. Then a BEC of about 10^6 atoms is illuminated with the photoassociation (PA) laser light for typically 0.5 ms to 10 ms. The PA laser beam has a waist radius of either 170 μm or 250 μm ($1/e^2$ radius) and is oriented along the weak axis of the QUIC trap. It has a linear polarization, which is chosen

to be orthogonal to the direction of the trapping magnetic bias field. Typical laser intensities are between $20\,\mathrm{W/cm^2}$ and $100\,\mathrm{W/cm^2}$. After each laser light pulse and after a free time-of-flight expansion of 12 ms we measure the atom number via absorption imaging. By tuning the PA laser frequency from shot to shot we obtain photoassociation spectra of the investigated excited molecular states. As an example, figure 6.1 shows the spectrum of the state $|1_g(\sim S_{1/2} + P_{3/2}), v = 152\rangle$, which exhibits a rich hyperfine line structure.

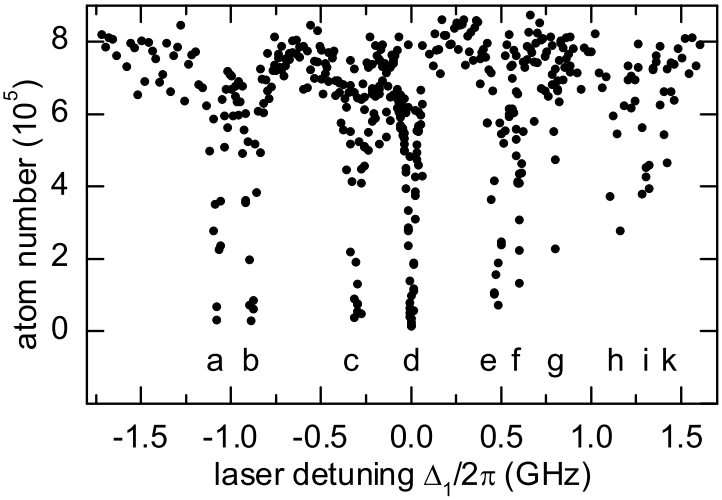

Figure 6.1: Photoassociation spectrum of the $|1_g(\sim S_{1/2} + P_{3/2}), v = 152\rangle$ state. The atom-loss spectrum is obtained after illuminating a BEC for 5 ms with a laser intensity of $90\,\mathrm{W/cm^2}$. In the plot we have arbitrarily chosen the zero of the detuning to coincide with the line labelled d. We can assign the lines a to k to molecular quantum numbers by comparing the measured spectrum to a calculation by E. Tiesinga [Tie04b]. The lines share the same total nuclear spin $i = 3$, but have different values ι for the projections of i onto the molecular axis. As ι is almost a good quantum number, it has fractional values close to integers. Further, the states depend on the total angular momentum f. We assign the following quantum numbers (f, ι) to the lines: a $\leftrightarrow$(2,-2.971), b $\leftrightarrow$(3,-2.929), c $\leftrightarrow$(1,-1.97) and (2,-1.94): not resolved, d $\leftrightarrow$(3,-1.895), e $\leftrightarrow$(1,-0.982), f $\leftrightarrow$(2,-0.948), g $\leftrightarrow$(3,-0.9), h $\leftrightarrow$(1,-0.048), i $\leftrightarrow$(2,-0.005), k $\leftrightarrow$(3,0.053).

Comparing Optical Coupling Strengths

To evaluate the transition strength of a given molecular rovibrational state, we measure the decay of the atom number for several laser detunings from the molecular line under investigation. This decay involves two atoms and is described by the differential equation (2.12). In the experiment we measure the decay rate $\gamma_{\mathrm{loss}} = \dot{N}/N$ and the peak atom density n_0. From n_0 we obtain

the spatially averaged density $\langle n \rangle = 4/7\, n_0$ by integrating over the density distribution $n(\boldsymbol{r})$ of a Thomas-Fermi BEC, see equations (3.8) and (3.9). As we mainly work in a regime of weak losses, we assume the averaged density to stay almost constant[1] and we obtain the inelastic collision rate coefficient $K_{\mathrm{inel}} = K_2/2 = \gamma_{\mathrm{loss}}/2\langle n \rangle$. This quantity is related to the relevant parameters of the optical coupling by equation (2.17):

$$K_{\mathrm{inel}} = \frac{2\pi\hbar}{m}\,\frac{1}{k}\,\frac{\Gamma_{\mathrm{stim}}\;\gamma_1}{\Delta_1^2 + (\gamma_1/2)^2}\;. \tag{6.1}$$

From a Lorentzian fit to the measured values for K_{inel} we can determine the spontaneous decay rate γ_1 of the excited molecular state. Figure 6.2 gives an example of such a fit to the experimental data. For the molecular levels in table 6.1, and at the given laser intensities, we find decay rates γ_1 ranging from about 18 MHz to 22 MHz.

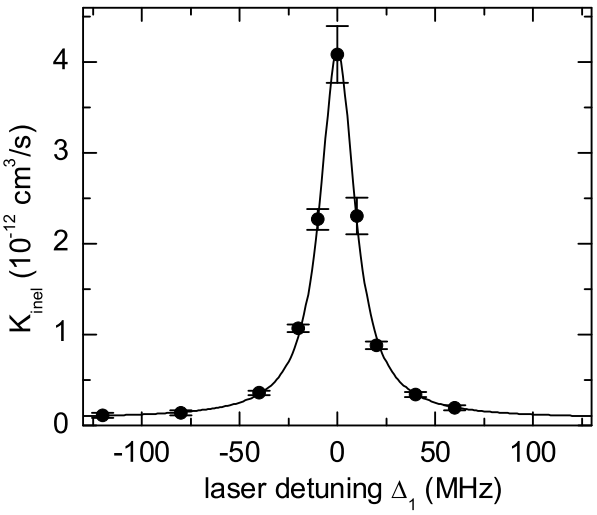

Figure 6.2: Losses from a BEC due to photoassociation. The inelastic collision rate coefficient K_{inel} is plotted for a coupling to the molecular state $|O_g^-(\sim S_{1/2} + P_{3/2}), v = 1, J = 2\rangle$. Here the laser intensity is $20\,\mathrm{W/cm^2}$ and the peak density $3.3 \times 10^{14}\,1/\mathrm{cm}^3$. From a Lorentzian fit to the data (solid line) we derive the parameters $\gamma_1 = 21\,\mathrm{MHz}$ and $\Gamma_{\mathrm{stim}} = 2.4\,\mathrm{kHz}$. To quote a value for Γ_{stim}, a collisional wave vector of $k = 2.47 \times 10^5\,\mathrm{m}^{-1}$ is used.

Equation (6.1) allows to determine the fraction Γ_{stim}/k from the measured loss rate constants. For a given laser intensity, this value is well defined and independent of the collisional wave vector k because Γ_{stim} is proportional to k,

[1] Actually, this approximation only applies to our measurements at detunings above 20 MHz. On resonance a more thorough analysis would be required. We estimate the corresponding error in Γ_{stim} to be about 40%.

see section 2.5.1. We use this quantity to compare the optical coupling for the transitions listed in table 6.1. Here, all transition strengths are given relative to the strength of the PA line that couples a $|F = 1, m_F = -1\rangle$ condensate to the state $|O_g^-(\sim S_{1/2} + P_{3/2}), v = 1, J = 2\rangle$, which we have chosen for the experiments on optical Feshbach resonances described below.

	excited molecular state	initial state	binding energy	relative strength
a)	$\|O_g^-(\sim S_{1/2} + P_{1/2}), v = 21, J = 0\rangle$	1	-23.0 cm^{-1}	0.1
b)	$\|1_g(\sim S_{1/2} + P_{3/2}), v = 152\rangle$ (*)	1	-24.1 cm^{-1}	0.1
c)	$\|1_g(\sim S_{1/2} + P_{3/2}), v = 183\rangle$ (*)	1	-6.0 cm^{-1}	2
d)	$\|O_g^-(\sim S_{1/2} + P_{3/2}), v = 1, J = 2\rangle$	1	-26.8 cm^{-1}	1
e)	$\|O_g^-(\sim S_{1/2} + P_{3/2}), v = 17, J = 2\rangle$	1	-13.6 cm^{-1}	0.9
f)	$\|O_g^-(\sim S_{1/2} + P_{3/2}), v = 1, J = 2\rangle$	2	-26.8 cm^{-1}	1

Table 6.1: Investigated molecular transitions and their relative coupling strengths. In the table the initial state of the BEC is indicated by a number, where $1 = |F = 1, m_F = -1\rangle$ and $2 = |F = 2, m_F = 2\rangle$. We give the binding energy of the molecular levels relative to the threshold quoted in the name of the respective states. The last column states the measured transition strength relative to the strength of transition d), which we estimate to have an error of about 60%. For the vibrational states marked by (*) the transition strength refers to the strongest line observed within the resolved hyperfine substructure.

The ^{87}Rb 0_g^- long-range potential has been analyzed in detail in [Fio01]. This article also compares photoassociation rates for the vibrational states, which amounts to comparing the Franck-Condon factors for an incident pure s-wave state. Amongst the states in the $O_g^-(\sim S_{1/2} + P_{3/2})$ potential that are located at least 7 cm^{-1} below the dissociation limit, the vibrational level with quantum number $v = 1$ is very promising, because it has a large Franck-Condon factor. Molecular levels that are bound by less than 7 cm^{-1} have to be excluded to avoid substantial losses via excitation of the atomic D_2 line transition. We have observed such a strong loss caused by the proximity of the D_2 line for state c) in table 6.1, which has a strong Franck-Condon factor as was indicated to us by John Bohn [Boh03]. The other investigated states in the 1_g potential are no good choice either, because they exhibit a rich hyperfine substructure of several lines spaced by typically 200 MHz. This would obviously complicate the signal in Feshbach tuning due to strong interference of the multitude of lines.

The Molecular State $|O_g^-(\sim S_{1/2}+P_{3/2}), v=1, J=2\rangle$

Figure 6.3 shows the photoassociation spectrum of the vibrational state $|O_g^-(\sim S_{1/2}+P_{3/2}), v=1\rangle$. This spectrum is recorded under the same conditions as used in our experiments on Feshbach tuning. As the optical coupling to the $J=2$ rotational state is stronger that the one to $J=0$, we use the state $|O_g^-(\sim S_{1/2}+P_{3/2}), v=1, J=2\rangle$ for all experiments described in the following. To abbreviate the notation this state will be referred to as state $|1\rangle$.

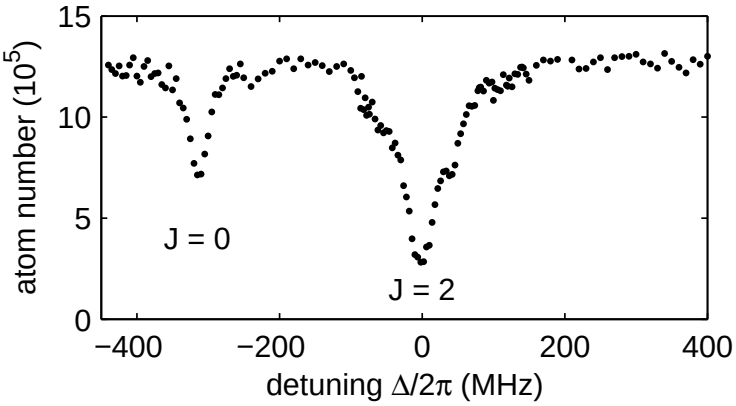

Figure 6.3: Photoassociation spectrum of the $|O_g^-(\sim S_{1/2}+P_{3/2}), v=1\rangle$ state. The spectrum is obtained after illuminating a BEC in the $|F=1, m_F=-1\rangle$ state for 70 μs with a laser intensity of 460 W/cm^2. Two rovibrational lines are visible corresponding to the rotational quantum numbers $J=0,2$ respectively. Here, the remaining atom number is plotted versus the laser detuning from the $J=2$ line. Every data point is an average of three measurements.

From the photoassociation measurements described above, the peak inelastic collision rate coefficient $K_{\mathrm{inel,max}} = K_{\mathrm{inel}}(\Delta_1{=}0)$ can be determined. According to equation (2.17), this quantity is proportional to Γ_{stim}/k and thus reflects the optical coupling strength. For a laser intensity of $I_1 = 460\,\mathrm{W/cm^2}$ we obtain a value of $K_{\mathrm{inel,max}} = (2\pm1)\times10^{-10}\,\mathrm{cm^3/s}$ for the excited molecular state $|1\rangle$. At the same laser intensity we measure a decay rate of $\gamma_1 = 21(\pm2)\,\mathrm{MHz}$. This value is significantly larger than the expected value of 12 MHz, which is given by twice the atomic linewidth [Boh97, Met99]. This might be caused by the Ti:Sa laser linewidth of about 4 MHz and a power broadening due to different light shifts of unresolved molecular hyperfine states. Another contribution to the increased width could stem from the existence of a d-wave shape resonance in the ^{87}Rb triplet ground state potential [Boe97]. As this resonance lies only 6 MHz above the dissociation threshold, the laser light can couple the excited molecular state to the d-wave resonance, which can increase the observed width γ_1 [Sim02].

When we vary the PA laser intensity we observe a strong frequency shift of the molecular line $|1\rangle$. Experimental data for this light shift are shown in figure 6.4. From a fit to the measured data points we extract a blue-shift

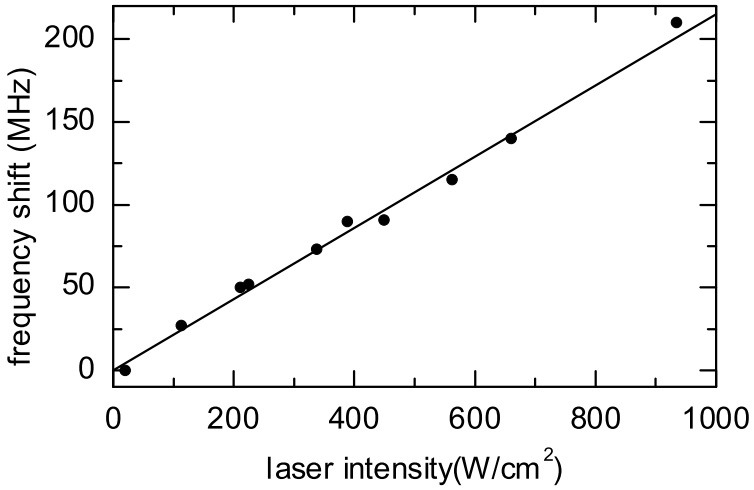

Figure 6.4: Observed light shift of the state $|O_g^-(\sim S_{1/2}+P_{3/2}), v=1, J=2\rangle$. Shown is the shift of the transition frequency versus laser intensity.

of 215 MHz/(kW cm^2). Similarly strong shifts have been observed in other photoassociation experiments with Na and Li [McK02, Ger01], but in the opposite direction. The light shift we observe might be caused by a coupling to the ^{87}Rb d-wave shape resonances mentioned above. Generally, such light shifts can have either sign because there are usually different (quasi-) bound levels that contribute with different signs depending on their location relative to threshold [Jul04a, Sim02]. In our experiments we always measure the detuning Δ_1 for a given intensity of the laser that couples collisional state $|0\rangle$ and excited state $|1\rangle$. This is consistent with the definition of the detuning entering equations (2.16) to (2.20), where the light shift has also been absorbed into the detuning Δ_1 (see also section 6.3.2).

At laser intensities above 500 W/cm^2 we observe a growing thermal component and an equivalent loss from the BEC. We attribute this effect to the appearance of a corrugation of the photoassociation laser beam due to back-reflections of laser light from the inside of the glass cell windows. This could give rise to an uncontrolled optical lattice, which transfers momentum components to the condensate. This assumption is supported by the fact that the effect becomes stronger if the beam passes the glass cell at a smaller angle of incidence and thus increases the overlap between PA beam and its back-reflection. As the effect can be neglected for laser intensities below 500 W/cm^2, we limit the laser power in our experiments to this value.

6.1.2 Two-Color Photoassociation: Molecules in the Ground State

The molecular states investigated in the previous section are electronically excited states and, consequently, exhibit a strong decay. For molecular levels in the ground state potential the situation is very different. Here the only relevant inherent decay mechanism is collision-induced de-excitation to vibrational states that are more deeply bound. The reason is that for homonuclear molecules optical dipole transitions within the same molecular potential are forbidden. In consequence, the lifetimes of ground state molecules are generally much longer than for excited molecules and line widths on the order of kHz have been observed [Ger00, Wyn00a].

We realize optical Raman transitions from the collisional state $|0\rangle$ to a molecular ground state $|2\rangle$ with two laser beams that are both derived from the PA Ti:Sa laser. Laser beam 1 is directly taken from the Ti:Sa and couples $|0\rangle$ to the intermediate state $|1\rangle$ (cf. figure 2.9). To obtain a second phase coherent laser beam 2, we use an AOM in a double pass configuration to frequency-shift some of the light extracted from the Ti:Sa laser. This light is detuned with respect to laser 1 by $\delta \approx 636\,\mathrm{MHz}$ and couples the excited state $|1\rangle$ to the second to last bound state in the $^{87}\mathrm{Rb}\ a\,^3\Sigma_u^+$ potential with a binding energy of about $h \times 636\,\mathrm{MHz}$ [Wyn00a]. In the following, $|2\rangle$ will always refer to this molecular ground state. Both laser beams are linearly polarized and are coupled into an optical fiber which delivers them to the experiment. In this way the two beams have always a good Gaussian profile and the spatial overlap is very stable. We have aligned the beams along the long axis of the condensed atom cloud. At the position of the atoms the beam waist radius is $76\,\mu\mathrm{m}$ ($1/\mathrm{e}^2$ radius). The polarization directions are parallel to each other and orthogonal to the bias magnetic field of the trap.

For the chosen molecular ground state $|2\rangle$, which is close to dissociation threshold, the Franck-Condon factor of the transition $|1\rangle \leftrightarrow |2\rangle$ is still quite large. This results in a strong optical bound-bound coupling, expressed in Rabi frequencies on the order of 10 MHz for laser intensities above $20\,\mathrm{W/cm^2}$, as used in the experiments on Feshbach resonances. In our experiment we are mainly limited by the coupling of state $|0\rangle$ to the molecular state $|1\rangle$ via laser 1. Thus, for a Raman transition there is less intensity required in laser beam 2 than in laser beam 1. Typical intensities of laser 1 are $5\,\mathrm{W/cm^2}$ to $300\,\mathrm{W/cm^2}$, while the intensity of laser 2 is up to a factor of 20 less for some measurements.

Figure 6.5 shows some examples of two-color photoassociation scans, which we use to investigate the molecular ground state $|2\rangle$. While the detuning Δ_1 of laser 1 from excited state $|1\rangle$ is fixed at a certain value, we scan laser 2 to reveal the position of the molecular level $|2\rangle$ via a dip in the atom number. In accordance with the expectation from equation (2.20), the resonance position

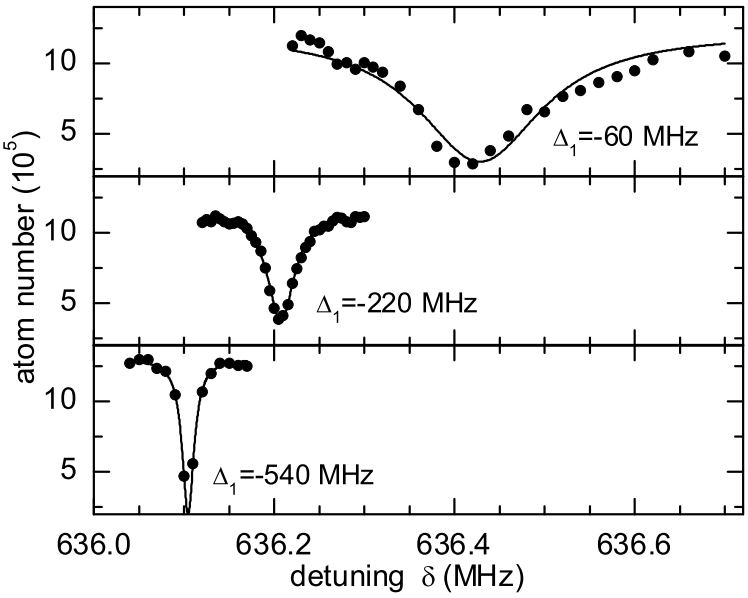

Figure 6.5: Two-color photoassociation spectra of the second to last bound state in the ^{87}Rb $a\,^3\Sigma_u^+$ potential, called state $|2\rangle$. Shown are scans of the detuning δ of the second laser from laser 1. The lines are Lorentzian fits to determine resonance positions and widths. For these data the intensities of both lasers are set to about 3 mW/cm^2. From top to bottom, the detuning of laser 1 from the intermediate state $|1\rangle = |O_g^-(\sim S_{1/2} + P_{1/2}), v = 21, J = 0\rangle$ is set to $\Delta_1 = -60$ MHz, -220 MHz and -540 MHz.

shifts with the detuning Δ_1. Furthermore, the width decreases for increasing values of Δ_1, as is expected from the discussion in sections 2.5.2 and 6.4.1. For the given laser intensities of about 3 W/cm^2, and for a large detuning Δ_1, we observe line widths of a few kHz, similar to the widths observed at low intensities in [Wyn00a] and [Rom04]. This demonstrates that these ground state molecules indeed exhibit a very narrow decay width on the order of kHz or less.

6.2 Measuring the Scattering Length

In order to study optically induced scattering resonances, an appropriate method is required to characterize the effect of an optical Feshbach resonance on atomic interactions. We monitor the value of the scattering length a via Bragg spectroscopy to detect optically induced changes of a. This section covers all aspects of measuring the scattering length in our experiments.

6.2.1 Methods to Quantify Ultracold Interactions

To obtain quantitative information on ultracold interactions in quantum gases there exist several experimental techniques. From equation (2.10) we know that the scattering length a enters the cross section for elastic scattering $\sigma_{\mathrm{el}} = 8\pi a^2$. In a first approach, one can exploit this relation to obtain the modulus of a from measuring elastic collision properties, as done in [Rob98] for example. The minimum time scale to perform such measurements is given by the time τ that we have to wait for a collision event to take place. In order to observe elastic scattering in our BEC, we could transfer some momentum to a part of the atoms and observe elastic scattering between the two momentum components. This can be done by pulsing on an optical lattice to transfer a few photon recoils to some atoms as described in [Den02]. Imaging the sample after a time-of-flight expansion reveals an isotropic sphere of elastically scattered atoms. As the number of atoms in this s-wave scattering sphere reflects the value of a, one could thus monitor the scattering length. For realistic conditions collision times τ are about a millisecond.

Another approach to determine the scattering length is to measure the mean-field energy

$$U_0 = \frac{4\pi\hbar^2}{m} a n \tag{6.2}$$

in the BEC. One way to do this is to extract U_0 from a free expansion of the condensate, see [Ino98]. The time τ_{e} that is required to convert the mean-field energy into kinetic energy depends on the trapping frequency ω_{trap}, see [Cas96], and it is given by $\tau_{\mathrm{e}} \approx 3/(\omega_{\mathrm{trap}})$. For our experimental conditions ($\omega_{\mathrm{trap}} = 2\pi \times 150\,\mathrm{Hz}$), this yields a time on the order of milliseconds again.

In our experiments we work in the proximity of a photoassociation resonance and, in consequence, we observe fast atom losses. For small detunings from the resonance these photoassociation losses limit our observation time to below $100\,\mu$s and fast measurements are vital. For this reason we employ the technique of Bragg spectroscopy [Ste99b], which is not limited by the kinematic time scales mentioned above.

Bragg Spectroscopy

Bragg spectroscopy uses stimulated two-photon scattering in a moving optical lattice in order to determine the BEC mean-field energy. The optical lattice is created from a pair of counter-propagating laser beams with wave vector k_l and a frequency difference Δf, which defines the velocity $v = \Delta f/(2k_\mathrm{l})$ of the moving lattice. In a stimulated Bragg scattering process atoms can absorb a photon from one lattice beam and emit another photon by stimulated emission into the second beam. Such a first order scattering event transfers a momentum of two photon recoils $2\hbar k_\mathrm{l}$ to the atoms. Because energy conservation has to be fulfilled the transferred photon energy is related to the change of momentum. For non-interacting atoms with an initial momentum p_i this requires the difference frequency Δf to match the transferred kinetic energy

$$h\Delta f_0 = \frac{(2\hbar k_\mathrm{l} + p_\mathrm{i})^2}{2m} - \frac{p_\mathrm{i}^2}{2m} = \frac{(2\hbar k_\mathrm{l})^2}{2m} + \frac{2\hbar k_\mathrm{l} p_\mathrm{i}}{m}\,. \tag{6.3}$$

The situation is altered for a condensate of interacting atoms because a particle moving through the BEC[2] with non-zero relative momentum experiences twice the mean-field energy that atoms in the BEC ground state perceive [Pit03, Hua87]. Thus the mean-field energy $4\pi\hbar^2\langle n\rangle a/m$ has to be added to the energy $h\Delta f_0$. Here the averaged density $\langle n\rangle$ occurs to account for the inhomogeneity of the condensate. In consequence, first order Bragg scattering becomes resonant for a frequency difference of the beams given by

$$\Delta f_\mathrm{r} = \Delta f_0 + \frac{2\hbar}{m}\langle n\rangle a\,. \tag{6.4}$$

According to this equation Bragg spectroscopy allows to obtain the mean-field energy from measuring the Bragg resonance frequency Δf_r.

6.2.2 Bragg Spectroscopy Measurements

In our setup the Bragg lattice is derived from a grating stabilized diode laser with a wavelength that is blue detuned from the ^{87}Rb D_2 line by 1.4 nm. We split the output of this laser into two counter-propagating laser beams, which are carefully overlapped and aligned to the atom cloud along the long glass cell axis (see figure 4.13). The diameter of the lattice beams is about 0.9 mm and the optical power per beam typically amounts to less than 8 mW. Both beams are linearly polarized with the direction of polarization orthogonal to the magnetic bias field of the trap. Each lattice beam passes one of two AOM's to

[2] As the transferred energies in our experiment are much larger than BEC mean-field energy, the Bragg lattice leads to single particle excitation rather than collective phonon-like excitations [Ste99b, SK99, Pit03] and the notion of a moving particle is adequate.

achieve experimental control of the difference frequency Δf. We obtain the signals to operate the AOM's from two frequency generators that are synchronized to ensure a stable and precisely defined value for Δf (precision $\sim 10\,\mathrm{Hz}$). From the wavelength of the lattice beams we get a value for the kinetic energy contribution to the Bragg resonance frequency of $\Delta f_0 = \hbar k_l^2/(\pi m) = 15.14\,\mathrm{kHz}$, if we assume the BEC to be at rest initially.

Measurement Procedure

To realize Bragg diffraction, we apply a square pulse of lattice light to the condensate with a duration of typically $70\,\mu\mathrm{s}$ to $100\,\mu\mathrm{s}$. Then we switch off the light and the magnetic trap to allow a free expansion of the condensate for 12 ms. After this expansion the diffracted atoms are spatially separated from the remaining BEC component and we use absorption imaging to determine the percentage of Bragg diffracted atoms, see figure 6.6.

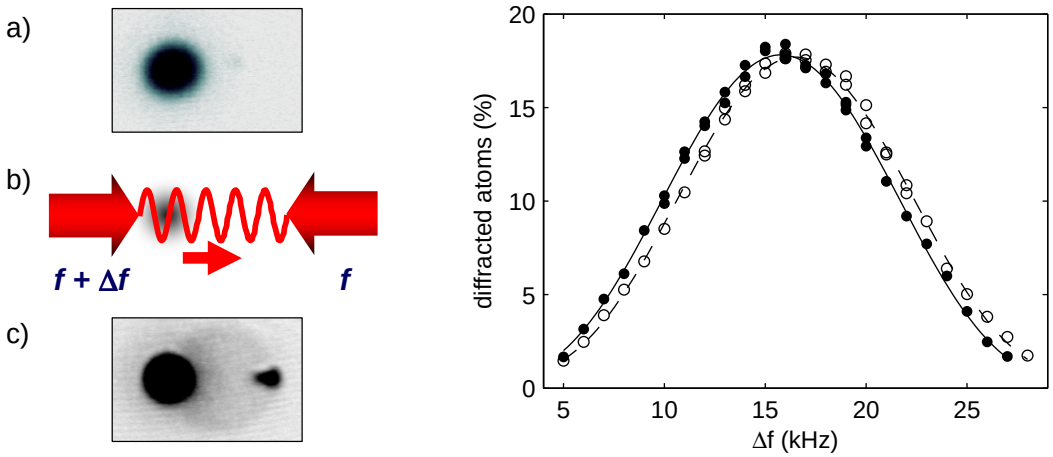

Figure 6.6: Left: Schematic depiction of a Bragg diffraction measurement. a) BEC component, b) Bragg lattice applied to the BEC, c) BEC plus Bragg diffracted atoms. Right: Typical Bragg resonance curves with a relative shift of 0.75 kHz. We plot the percentage of diffracted atoms versus the lattice difference frequency Δf. The shift is induced by optically modifying the mean-field energy with the PA laser. In the plot the two lines represent fits to the data. For better comparison the right curve is scaled by a factor of 1.09.

A Bragg spectroscopy measurement consists of varying the frequency difference Δf of the lattice beams and observing the percentage of diffracted atoms. Figure 6.6 shows typical Bragg resonance curves obtained by scanning Δf. We always adjust the Bragg lattice intensity so that about 15% of the atoms are diffracted on resonance irrespective of the used pulse length. Due to the short illumination times T the width of these curves is Fourier limited

by the light pulse duration. We use the Fourier transform of the rectangular pulse, $\propto \sin^2(\pi T(\Delta f - \Delta f_\mathrm{r}))/(\Delta f - \Delta f_\mathrm{r})^2$, to fit the data and extract the resonance position Δf_r. We have checked our Bragg spectroscopy measurements by varying the BEC density and verifying that the Bragg resonances exhibit the frequency shift expected from equation (6.4). From this and other measurements we know that we can resolve the resonance frequency to better than $\pm 100\,\mathrm{Hz}$, which is less than 1% of the $\sim 13\,\mathrm{kHz}$ width of the Bragg curve observed for a $70\,\mu\mathrm{s}$ light pulse.

We find from our Bragg measurements that the BEC has an initial momentum p_i of up to $0.1\hbar k_\mathrm{l}$, which we attribute to a combination of two effects. First, a slightly non-centered photoassociation laser beam exerts dipole forces on the atom cloud, which give rise to a certain velocity. Second, we observe a forced oscillation of the condensate in the magnetic trap at a frequency of 150 Hz which unfortunately matches the radial trap frequency. This frequency is a higher harmonic of the 50 Hz power line frequency and is in phase with the line. Because our experiment is synchronized to the line frequency, the oscillatory phase remains sufficiently stable over the time needed to record at least two Bragg resonance curves. As the initial momentum p_i is constant during a Bragg resonance measurement, we can eliminate the term containing p_i from the equation for the Bragg resonance frequency. To this end we alternately measure Bragg resonance curves for diffraction to the $+2\hbar k_\mathrm{l}$ and $-2\hbar k_\mathrm{l}$ momentum component. In equations (6.3) and (6.4) only the p_i term changes sign, thus it can be cancelled out. We end up with a remaining fluctuation of the resonance frequency that corresponds to momenta p_i below $0.01\hbar k_\mathrm{l}$.

Extracting the Scattering Length

From the measured values of the Bragg resonance frequency Δf_r we have to extract the scattering length a. According to equation (6.4) this requires the averaged atom density $\langle n \rangle$. For a Thomas-Fermi BEC the spatial average $\langle n \rangle$, as defined in equation (2.12), is related to the peak atoms density n_0 by $\langle n \rangle = 4/7 n_0$. According to equation (3.11) n_0 is proportional to $N^{2/5} a^{-3/5}$, and by measuring the atom number N one could obtain the scattering length a from Δf_r. However, the usage of this average is only appropriate if losses can be neglected and if the density is constant over time to a good approximation.

As we measure the scattering length in the proximity of a photoassociation resonance, we face fast atom losses. Very close to the resonance they happen on a timescale $t_\mathrm{loss} \sim 100\,\mu\mathrm{s}$ which is much shorter than the timescale of atomic movement in the trap $t_\mathrm{trap} = 1/\omega_\mathrm{trap} > 6.6\,\mathrm{ms}$. In this regime losses are described by a local differential equation for the density $\dot{n}(t, \boldsymbol{r}) = -2K_\mathrm{inel} n^2(t, \boldsymbol{r})$. The corresponding density distribution $n(t, \boldsymbol{r}) = n(0, \boldsymbol{r})/(1 + 2K_\mathrm{inel} n(0, \boldsymbol{r}) t)$ is dynamically flattened by the fast losses. A spatial integration of $n(t, \boldsymbol{r})$ for the case of an initial Thomas-Fermi density distribution $n(0, \boldsymbol{r})$ yields the atom

number N in the BEC [McK02]:

$$\frac{N(\eta)}{N(0)} = \frac{15}{2}\eta^{-5/2}\left(\eta^{1/2} + \frac{1}{3}\eta^{3/2} - (1+\eta)^{1/2}\tanh^{-1}\sqrt{\eta/(1+\eta)}\right), \qquad (6.5)$$

where $\eta = 2K_{\text{inel}}\, n_0\, t$ denotes the product of loss rate coefficient, initial peak density and time. We use this equation to obtain K_{inel} from the atom numbers measured before and after the photoassociation light pulse. Thus we know the full spatially resolved time evolution of the density distribution $n(t, \boldsymbol{r})$ and can determine the relevant density average $\langle n \rangle = n_{\text{eff}}$ to be entered in Eq. (6.4).

Determining the Density Average n_{eff}

To obtain n_{eff}, we use a numerical simulation of Bragg diffraction that resolves the process in space and time. Before explaining the numerical procedure, it should be noted that first order Bragg diffraction can be viewed as a stimulated two-photon Raman process. In this scheme the Bragg lattice beams lead to a Raman coupling between two different momentum states of the atoms. Therefore we can model Bragg diffraction by a coupled two level system, where the coupling is described by an effective Rabi frequency. The two levels in this system correspond to the initial BEC component and the Bragg diffracted atoms.

In the first step of the numerical simulation, the condensed cloud is divided into separate classes of constant density. For each density class Bragg diffraction is described by a two level system, where the population transfer from the initial BEC component to the diffracted component is controlled by a Rabi frequency. This frequency is set to a value that yields the observed diffraction efficiencies of about 15% after the Bragg pulse duration T. To account for atom loss due to photoassociation, the resonance frequency of the Rabi system is time dependent and reflects the varying mean-field contribution $\Delta f_{\text{mf}}(t) = (2\hbar a/m)n(t)$, cf. equation (6.4). We finally average the Bragg diffraction efficiencies obtained for the separate density classes and end up with the overall diffraction efficiency $\eta = N_{\text{diff}}/(N_{\text{BEC}} + N_{\text{diff}})$. Here N_{diff} is the number of Bragg diffracted atoms, while N_{BEC} is the atom number in the BEC component. For the averaging procedure the density classes are weighted with their atom number at the end of the Bragg lattice pulse.

Repeating this procedure for several detunings Δf from the initial resonance of the two level Rabi system, we obtain Bragg resonance curves $\eta(\Delta f)$ similar to those in figure 6.6. From the determined resonance position $\Delta f_{\text{res}} = (2\hbar/m)\, a\, n_{\text{eff}}$ the effective density is finally deduced by solving for n_{eff}. For every Bragg spectroscopy measurement we determine the effective density n_{eff} with this procedure and insert it into equation (6.4) to obtain the scattering length from the measured Bragg frequency Δf_{r}.

6.3 One-Color Optical Feshbach Resonances

This section describes our realization of optical tuning of atomic interactions and relates the results to the theoretical findings by Bohn and Julienne [Boh97, Boh99]. We employ optical transitions to couple the collisional state to an excited molecular level and measure the effect of an optically induced Feshbach resonance on the atomic scattering length. Furthermore, the dependence on both experimental parameters, the laser detuning and intensity, is investigated.

6.3.1 Observation of Optical Feshbach Tuning

For our experiments we prepare a ^{87}Rb BEC of about 10^6 atoms in the $|F = 1, m_F = -1\rangle$ state with a thermal background cloud containing typically 2×10^5 non-condensed atoms. In this way we obtain a high number of atoms in the condensate together with good reproducibility (cf. section 5.4). With our photoassociation Ti:Sa laser (laser 1) we couple pairs of atoms in the collisional state, denoted by $|0\rangle$, to the excited molecular level $|1\rangle = |O_g^-(\sim S_{1/2} + P_{3/2}), v = 1, J = 2\rangle$ described in section 6.1.1. At the position of the condensate the laser beam has a waist of 76 μm ($1/e^2$ radius). As in the photoassociation experiments of section 6.1, this beam is oriented along the long axis of the BEC and it is linearly polarized, with the direction of polarization orthogonal to the 2 Gauss bias B-field of the trap. The optical lattice used for the Bragg spectroscopy is also aligned in a horizontal direction but orthogonal to the PA laser beam (see right part of figure 6.7).

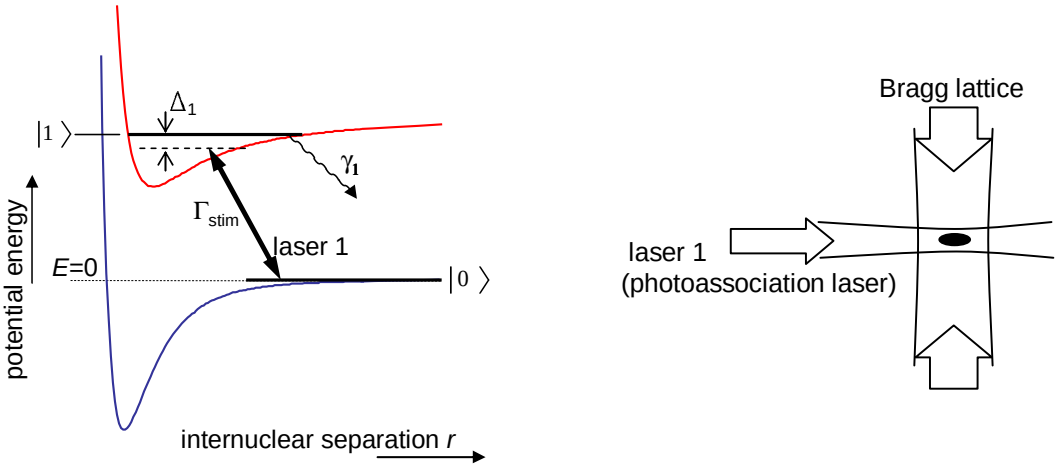

Figure 6.7: Left: Schematic diagram of an optical Feshbach resonance. The involved states and the employed laser transition are shown. Right: Arrangement of the photoassociation laser and the Bragg lattice beams relative to the BEC (top view).

Optical Feshbach Tuning via the Laser Detuning

To investigate optical Feshbach resonances, we study how the atomic scattering length a depends on the detuning Δ_1 of laser 1 from the observed position of the photoassociation resonance. For this experiment the laser intensity is kept fixed at a value of $I_1 = 460\,\mathrm{W/cm^2}$ and the BEC is illuminated for $70\,\mu$s with a square light pulse. At the same time we shine in a Bragg lattice pulse with equal duration. For every data point displayed in the following, we perform a full Bragg spectroscopy measurement as described in section 6.2.2. This typically involves between 20 and 30 single measurements to obtain a Bragg resonance curve, from which we determine the resonance frequency Δf_r.

In order to explore the tunability of the scattering length, we scan the photoassociation laser frequency over the optical resonance and record the Bragg resonance frequency Δf_r as well as the number of atoms at the end of the laser pulse. In figure 6.8 the measured data are plotted versus the detuning of laser 1. The upmost panel (a) of this figure displays the atom number, which exhibits a symmetric loss feature. At the position of maximum loss only about 10% of the initial number of atom remain. This strong loss feature indicates the position of the molecular resonance and thus the zero of the detuning Δ_1.

Figure 6.8(b) shows the measured resonance frequencies for Bragg diffraction. If we consider large positive (or negative) detunings, the measurement delivers a Bragg frequency of $\Delta f_\mathrm{r} = 16.6\,\mathrm{kHz}$, marked by a dotted line in the figure. This value agrees with the one obtained from equation (6.4) if we use the background scattering length $a_\mathrm{bg} = 100\,a_0$ [Tie04a, Jul04b] and insert the averaged density for a Thomas-Fermi BEC with 8.2×10^5 atoms. Tuning across the resonance, we observe a distorted dispersive variation of the measured resonance frequencies. Actually, such a variation is to be expected because the Bragg resonance frequency is proportional to the product of (averaged) density n and scattering length a. For this reason two effects are superimposed here: The density shows a dip due to photoassociation losses, which alone would result in a symmetrical reduction of Δf_r. On the other hand, the scattering length is expected to vary with a dispersive shape according to equation (2.16). If density was constant, the same dispersive behavior would be exhibited by Δf_r as well. Depending on the sign of Δ_1 both effects shift the resonance frequency either in the same or in opposite directions. On the left-hand side of the resonance, the reduction due to the density nearly compensates the positive contribution of the scattering length. Whereas on the other side the two effects add up and lead to a strong decrease of Δf_r.

As a consequence, we have to take into account the varying density in order to extract the scattering length a from Δf_r. With the procedure explained in section 6.2.2 this can be done, and we obtain the values for a that are plotted in figure 6.8(c). The graph shows that we are indeed able to tune the scattering length a over a considerable range. It can be set to any value in the interval

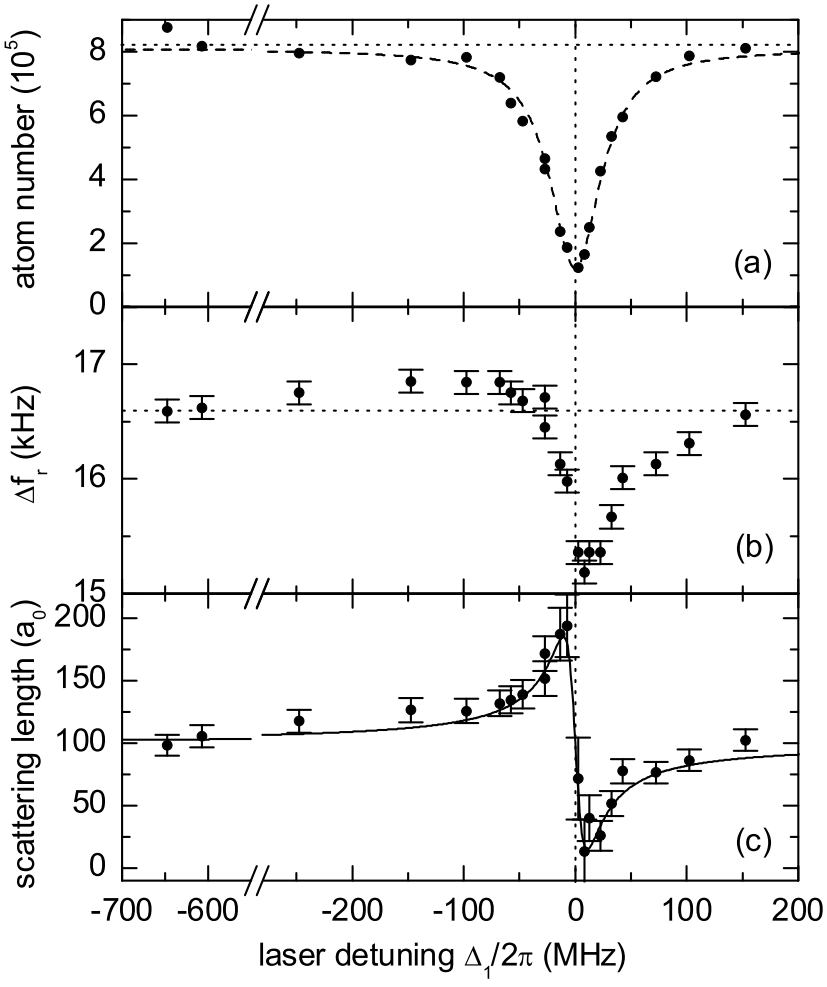

Figure 6.8: Optical Feshbach resonance. Panel (a) shows the number of condensed atoms at the end of the light pulse. The data are plotted versus the detuning of the photoassociation laser 1. A Lorentzian fit to the loss feature is presented by the dashed line. In (b) the measured Bragg resonance frequencies Δf_{r} are depicted. Here the horizontal dotted line denotes the off-resonant value of Δf_{r}. Plot (c) displays the values for the scattering length that are extracted from the data in (a) and (b). The solid line is a fit of equation 2.16 to the experimental values.

from $10\,a_0$ to $190\,a_0$ for the used laser intensity of $460\,\mathrm{W/cm^2}$ and the chosen excited state $|1\rangle$.

Also shown in figure 6.8 is a fit of equation (2.16) to the experimental data. From this fit we obtain a spontaneous decay width of $\gamma_1 = 20\,\mathrm{MHz}$ and a resonant inelastic collision rate $K_{\mathrm{inel,max}} = 1.7 \times 10^{-10}\,\mathrm{cm^3/s}$. These values agree with those obtained from the atom loss measurements in section 6.1.1.

This means that our measurements are consistent with equation (2.17) and equation (2.16) simultaneously. Therefore they confirm the intrinsic relation between a and K_{inel} expressed by these equations.

Optical Feshbach Tuning via the Laser Intensity

Optical Feshbach resonances allow to control atomic interactions not only by varying the laser detuning Δ_1 but also with the help of the laser intensity I_1. According to equation (2.16) the intensity I_1 enters the scattering length via $\Gamma_{\mathrm{stim}} \propto I_1$. We verify this linear dependence experimentally. To this end we measure the Bragg resonance frequency Δf_{r} for two symmetrical detunings $\Delta_{1\pm} = \pm 50\,\mathrm{MHz}$ and vary the intensity of the photoassociation laser. By working at symmetrical detunings, the atom numbers and thus the densities are the same. Therefore a non-zero difference $\Delta f_{\mathrm{r}}(+50\,\mathrm{MHz}) - \Delta f_{\mathrm{r}}(-50\,\mathrm{MHz})$ of the resonance frequencies proves that the scattering length a has different values on the left and the right of the resonance. This frequency difference is plotted in figure 6.9 for different laser intensities. In this experiment we

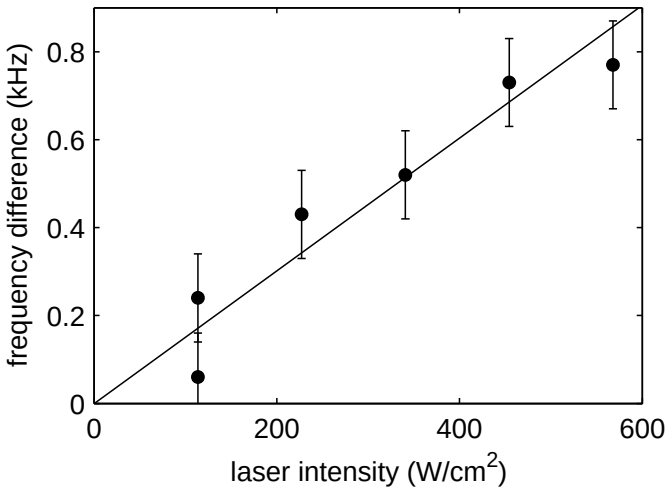

Figure 6.9: Intensity dependence of the mean-field shift induced by an optical Feshbach resonance. For constant density the difference of the Bragg resonance frequency, $\Delta f_{\mathrm{r}}(+50\,\mathrm{MHz}) - \Delta f_{\mathrm{r}}(-50\,\mathrm{MHz})$, is plotted versus laser intensity (see text).

adjust the duration of the laser pulse to keep the final atom number in the BEC constant for all intensities. Hence, we are able to ensure that a variation of the frequency difference $\Delta f_{\mathrm{r}}(+50\,\mathrm{MHz}) - \Delta f_{\mathrm{r}}(-50\,\mathrm{MHz})$ can only be caused by a change of the scattering length.

Due to the light shift (see section 6.1.1) and broadening of the photoassociation line, the measurement is somewhat complicated because we require

a constant atom number. For this reason the detunings $\Delta_{1\pm}$ are only determined with an uncertainty of about 10 MHz. Nevertheless, figure 6.9 clearly confirms that the induced mean-field shift varies linearly with intensity, just as expected.

6.3.2 Theoretical Description and Discussion

In the last section the experimental findings have already been compared to equations (2.16) and (2.17) given in section 2.5. These expressions can be obtained from the comprehensive theoretical description of cold collisions in the presence of laser light by Bohn and Julienne [Boh99]. From this theory, which is based on a quantum-defect treatment of atomic scattering, one obtains the scattering matrix S (see section 6.5). According to equation (2.8) this matrix determines the cross section for elastic collisions and, similarly, also the inelastic cross section. Introducing a complex scattering phase shift $\delta_0 = \lambda + i\mu$ the scattering matrix element S_{00} for elastic scattering can be written as $S_{00} = \exp(2i\delta_0)$. Here δ_0 has to be a complex number, because losses are present and we have $|S_{00}|^2 < 1$. Applying the definition in equation (2.11) this yields a complex scattering length A_c, from which the elastic scattering length a is obtained by taking the real part

$$a = \mathrm{Re}(A_c) = a_{\mathrm{bg}} + \frac{1}{2k}\,\frac{\Gamma_{\mathrm{stim}}\;(E - E_1(I_1) - \Delta)}{(E - E_1(I_1) - \Delta)^2 + (\gamma_1/2)^2 - (\Gamma_{\mathrm{stim}}/2)^2}\,. \qquad (6.6)$$

Here E denotes the collision energy, which can be set to zero for our experiments in the regime of ultracold collisions. The detuning Δ measures the difference between laser frequency ω_1 and the transition frequency to the (unperturbed) molecular state $E_1/\hbar = E_1(I_1 = 0)/\hbar$. We remove the intensity-dependent energy shift $E_1(I_1)$ of the excited state $|1\rangle$ from this equation by introducing the detuning $\Delta_1 = E_1(I_1)/\hbar - \omega_1$ measured from the observed position of the molecular line. Then the equation reads

$$a = a_{\mathrm{bg}} - \frac{1}{2k}\,\frac{\Gamma_{\mathrm{stim}}\;\Delta_1}{\Delta_1^2 + (\gamma_1/2)^2 - (\Gamma_{\mathrm{stim}}/2)^2}\,. \qquad (6.7)$$

The inelastic collision rate K_{inel} is determined by the imaginary part of A_c. For a cloud of condensed atoms, and after introducing the same detuning Δ_1 as above, K_{inel} is given by

$$K_{\mathrm{inel}} = \frac{2\hbar k}{m}\sigma_{\mathrm{inel}} = \frac{2\pi\hbar}{m}\;\frac{1}{k}\;\frac{\Gamma_{\mathrm{stim}}\;\gamma_1}{\Delta_1^2 + (\gamma_1/2 + \Gamma_{\mathrm{stim}}/2)^2}\,. \qquad (6.8)$$

As explained in section 2.2 this rate coefficient is reduced by a factor of 2 relative to a thermal gas. The terms containing Γ_{stim} and γ_1 in the denominators of equations (6.7) and (6.8) have to be different. In fact, if one does the full

calculations (as indicated in section 6.5), one finds that otherwise the unitarity of the scattering matrix S is violated. However, the difference is not important, because the two equations are defined in the limit $k \to 0$ and in consequence $\Gamma_{\text{stim}} \propto k$ is very small. From the measured values of K_{inel} in section 6.1.1 we obtain a value for Γ_{stim} of $\sim 50\,\text{kHz}$ at a laser intensity of $460\,\text{W/cm}^2$. Here a value of $k = 2.47 \times 10^5\,\text{m}^{-1}$ is used[3]. This means that Γ_{stim} is three orders of magnitude less than γ_1. Thus, Γ_{stim} can be omitted in the denominator and we get the equations (2.16) and (2.17) quoted in chapter 2:

$$a = a_{\text{bg}} - \frac{1}{2k} \frac{\Gamma_{\text{stim}}\ \Delta_1}{\Delta_1^2 + (\gamma_1/2)^2} \tag{6.9}$$

$$K_{\text{inel}} = \frac{2\pi\hbar}{m} \frac{1}{k} \frac{\Gamma_{\text{stim}}\ \gamma_1}{\Delta_1^2 + (\gamma_1/2)^2}\ . \tag{6.10}$$

These are the appropriate expressions to fit the experimental data for a and K_{inel}, as has been done successfully in the previous section.

Discussion

Analyzing the findings from figure 6.8 we see that a significant change in scattering length is achieved at small detunings, but it is accompanied by a substantial loss of atoms. To optimize the ratio of the desired change in scattering length to the limiting atom loss, one has to maximize the factor $(a - a_{\text{bg}})/K_{\text{inel}} \propto \Delta_1$. This clearly suggests to use large detunings Δ_1 together with a strong free-bound coupling Γ_{stim}, which ensures a sizeable change of the scattering length while losses are as small as possible. In view of this recipe it is important to choose an excited molecular state $|1\rangle$ that exhibits a large optical transition rate and a moderate spontaneous decay.

Recently it has been suggested in [Ciu04] to use an intercombination transition in alkaline-earth atoms, such as ^{40}Ca for instance. Because this intercombination line allows a better ratio of stimulated transition rate to spontaneous decay, the scattering length could be tuned over a large range while loss rates remain small.

But optical Feshbach tuning can be of interest for alkali atoms as well, when a high degree of control of atomic interactions is needed on a short time scale. Under these conditions one could take advantage of the two experimental parameters at hand to control the scattering length. Another benefit of optical Feshbach resonances is the possibility to switch interactions very fast, which is always a problem for magnetically induced resonances. In addition, spatially varying intensity distributions can easily be realized and they can be applied to tune the scattering length only locally within an atomic sample.

[3]The value of k is obtained by setting $k \approx \pi/(\sqrt{2}R_{\text{TF}})$, where R_{TF} is the Thomas-Fermi radius of the BEC. This estimate agrees very well with the value that follows from the equations (28) to (30) in [Jul04c].

6.4 Optical Feshbach Tuning with Raman Transitions

In the case of optical Feshbach resonances that are induced with a single laser, substantial atom losses via the excited state $|1\rangle$ occur in the proximity of the resonance. Compared to electronically excited molecular states, ground state molecules have a much longer lifetime. Therefore we might ask the interesting question whether the situation is improved by employing two-color Raman transitions to couple the collisional state $|0\rangle$ to a molecular level $|2\rangle$ in the ground state potential. This section investigates how Raman schemes can be applied for Feshbach tuning of ultracold interactions. It presents experimental results, which demonstrate that two-color Raman transitions can indeed be used for optical Feshbach tuning. Furthermore, the Raman coupling is compared to the one-color process discussed in section 6.3.

6.4.1 Raman Scheme for Optical Feshbach Resonances

The single-photon scheme described in 6.3 can be extended by an additional laser with frequency ω_2, that is phase coherent with laser 1. Together both lasers constitute a Raman coupling between the colliding atoms and the molecular ground state $|2\rangle$. Figure 6.10 depicts this two-color laser scheme. Now the excited molecular state $|1\rangle$ acts as an intermediate level for the two-photon

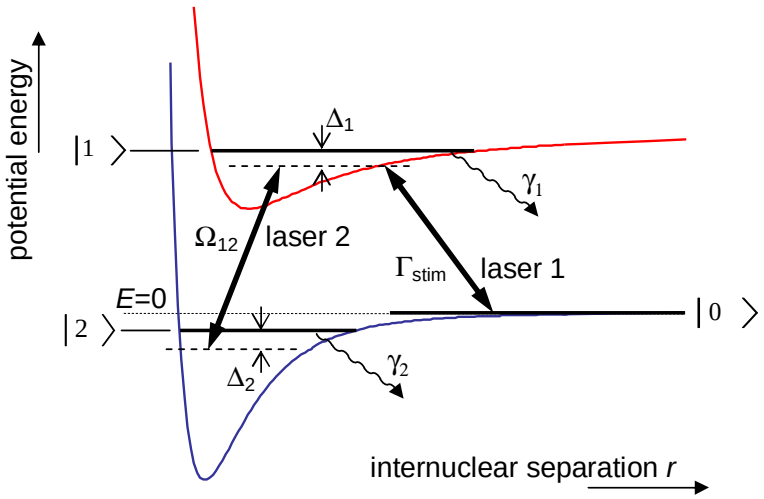

Figure 6.10: Raman scheme for optical two-color Feshbach resonances. The figure shows the two bound molecular states $|1\rangle$ and $|2\rangle$, the incident collision state $|0\rangle$ and the employed Raman lasers 1 and 2.

coupling of states $|0\rangle$ and $|2\rangle$. As before, the stimulated resonant transition rate

$$\Gamma_{\text{stim}} = (4\pi^2/c)\, I_1\, d_{01}^2\, |\langle\psi_0(r)|\psi_1(r,k)\rangle|^2 \tag{6.11}$$

characterizes the free-bound coupling due to laser 1 and is proportional to its intensity I_1. The chosen excited state is reflected by the dipole matrix element d_{01} of the transition $|0\rangle \leftrightarrow |1\rangle$ and the Franck-Condon overlap $\langle\psi_0(r)|\psi_1(r,k)\rangle$ of the respective wave functions[4]. To describe the bound-bound transition strength it is adequate to use the resonant Rabi frequency Ω_{12}, which is also determined by a dipole transition matrix element d_{12} and a Franck-Condon factor $\langle\psi_1(r)|\psi_2(r)\rangle$:

$$\Omega_{12} = \sqrt{2\pi/c\hbar^2}\sqrt{I_2}\; d_{12}|\langle\psi_1(r)|\psi_2(r)\rangle|\,, \tag{6.12}$$

see [Wei99, Jul01] for example. Here the intensity I_2 of laser 2 appears and introduces a second experimental parameter that controls the coupling strength of the Raman transition. There are two more variables that influence the Raman process, the detuning Δ_1 of laser 1 from state $|1\rangle$ and the cumulative detuning $\Delta_2 = E_2/\hbar - (\omega_1 - \omega_2)$ of the two photon transition from the energy of state $|2\rangle$.

To discuss the effect of a Raman coupling on scattering length and atom loss, we use analytic expressions that are, again, obtained from the theory by Bohn and Julienne [Boh99]. This general formalism allows to introduce additional bound states and further lasers which drive optical transitions between any pair of states in the system (see section 6.5). Again a scattering matrix S can be obtained, from which we derive the scattering length a and the inelastic collision rate coefficient K_{inel}. In general, we have two inelastic loss channels in the three level system depicted in figure 6.10. They originate from the decay of state $|1\rangle$ and $|2\rangle$ with decay rates γ_1 and γ_2, respectively. Thus there are two contributions to K_{inel}, which are expressed by the decay probabilities $|S_{0,\gamma_1}|^2$ and $|S_{0,\gamma_2}|^2$, i.e. by the squares of the respective scattering matrix elements, cf. section 6.5. Therefore we have $K_{\text{inel}} = 2\pi\hbar/(mk)\ (|S_{0,\gamma_1}|^2 + |S_{0,\gamma_2}|^2)$. The scattering length a is determined from the matrix element for elastic scattering S_{00} in the same way as in section 6.3.2.

Basic Properties of Two-Color Feshbach Resonances

In a first approach to Feshbach tuning with a Raman coupling scheme, we neglect losses from the molecular ground state $|2\rangle$ and set $\gamma_2 = 0$. As before, we use the fact that $\Gamma_{\text{stim}} \ll \gamma_1$ to simplify the denominators and write down K_{inel} for the case of losses from a BEC. Under these conditions we obtain the

[4]Note that here again the collisional wave function $\psi_1(r,k)$ is energy normalized. Thus we have $\Gamma_{\text{stim}} \propto k$ (cf. section 2.4).

following expressions from the theory in [Boh99]:

$$a = a_{\mathrm{bg}} - \frac{1}{2k}\,\frac{\Gamma_{\mathrm{stim}}\,(\Delta_1 - \Omega_{12}^2/\Delta_2)}{(\Delta_1 - \Omega_{12}^2/\Delta_2)^2 + (\gamma_1/2)^2} \tag{6.13}$$

$$K_{\mathrm{inel}} = \frac{2\pi\hbar}{m}\,\frac{1}{k}\,\frac{\Gamma_{\mathrm{stim}}\,\gamma_1}{(\Delta_1 - \Omega_{12}^2/\Delta_2)^2 + (\gamma_1/2)^2}\,. \tag{6.14}$$

By setting $\Omega_{12} = 0$ in these equations, which corresponds to switching off laser 2, we recover equations (6.9) and (6.10) for a one-color optical Feshbach resonance.

To explore the new possibilities of tuning atomic interactions, we keep Δ_1 fixed at a certain value and scan the Raman detuning Δ_2. Equations (6.13) and (6.14) show that the resonance occurs at $\Delta_2 = \Omega_{12}^2/\Delta_1$. Therefore the resonance position shifts when either the intensity of laser 2 or the detuning Δ_1 is changed. This can be seen in figure 6.11, which illustrates the content of equations (6.13) and (6.14) for two different values of Δ_1. Another remarkable difference to the curves for a and K_{inel} presented in section 6.3 is the asymmetric shape, which becomes more prominent for smaller detuning Δ_1.

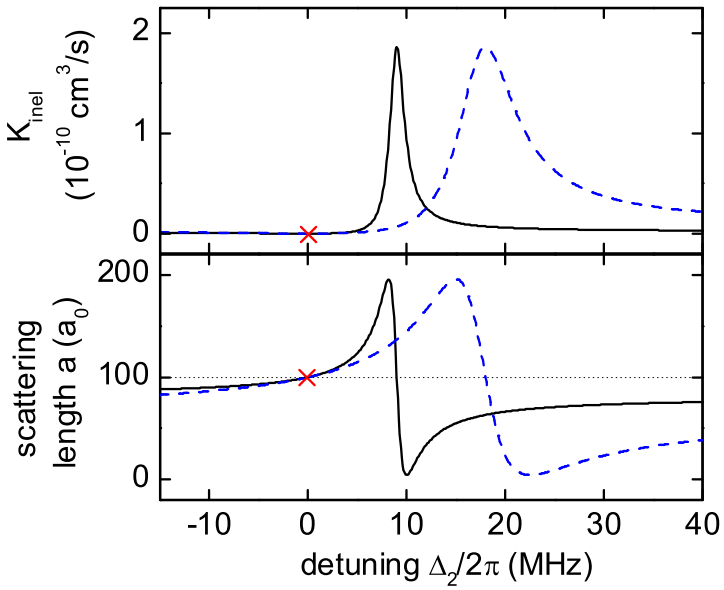

Figure 6.11: Results of the equations (6.13) and (6.14) for optical Feshbach resonances induced with a Raman coupling scheme. Here a molecular state $|2\rangle$ with negligible decay rate ($\gamma_2 = 0$) is assumed. The solid line corresponds to $\Delta_1/2\pi = 100\,\mathrm{MHz}$ and the broken line to $\Delta_1/2\pi = 50\,\mathrm{MHz}$. Other parameters: $\Gamma_{\mathrm{stim}}/2\pi = 50\,\mathrm{kHz}$, $\Omega_{12}/2\pi = 30\,\mathrm{MHz}$, $\gamma_1/2\pi = 20\,\mathrm{MHz}$, $k = 2.5 \times 10^5\,\mathrm{m}^{-1}$. In the lower graph the dotted line marks the background scattering length $a_{\mathrm{bg}} = 100\,a_0$. The crosses indicate the positions where $\Delta_2 = 0$.

In the limit of large Δ_1, the curves become symmetric and they resemble the features from the one-color optical resonances. At a Raman detuning of Δ_2=0 (marked in figure 6.11 by a cross), and irrespective of the value of Δ_1, losses via state $|1\rangle$ are completely suppressed due to a quantum interference between two decay paths: $|0\rangle \rightarrow |1\rangle \rightarrow \text{loss}\,\gamma_1$ and $|0\rangle \rightarrow |1\rangle \rightarrow |2\rangle \rightarrow |1\rangle \rightarrow \text{loss}\,\gamma_1$ [Boh96]. However, for this detuning the scattering length a is equal to its background value a_{bg}, i.e. tuning a while eliminating losses is not possible.

Comparing (6.13) and (6.14) to the equations for a one-color Feshbach resonance reveals that the expressions have the same general form. In consequence, for a given change of scattering length a, the accompanying losses are the same for both coupling schemes. Also, the maximum range of accessible values of a stays the same if we employ a Raman transition instead of a one-photon coupling.

A determination of the full width at half maximum (FWHM) of $K_{\text{inel}}(\Delta_2)$ in equation (6.14) yields the resonance width

$$\widetilde{\gamma} = \gamma_1 \left(\frac{\Omega_{12}}{\Delta_1}\right)^2 , \tag{6.15}$$

if we assume that $|\Delta_1| \gg \gamma_1$. The latter condition is necessary for this definition of the resonance width to make sense and it can be easily fulfilled. Note that equation (6.15) agrees with the width obtained from the Taylor expansion in section 2.5.2.

According to equation (6.15) we have experimental control over this width via the bound-bound coupling $\Omega_{12} \propto \sqrt{I_2}$ and the detuning Δ_1. This has experimental advantages, since in the experiment we can choose values of Δ_1 and Ω_{12} for which the resonance width becomes equal to, or smaller than the scan range of an acousto-optical modulator (AOM). Under such conditions we can conveniently scan over the whole Feshbach resonance without an involved tunable laser system.

Influence of a Finite Decay Rate of State $|2\rangle$

To see how losses due to a decay of the lower molecular state $|2\rangle$ influence two-color optical Feshbach resonances induced via a Raman scheme, it is instructive to investigate the expressions for a and K_{inel} where $\gamma_2 > 0$. They result from the same theoretical model as the equations before, see [Boh99]. Again we exploit that $\Gamma_{\text{stim}} \ll \gamma_1$ to simplify the denominator and obtain

$$a = a_{\text{bg}} - \frac{1}{2k}\,\frac{\Gamma_{\text{stim}}\,(\Delta_1 - \frac{\Omega_{12}^2}{\Delta_2} + \frac{\gamma_2^2}{4}\frac{\Delta_1}{\Delta_2^2})}{(\Delta_1 - \frac{\Omega_{12}^2}{\Delta_2} - \frac{\gamma_1\gamma_2}{4\Delta_2})^2 + (\frac{\gamma_1}{2} + \frac{\gamma_2}{2}\frac{\Delta_1}{\Delta_2})^2} \tag{6.16}$$

$$K_{\text{inel}} = \frac{2\pi\hbar}{m}\,\frac{1}{k}\,\frac{\Gamma_{\text{stim}}\gamma_1\,(1 + \frac{\gamma_2^2}{4\Delta_2^2}) + \Gamma_{\text{stim}}\gamma_2\,\frac{\Omega_{12}^2}{\Delta_2^2}}{(\Delta_1 - \frac{\Omega_{12}^2}{\Delta_2} - \frac{\gamma_1\gamma_2}{4\Delta_2})^2 + (\frac{\gamma_1}{2} + \frac{\gamma_2}{2}\frac{\Delta_1}{\Delta_2})^2} \,. \tag{6.17}$$

These general results reproduce the simplified expressions (6.13) and (6.14) by setting γ_2 to zero. If we coose $\Omega_{12} = 0$, i.e. switch off the coupling between states $|1\rangle$ and $|2\rangle$, we obtain the results for a one-color optical Feshbach resonance. Essentially, the shape of these equations for a and K_{inel} is the same as before except for the numerator of equation (6.17). Because of the two loss channels, which are due to the decay of state $|1\rangle$ and $|2\rangle$, two contributions add up to yield K_{inel}. Yet, the two-color optical Feshbach resonance still scales linearly with Γ_{stim} and thus with the intensity I_1 of laser 1.

Concerning Feshbach tuning of interactions, the most important difference is a reduction in the tuning range of a. As depicted in figure 6.12 this unwelcome effect is small for $\gamma_2 < 200\,\text{kHz}$ while it becomes prominent for decay rates above 1 MHz. If $\gamma_2 > 0$ is kept fixed and the tuning range is studied as a function of Δ_1, one also finds a reduction of $a - a_{bg}$ with increasing Δ_1. Analyzing equations (6.16) and (6.17) in more detail shows that the ratio of change-in-scattering-length to inelastic losses, $(a - a_{bg})/K_{\text{inel}}$, becomes smaller if γ_2 is increased for any choice of Δ_1 and Δ_2. Thus losses from the lower molecular state always deteriorate the tuning properties of a two-color optical Feshbach resonance.

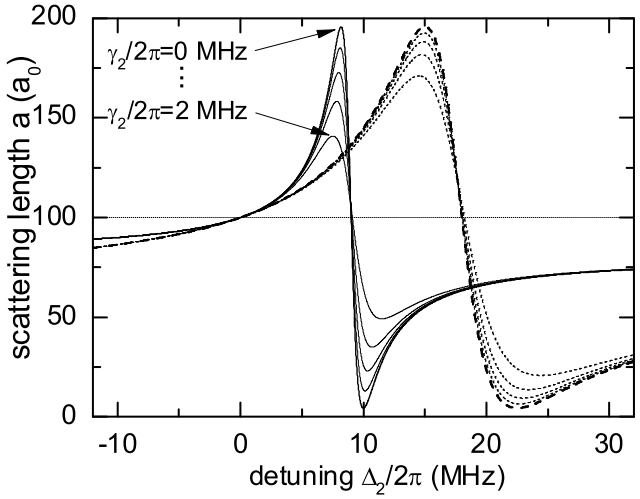

Figure 6.12: Theoretical results for a two-color optical Feshbach resonance with different decay rates γ_2 of molecular state $|2\rangle$: $\gamma_2/2\pi = 0\,\text{kHz}$, 200 kHz, 500 kHz, 1 MHz, 2 MHz. We plot equation (6.16) for $\Delta_1/2\pi = 100\,\text{MHz}$ (solid line) and 50 MHz (dashed line). The horizontal line indicates the background scattering length $a_{bg} = 100\,a_0$. Other parameters: $\Gamma_{\text{stim}}/2\pi = 50\,\text{kHz}$, $\Omega_{12}/2\pi = 30\,\text{MHz}$, $\gamma_1/2\pi = 20\,\text{MHz}$, $k = 2.5 \times 10^5\,\text{m}^{-1}$.

6.4.2 Experimental Realization of Two-Color Optical Feshbach Resonances

The experimental configuration we use to investigate two-color optical Feshbach resonances is quite similar to the one for the single-laser Feshbach resonance in section 6.3. Essentially, we have only added a second laser to optically couple the molecular states $|1\rangle$ and $|2\rangle$. Here, $|1\rangle$ is the same state as in section 6.3 and $|2\rangle$ denotes the second to last bound state in the ^{87}Rb $a\,^3\Sigma_u^+$ potential with binding energy $E_2 \approx 636\,\mathrm{MHz}$. The second Raman laser beam propagates along the same direction as laser beam 1 (see figures 6.7 and 4.13). These two laser beams are linearly polarized and their parallel directions of polarization are, again, orthogonal to the bias field of the magnetic trap. As explained in section 6.1.2, we derive both beams from the PA Ti:Sa laser. To obtain the required frequency difference between the lasers the frequency of laser 2 is shifted with an acousto optical modulator by about 636 MHz. At the position of the BEC the Raman laser beams have a waist radius of 76 μm, just as before in the one-photon Feshbach experiments. Typical laser intensities are $I_1 = 300\,\mathrm{W/cm^2}$ for laser 1 and $I_2 = 60\,\mathrm{W/cm^2}$ for laser 2.

Feshbach Tuning via Δ_2

We use exactly these intensities for the measurements shown in figure 6.13. The data are obtained by illuminating a BEC of initially 1.4×10^6 atoms for 100 μs with the two Raman lasers and performing a Bragg spectroscopy measurement at the same time. During this experiment the detuning of laser 1 is kept constant at a value of $\Delta_1 = 60\,\mathrm{MHz}$. In the first graph the number of atoms remaining after the light pulse is plotted versus the detuning Δ_2 of the Raman transition from the unperturbed position of molecular state $|2\rangle$. For all plots shown in this section we have set the binding energy $E_2 = E_2(I_2 = 0)$ of state $|2\rangle$ to $E_2 = 636.01\,\mathrm{MHz}$. This value is obtained from various atom loss measurements similar to those reported in section 6.1.2. The atom losses shown in figure 6.13(a) exhibit an asymmetric shape, which distinguishes the two-color measurement from the results in figure 6.8. This asymmetry is expected from the theory in section 6.4.1 and becomes less prominent for larger detunings Δ_1. If we use equation (6.5) to calculate the atom number from K_{inel} according to (6.14) we obtain the same line shape as in the experiment.

Figure 6.13(b) shows the measured Bragg resonance frequencies Δf_r. Again the value of Δf_r is controlled by both, the varying density and the changing scattering length a. To illustrate the influence of the two contributions, the dashed line shows the effect on Δf_r if only the density was changing according to the atom numbers shown in (a). As we observe the Bragg resonance frequencies to deviate from the dashed curve, it is clear that we can, in fact, tune the scattering length with a Raman coupling scheme. If we apply again

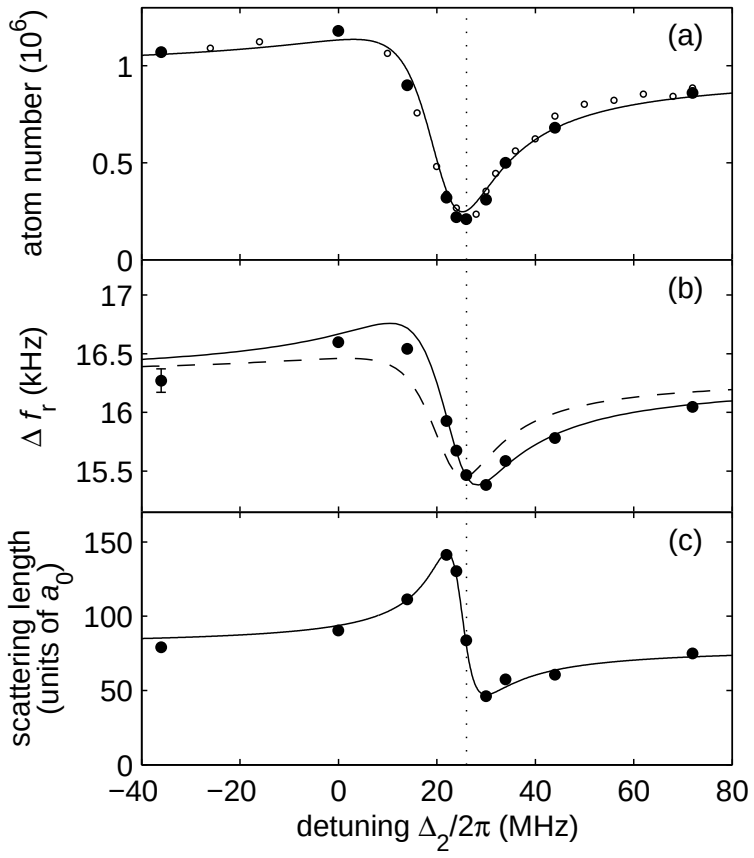

Figure 6.13: Two-color optical Feshbach resonance. Panel (a) displays the remaining atom number after the Raman light pulse as a function of Δ_2. (Filled circles correspond to the data from the same measurement as in the other two panels, while the open circles stem from an additional atom loss measurement.) The vertical dotted line marks the position of maximum atom loss. In (b) the measured Bragg resonance frequencies Δf_r are shown. Here the dashed line indicates the effect on Δf_r if only losses were present and the scattering length a was constant. Plot (c) presents the values for a that are extracted from the data in (a) and (b). Shown as solid lines in all three panels are the result from an extended model described in section 6.4.3.

the method explained in section 6.2.2 to extract a from the measured data, we obtain the values plotted in figure 6.13 (c). The scattering length varies over a considerable range of almost $100\,a_0$ and exhibits a slightly asymmetric behavior, which is predicted by equation (6.13), cf. figure 6.11. Also in accordance with the discussion in section 6.4.1, the resonance position is shifted to a detuning $\Delta_2 > 0$. For large values of Δ_2 we observe a scattering length of $80\,a_0$ and not $a = a_{bg} = 100\,a_0$. This offset is due to the presence of laser 1 and agrees with the one predicted by our measurements of the single-laser Fesh-

bach resonance. From the results in the last section one deduces that $a - a_{\mathrm{bg}}$ changes linearly with the intensity I_1 of laser 1. Further we expect from expression (6.13) the same tuning range as for a single laser Feshbach resonance, if the decay γ_2 can be neglected. Scaling the tuning range of a observed in figure 6.8 with the ratio of the intensities, we obtain a tuning range of $120\,a_0$, which is larger than range we find here. This already indicates that the decay of the lower molecular state $|2\rangle$ has to be taken into account. The solid lines shown in figure 6.13 are from a detailed calculation based on the theoretical model by Bohn and Julienne. This calculation also includes a notable decay rate of state $|2\rangle$, see section 6.4.3.

Dependence on Detuning Δ_1 and Intensity I_2

When we change the detuning Δ_1 from the excited molecular state and perform analogous measurements and analysis as above, we obtain scattering length curves as plotted in figure 6.14. The data were taken for laser intensities of

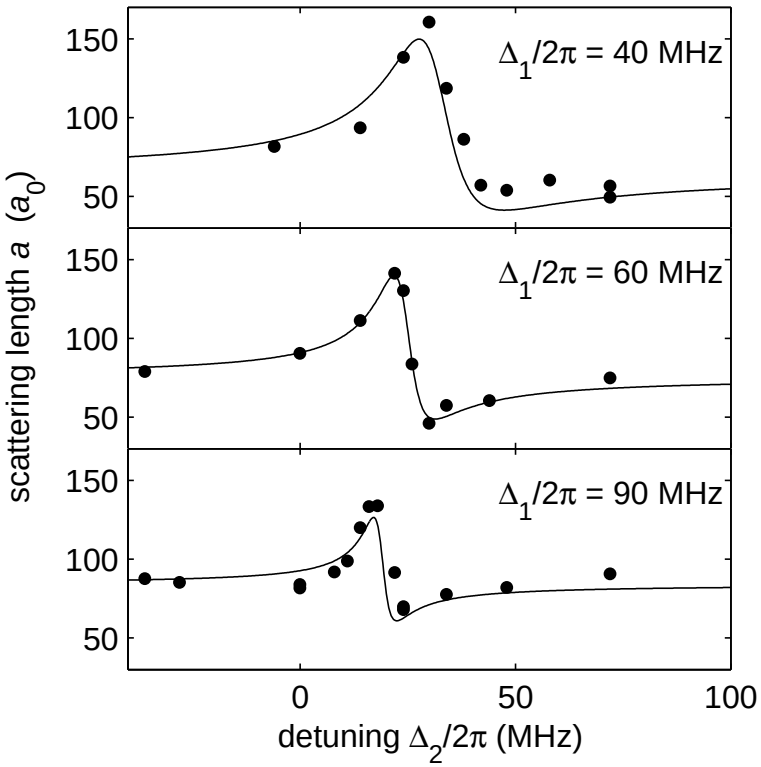

Figure 6.14: Two-color optical Feshbach resonances for different detunings Δ_1 from molecular state $|1\rangle$. The solid line shows the result of the extended model in section 6.4.3 and section 6.5. In the model calculation only the parameter Δ_1 is varied to produce the three plots.

$I_1 = 300\,\mathrm{W/cm^2}$ and $I_2 = 60\,\mathrm{W/cm^2}$, while the duration of the laser pulse was again set to 100 µs. In agreement with the expectation from section 6.4.1 the resonance position, i.e. the center of the negative slope of $a(\Delta_2)$, shifts to smaller detunings Δ_2 when we increase Δ_1. Also, this shift is accompanied by a reduction of the resonance width for larger values of Δ_1. This dependence follows the results from the simple theoretical model (6.13), (6.14), cf. the discussion in section 6.1.2.

In addition, we find a considerable reduction of the tuning range if Δ_1 is increased. According to figure 6.12 this reduction can be explained by a substantial decay rate γ_2 of the molecular ground state $|2\rangle$. However, the more detailed analysis in the next section identifies a second contribution to the decrease of Δa, which is due to the presence of another excited molecular state in the vicinity of $|1\rangle$. Both aspects are taken into account in the model calculations that are shown in figure 6.14 as solid lines. These calculations result from the same model as used in figure 6.13. The detuning Δ_1 is the only parameter we vary to obtain the three curves in figure 6.14.

To investigate how the optical Feshbach resonance depends on the intensity I_2 of laser 2 we study the maximum variation Δa of the scattering length as a function of I_2. These experiments are done for a constant detuning $\Delta_1/2\pi = 60\,\mathrm{MHz}$ and a fixed intensity $I_1 = 300\,\mathrm{W/cm^2}$ of laser 1. Figure 6.15 shows the data obtained from these measurements. For every data point a complete

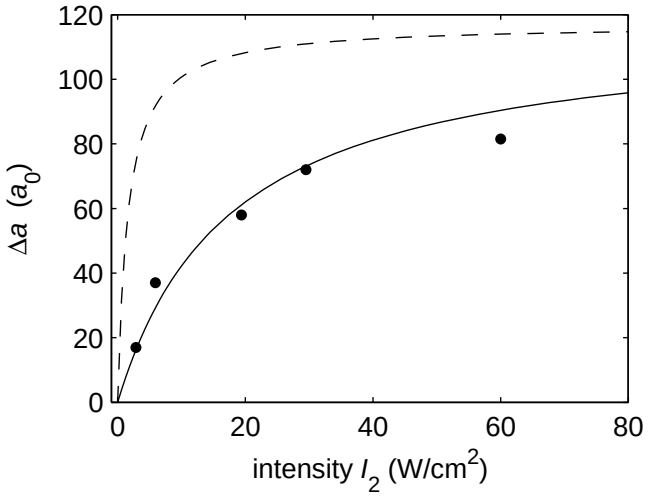

Figure 6.15: Maximum tuning range Δa of the scattering length versus intensity I_2. The experimental data are obtained for $\Delta_1/2\pi = 60\,\mathrm{MHz}$ and an intensity $I_1 = 300\,\mathrm{W/cm^2}$. For every data point a full resonance curve is taken, from which we determine $\Delta a = a_{\max} - a_{\min}$. The figure also displays the results of our extended theoretical model (see section 6.4.3). While for the dashed line $\gamma_2/2\pi$ is set to 100 kHz, the solid line corresponds to $\gamma_2/2\pi = 2\,\mathrm{MHz}$.

scattering length curve, as shown in figure 6.13, is measured and from a fit to our results we determine the maximum tuning range Δa. Since the involved Bragg spectroscopy measurements are quite time-consuming, it takes one day to obtain one data point in figure 6.15.

In our measurements we observe an increase of Δa with the intensity I_2 which finally saturates. This is not expected from the simplified equation (6.13). According to this expression the maximum tuning range is independent of Ω_{12} and thus of I_2. The reason is that equation (6.13) neglects the decay rate γ_2 of the lower molecular state. If we allow for a finite γ_2, the theoretical description reproduces a continuous increase of Δa and an eventual saturation. The dashed and the solid line in figure 6.15 show again the result from our extended theoretical model described in section 6.4.3 and section 6.5. Here decay rates of $\gamma_2/2\pi = 100\,\mathrm{kHz}$ (dashed line) and $\gamma_2/2\pi = 2\,\mathrm{MHz}$ (solid line) have been used for the calculation. From theory we find the saturation to occur at lower intensities I_2 if the decay rate γ_2 is decreased. This connects the case of large decay rates to the limit of $\gamma_2 \to 0$, where the tuning range Δa is constant.

6.4.3 Comparison to Theoretical Models, Discussion

The theoretical model described in section 6.4.1 contains only one excited molecular state $|2\rangle$. Yet we know from our photoassociation measurements that the rotational state $|3\rangle = |O_g^-(\sim S_{1/2} + P_{3/2}), v = 1, J = 0\rangle$ lies only about 300 MHz below state $|2\rangle$, see figure 6.3. Such a rather small separation demands to extend our theoretical description and to include this rotational state. In addition, we have seen that our experimental data require to introduce a seizable decay rate γ_2 into the theoretical model to describe the measurements consistently. These two issues are addressed in the following.

Extended Four-Level Model

To analyze our experiments in more detail, we extend the Bohn and Julienne model to include the additional excited molecular state $|3\rangle$ as depicted in figure 6.16. Since this state is in the vicinity of state $|1\rangle$ the Raman laser 1 also couples the collisional state $|0\rangle$ and state $|3\rangle$. Likewise, we obtain an optical coupling between states $|2\rangle$ and $|3\rangle$ due to laser 2. As the Bohn Julienne theory [Boh99] is quite general, it can be readily extend by introducing the additional state $|3\rangle$, its spontaneous decay rate γ_3 and the mentioned additional laser couplings.

There is some further coupling, which should be taken into account. The binding energy of state $|2\rangle$ is only about $E_2/h \approx 636\,\mathrm{MHz}$, and in consequence its separation from state $|0\rangle$ is small enough for some residual coupling between level $|2\rangle$ and the two excited molecular states $|1\rangle$ and $|3\rangle$ due to laser 1. Our

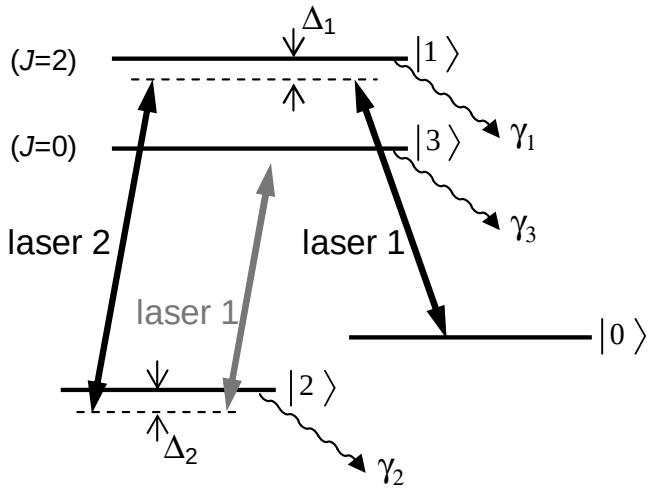

Figure 6.16: Extended model with four levels. This model includes the excited molecular state $|3\rangle$ with rotational quantum number $J = 0$ and a coupling of state $|2\rangle$ to the excited molecular levels due to laser 1.

extended four-level model also includes this coupling and is explained further in section 6.5. From this full four-level model we obtain all theoretical curves that are shown as solid lines in section 6.4.2.

We can estimate how much the couplings $|2\rangle \leftrightarrow |3\rangle$ and $|2\rangle \leftrightarrow |1\rangle$ due to laser 1 contribute to the observed width γ_2 of the ground state molecules. The increase of γ_2 due to the coupling to state $|3\rangle$ is given by

$$\triangle\gamma_2 = \gamma_3 \frac{\Omega_{3'2}^2}{\Delta_{\mathrm{eff},3}^2 + (\gamma_3/2)^2} \,,$$

where $\gamma_3 \approx \gamma_1 \approx 20\,\mathrm{MHz}$ is the decay rate of the excited state $|3\rangle$ and $\Delta_{\mathrm{eff},3} \approx 400\,\mathrm{MHz}$ the detuning of laser 1 from the transition $|2\rangle \rightarrow |3\rangle$. The optical coupling is described by a Rabi frequency $\Omega_{3'2}$, which is about 60 MHz for our laser intensity of $I_1 = 300\,\mathrm{W/cm^2}$, cf. section 6.5. With an analogue expression, we obtain the (smaller) contribution from state $|1\rangle$. Together the two couplings lead to an increase of γ_2 on the order of 100 kHz. From figure 6.15 it is obvious that this value is still too small to explain our data and accounts only for a part of the width γ_2.

Raman Feshbach Resonance as a Function of Δ_1

With the four-level model at hand, we analyze the two-laser optical Feshbach resonance as a function of the detuning Δ_1 in more detail. Figure 6.17 displays the maximum tuning range $\Delta a = a_{\max} - a_{\min}$ of the scattering length as a function of Δ_1. For these measurements we keep the laser intensities fixed

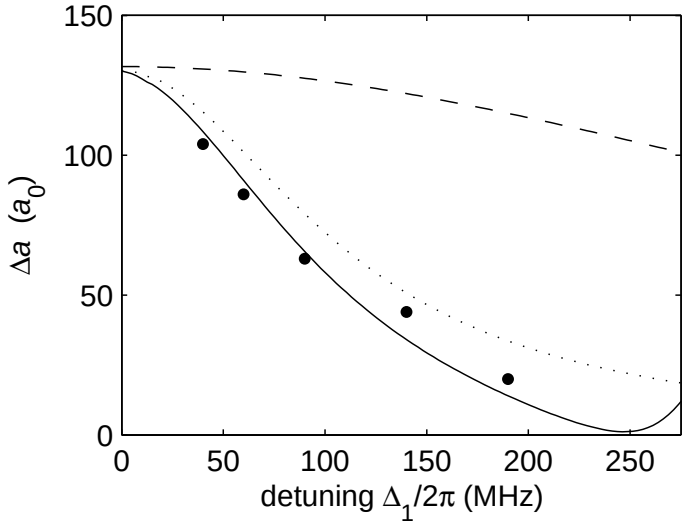

Figure 6.17: Maximum variation Δa of the scattering length plotted versus the detuning Δ_1 of laser 1. Each data point is derived from a full scattering length curve $a(\Delta_2)$. Here the dashed and the dotted line are the result of the three level model (6.16) with γ_2 set to 100 kHz and 2 MHz respectively. The solid line is obtained from the extended model described in section 6.5.

at values of $I_1 = 300\,\mathrm{W/cm^2}$ and $I_2 = 60\,\mathrm{W/cm^2}$. While the simple three level model (6.13) for a lossless molecular ground state $|2\rangle$ predicts a constant tuning range, we find Δa to decrease considerably if Δ_1 becomes larger. This observation is in agreement with the qualitative discussion of figure 6.14. If we include a substantial decay of molecular state $|2\rangle$ the three-level model from section 6.4.1 also produces a reduction of Δa for increasing detuning. This is depicted by the dashed and the dotted line in figure 6.17 for decay rates $\gamma_2 = 100\,\mathrm{kHz}$ and $\gamma_2 = 2\,\mathrm{MHz}$, respectively. While the first value of γ_2 only leads to a slow reduction of the tuning range, the dotted line is already close to the results of our measurements. However, the solid line describes the data even better. It stems from the extended model and also assumes a spontaneous decay rate $\gamma_2 = 2\,\mathrm{MHz}$. On the other hand, if one sticks to the full four-level model but uses smaller values of γ_2 it is not possible to properly describe the measured data either.

This indicates that two effects are responsible for the decrease of Δa. First, a quantum interference involving the states $|1\rangle$ and $|3\rangle$ cancels out the two-color Feshbach resonance for $\Delta_1/2\pi \approx 250\,\mathrm{MHz}$ which should also be observed if γ_2 vanishes. In the proximity of state $|3\rangle$ the atoms can be coupled back to the initial scattering channel along the path $|0\rangle \to |3\rangle \to |2\rangle \to |3\rangle \to |0\rangle$ and along a path where state $|3\rangle$ is replaced by state $|1\rangle$. This gives rise to quantum interference similar to the effect mentioned in section 4.5, page 100. The extended four-level model indeed reproduces an interference effect, see the

solid line in figure 6.17. Experimentally we observe this interference effect via a disappearance of the atom loss signal in two-color photoassociation scans as well.

The second reason for the reduction of Δa is the large decay rate $\gamma_2/2\pi \approx 2\,\mathrm{MHz}$, which we have to associate to state $|2\rangle$ in order to describe our measurements with the theoretical models. Actually, this is a surprisingly large decay width for a molecular ground state. As we have observed very narrow linewidths of a few kHz for low laser intensities (see section 6.1.2), this broadening must be caused by a coupling via laser light. One possibility is a coupling to additional excited molecular states. From a variety of measurements in the vicinity ($\sim$ several hundred MHz) of the two excited molecular states $|1\rangle$ and $|3\rangle$ we have found no further molecular levels close.by. Furthermore, our experimental data do show no further resonances of scattering length or atom loss, which would be the consequence of an state lying within our tuning range. Rather, we observe a fairly constant value of the ground state decay γ_2 over our whole experimental range. The constant background of losses makes it possible to consistently describe our measured data with a four-level model and a fixed parameter γ_2. Another contribution to the observed decay width γ_2 could stem from a coupling of state $|2\rangle$ to the ^{87}Rb d-wave shape resonance in the collisional channel [Boe97, Sim02], already mentioned in section 6.1.1.

It is an interesting question to determine the detailed origin of the large decay rate. However, finding a definite answer requires more involved theoretical models and is beyond the aim of the presented experiments, which focus on optical Feshbach tuning of interactions. Although our model does not explain the reason for the width of state $|2\rangle$, it is well suited to describe our experimental data for scattering length and atom loss consistently.

Prospects of Two-Color Feshbach Resonances

As shown in this and the previous section, we can indeed induce optical Feshbach resonances with two-color Raman coupling schemes. For typical laser powers of $I_1 = 300\,\mathrm{W/cm^2}$ and $I_2 = 60\,\mathrm{W/cm^2}$ we observe the scattering length to vary over a considerable range of up to $100\,a_0$, when the Raman detuning Δ_2 is scanned. If we tune over resonance, we observe similar strong atom losses as in the case of a single-laser resonance. This is also expected from theory, which states that for a given change in scattering length the losses can not be reduced by using a Raman coupling scheme.

In our measurements the tuning range of the scattering length a is reduced discernably with respect to a one-color Feshbach resonance because of a large decay rate γ_2 of the molecular ground state. However, for values of γ_2 below a few hundred kHz the reduction is expected to be very small according to the theoretical model of two-color Feshbach resonances. It is well possible that for

other sets of molecular states and for other species the effective decay rate γ_2 is in this range. In consequence, the tuning range of a stays almost the same as in the one-color scheme. In that case a Raman scheme offers experimental advantages and might be superior to a single-laser Feshbach resonance. The reason for this is that a Raman coupling scheme allows to modify the resonance width by varying the detuning Δ_1 of laser 1. In our experiments we achieve resonances that are narrow enough to scan over the whole tuning range of a with the help of an acousto-optical modulator. This allows convenient control of the scattering properties without a complex laser system that can be tuned over the typical width of 100 MHz for the one-color optical Feshbach resonance.

6.5 Details of the Theoretical Model

For the discussion of our experimental results on optical Feshbach tuning, we have used a theoretical model by Bohn and Julienne [Boh99] to characterize the variation of scattering length a and inelastic collision rate K_{inel}. This section outlines the essential procedure to obtain a and K_{inel} from this theory. Furthermore, it describes in more detail the model used in the previous section to discuss our experimental findings.

In scattering theory the whole physics of elastic and inelastic collision processes is contained in the unitary scattering matrix S. From this matrix the scattering cross sections for the different output channels $|f\rangle$ and a given initial channel $|0\rangle$ can be calculated. For identical bosons one obtains:

$$\sigma_f(k) = \sum_{l\,even} \sigma_f(k,l) = \frac{2\pi}{k^2} \sum_{l\,even} (2l+1)|\delta_{0f} - S_{0,f}(l)|^2. \tag{6.18}$$

Here k denotes the collision momentum and l the angular momentum of the partial wave (cf. chapter 2), while δ_{ij} is the Kronecker δ-symbol. In this work we only distinguish between elastic scattering ($f = 0$) and inelastic scattering ($f \neq 0$) and merge all inelastic processes into $\sigma_{\mathrm{inel}} = \sum_{f\neq 0} \sigma_f$. As our collisions are ultracold and no thermal averaging is required, the inelastic collision rate coefficient K_{inel} is given by[5]

$$K_{\mathrm{inel}} = \sum_{f\neq 0} K_{0,f} = \sum_{f\neq 0} \frac{2\hbar k}{m} \sigma_f(k, l=0) = \frac{4\pi\hbar}{mk} \sum_{f\neq 0} |S_{0,f}|^2 \,. \tag{6.19}$$

This value is decreased by a factor of 2 for losses from a BEC (cf. section 2.2). The s-wave scattering length for elastic collisions is determined from $S_{0,0} = \exp(2i\delta_0)$ by introducing the scattering phase δ_0 and applying the definition (2.11). When inelastic collision channels are accessible, we have $|S_{0,0}|^2 < 1$ because the unitarity of S requires $\sum_f |S_{0,f}|^2 = 1$. In consequence, δ_0 is complex valued and in (2.11) we have to take the real part to obtain the elastic scattering length a:

$$a = \mathrm{Re}(A_{\mathrm{c}}) = \mathrm{Re}\left(-\tan(\delta_0(k))/k\right) = -\frac{1}{2k} \frac{\mathrm{Im}(S_{0,0})}{\mathrm{Re}(S_{0,0})}. \tag{6.20}$$

Note that this equation is valid only in the limit $k \to 0$, see section 2.1.

Bohn and Julienne [Boh97] have presented a convenient model to describe optical scattering resonances. In [Boh99] they give an extended version of this model, which allows to obtain the elastic and inelastic scattering properties for a system with an arbitrary number of molecular levels and optical couplings. From this generalized formalism all expressions for the two-photon Raman scheme used in this work processes can be calculated.

[5] Due to the Wigner threshold law only the s-wave contribution remains for ultracold scattering, see section 2.1.

Full Result for a Three-Level System

The following paragraph demonstrates, how we can derive a and K_{inel} according to the theoretical model [Boh99]. In order to outline the general procedure, the the three-level Raman scheme depicted in figure 6.10 is used. Besides the continuum state $|0\rangle$ we have to consider the two molecular levels $|1\rangle$ and $|2\rangle$ with their respective decay rates γ_1, γ_2. To include the decay, artificial output channels $|a_i\rangle$ are introduced and coupled to the corresponding molecular states $|i\rangle$ to reproduce the loss rates γ_i. When we switch on the Raman lasers, we obtain optical coupling of states $|0\rangle$ and $|1\rangle$ and of states $|1\rangle$ and $|2\rangle$. The first (free-bound) coupling is described by the stimulated rate $\Gamma_{\mathrm{stim}} = \Gamma_{01}$, while the Rabi frequency Ω_{12} defines the coupling between $|1\rangle$ and $|2\rangle$, cf. section 6.4.1. These quantities enter a reaction matrix K, which is the central term of the Bohn and Julienne theory [Boh99]. To write down this matrix the involved state are arranged in the order $(0, a_1, a_2, 1, 2)$ and used as row and column indices for K. Then K can be divided into sub-matrices describing the closed channels (i.e. channels 1,2) and the coupling between closed channels and open channels $(0, a_1, a_2)$:

$$K = \begin{pmatrix} \mathbf{0} & K^{\mathrm{oc}} \\ K^{\mathrm{co}} & K^{\mathrm{cc}} \end{pmatrix}, \tag{6.21}$$

where the sub-matrices are given by

$$K^{\mathrm{oc}} = \begin{pmatrix} \sqrt{\Gamma_{01}/2} & 0 \\ \sqrt{\gamma_1/2} & 0 \\ 0 & \sqrt{\gamma_2/2} \end{pmatrix} \quad \text{and} \quad K^{\mathrm{cc}} = \begin{pmatrix} E_1/\hbar & \Omega_{12} \\ \Omega_{12} & 0 \end{pmatrix}. \tag{6.22}$$

In equation (6.21) K^{co} denotes the transposed matrix of K^{oc}. We set the intensity dependent energy E_1 of state $|1\rangle$ to zero in the matrix K^{cc}. This corresponds to absorbing the light shift of this level into the detuning Δ_1 by defining Δ_1 relative to the observed one-photon resonance, cf. section 6.3.2.

After writing down the K matrix, the second step is to eliminate the closed channels, which amounts to the requirement that the closed channel wave functions vanish at large internuclear distances. This step is realized by calculating a reduced matrix

$$K^{\mathrm{red}} = K^{\mathrm{oc}}(D - K^{\mathrm{cc}})^{-1} K^{\mathrm{co}}, \quad \text{where} \quad D = \begin{pmatrix} \Delta_1 & 0 \\ 0 & \Delta_2 \end{pmatrix} \tag{6.23}$$

contains the detunings as defined in sections 6.3.2 and 6.4.1. Note that the collision energy E does not appear here, because we are describing ultracold interactions and set $E \approx 0$. From K^{red} the scattering matrix S is finally obtained by

$$S = \exp(i\eta)(1 + iK^{\mathrm{red}})(1 - iK^{\mathrm{red}})^{-1} \exp(i\eta). \tag{6.24}$$

Here the diagonal matrix $\exp(i\eta)$ of elastic phase shifts occurs. For our purposes it only has the effect to produce the background scatting length a_{bg} in equations (6.20) and (6.26).

Once the scattering matrix S is calculated, it is straight forward to determine a and K_{inel} with the help of equations (6.19) and (6.20). For atoms in a BEC we obtain the result:

$$K_{\mathrm{inel}} = \frac{2\pi\hbar}{m}\,\frac{1}{k}\frac{\Gamma_{01}\gamma_1\,(\Delta_2^2+\frac{\gamma_2^2}{4})+\Gamma_{01}\gamma_2\,\Omega_{12}^2}{(\Delta_1\Delta_2-\Omega_{12}^2-\frac{\gamma_2(\gamma_1+\Gamma_{01})}{4})^2+(\frac{(\gamma_1+\Gamma_{01})}{2}\Delta_2+\frac{\gamma_2}{2}\Delta_1)^2} \tag{6.25}$$

$$a = a_{\mathrm{bg}} - \frac{1}{2k}\,\frac{\Gamma_{\mathrm{stim}}(\Delta_1\Delta_2-\Omega_{12}^2+\frac{\gamma_2^2}{4}\frac{\Delta_1}{\Delta_2})\Delta_2}{(\Delta_1\Delta_2-\Omega_{12}^2-\frac{\gamma_2(\gamma_1-\Gamma_{01})}{4})(\Delta_1\Delta_2-\Omega_{12}^2-\frac{\gamma_2(\gamma_1+\Gamma_{01})}{4})+\beta_+\beta_-}, \tag{6.26}$$

with the following abbreviation

$$\beta_\pm = \left(\frac{(\gamma_1 \pm \Gamma_{01})}{2}\Delta_2 + \frac{\gamma_2}{2}\Delta_1\right).$$

If $\Gamma_{\mathrm{stim}} := \Gamma_{01} \ll \gamma_1$ these results can be replaced by the approximated expressions (6.16) and (6.17).

Full Four-Level Model

In the previous paragraph a three-level model has been used to explain how the scattering length and the inelastic collision rate coefficient are obtained from the Bohn and Julienne theory. However, this model neglects the existence of the $J = 0$ rovibrational level, see figures 6.3 and 6.16. We extend the model to include this additional excited state $|3\rangle = |O_g^-(\sim S_{1/2} + P_{3/2}), v = 1, J = 0\rangle$. The coupling of this state to the continuum $|0\rangle$ is represented by a stimulated transition rate Γ_{03}, while the Rabi frequency Ω_{32} describes the coupling between $|2\rangle$ and $|3\rangle$. This system and the involved couplings are depicted in the right part of figure 6.18. Further, the coupling of state $|2\rangle$ to the excited molecular states $|1\rangle$ and $|3\rangle$ due to laser 1 is taken into account in our full four-level model. To this end two artificial copies $|1'\rangle$ and $|3'\rangle$ of the excited states are introduced and connected to the ground state $|2\rangle$ via the Rabi frequencies $\Omega_{1'2}$ and $\Omega_{3'2}$ (left-hand side of figure 6.18). The intensity dependance $\Omega \propto \sqrt{I}$ of the Rabi frequencies completely defines $\Omega_{1'2}$ and $\Omega_{3'2}$, which are given by $\Omega_{1'2} = \sqrt{I_1/I_2}\;\Omega_{12}$ and $\Omega_{3'2} = \sqrt{I_1/I_2}\;\Omega_{32}$.

To obtain K_{inel} and a according to this model, the same recipe is followed as for the three-level system explained above. Only the matrix dimensions increase. With this model the data presented in section 6.4 have been fitted consistently and the results are shown in figures 6.13 to 6.17 as solid lines. We have also successfully checked the consistency of the full four-level model on the basis of several atom loss measurement similar to the plot in figure 6.13(a).

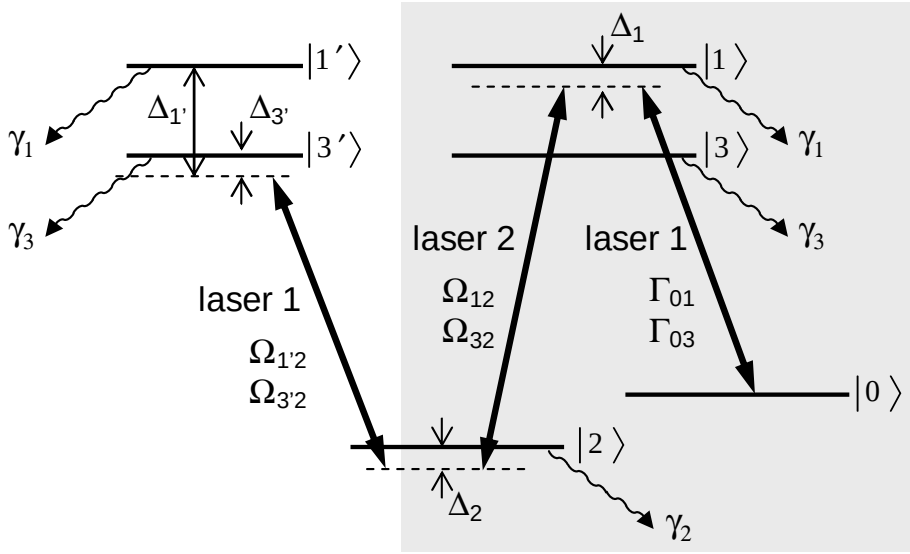

Figure 6.18: Model for the full four-level scheme. Two artificial copies of the excited molecular states $|1\rangle$ and $|3\rangle$ are included (left part). In this way the additional coupling between level $|2\rangle$ and the excited states due to laser 1 can be taken into account.

Although this model fits the experimental data very well, it is not a complete description of the physical system and we have to attribute a large decay width to the molecular ground state $|2\rangle$, see the discussion in section 6.4.3. In consequence the obtained fit parameters are not the real values of the rather complex system. However, the parameters shall be quoted here to give a full account of our data analysis. Except for figure 6.15 the laser intensities have been $I_1 = 300\,\mathrm{W/cm^2}$ and $I_2 = 60\,\mathrm{W/cm^2}$ and the corresponding fit results are: $\Gamma_{01}/2\pi = \Gamma_{\mathrm{stim}}/2\pi = 42\,\mathrm{kHz}$, $\Gamma_{03}/2\pi = 8\,\mathrm{kHz}$, $\Omega_{12}/2\pi = 32\,\mathrm{MHz}$, $\Omega_{23}/2\pi = 12\,\mathrm{MHz}$, $\gamma_1/2\pi = 25\,\mathrm{MHz}$, $\gamma_3/2\pi = 22\,\mathrm{MHz}$, $\gamma_2/2\pi = 2\,\mathrm{MHz}$. These parameters have been obtained by using a collisional wave number of $k = 2.5 \times 10^{-5} m^{-1}$.

Chapter 7

Summary and Outlook

In this work the experimental realization of optical Feshbach tuning of atomic interactions has been reported. We performed our experiments with a ^{87}Rb BEC, which was produced in our new apparatus described in this thesis.

Our first observation of optical Feshbach resonances was achieved with a single-frequency excitation scheme. This scheme uses laser light tuned close to a photoassociation transition. As a first step, we investigated several excited molecular states via photoassociation spectroscopy to identify a photoassociation transition with a strong optical coupling. For optical Feshbach tuning we always started from a ^{87}Rb BEC in the $|F = 1, m_F = -1\rangle$ state and coupled pairs of atoms to the excited molecular level $|O_g^-(\sim S_{1/2} + P_{3/2}), v = 1, J = 2\rangle$. By tuning the laser over the photoassociation resonance we were able to tune the atomic s-wave scattering length between $10\,a_0$ and $190\,a_0$. Close to the resonance position we observed substantial atom losses that limited the timescale of our experiments to about 100 µs. Our data confirm the theoretical results from Bohn and Julienne [Boh97, Boh99], which relate scattering length and losses via equations (6.9) and (6.10).

In a further experiment we demonstrated that optical Feshbach resonances can also be induced with a two-color Raman scheme. Using the same excited molecular state, we employed an additional laser to couple the scattering state to a ground state molecular level. This level was the second to last bound level in the ^{87}Rb $^3\Sigma_u^+$ ground state potential. As expected from theory, the tuning range of the scattering length did not improve with respect to the one-color scheme. Actually, a reduction of the tuning range was found due to losses from the molecular ground state. However, the Raman scheme allows for the control of the resonance width, which constitutes an experimental advantage over a one-color scheme. We were again able to describe our experimental results with the theoretical model by Bohn and Julienne, this time applied to a multilevel system.

The experiments presented here show that optical Feshbach resonances carry forward the exquisite control one has over laser fields to the control of

the atomic scattering length. Thus optical scattering resonances may become a valuable tool for fast switching of atom-atom interactions or to control them in a spatially resolved way. The inherent atom losses suggest the use of large detunings and a strong optical coupling in order to improve the signal-to-loss ratio. According to Ciurylo *et al.* [Ciu04], very promising applications might be found in gases of earth alkali atoms, such as ^{40}Ca, which exhibits no magnetic Feshbach resonances. For the $^1S_0$-$^3P_1$ intercombination line, Ciurylo *et al.* predict large optically induced changes of the scattering length, while losses remain small.

Outlook

Now that this work has demonstrated how optical Feshbach resonances can be applied successfully to tune ultracold interactions, a next step consists of the application of optical Feshbach tuning and photoassociation to atoms stored in three-dimensional optical lattices.

Such optical lattices constitute a particularly promising environment to apply the optical technologies implemented in this thesis. This is mainly because of two different reasons. First, atoms in the lattice wells are subject to a strong trapping potential, which is expected to strongly enhance the Franck-Condon factor for transitions between atomic states and bound molecular levels [Jak02]. This enhancement results in a stronger optical coupling and the ratio of change-in-scattering-length to atom loss can be improved by using larger laser detunings, according to the discussion in section 6.3.2. The second advantage of optical lattice potentials concerns ground state molecules that can be produced via photoassociation or with the help of Feshbach resonances. While in a normal cloud ground state molecules decay via inelastic collisions, a lattice with only one molecule per lattice site inhibits this process. As an important result molecular lifetimes increase and collisional broadening is absent in the molecular spectra. First experiments on molecules in three-dimensional lattices are reported in [Rom04], and many interesting experiments with ultracold molecules in this environment will likely follow.

Optical lattices have been proposed for use as quantum registers and to perform quantum operations on atomic qubits. Single neutral atoms stored in the lattice wells can serve as register qubits, where information is encoded via their internal state. To perform quantum operations between different qubits, two atoms are brought together and are allowed to interact for a certain time, see for example [Cal04]. For a quantum gate operation this interaction has to be controlled. This can be done with the help of Feshbach resonances, as proposed in [Cal04]. Here, optical Feshbach resonances might be an interesting option due to the fast control over interactions. Since, in an optical lattice, the enhanced Franck-Condon factor improves the optical coupling, optical Feshbach tuning should be possible at reduced loss rates in this application.

Latest Developments of our Experiment

Our experiments on two-color optical Feshbach resonances have been performed by applying two Raman laser beams and scanning laser 2, which couples the two molecular levels in the excited and the ground state potential. With the same setup we have done another experiment by keeping the frequency of laser 2 fixed and scanning laser 1, which realizes the free-bound coupling between atoms and excited molecules (cf. figure 6.10). This yields so-called Autler-Towns spectra, which exhibit a clear double peak structure of atomic losses. Between the atom loss peaks we observe a suppression of losses, which provides evidence of the coherence in the free-bound Raman transition. This coherence is relevant to evaluate proposed STIRAP schemes [Mac04, Dru02] for transferring BEC atoms to a molecular BEC state. The experiments on this topic and their analysis are about to be published [Win05].

Extending our experimental setup, a three-dimensional optical lattice at a wavelength of 830 nm has been realized, taking advantage of the good optical access to the glass cell. After completing these extensions, we have observed the transition between the superfluid BEC phase and the Mott insulator phase [Gre02, Jak98] in our experiment. To realize this phase transition, a BEC is loaded into the lattice by adiabatically increasing the intensity of the lattice lasers. If the lattice is ramped up to a depth of more than about 15 recoil energies, we observe the system to enter the Mott insulator phase. Also, preliminary photoassociation experiments in the Mott insulator have been performed.

These recent achievements open up interesting experimental possibilities for applying the optical technologies studied in this thesis to atoms confined in a three-dimensional optical lattice. In particular, the proposals to realize quantum computation with neutral atoms in optical lattices could profit from optical Feshbach resonances.

Appendix A

Rubidium-87 Properties

atomic number	Z	37	
atomic mass	m	86.90918520(15) u	[Bra99]
natural abundance		27.83(2)%	[Lid00]
melting point	T_{M}	39.31 °C	[Lid00]
vapor pressure at 25 °C		4.0×10^{-7} mbar	[Nes63]
atomic mass unit	u	$1.66053873(13) \times 10^{-27}$ kg	[Moh99]
Bohr magneton	μ_{B}	$9.27400899(37) \times 10^{-24}$ J/T	[Moh99]
Bohr radius	a_0	$5.29177249(24) \times 10^{-11}$ m	[Moh99]
nuclear spin	I	3/2	
hyperfine splitting (ground state)	$\frac{\Delta E_{hf}}{h}$	6. 834 682 610 904 29(9) GHz	[Biz99]
Landé factor, F=1,2 (ground state)	g_F	-1/2, +1/2	[Ste02]
D_2 line vacuum wavelength	λ_{D_2}	780.24629 nm	[Ye96]
D_2 linewidth	$\frac{\Gamma_{D_2}}{2\pi}$	6.065(9) MHz	[Ste02]
saturation intensity (MOT cycling transition)	I_{sat}	1.669(2) mW/cm^2	[Ste02]
Doppler temperature	T_{D}	146 μK	[Ste02]
D_1 line vacuum wavelength	λ_{D_2}	794.97885 nm	[Bar91]
D_1 linewidth	$\frac{\Gamma_{D_1}}{2\pi}$	5.746(8) MHz	[Ste02]

Table A.1: Selected properties of the ^{87}Rb isotope and fundamental constants.

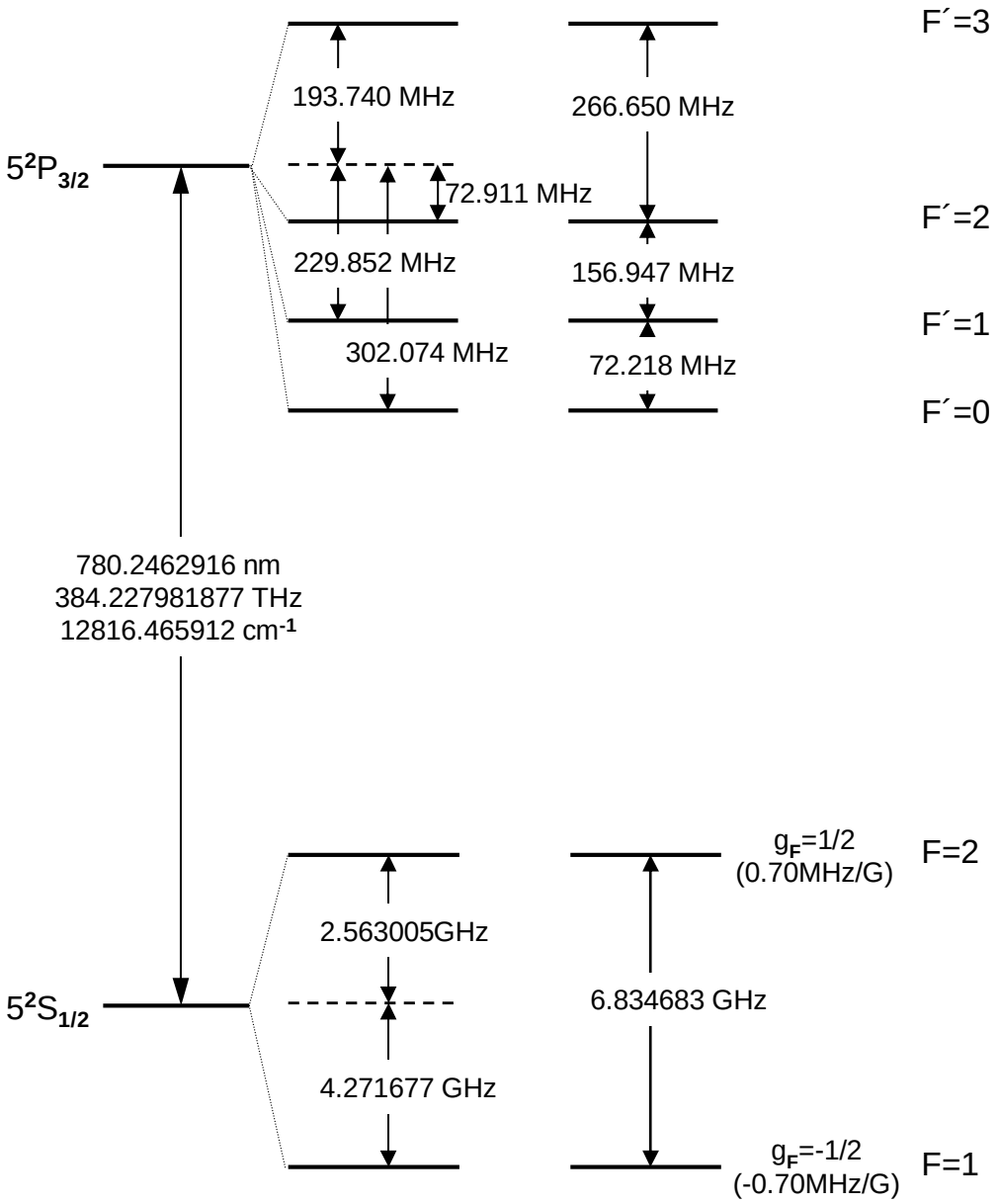

Figure A.1: ^{87}Rb D_2 line structure (not to scale). The hyperfine levels and their frequency splittings are shown. In addition the Landé factors g_F and the slopes $\partial E/\partial B = g_F \mu_B$ for the Zeeman substates with $m_F = 1$ are given for the ground state. Data taken from [Ste02].

Appendix B

Index to Important Data Files

This appendix lists the most important data files concerning the design of the experiment, the data acquisition and the analysis of the measured quantities. Table B.1 organizes these files in four sections. The first section contains AutoCAD drawings of the vacuum setup and the magnetic coils. Afterwards Matlab m-files are listed that have been used to design the magnetic fields for the transfer and the QUIC trap. The files that generate the current sequences for the transport are also included here. In the following section LabView and Matlab files are collected, which we use to run the experiments and record experimental data. Finally important m-files we employ to analyze the experimental data are listed.

The files from the last two categories are continually modified to apply to the measurements currently performed. Therefore table B.1 quotes only very important and essential files. The situation is different for the first two sections of the table. Here information on the construction of the apparatus and the design of the transfer is given, which will not be required during normal operation of the experiment. To guide future operators through the files, these topics are covered in more detail.

In the table all file locations are given relative to a main directory called "rb_files". This directory can be found on the main lab computer and should only serve as a backup archive. Up-to-date versions of most files are usually found in the directory "steuerung".

Content	File Name	Location
overview complete vacuum system	overview_vacuum.dwg	../vac/
MOT chamber	rezipient_mat_final.dwg	../vac/
XUHV chamber	rezipient_mat20_09.dwg	../vac/
glass cell	glaszelle_englisch.dwg	../vac/
QUIC housing	quic_koerper3.dwg	../vac/
coil housings	spulenkoerper05.dwg	../vac/
vacuum system and magnetic coils	kammer3_mat.dwg	../vac/
central chamber, transfer coils (3D)	vacuum_system_3d.dwg	../vac/
simulation of magnetic fields	biotsavart5.m	../m/biot/
optimize coil geometry	loop_optimation4.m	../m/biot/
calculate currents for transfer	biotsavart5_strom.m	../m/biot/
simulate transfer, plot parameters	biotsavart5_tranf.m	../m/biot/
calculate currents for transfer 2	biot_strom5.m	../strg/m/biot/
generate time sequence for transfer	biot_strom_splines.m	../strg/m/biot/
generate time sequ. for transfer 2	biot_timesequ.m	../strg/m/biot/
compensate freq. response of coils	delta.m	../strg/m/biot/
generate final transfer sequence	delta_switch.m	../strg/m/biot/
control interface for experiment	steuerung2.vi	../strg/vi/
calculate tables for control system	steuerung2.m	../strg/m/
view and save experimental data	view.vi	../strg/vi/
fit temperature to tof-data	tempfit.vi	../strg/vi/
analyze images, fit thermal distrib.	ccd2d.m	../strg/m/
analyze images, fit bimodal distrib.	ccd2d_bec.m	../strg/m/
determine Bragg diffrac. efficiency	effizienz_bragg.m	../analyze/
fit Bragg resonance frequency	ploteff.m	../analyze/
extract scattering length	scattlength.m	../analyze/

Table B.1: List of the most important data files and where they are stored. The extensions correspond to the following files types: *.dwg = AutoCAD drawing, *.m = Matlab m-file, *.vi = LabView vi-file.

Appendix C

Publications

Tuning the Scattering Length with an Optically Induced Feshbach Resonance

M. Theis,[1] G. Thalhammer,[1] K. Winkler,[1] M. Hellwig,[1] G. Ruff,[1,*] R. Grimm,[1,2] and J. Hecker Denschlag[1]
[1]*Institut für Experimentalphysik, Universität Innsbruck, Technikerstraße 25, 6020 Innsbruck, Austria*
[2]*Institut für Quantenoptik und Quanteninformation, Österreichische Akademie der Wissenschaften, 6020 Innsbruck, Austria*
(Received 21 April 2004; published 15 September 2004)

We demonstrate optical tuning of the scattering length in a Bose-Einstein condensate as predicted by Fedichev *et al.* [Phys. Rev. Lett. **77**, 2913 (1996)]. In our experiment, atoms in a ^{87}Rb condensate are exposed to laser light which is tuned close to the transition frequency to an excited molecular state. By controlling the power and detuning of the laser beam we can change the atomic scattering length over a wide range. In view of laser-driven atomic losses, we use Bragg spectroscopy as a fast method to measure the scattering length of the atoms.

DOI: 10.1103/PhysRevLett.93.123001 PACS numbers: 34.50.Rk, 03.75.Nt, 32.80.Pj, 34.20.Cf

The great progress in the field of ultracold quantum gases in recent years can be largely attributed to the existence of magnetically tunable Feshbach resonances [1]. Since their first experimental introduction into the field [2–4], they have been widely used to arbitrarily tune the interactions between atoms.

In general, a Feshbach resonance occurs when a colliding pair of atoms is resonantly coupled to a molecular bound state. A magnetically tunable Feshbach resonance is based on Zeeman shifting a bound molecular state into resonance with the scattering state. Alternative coupling schemes for inducing Feshbach resonances have been proposed but never experimentally applied to control atomic interactions. The use of radio frequency [5] and static electric fields [6] was suggested. Fedichev *et al.* [7] proposed optical coupling of the scattering state with the molecular state, which was theoretically analyzed further in [8,9]. This scheme, often referred to as "optical Feshbach resonance," can be controlled via laser detuning and laser power.

Inducing Feshbach resonances with optical fields offers experimental advantages compared to magnetic fields. The intensity and detuning of optical fields can be rapidly changed. Furthermore, complex spatial intensity distributions can be easily produced which result in corresponding scattering length patterns across the sample. Optical transitions are always available, even when no magnetic Feshbach resonances exist. Recently, Fatemi *et al.* [10] observed optical Feshbach resonances in photoassociation spectroscopy. They used photoionization to probe optically induced changes in the scattering wave function. However, the direct influence of the optical Feshbach resonance on the atomic scattering properties was not studied.

In this Letter, we report a direct measurement of the atomic scattering length a in a BEC of ^{87}Rb $|F = 1, m_F = -1\rangle$ as we cross an optical Feshbach resonance. With moderate laser intensities of about 500 W/cm^2, we can change the scattering length over 1 order of magnitude from 10 a_0 to 190 a_0 (a_0 = 1 Bohr radius).

To optically modify the scattering length, we use laser light tuned close to a photoassociation resonance which couples the continuum state of incoming free atoms to an excited molecular level (see inset in Fig. 1). This changes the wave function and consequently the scattering length of the scattering state. It also leads to atomic loss due to spontaneous decay via the molecular state. The resonant transition rate between the continuum state and the molecular state, which we denote Γ_{stim}, is proportional to the laser intensity. In our experiment, $\Gamma_{\mathrm{stim}}/2\pi$ is on the order of a few 10 kHz. This is 3 orders of magnitude less than the spontaneous decay rate Γ_{spon} from the excited molecular state. In [8], Bohn and Julienne give convenient expressions for the scattering length a and the inelastic collision rate coefficient K_{inel} which describes the photoassociation loss. For $\Gamma_{\mathrm{stim}} \ll \Gamma_{\mathrm{spon}}$, these expressions can

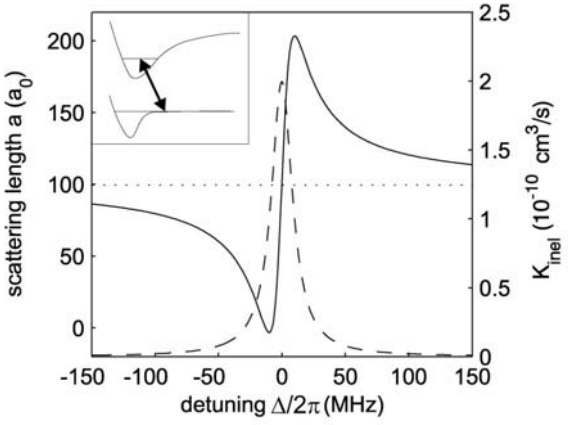

FIG. 1. Scattering length a (solid line) and inelastic collision rate coeffient K_{inel} (broken line) as a function of the laser detuning from the photoassociation resonance. The curves are based on Eqs. (1) and (2) for typical experimental parameters: $\Gamma_{\mathrm{stim}}/2\pi = 54$kHz, $\Gamma_{\mathrm{spon}}/2\pi = 20$MHz, $k_i = 2.47 \times 10^5 \mathrm{m}^{-1}$, $a_{\mathrm{bg}} = 100 a_0$ (dotted line). Inset: Scheme for optically coupling the scattering state with an excited molecular state.

 0031-9007/04/93(12)/123001(4)$22.50

be approximated and, for a condensate [11], read:

$$a = a_{\mathrm{bg}} + \frac{1}{2k_i}\frac{\Gamma_{\mathrm{stim}}\Delta}{\Delta^2 + (\Gamma_{\mathrm{spon}}/2)^2} \quad (1)$$

$$K_{\mathrm{inel}} = \frac{2\pi\hbar}{m}\frac{1}{k_i}\frac{\Gamma_{\mathrm{stim}}\Gamma_{\mathrm{spon}}}{\Delta^2 + (\Gamma_{\mathrm{spon}}/2)^2} \quad (2)$$

where a_{bg} is the scattering length in the absence of light, Δ is the detuning from the photoassociation line, m the atomic mass, and $\hbar k_i$ the relative momentum of the collision. Figure 1 shows a and K_{inel} as functions of the detuning Δ for typical experimental parameters. According to Eqs. (1) and (2), one should in general choose large detuning and strong coupling in order to maximize the change in scattering length while keeping the losses low.

Our experiments are carried out with an almost pure ^{87}Rb condensate in the $|F = 1, m_F = -1\rangle$ spin state with typically 1×10^6 atoms. The setup uses a magnetic transport scheme [12] to transfer atoms from a magneto-optical trap (MOT) chamber to a glass cell where the BEC is produced by rf-evaporation in a cigar shaped quadrupole and Ioffe configuration (QUIC) trap [13] with trap frequencies $\omega_{\mathrm{axial}}/2\pi = 15$Hz and $\omega_{\mathrm{radial}}/2\pi = 150$Hz. The intensity stabilized photoassociation laser beam (≈ 40 mW) is derived from a Ti:Sa laser. It is aligned along the axial direction of the cigar shaped BEC and has a waist radius of 76 μm. Its linear polarization is perpendicular to the trapping magnetic bias field of 2 Gauss. In our experiments, we limit the maximum laser intensities to about 500 W/cm^2 because we observe the appearance of a growing component of thermal atoms for higher intensities. This effect is negligible for laser powers below 500 W/cm^2.

In order to identify a suitable molecular level with strong coupling to the continuum state, we investigated molecular lines in the 1_g and 0_g^- potentials, which connect to the $(S_{1/2} + P_{3/2})$ and $(S_{1/2} + P_{1/2})$ asymptotes. We choose the excited state $|0_g^-(\sim S_{1/2} + P_{3/2}), \nu = 1, J = 2\rangle$ which is located 26.8 cm^{-1} below the $D2$ line [14]. Figure 2 shows the corresponding photoassociation line together with the line for $J = 0$. At a laser intensity of 460 W/cm^2, the measured atom losses yield a peak inelastic collision rate $K_{\mathrm{inel}} = (2 \pm 1) \times 10^{-10}$cm^3/s, which is a factor of 5 weaker than K_{inel} in the example of [8]. Losses due to excitation of the $D2$ line can be neglected. We observe a strong intensity dependent light shift of 215 MHz/(kW cm^{-2}) of the photoassociation line which might be mainly explained by coupling to a d-wave shape resonance [15].

Measuring the scattering length close to a photoassociation resonance requires a fast experimental method as atom losses restrict the observation time to below 100 μs in our experiments. Thus, the scattering length can neither be extracted from measurements of the collision rate

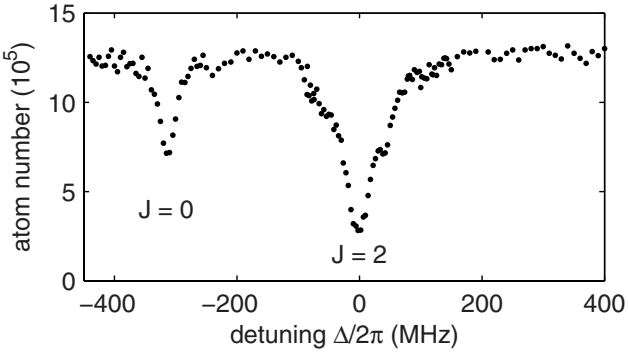

FIG. 2. Photoassociation spectrum of the excited molecular state used in the experiment. The two lines belong to the state $|0_g^-(\sim S_{1/2} + P_{3/2}), \nu = 1\rangle$ and have rotational quantum numbers $J = 0, 2$, respectively. Shown is the remaining atom number after exposing a BEC to a 70 μs light pulse of 460 W/cm^2 intensity. The detuning is given relative to the $J = 2$ line. Each data point is an average of three measurements.

[4] nor from the mean-field energy in a condensate expansion [2], both of which require a few ms. Instead, we use Bragg spectroscopy [16] to determine the mean-field energy by imposing on the atoms a moving optical lattice composed of two counter-propagating laser beams with wave number k and an adjustable frequency difference Δf. The Bragg lattice transfers a momentum of $2\hbar k$ to the atoms in a first order diffraction process. This is resonant when energy conservation is fulfilled, which for *noninteracting* atoms reads $h\Delta f_0 = (2\hbar k)^2/2m$. For a condensate, however, the resonance frequency Δf_r is shifted by the mean-field energy. In the Thomas-Fermi approximation, this yields a value of

$$\Delta f_r = \Delta f_0 + \frac{8\hbar}{7m} n_0 a \quad (3)$$

where n_0 denotes the atomic peak density [16]. Observing this shift of the Bragg resonance frequency therefore allows to measure the product of density and scattering length.

We derive the two Bragg beams from a laser which is 1.4 nm blue detuned relative to the ^{87}Rb $D2$ line. This determines Δf_0 to be 15.14 kHz. Two acousto-optical modulators are used to control the frequency difference Δf between the two counter-propagating beams. The beams have a diameter of ≈ 900 μm and are aligned along the radial trap axis in a horizontal direction. In our measurements, we apply a 70 μs square-pulse of Bragg light to the condensate. After 12 ms of time of flight, when the momentum components of the condensate have spatially separated, we use absorption imaging to measure the portion of condensate atoms that have been diffracted. We always choose the intensity of the lattice such that about 15%–20% of the atoms are diffracted at resonance. Scanning Δf and determining the percentage

of diffracted atoms yields curves as shown in Fig. 3 from which we extract the resonance positions. Shining in a photoassociation laser pulse (70 μs square-pulse) at the same time as the Bragg pulse shifts the resonance position. This shift depends on the detuning Δ from the molecular line (filled and open circles in Fig. 3).

For short illumination times T as in our experiment, the shape of the spectra fits well to the Fourier transform of the rectangular light pulse, $\sin^2[\pi(\Delta f - \Delta f_r)T]/(\Delta f - \Delta f_r)^2$, which we use to fit the data (see Fig. 3). Our measurements show that in spite of the Fourier-limited width of the Bragg resonance of 13 kHz (FWHM), we can resolve the peak position to better than ± 100 Hz.

When we invert the frequency difference of the Bragg laser beams and diffract atoms to a momentum state with $-2\hbar k$ instead of $+2\hbar k$, we notice that the absolute value of the resonance frequency $|\Delta f_r|$ changes. This can be explained by an initial condensate momentum of up to 0.05 $\hbar k$ which we find to slowly vary from day to day. This initial momentum is due to residual experimental imperfections like optical dipole forces of a slightly noncentered photoassociation beam. To eliminate this effect, we always measure Δf_r for $+2\hbar k$ as well as for $-2\hbar k$ and then take the difference.

Figure 4 shows the data we obtain from scanning the photoassociation laser over the optical resonance for a fixed laser intensity of 460 W/cm^2. The number of atoms in the condensate at the end of the laser pulse is plotted in Fig. 4(a) indicating the position of the molecular line. On resonance, about 90% of the atoms are lost after the 70 μs of interaction time. Figure 4(b) shows the resonance frequency Δf_r for Bragg diffraction as a function of laser detuning Δ. For large positive (and negative) detuning Δ, the value of Δf_r agrees with the 16.6 kHz expected from theory for the background scattering length $a_{bg} = 100\ a_0$ [17,18] and a BEC with $\approx 8.2 \times 10^5$ atoms. As we tune across the molecular resonance, the measured resonance frequencies exhibit a distorted dispersive shape. Following Eq. (3), this is the result of the combination of two effects: first, the scattering length a varies with Δ which alone should result in a dispersive line shape as in Fig. 1. Second, the atomic density n_0 decreases due to photoassociation losses which would, if the scattering length was constant, result in a symmetrical dip for Δf_r. On the right-hand side of the resonance, these two effects nearly compensate each other whereas on the left-hand side, the effects add up to produce a prominent dip in Δf_r.

In order to extract the scattering length a from the measured frequencies one can, in a first approach, replace the dynamically changing density n_0 in Eq. (3) by a time averaged value $\langle n_0 \rangle_t$. The average $\langle n_0 \rangle_t$ can be derived from the rate equation for the local density $\dot{n} = -2K_{inel}n^2$ [19] describing two-atom losses. This yields values for a which differ only marginally from the ones in Fig. 4(c). The data in Fig. 4(c) were obtained from a more

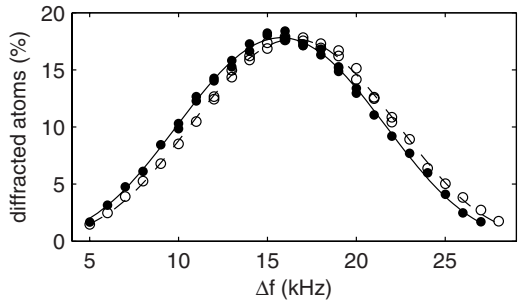

FIG. 3. Two Bragg resonance curves with an optically induced relative shift of 0.75 kHz. The percentage of the diffracted atoms is plotted against the frequency difference of the lattice beams. The two curves correspond to a detuning $\Delta/2\pi = -47$ MHz (filled circles) and $\Delta/2\pi = +47$ MHz (open circles) at a photoassociation laser intensity of 460 W/cm^2. The lines shown are fits to the data. For better comparison the right curve (open circles) has been scaled by a factor of 1.09 to the same height as the left one.

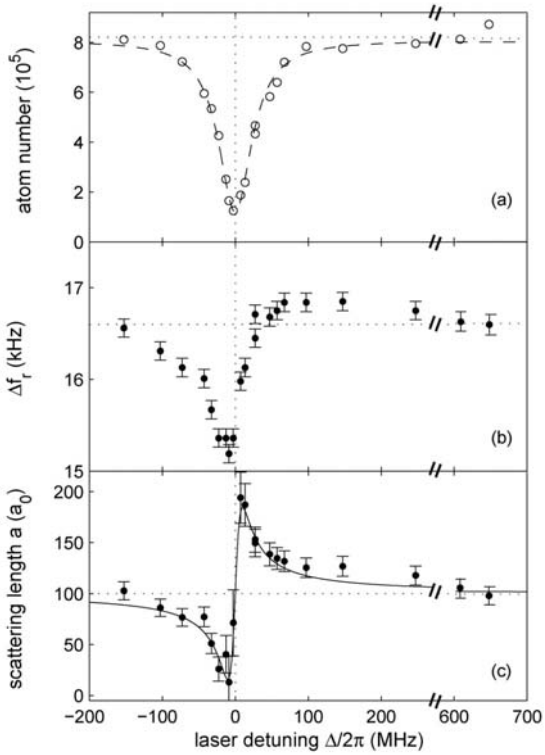

FIG. 4. Optical Feshbach resonance. In (a), the final atom number is plotted versus the detuning of the photoassociation laser (the dashed line is a Lorentz curve to guide the eye). The data in (b) display the measured Bragg resonance frequencies. In (c), the values for the scattering length obtained from the data in (a) and (b) are plotted. The continuous line is a fit of Eq. (1) to the data.

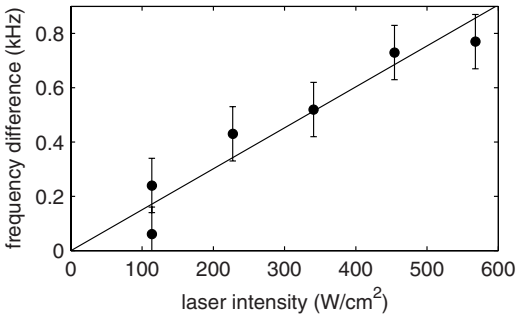

FIG. 5. Dependence of the optically induced mean-field shift on the laser intensity.

detailed examination which takes into account the full spatially resolved time evolution of the condensate density [20]. This includes the dynamical flattening of the condensate density profile caused by the rapid atom loss which is much faster than the trap frequencies [19]. Figure 4(c) shows that with a laser power of 460 W/cm^2, we can tune the scattering length over a range from 10 a_0 to 190 a_0. A fit of Eq. (1) to these data for a yields a spontaneous decay width $\Gamma_{\text{spon}}/2\pi$ of 20 MHz and a resonant inelastic collision rate coefficient $K_{\text{inel}} = 1.7 \times 10^{-10}\text{cm}^3/\text{s}$. These values agree with those we obtain from atom loss measurements. Thus, our data consistently confirm the intrinsic relation between a and K_{inel} as expressed in Eqs. (1) and (2).

The measured width $\Gamma_{\text{spon}}/2\pi$ of 20 MHz is larger than the expected molecular decay width of 12 MHz (corresponding to 2 times the atomic width). This might be explained by the line width of the Ti:Sa laser of about 4 MHz and a power broadening of the line due to different light shifts of unresolved molecular hyperfine states [18,19].

Figure 5 demonstrates the linear dependence of the scattering length a on the photoassociation laser intensity. For these measurements, we determine the Bragg resonance frequency for the detunings $\Delta/2\pi \approx \pm 50$ MHz at various photoassociation laser intensities. This is slightly complicated by the light shift and broadening of the photoassociation line which lead to an uncertainty in $\Delta/2\pi$ of ± 10 MHz. We keep the final atom number and density fixed by adjusting the pulse duration for each laser intensity. This ensures that only changes in a are reflected in the varying mean-field shift. In Fig. 5, we plot the frequency difference $\Delta f(+50\text{MHz}) - \Delta f(-50\text{MHz})$ which increases our signal.

In conclusion, our experiments demonstrate the tunability of the scattering length in ultracold samples by optically coupling free atoms to a bound molecular state. Because of the exquisite control one has over laser fields, we expect optical Feshbach resonances to be valuable when it comes to controlling atom-atom interactions in demanding applications. The inherent losses suggest the use of high laser intensities at large detuning and a good choice of the molecular state in order to optimize the ratio of change in scattering length and loss rate. Optical Feshbach tuning could be particularly useful to control atomic interactions in optical lattices which are discussed as potential future quantum information processors.

We thank Paul Julienne, Eite Tiesinga, John Bohn, Olivier Dulieu, Peter Fedichev, Andrea Micheli, and Helmut Ritsch for very helpful discussions. This work was supported by the Austrian Science Fund (FWF) within SFB 15 (project part 17) and by the European Union in the frame of the Cold Molecules TMR Network under Contract No. HPRN-CT-2002-00290.

*Permanent address: Department of Physics, Bates College, Lewiston, ME 04240.

[1] E. Tiesinga, B. J. Verhaar, and H. T. C. Stoof, Phys. Rev. A **47**, 4114 (1993).
[2] S. Inouye *et al.*, Nature (London) **392**, 151 (1998).
[3] Ph. Courteille *et al.*, Phys. Rev. Lett. **81**, 69 (1998).
[4] J. L. Roberts *et al.*, Phys. Rev. Lett. **81**, 5109 (1998).
[5] A. J. Moerdijk, B. J. Verhaar, and T. M. Nagtegaal, Phys. Rev. A **53**, 4343 (1996).
[6] M. Marinescu and L. You, Phys. Rev. Lett. **81**, 4596 (1998).
[7] P. Fedichev, Yu Kagan, G.V. Shlyapnikov, and J. T. M. Walraven, Phys. Rev. Lett. **77**, 2913 (1996).
[8] J. Bohn and P. S. Julienne, Phys. Rev. A **56**, 1486 (1997).
[9] V. Kokoouline, J. Vala, and R. Kosloff, J. Chem. Phys. **114**, 3046 (2001).
[10] F. K. Fatemi, K. M. Jones, and P. D. Lett, Phys. Rev. Lett. **85**, 4462 (2000).
[11] For condensed atoms, the collision rate coefficient is only half of the coefficient for thermal atoms as all atoms share the same quantum state.
[12] M. Greiner, I. Bloch, T. W. Hänsch, and T. Esslinger, Phys. Rev. A **63**, R031401 (2001).
[13] T. Esslinger, I. Bloch, and T. W. Hänsch, Phys. Rev. A **58**, R2664 (1998).
[14] A. Fioretti *et al.*, Eur. Phys. J. D **15**, 189 (2001).
[15] A. Simoni, P. S. Julienne, E. Tiesinga, and C. J. Williams, Phys. Rev. A **66**, 063406 (2002).
[16] J. Stenger *et al.*, Phys. Rev. Lett. **82**, 4569 (1999).
[17] Eberhard Tiemann (private communication).
[18] Paul Julienne and Eite Tiesinga (private communication).
[19] C. McKenzie *et al.*, Phys. Rev. Lett. **88**, 120403 (2002).
[20] This calculation is a simulation of the Rabi flopping between two levels corresponding to the condensate component at rest and the component with momentum $2\hbar k$. The changing density due to the loss is included by introducing a time dependent detuning.

Inducing an optical Feshbach resonance via stimulated Raman coupling

Gregor Thalhammer,[1] Matthias Theis,[1] Klaus Winkler,[1] Rudolf Grimm,[1,2] and Johannes Hecker Denschlag[1]
[1]*Institut für Experimentalphysik, Universität Innsbruck, Technikerstraße 25, 6020 Innsbruck, Austria*
[2]*Institut für Quantenoptik und Quanteninformation, Österreichische Akademie der Wissenschaften, 6020 Innsbruck, Austria*
(Received 23 September 2004; published 8 March 2005; publisher error corrected 11 March 2005)

We demonstrate a method of inducing an optical Feshbach resonance based on a coherent free-bound stimulated Raman transition. In our experiment atoms in a ^{87}Rb Bose-Einstein condensate are exposed to two phase-locked Raman laser beams which couple pairs of colliding atoms to a molecular ground state. By controlling the power and relative detuning of the two laser beams, we can change the atomic scattering length considerably. The dependence of scattering length on these parameters is studied experimentally and modeled theoretically.

DOI: 10.1103/PhysRevA.71.033403 PACS number(s): 34.50.Rk, 32.80.Pj, 03.75.Nt, 34.20.Cf

I. INTRODUCTION

Feshbach resonances have become a central tool in the physics of ultracold quantum gases during the last years because they allow for a tuning of the interactions between atoms. Controlling interparticle interactions is a central key in many fields of modern physics and is especially relevant for future applications in quantum computation and exploring novel many-particle quantum effects. Beautiful experiments using magnetically tunable Feshbach resonances [1,2] have been performed, ranging from ultrahigh-resolution molecular spectroscopy [3] to the coherent coupling of atomic and molecular states [4] as well as the creation of bright matter wave solitons [5]. It also led to the production of new atomic [6] and molecular [7] Bose-Einstein condensates (BEC's) and allowed control of pairing in ultracold fermionic gases [8].

Recently we demonstrated how atom-atom interactions in a ^{87}Rb BEC can also be tuned with an optically induced Feshbach resonance [9] (see also [10]), a scheme which was originally proposed by Fedichev *et al.* [11,12]. Optically induced Feshbach resonances offer advantages over magnetically tuned Feshbach resonances since the intensity and detuning of optical fields can be rapidly changed. Furthermore, complex spatial intensity distributions can be easily produced and optical transitions are always available even when no magnetic Feshbach resonances exist. A disadvantage of optically induced Feshbach resonance is the inherent loss of atoms due to excitation and spontaneous decay of the molecular state [9]. Typical lifetimes for excited molecular states are on the order of 10 ns which corresponds to a linewidth of $2\pi\times 16$ MHz. Evidently, coupling to molecular states with longer lifetime should improve the situation. Ground-state molecules are stable against radiative decay, and narrow transition linewidths on the order of kHz have been observed in two-photon Raman photoassociation [13,14]. This raises the question whether it is possible to create optical Feshbach resonances using stimulated Raman transitions and whether this scheme might be advantageous compared to the one-photon optical Feshbach resonance.

In this paper we indeed demonstrate that optical Feshbach resonances can be induced using a coherent two-color Raman transition to a highly vibrationally excited molecular ground state in a ^{87}Rb BEC. In the experiment we show how the scattering length and loss rates can be tuned as a function of the intensity of the lasers and their detuning from molecular lines. We use Bragg spectroscopy [15] as a fast method to measure the scattering length in our sample [9]. To fit and analyze our data we use a model by Bohn and Julienne [16]. We find that using the Raman scheme for optically induced Feshbach resonances leads to similar results in tuning of the scattering length as for the single-photon Feshbach scheme. The Raman scheme does not lead to an improvement compared to the one-photon scheme because its atomic loss rate is not lower for a given change in scattering length. However, using a stimulated Raman transition does offer experimental advantages. To tune over the Feshbach resonance, the relative frequency of the two laser beams only has to be changed typically by several MHz which can be conveniently done using an acousto-optic modulator. This allows for very fast and precise control of the scattering length. On the other hand, working with a one-photon optical Feshbach resonance in the low-loss regime typically requires large detunings and scan ranges on the order of GHz. The Raman scheme relaxes the necessity for absolute frequency control of the lasers which can be tedious to maintain far away from atomic lines. Since off-resonant light fields in general lead to dipole forces acting on the atoms, a variation of the scattering length via optical tuning leads to a variation of the dipole forces on the atomic sample. This unwanted effect can be made negligible for the Raman scheme which tunes over resonance within a small frequency range.

The paper is organized as follows: We start in Sec. II by discussing the Raman scheme with a simple theoretical model. In Sec. III we describe in detail our experimental setup and the measurement method. In Sec. IV we discuss the experimental results which are compared with a theoretical model. The Appendix gives details of the model that is used to describe the data.

II. RAMAN SCHEME FOR OPTICAL FESHBACH TUNING

Before discussing optical Feshbach tuning based on a two-photon Raman transition, it is instructive to briefly recall

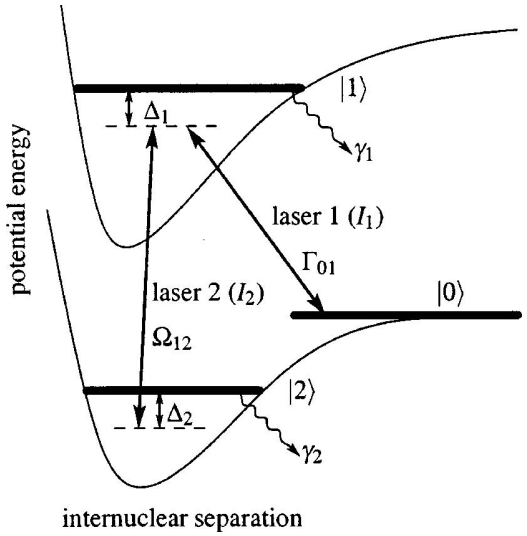

FIG. 1. Schematic diagram of the transitions used for optically coupling the collisional state $|0\rangle$ to molecular states $|1\rangle$ and $|2\rangle$. $|1\rangle$ is electronically excited whereas $|2\rangle$ is in the electronic ground state. Δ_1 and Δ_2 are defined to be positive for the shown configuration.

the one-photon scheme first [9,11,12]. This configuration uses a single laser beam tuned close to a transition from the scattering state of colliding atoms to a bound level in an excited molecular potential (states $|0\rangle$ and $|1\rangle$ in Fig. 1). Varying the detuning Δ_1 or the intensity I_1 modifies the coupling and hence the scattering length. Atomic loss can occur through population of the electronically excited molecular state which has a decay width of γ_1.

Introducing a second laser as shown in Fig. 1 will now couple the collisional state $|0\rangle$ to a bound level $|2\rangle$ in the ground-state potential. As we will show, this allows for a tuning of the scattering length similar to the one-photon scheme. We now have, however, four parameters which can be used to influence the scattering length: the intensities I_1 and I_2 of lasers 1 and 2 and the detunings Δ_1 and Δ_2 as shown in Fig. 1.[1]

From [16] [Eqs. (4.8)–(4.11)] one can extract approximate expressions for the inelastic collision rate coefficient K_{inel} and the scattering length a in a Bose-Einstein condensate:[2]

$$K_{\text{inel}} = \frac{2\pi\hbar}{m}\frac{1}{k_{\text{i}}}\frac{\Gamma_{01}\gamma_1}{(\Delta_1 - \Omega_{12}^2/\Delta_2)^2 + (\gamma_1/2)^2}, \tag{1}$$

[1]As we observe a significant light shift of level $|1\rangle$, depending on the intensity I_1 of laser 1 [9], we measure the detuning Δ_1 from the observed position of the one-photon line at a given intensity of laser 1. Note that Δ_1 is a one-photon detuning whereas Δ_2 is a two-photon detuning.

[2]K_{inel} is reduced by a factor of 2 as compared to the case of thermal atoms. This is because in a BEC all atoms share the same quantum state.

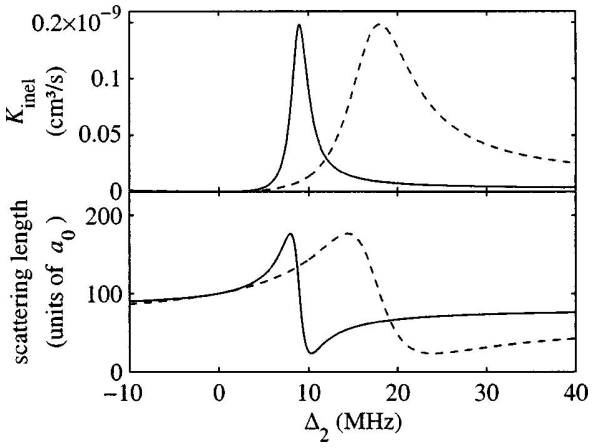

FIG. 2. K_{inel} and scattering length a according to Eqs. (1) and (2), plotted for two values of Δ_1. Solid line: $\Delta_1/2\pi = 100$ MHz. Dashed line: $\Delta_1/2\pi = 50$ MHz. The other parameters are $\Gamma_{01}/2\pi = 50$ kHz, $\Omega_{12}/2\pi = 30$ MHz, and $\gamma_1/2\pi = 25$ MHz. The wave number $k_{\text{i}} = 2.5\times10^5$ m^{-1} corresponds to the finite size of the condensate wave function. a_0 is the Bohr radius.

$$a = a_{\text{bg}} - \frac{1}{2k_{\text{i}}}\frac{\Gamma_{01}(\Delta_1 - \Omega_{12}^2/\Delta_2)}{(\Delta_1 - \Omega_{12}^2/\Delta_2)^2 + (\gamma_1/2)^2}. \tag{2}$$

Here Γ_{01} denotes the on-resonance stimulated transition rate from $|0\rangle$ to $|1\rangle$ which is proportional to I_1. Ω_{12} is the Rabi frequency for the coupling of the states $|1\rangle$ and $|2\rangle$ and is proportional to $\sqrt{I_2}$. $\hbar k_{\text{i}}$ is the relative momentum of the collision, where $\hbar$ is Planck's constant divided by 2π. a_{bg} is the background scattering length and m is the atomic mass.

Equations (1) and (2) neglect spontaneous decay from state $|2\rangle$ ($\gamma_2 = 0$) and assume $\Gamma_{01} \ll \gamma_1$. Setting $\Omega_{12} = 0$ yields the expressions for the one-photon Feshbach resonance as given in [9]. Equations (1) and (2) yield a Lorentzian and a corresponding dispersive line shape as a function of Δ_1. In our experiments, however, we hold Δ_1 constant and scan Δ_2. Figure 2 shows typical curves for K_{inel} and a for two detunings Δ_1. The curves for K_{inel} are slightly asymmetric, but for $\Delta_1 \gg \Omega_{12}$ they can be well approximated by Lorentzians. This can be seen by expanding the denominator of Eq. (1) in terms of Δ_2 at the resonance position. A light shift displaces the position of the resonance to ${\Omega_{12}}^2/\Delta_1$. It is also interesting to note that the resonance width decreases with increasing detuning Δ_1 as $\gamma_1(\Omega_{12}/\Delta_1)^2$.

In a sense the two-photon Raman-Feshbach resonance can be coined in terms of a one-photon Feshbach scheme. The detuning Δ_2 effectively replaces the detuning Δ_1 of the one-photon Feshbach scheme.[3]

Since Eqs. (1) and (2) have exactly the same form as for the one-photon Feshbach resonance, it follows that, given a

[3]There is even a more direct way to understand the two-photon Feshbach resonance in terms of a one-photon Feshbach resonance. Laser 1 couples the collision state $|0\rangle$ to a virtual level $|2'\rangle$, which is generated by laser 2 acting on level $|2\rangle$. The splitting between $|2'\rangle$ and $|1\rangle$ is given by $\Delta_{2'} = \Delta_1 - \Delta_2$. Its linewidth is $\gamma_1(\Omega_{12}/\Delta_{2'})^2$ and the transition rate $\Gamma_{02'} = \Gamma_{01}(\Omega_{12}/\Delta_{2'})^2$.

fixed free-bound transition rate Γ_{01}, the maximum tuning range of the scattering length for the two-photon case cannot be larger than in a one-photon scheme. Furthermore, given a fixed change in scattering length, the loss rate as determined by K_{inel} is not lower for the Raman scheme than for the one-photon scheme.

III. EXPERIMENTAL SETUP AND METHODS

A. Production of BEC's

For the experiments we produce ^{87}Rb BEC's of typically 1.2×10^6 atoms in the spin state $|F=1,m_F=-1\rangle$. Our setup comprises a magnetic transfer line [17] to transport atoms from a magneto-optic trap (MOT) chamber to a glass cell where the BEC is produced and all experiments are carried out. In a first step about 3×10^9 atoms are loaded within 4 s into a MOT directly from the background gas and are then cooled further to about 50 μK in a molasses cooling phase. After optically pumping into the $|F=1,m_F=-1\rangle$ state we load the atom cloud into a magnetic quadrupole trap with a gradient of 130 G/cm in the (strong) vertical direction. Within 1.4 s the atoms are then moved via a magnetic transfer line[4] over a distance of 48 cm including a 120° corner into a glass cell which is at a pressure below 10^{-11} mbar. In this cell we finally load the cloud into a QUIC trap (a type of magnetic trap that incorporates the quadrupole and Ioffe configuration) [18], ending up with typically 4×10^8 atoms at a temperature of about 250 μK. All three coils of the QUIC trap are operated at a current of 40 A, dissipating 350 W. This results in trap frequencies of $\omega_{\mathrm{radial}}/2\pi=150$ Hz and $\omega_{\mathrm{axial}}/2\pi=15$ Hz at a magnetic bias field of 2 G. To achieve Bose-Einstein condensation we use forced radio-frequency evaporation for a period of 20 s. The stop frequency is chosen so that we end up with condensates with a thermal background of about 25% of noncondensed atoms. At this value we concurrently get the highest number of atoms in the condensate and good reproducibility. For our measurements we consider only the condensed atoms.

B. Raman lasers

To realize the Raman scheme shown in Fig. 1 we use the electronically excited molecular state $|1\rangle=|0_g^-,\ \nu=1,\ J=2\rangle$ located 26.8 cm^{-1} below the $(S_{1/2}+P_{3/2})$ dissociation asymptote [9,19]. About 290 MHz below the $J=2$ line, there is another rotational level with $J=0$.[5] Although about 5 times weaker than the $J=2$ line, its effect cannot be totally neglected in our experiment. We choose level $|2\rangle$ to be the second to last bound state in the ground-state potential. It has a binding energy of 636 MHz$\times h$ [13] where h is Planck's constant.

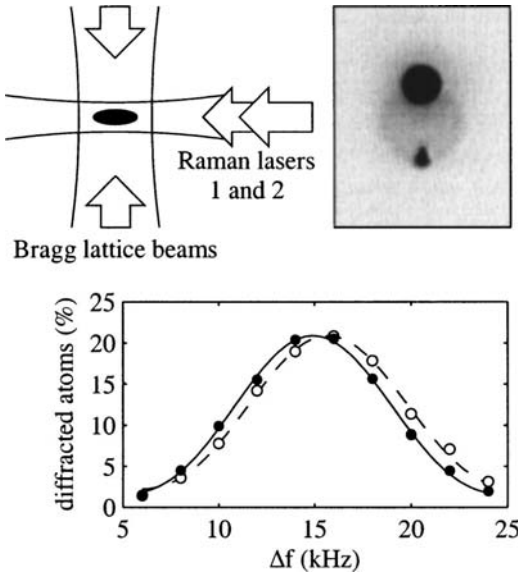

FIG. 3. Top left: experimental arrangement of the laser beams (top view). Top right: absorption image obtained after Bragg-diffracting a portion of the atoms to a state with a momentum of two photon recoils (lower atom cloud) and subsequent time of flight expansion. Bottom: Bragg resonance curves for two different relative detunings of the Raman lasers. The relative shift of 700 Hz is due to two different scattering lengths which are optically induced in the condensates. The atom numbers are the same for both curves. Shown is the percentage of diffracted atoms versus the frequency difference of the Bragg lattice beams. For better comparison we have scaled up the right curve by 10%.

The Raman laser beams are derived from a Ti:sapphire laser using an acousto-optical modulator at a center frequency of about 318 MHz in a double-pass configuration. This allows precise control of their relative frequency difference over several tens of MHz. Both Raman lasers propagate collinearly and are aligned along the weak axis of the magnetic trap (see Fig. 3). They have a $1/e^2$ waist of 76 μm, and their linear polarization is perpendicular to the magnetic bias field of the trap.

The Ti:sapphire laser is intensity stabilized and its frequency has a linewidth of about 3 MHz. In order to stabilize its frequency relative to the photoassociation lines, the laser is offset locked relative to the D_2 line of atomic rubidium with the help of a scanning optical cavity. This yields an absolute frequency accuracy of better than 10 MHz. In all our experiments the Raman laser intensities were set to $I_1=300$ W/cm^2 and $I_2=60$ W/cm^2 at the location of the condensate, if not stated otherwise.

C. Bragg spectroscopy

To measure optically induced changes in the scattering length a, we use Bragg spectroscopy [9,15]. This method allows for a fast measurement on time scales below 100 μs which is vital because of the rapid photoassociation losses

[4]For our magnetic transport (similar to that described in [17]) 13 pairs of quadrupole coils are used. These transfer coils each have an inner diameter of 23.6 mm, an outer diameter of 65 mm, and a height of 5.7 mm and consist of 34 windings. They are arranged in two layers above and below the vacuum chamber with a separation of 50 mm. Peak currents of 75 A are necessary to maintain a vertical gradient of 130 G/cm during transfer.

[5]Due to different light shifts [9] for the $J=0$ and $J=2$ lines, their splitting is intensity dependent. The value of 290 MHz is valid for an intensity of 300 W/cm^2.

we experience in our experiments. A moving lattice composed of two counter propagating beams with wave number k and a frequency difference Δf is used to diffract some of the condensate atoms to a state with nonzero momentum. When energy and momentum conservation are fulfilled, the Bragg lattice resonantly transfers a momentum of two photon recoils $2\hbar k$ in a first-order diffraction process. For the case of a homogeneous condensate of density n, the resonance energy for Bragg diffraction is given by the sum of transferred kinetic energy $h\Delta f_0=(2\hbar k)^2/2m$ and the change in mean-field energy $4\pi\hbar^2 na/m$.[6] This corresponds to a frequency difference of the Bragg lasers of

$$\Delta f_r = \Delta f_0 + \frac{2\hbar}{m} na. \tag{3}$$

If the condensate is initially not at rest, the kinetic energy contribution Δf_0 to the Bragg resonance frequency [Eq. (3)] contains an additional term $2\hbar kp/m$, where p is the initial atom momentum in the direction of the Bragg lattice. In our experiments we observe such a motional shift corresponding to condensate momentum of up to $p=0.1\ \hbar k$. This momentum can partly be attributed to optical dipole forces of Raman beams which are slightly noncentered on the condensate. Partly it can be attributed to a forced oscillation of the condensate in the magnetic trap at 150 Hz which coincides with the trapping frequency. Since this oscillation is driven by a higher harmonic of the line frequency (50 Hz), it is in phase with the line frequency and we are able to stabilize the initial condensate momentum by synchronizing the experiment to the line. A stable initial condensate momentum can then be determined and canceled out by measuring Δf_r alternately for Bragg diffraction to the $+2\hbar k$ and $-2\hbar k$ momentum components. After these measures we were left with a residual momentum noise level of up to $p=0.01\ \hbar k$.

In our setup the Bragg lattice beams are oriented along the horizontal direction perpendicular to the Raman laser beams (see Fig. 3) and have a width of ≈ 0.9 mm. We extract both beams from a single grating-stabilized diode laser and use two acousto-optical modulators to control the frequency difference. The laser is tuned 1.4 nm below the ^{87}Rb D_2 line which defines Δf_0 in Eq. (3) to be 15.14 kHz. This frequency is much larger than the typical mean-field contribution, $2\hbar na/m$, which in our experiments was below 3 kHz.

We illuminate the trapped condensate for 100 μs with the Bragg lattice light. After 12 ms of free expansion the diffracted atoms are spatially separated from the remaining atoms. Absorption imaging allows us to determine the diffraction efficiency. By adjusting the Bragg laser intensity (typically 1 mW) we keep the maximum diffraction efficiency between 15% and 20%. When we scan the frequency difference Δf and measure the fraction of Bragg-diffracted atoms we obtain curves as shown in Fig. 3 (bottom). These curves have a width of approximately 9 kHz as determined by the 100 μs length of our Bragg pulses. The shape of the curves is given by the Fourier transform of our square light pulses which we use to fit the data to obtain the resonance position Δf_r [9]. The shift between the two Bragg spectroscopy curves in Fig. 3 (bottom) is optically induced by shining in the Raman lasers at the same time as the Bragg lattice. For both curves the atom numbers are the same and $\Delta_1 = 60$ MHz. Only the Raman detuning Δ_2 differs by 26 MHz. According to Eq. (3) this observed shift in Bragg resonance frequency is then due to a change in scattering length, induced by tuning Δ_2. This demonstrates that we can tune the scattering length a with a Raman Feshbach resonance.

[6]This is valid in the limit that only a small fraction of the condensate is diffracted.

D. Determination of scattering length

We use Eq. (3) to determine the scattering length a from the measurements of the Bragg resonance frequency Δf_r. Equation (3), however, is derived for the case of a homogeneous condensate. Our trapped condensate, in contrast, which is subject to photoassociation losses, exhibits a time- and position-dependent density n. This can be taken into account by replacing the density n in Eq. (3) by an appropriate effective value $\bar{n}$.

A simple approach to estimate $\bar{n}$ is to calculate the spatial and time average of the condensate density n over the duration of the Raman pulse length T. For this we use the rate equation for the local density $\dot{n}=-2K_{\mathrm{inel}}n^2$ for two-atom losses. The inelastic collision rate coefficient K_{inel} governing this process is obtained from measuring the atom number at the beginning and end of the light pulse. This procedure already yields good results which differ less than 10% from an improved approach which we use for our data analysis and which is explained in the following.

The improved approach consists of a full numerical simulation which describes Bragg diffraction in a dynamically and spatially resolved way. We divide the condensate into density classes and treat their time dependence individually. The Bragg diffraction process is identified as a Rabi oscillation between a coherent two level system—i.e., the BEC component at rest and the Bragg-diffracted component. The changing density of the condensate due to loss is reflected in a time-dependent resonance frequency [see Eq. (3)]. As a result of these calculations we obtain for each density class a Bragg resonance curve similar to the experimental ones shown in Fig. 3. Averaging over these resonance curves and determining the center position yields the simulated value for the Bragg resonance Δf_r. Using $\Delta f_r=\Delta f_0+2\hbar\bar{n}a/m$ we can then determine the effective density $\bar{n}$.

IV. RESULTS

A. Raman scans

Figure 4 presents measurements where the detuning Δ_1 of laser 1 from the excited molecular state is set to $\Delta_1/2\pi = 60$ MHz. The intensities of the Raman lasers 1 and 2 are 300 W/cm^2 and 60 W/cm^2, respectively. Figure 4(a) shows the atom number after illuminating a condensate of initially 1.4×10^6 atoms for 100 μs with the Raman lasers. Scanning the Raman detuning Δ_2 we find a strong loss of atoms on resonance. As already expected from Eq. (1) the line shape is slightly asymmetric. Figure 4(b) shows the resonance fre-

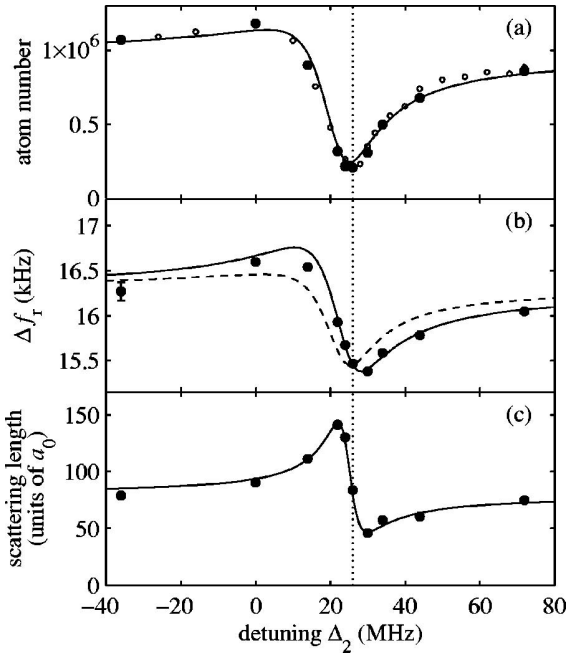

FIG. 4. Optical Feshbach resonance using a Raman scheme. (a) shows the measured atom number after the Raman pulse, (b) the measured Bragg resonance frequency, and (c) the scattering length, as determined from (a) and (b). In (a) the solid circles correspond to measurements where Bragg spectroscopy was used to determine the scattering length, while the small open circles stem from additional loss measurements without Bragg spectroscopy. From our measurements we estimate the uncertainty of the Bragg resonance frequency to be smaller then ±100 Hz, as indicated by the error bar in (b). The solid lines in (a), (b), and (c) are from a model calculation (see the Appendix and text). The dashed line in (b) shows the expected signal if there was only loss in atom number but no change in scattering length (see also discussion in text). The vertical line indicates the location of maximal loss in (a) and helps to compare the relative positions of the three curves.

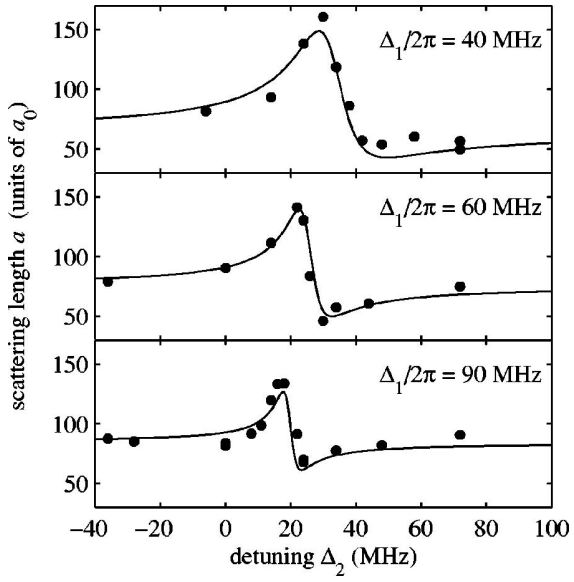

FIG. 5. Variation of the scattering length with Raman detuning for three various detunings Δ_1 from the excited molecular state. The solid line is a calculation (see the Appendix) which uses a single set of parameters for all curves.

quency Δf_r as measured by Bragg spectroscopy. When we analyze the data in Figs. 4(a) and 4(b) with the improved procedure described in Sec. III D we obtain values for the scattering length which are shown in Fig. 4(c). The scattering length a shows a dispersive variation between $50\,a_0$ and $140\,a_0$ as we scan over the resonance. The dispersive scattering length curve is offset by about $20\,a_0$ from the background scattering length $a_{bg}=100\,a_0$ for ^{87}Rb in the $|F=1, m_F=-1\rangle$ state [20–22]. This is due to the one-photon Feshbach tuning of laser 1, in agreement with our previous measurements [9].

We find that Eqs. (1) and (2) are not sufficient to describe these data properly, mainly because they neglect the decay rate γ_2. A more complete model (see the Appendix), also taking into account both the $J=0$ and $J=2$ rotational levels, was used for creating fit curves,[7] depicted as solid lines in Fig. 4. The fact that the data for atomic loss as well as for the scattering length a are both well described by the theoretical curves is an intrinsic consistency check for our model and our data analysis.

The shape of the signal Δf_r in Fig. 4(b) is a combination of the effects of the varying scattering length a and the varying atom number [see Eq. (3)]. This is illustrated by the dashed and continuous lines in Fig. 4(b): The dashed line shows the expected signal if only the variations in atom number would occur and the scattering length stayed constant.[8] The solid line takes the variations in both atom number and scattering length into account. The deviation of the measured data points from the dashed line is due to an optical induced change of the scattering length.

B. Dependence on detuning

We now investigate how detuning Δ_1 affects the scattering length a. Figure 5 shows a set of three curves showing the scattering length for detunings $\Delta_1/2\pi=40$, 60, and 90 MHz.

The measurements clearly show that the position and width of the resonances depend on Δ_1. The change in position can be mainly explained as light shifts of levels $|1\rangle$ and $|2\rangle$ due to laser 2. The decrease of the resonance width with increasing detuning Δ_1 follows directly our discussion in Sec. II. The solid lines are model calculations as described in detail in the Appendix. They are derived from a simultaneous fit to the data shown in Fig. 5 and a large number of atom loss measurements with different detunings (not shown). The set of fit parameters is listed in the Appendix. We also use this same set of parameters for the theoretical curves in Figs. 6 and 7.

[7]The resulting fit parameters are similar to those given in the Appendix.

[8]To account for the one-photon Feshbach tuning of laser 1, a value for the background scattering length $a_{bg}=80\,a_0$ was used for the calculation.

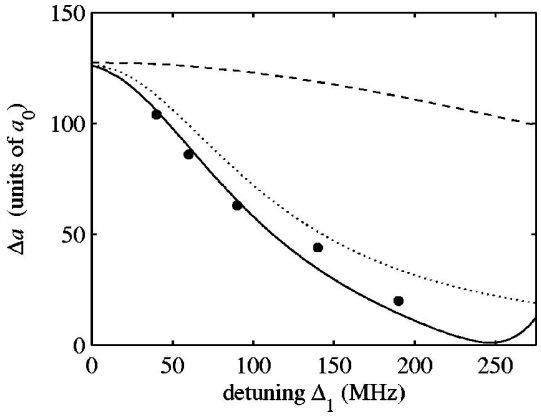

FIG. 6. Maximum variation in scattering length $\Delta a = a_{\max} - a_{\min}$ versus one-photon detuning Δ_1. Solid line: full model calculation (see the Appendix). Dotted line: three-level model (see Fig. 1), with $\gamma_2/2\pi = 2$ MHz. Dashed line: three-level model, with $\gamma_2/2\pi = 100$ kHz.

It is interesting to note from Fig. 5 that the amplitude of the dispersive scattering length signal decreases as Δ_1 becomes larger. This is not to be expected from the simple model Eqs. (1) and (2). To investigate this effect we have performed scans for atom loss and scattering length for several detunings Δ_1. Figure 6 shows the maximum variation in scattering length, $\Delta a = a_{\max} - a_{\min}$, obtained for detunings Δ_1 ranging from 40 MHz to 200 MHz. Here, $a_{\max}$ and $a_{\min}$ are the maximal and minimal scattering length values for corresponding scan curves. Typical scan curves are shown in Fig. 5. Each data point in Fig. 6 was derived from a complete scan and corresponds to one day of data collection.

An analysis of our data using our theoretical model indicates that the decrease of Δa as a function of Δ_1 is a consequence of two effects.

(i) To properly model these measurements we have to assign to the molecular state $|2\rangle$ in the ground-state potential a non-negligible decay width $\gamma_2/2\pi \approx 2$ MHz. For comparison, two calculations of a three-level model are plotted in Fig. 6. For small $\gamma_2/2\pi = 100$ kHz (dashed line) Δa decreases only weakly. For $\gamma_2/2\pi = 2$ MHz (dotted line) the theory fits the data much better. Such a large decay rate of a ground-state level is surprising. It seems too large to be explained purely by collisions. We find that the decay rate increases with the light intensity. At low light powers of a few $\mathrm{W/cm^2}$ we have observed very narrow linewidths $\gamma_2/2\pi$ on the order of a few kHz, similar to the values reported by [13,14]. The broadening of the molecular ground level could be due to coupling to excited molecular levels. We can exclude, however, from our experimental data that these levels are located within our experimental scanning range between the states $|1\rangle$ and $|3\rangle$. This would lead to additional resonance features in the scattering length, absorption, and light shifts, which are inconsistent with our data. In contrast, our data indicate a relatively constant background loss rate of the ground level over the experimental scan range. This allows us to analyze the data successfully with our simple few-level model. Besides coupling to excited molecular states, we suspect that coupling to the *d*-wave shape resonance of the scattering channel also gives rise to a sizable contribution to the molecular decay rate. Because the *d*-wave shape resonance is located very close (a few MHz) to threshold, it is resonantly coupled to the molecular ground-state level via the Raman transition. To include the shape resonance is beyond the reach of our simple model and has to be investigated later.

(ii) The second reason for the decrease in Δa is a quantum interference effect involving both the $J=2$ and $J=0$ rotational levels as predicted by our model. At a detuning of $\Delta_1/2\pi \approx 250$ MHz the interference effect leads to a complete disappearance of the optical Feshbach resonance. We observe this in a corresponding disappearance of the atom loss feature in our measurements (not shown). The interference effect alone—i.e., without a 2 MHz linewidth—is not sufficient to explain the experimental data in Fig. 6.

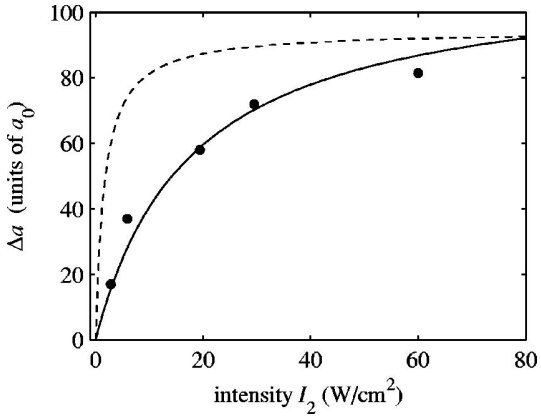

FIG. 7. Maximum variation in scattering length $\Delta a = a_{\max} - a_{\min}$ versus I_2. For this data set $I_1 = 300\ \mathrm{W/cm^2}$ and $\Delta_1 = 60$ MHz. The solid line is a full model calculation (see the Appendix). The dashed line stems from the same model, but with $\gamma_2/2\pi$ set to 100 kHz and is scaled by a factor of 0.84 for better comparison.

C. Dependence on intensity

From the simple model Eq. (2) it is clear that the maximum variation in scattering length Δa is proportional to Γ_{01} and consequently scales linearly with the intensity I_1 of laser 1. We have verified this dependence recently [9] for the case of a one-photon optical Feshbach resonance.

In contrast, the dependence of Δa on intensity I_2 of laser 2 is not so trivial. According to the simple model, Eqs. (1) and (2), which neglects the decay rate γ_2, the maximum change Δa is independent of I_2. It is also clear, that for $I_2 = 0$ we have $\Delta a = 0$ since there is no dependence of scattering length on Δ_2 at all. This unphysical discontinuous behavior can be resolved if we introduce a finite decay rate $\gamma_2 > 0$. We then find that for increasing intensity $I_2, \Delta a$ rises monotonously from zero to a value where it saturates. We observe this general behavior in our measurements presented in Fig. 7. Our full model, as described in the Appendix, describes the measured data well if we set the decay rate to $\gamma_2/2\pi = 2$ MHz (solid line). In contrast, the dashed line in Fig. 7 shows the calculation for the same model where γ_2 is set to

$\gamma_2/2\pi=100$ kHz. Saturation then occurs at a much lower intensity I_2 than for $\gamma_2/2\pi=2$ MHz.

V. CONCLUSION

Our experiments demonstrate the use of an optical Feshbach resonance for tuning of the scattering length via stimulated Raman coupling to a bound molecular state. Our results show that there is no advantage over a one-photon scheme when comparing tuning range and loss rate. However, for certain applications a Raman scheme is experimentally more favorable since it demands a lower tuning range of the lasers. Our presented theoretical model is in good agreement with our data and might be helpful when tailoring experimental parameters for a specific application. Furthermore, it gives insight into the process of creating stable ultracold molecules via two-photon photoassociation.

ACKNOWLEDGMENTS

We appreciate the help of George Ruff and Michael Hellwig at an early stage of the experiment. We thank Paul Julienne, Eite Tiesinga, John Bohn, Olivier Dulieu, Peter Fedichev, Andrea Micheli, and Helmut Ritsch for valuable discussions. This work was supported by the Austrian Science Fund (FWF) within SFB 15 (project part 17) and the European Union in the frame of the Cold Molecules TMR Network under Contract No. HPRN-CT-2002-00290.

APPENDIX: THEORETICAL MODEL AND FIT PARAMETERS

We use a theoretical model by Bohn and Julienne [16] to fit the data in Figs. 4–7. In the following we give a short summary of this model and present the procedure to calculate the scattering matrix S, the loss coefficient K_{inel}, and the scattering length a. The model has the advantage that it is concise and intuitive and it allows treatment of multilevel systems with several couplings between the levels. The numerical calculations involve simple manipulations of small matrices.

In Fig. 8 the level scheme for our two models involving four and six levels are shown. We first restrict our description to the four-level model as shown in the right part of Fig. 8. In this way our description stays compact and matrices are kept small. The extension to six or more levels follows the same scheme.

Four-level model

Compared to Fig. 1 an additional excited level $|3\rangle$ is added. This level corresponds to the rotational level $J=0$ and lies 290 MHz below the $J=2$ rotational level $|1\rangle$ [9]. We work in the dressed atom picture and every level $|i\rangle$ is attributed a detuning Δ_i (see Fig. 8). Δ_0 is arbitrarily set to 0. The transition strengths from the continuum $|0\rangle$ to levels $|1\rangle$ and $|3\rangle$ are described by stimulated rates Γ_{01} and Γ_{03} which are proportional to the intensity I_1 of laser 1. The transitions between the bound levels $|2\rangle$ and $|1\rangle,|3\rangle$ are characterized by the Rabi frequencies Ω_{12} and Ω_{23}, respectively, which are

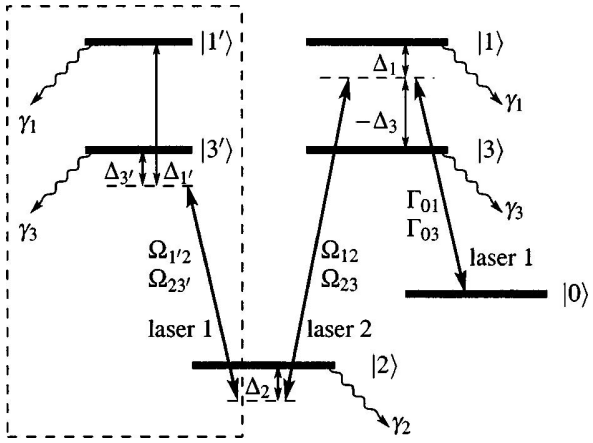

FIG. 8. Extended level scheme (compare to Fig. 1) for the four-level model (right-hand side) and its extension with six levels. State $|3\rangle$ corresponds to the $J=0$ level and lies 290 MHz below the $J=2$ level $|1\rangle$. The four-level model is based on levels $|0\rangle,|1\rangle,|2\rangle$, and $|3\rangle$. The auxiliary levels $|1'\rangle$ and $|3'\rangle$ are introduced in the extended model to describe the coupling between $|2\rangle$ and $|1\rangle,|3\rangle$, respectively, due to laser 1 (see text).

proportional to $\sqrt{I_2}$. Spontaneous decay from the bound levels leading to atomic losses is formally taken into account by introducing artificial levels $|\mathrm{a}_i\rangle$ for each level $|i\rangle$ to which a transition at rate γ_i takes place (not shown in Fig. 8). All these couplings between different levels are summarized in the symmetric reaction matrix K. We arrange the level names in the order $(0, \mathrm{a}_1, \mathrm{a}_2, \mathrm{a}_3, 1, 2, 3)$ and use them as row and column indices. The nonzero matrix elements of the K matrix then read $K_{01}=\sqrt{\Gamma_{01}/2}$, $K_{03}=\sqrt{\Gamma_{03}/2}$, $K_{i\mathrm{a}_i}=\sqrt{\gamma_i/2}$, $K_{12}=\Omega_{12}$, and $K_{23}=\Omega_{23}$. Levels 0, a_1, a_2, and a_3 are referred to as open channels, levels 1, 2, and 3 as closed channels. The reaction matrix K is partitioned into open and closed channel blocks,

$$K=\begin{pmatrix} \mathbf{0} & K^{\mathrm{oc}} \\ K^{\mathrm{co}} & K^{\mathrm{cc}} \end{pmatrix}.$$

K^{oc} reads in our case

$$K^{\mathrm{oc}}=\begin{pmatrix} \sqrt{\Gamma_{01}/2} & 0 & \sqrt{\Gamma_{03}/2} \\ \sqrt{\gamma_1/2} & 0 & 0 \\ 0 & \sqrt{\gamma_2/2} & 0 \\ 0 & 0 & \sqrt{\gamma_3/2} \end{pmatrix}.$$

K^{co} is the transposed matrix of K^{oc} and

$$K^{\mathrm{cc}}=\begin{pmatrix} 0 & \Omega_{12} & 0 \\ \Omega_{12} & 0 & \Omega_{23} \\ 0 & \Omega_{23} & 0 \end{pmatrix}.$$

From K the reduced K matrix

$$K^{\mathrm{red}}=K^{\mathrm{oc}}(D-K^{\mathrm{cc}})^{-1}K^{\mathrm{co}}$$

is calculated, eliminating the closed channels 1–3, where D denotes a diagonal matrix with diagonal elements

$(\Delta_1, \Delta_2, \Delta_3)$. This determines the unitary 4×4 scattering matrix S:

$$S = (\mathbf{1} + iK^{\mathrm{red}})(\mathbf{1} - iK^{\mathrm{red}})^{-1}.$$

From the matrix elements S_{ij} of S the trap loss coefficient K_{inel} is calculated by

$$K_{\mathrm{inel}} = \frac{\pi\hbar}{\mu k_{\mathrm{i}}} \sum_i |S_{0a_i}|^2 = \frac{\pi\hbar}{\mu k_{\mathrm{i}}}(1 - |S_{00}|^2),$$

where $\mu = m_{\mathrm{Rb}}/2$ is the reduced Rb mass and $\hbar k_{\mathrm{i}}$ the relative momentum of the colliding atoms. The scattering length is obtained from S_{00} via

$$a = a_{\mathrm{bg}} - \frac{1}{2k_{\mathrm{i}}} \frac{\mathrm{Im}(S_{00})}{\mathrm{Re}(S_{00})},$$

where $\mathrm{Re}(S_{00})$ and $\mathrm{Im}(S_{00})$ denote the real and imaginary parts of S_{00}, respectively.

In the limit of small relative momentum $\hbar k_{\mathrm{i}}$ and small coupling strengths $\Gamma_{0i} \ll \gamma_i$, K_{inel} and the light-induced change of the scattering length $a - a_{\mathrm{bg}}$ are independent of k_i because the Γ_{0i} are proportional to k_{i} (Wigner threshold regime) [16].

Extension of the four-level model

The four-level model neglects that laser 1 (of which the intensity is typically 5 times greater than that of laser 2) also couples the levels $|2\rangle$-$|1\rangle$ and $|2\rangle$-$|3\rangle$. However, this coupling should be taken into account since laser 1 is not far detuned from these transitions (see Fig. 8) due to the small binding energy of state $|3\rangle$ (636 MHz$\times h$) which is comparable to typical detunings Δ_1. It mainly leads to broadening and light shifting of level $|2\rangle$. The additional coupling can approximately be taken care of by adding another two auxiliary levels $|1'\rangle$ and $|3'\rangle$ with detunings $\Delta_{1'} = \Delta_1 + \Delta_2 + 2\pi \times 636$ MHz and $\Delta_{3'} = \Delta_3 + \Delta_2 + 2\pi \times 636$ MHz as shown in Fig. 8. The coupling strengths $\Omega_{1'2}$ and $\Omega_{23'}$ are fixed by $\Omega_{1'2} = \Omega_{12}\sqrt{I_1/I_2}$ and $\Omega_{23'} = \Omega_{23}\sqrt{I_1/I_2}$. Compared to the four-level model no new fit parameters are introduced. We can calculate K_{inel} and the scattering length a following the same recipe as for the four-level model, only with larger matrices. Fitting the data in Figs. 4–7 this extended model produced much better results than the four-level model. For completeness we give here the fit parameters which were used in the calculations in Figs. 5–7 ($I_1 = 300$ W/cm^2 and $I_2 = 60$ W/cm^2): $\Gamma_{01}/2\pi = 42$ kHz, $\Gamma_{03}/2\pi = 8$ kHz, $\Omega_{12}/2\pi = 32$ MHz, $\Omega_{23}/2\pi = 12$ MHz, $\gamma_1/2\pi = 25$ MHz, $\gamma_3/2\pi = 22$ MHz, and $\gamma_2/2\pi = 2$ MHz. We used $k_{\mathrm{i}} = 2.5\times10^{-5}$ m^{-1}. Due to the limitations of our model, these fit parameters should not be mistaken as the true values of the corresponding physical quantities.

[1] E. Tiesinga, B. J. Verhaar, and H. T. C. Stoof, Phys. Rev. A **47**, 4114 (1993).

[2] S. Inouye *et al.*, Nature (London) **392**, 151 (1998); Ph. Courteille, R. S. Freeland, D. J. Heinzen, F. A. van Abeelen, and B. J. Verhaar, Phys. Rev. Lett. **81**, 69 (1998); J. L. Roberts *et al.*, *ibid.* **81**, 5109 (1998).

[3] C. Chin, V. Vuletic, A. J. Kerman, and S. Chu, Phys. Rev. Lett. **85**, 2717 (2000); A. Marte *et al.*, *ibid.* **89**, 283202 (2002).

[4] E. A. Donley, N. R. Claussen, S. T. Thompson, and C. E. Wieman, Nature (London) **417**, 529 (2002).

[5] L. Khaykovich *et al.*, Science **296**, 1290 (2002); K. E. Strecker, G. B. Partridge, A. G. Truscott, and R. G. Hulet, Nature (London) **417**, 150 (2002).

[6] S. L. Cornish, N. R. Claussen, J. L. Roberts, E. A. Cornell, and C. E. Wieman, Phys. Rev. Lett. **85**, 1795 (2000); T. Weber, J. Herbig, M. Mark, H.-C. Nägerl, and R. Grimm, Science **299**, 232 (2003).

[7] S. Jochim *et al.*, Science **302**, 2101 (2003); M. Greiner, C. A. Regal, and D. S. Jin, Nature (London) **426**, 537 (2003); M. Zwierlein *et al.*, Phys. Rev. Lett. **91**, 250401 (2003); T. Bourdel *et al.*, *ibid.* **93**, 050401 (2004).

[8] C. A. Regal, M. Greiner, and D. S. Jin, Phys. Rev. Lett. **92**, 040403 (2004); M. W. Zwierlein *et al.*, *ibid.* **92**, 120403 (2004); C. Chin *et al.*, Science **305**, 1128 (2004).

[9] M. Theis *et al.*, Phys. Rev. Lett. **93**, 123001 (2004).

[10] F. K. Fatemi, K. M. Jones, and P. D. Lett, Phys. Rev. Lett. **85**, 4462 (2000).

[11] P. O. Fedichev, Y. Kagan, G. V. Shlyapnikov, and J. T. M. Walraven, Phys. Rev. Lett. **77**, 2913 (1996).

[12] J. L. Bohn and P. S. Julienne, Phys. Rev. A **56**, 1486 (1997).

[13] R. Wynar, R. S. Freeland, D. J. Han, C. Ryu, and D. J. Heinzen, Science **287**, 1016 (2000).

[14] T. Rom *et al.*, Phys. Rev. Lett. **93**, 073002 (2004); Ch. Lisdat, N. Vanhaecke, D. Comparet, and P. Pillet, Eur. Phys. J. D **21**, 299 (2002).

[15] J. Stenger *et al.*, Phys. Rev. Lett. **82**, 4569 (1999).

[16] J. L. Bohn and P. S. Julienne, Phys. Rev. A **60**, 414 (1999).

[17] M. Greiner, I. Bloch, T. W. Hänsch, and T. Esslinger, Phys. Rev. A **63**, 031401 (2001).

[18] T. Esslinger, I. Bloch, and T. W. Hänsch, Phys. Rev. A **58**, R2664 (1998).

[19] A. Fioretti *et al.*, Eur. Phys. J. D **15**, 189 (2001).

[20] E. Tiemann (private communication).

[21] P. Julienne and E. Tiesinga (private communication).

[22] P. S. Julienne, F. H. Mies, E. Tiesinga, and C. J. Williams, Phys. Rev. Lett. **78**, 1880 (1997).

Bibliography

[And95] M. H. Anderson, J. R. Ensher, M. R. Matthews, C. E. Wieman, and E. A. Cornell, *Observation of Bose-Einstein Condensation in a Dilute Atomic Vapor*, Science **269**, 198 (1995).

[Bar91] G. P. Barwood, P. Gill, and W. R. C. Rowley, *Frequency Measurements on Optically Narrowed Rb-Stabilized Laser Diodes at 780 nm and 795 nm*, Appl. Phys. B **53**, 142 (1991).

[Bar04a] M. Bartenstein, A. Altmeyer, S. Riedl, S. Jochim, C. Chin, J. Hecker Denschlag, and R. Grimm, *Collective excitations of a degenerate gas at the BEC-BCS crossover*, Phys. Rev. Lett **92**, 203201 (2004).

[Bar04b] M. Bartenstein, A. Altmeyer, S. Riedl, S. Jochim, C. Chin, J. Hecker Denschlag, and R. Grimm, *Crossover from a Molecular Bose-Einstein Condensate to a Degenerate Fermi Gas*, Phys. Rev. Lett. **92**, 120401 (2004).

[Ber87] T. Bergeman, G. Erez, and H. Metcalf, *Magnetostatic trapping fields for neutral atoms*, Phys. Rev. A **35**, 1535 (1987).

[Ber01] F. Bertinetto, P. Cordiale, G. Galzerano, and E. Bava, *Frequency Stabilization of DBR Diode Laser Against Cs Absorption Lines at 852 nm Using the Modulation Transfer Method*, IEEE Transactions on Instrumentation and Measurement **50**, 490 (2001).

[Biz99] S. Bize, Y. Sortais, M. S. Santos, C. Mandache, A. Clairon, and C. Salomon, *High-accuracy measurement of the ^{87}Rb ground state hyperfine splitting in an atomic fountain*, Europhys. Lett. **45**, 558 (1999).

[Bjo80] G. C. Bjorklund, *Frequency-modulation spectroscopy: a new method for measuring weak absorptions and dispersions.*, Optics Letters **5**, 15 (1980).

[Bla00] G. Blasbichler, *Ein Lambdameter mit 10^{-7} Meßunsicherheit*, Master's thesis, Universität Innsbruck (2000).

[Boe96a] H. M. J. M. Boesten, A. J. Moerdijk, and B. J. Verhaar, *Dipolar decay in two recent Bose-Einsten condensation experiments*, Phys. Rev. A **54**, R29 (1996).

[Boe96b] H. M. J. M. Boesten, J. M. Vogels, J. G. C. Tempelaars, and B. J. Verhaar, *Properties of cold collisions of ^{39}K atoms and of ^{41}K atoms in relation to Bose-Einstein condensation*, Phys. Rev. A **54**, R3726 (1996).

[Boe97] H. M. J. M. Boesten, C. C. Tsai, J. R. Gardner, D. J. Heinzen, and B. J. Verhaar, *Observation of a shape resonance in the collision of two cold ^{87}Rb atoms*, Phys. Rev. A **55**, 636 (1997).

[Bog47] N. Bogoliubov, *On the theory of superfluidity*, J. Phys. **11**, 23 (1947).

[Boh96] J. L. Bohn and P. S. Julienne, *Semianalytic treatment of two-color photoassociation spectroscopy and control of cold atoms*, Phys. Rev. A **54**, R4637 (1996).

[Boh97] J. L. Bohn and P. S. Julienne, *Prospects for influencing scattering lengths with far-off-resonant light*, Phys. Rev. A **56**, 1486 (1997).

[Boh99] J. L. Bohn and P. S. Julienne, *Semianalytic theory of laser-assisted resonant cold collisions*, Phys. Rev. A **60**, 414 (1999).

[Boh03] J. Bohn (2003), private communication.

[Bon02] K. Bongs and K. Sengstock, *Introduction to Bose-Einstein Condensation*, in: M. Weidemüller and C. Zimmermann (Eds.), *Interactions in Ultracold Gases*, Wiley-VHC, Weinheim, 2002.

[Bou04] T. Bourdel, L. Khaykovich, J. Cubizolles, J. Zhang, F. Chevy, M. Teichmann, L. Tarruell, S. J. J. M. F. Kokkelmans, and C. Salomon, *Experimental Study of the BEC-BCS Crossover Region in Lithium 6*, Phys. Rev. Lett. **93**, 050401 (2004).

[Bra95] C. C. Bradley, C. A. Sackett, J. J. Tollett, and R. G. Hulet, *Evidence of Bose-Einstein Condensation in an Atomic Gas with Attractive Interactions*, Phys. Rev. Lett. **75**, 1687 (1995), *ibid.* **79**, 1170 (1997).

[Bra99] M. P. Bradley, J. V. Porto, S. Rainville, J. K. Thompson, and D. E. Pritchard, *Penning Trap Measurements of the Masses of ^{133}Cs, $^{87,85}Rb$ and ^{23}Na with Uncertainties $\leq 0.2ppb$*, Phys. Rev. Lett. **83**, 4510 (1999).

[Bur97] E. A. Burt, R. W. Ghrist, C. J. Myatt, M. J. Holland, E. A. Cornell, and C. E. Wieman, *Coherence, Correlations, and Collisions: What One Learns about Bose-Einstein Condensates from Their Decay*, Phys. Rev. Lett. **79**, 337 (1997).

[Bur02] K. Burnett, P. S. Julienne, P. D. Lett, E. Tiesinga, and C. J. Williams, *Quantum encounters of the cold kind*, Nature **417**, 225 (2002).

[Cal04] T. Calarco, U. Dorner, P. S. Julienne, C. J. Williams, and P. Zoller, *Quantum computations with atoms in optical lattices: Marker qubits and molecular interactions*, Phys. Rev. A **70**, 012306 (2004).

[Cas96] Y. Castin and R. Dum, *Bose-Einstein Condensates in Time-Dependent Traps*, Phys. Rev. Lett. **77**, 5315 (1996).

[Chi00] C. Chin, V. Vuletić, A. J. Kerman, and S. Chu, *High Resolution Feshbach Spectroscopy of Cesium*, Phys. Rev. Lett. **85**, 2717 (2000).

[Chi04a] C. Chin, M. Bartenstein, A. Altmeyer, S. Riedl, S. Jochim, J. Hecker Denschlag, and R. Grimm, *Observation of the pairing gap in a strongly interacting Fermi gas*, Science **305**, 1128 (2004), published online 22 July 2004; 10.1126/science.1100818.

[Chi04b] C. Chin, T. Kraemer, M. Mark, J. Herbig, , P. Waldburger, H.-C. Nägerl, and R. Grimm, *Observation of Feshbach-like resonances in collisions betweeen ultracold molecules* (2004), arXiv:cond-mat/0411258.

[Chu98] S. Chu, *The manipulation of neutral particles*, Rev. Mod. Phys. **70**, 685 (1998).

[Ciu04] R. Ciurylo, E. Tiesinga, and P. S. Julienne, *Optical tuning of the scattering length of cold alkaline earth atoms* (2004), arXiv:physics/0412111.

[Cor00] S. L. Cornish, N. R. Claussen, J. L. Roberts, E. A. Cornell, and C. E. Wieman, *Stable ^{85}Rb Bose-Einstein Condensates with Widely Tunable Interactions*, Phys. Rev. Lett. **85**, 1795 (2000).

[Cou98] P. Courteille, R. S. Freeland, D. J. Heinzen, F. A. van Abeelen, and B. J. Verhaar, *Observation of a Feshbach Resonance in Cold Atom Scattering*, Phys. Rev. Lett. **81**, 69 (1998).

[CT98] C. N. Cohen-Tannoudji, *Manipulating atoms with photons*, Rev. Mod. Phys. **70**, 707 (1998).

[Dal99a] F. Dalfovo, S. Giorgini, L. P. Pitaevskii, and S. Stringari, *Theory of Bose-Einstein condensation in trapped gases*, Rev. Mod. Phys. **71**, 463 (1999).

[Dal99b] J. Dalibard, *Collisional dynamics of ultra-cold atomic gases*, in: M. Inguscio, S. Stringari, and C. E. Wieman (Eds.), *Proceedings of the International School of Physics - Enrico Fermi*, 321, IOS Press, 1999.

[Dav95] K. B. Davis, M.-O. Mewes, M. R. Andrews, N. J. van Druten, D. S. Durfee, D. M. Kurn, and W. Ketterle, *Bose-Einstein Condensation in a Gas of Sodium Atoms*, Phys. Rev. Lett. **75**, 3969 (1995).

[Den02] J. H. Denschlag, J. E. Simsarian, H. Häffner, C. McKenzie, A. Browaeys, D. Cho, K. Helmerson, S. L. Rolston, and W. D. Phillips, *A Bose-Einstein condensate in an optical lattice*, J. Phys. B **35**, 3095 (2002).

[Don02] E. A. Donley, N. R. Claussen, S. T. Thompson, and C. E. Wieman, *Atom-molecule coherence in a Bose-Einstein condensate*, Nature **417**, 529 (2002).

[Dru02] P. D. Drummond, K. V. Kheruntsyan, D. J. Heinzen, and R. H. Wynar, *Stimulated Raman adiabatic passage from an atomic to a molecular Bose-Einstein condensate*, Phys. Rev. A **65**, 063619 (2002).

[Dür04] S. Dürr, A. Volz, T. Marte, and G. Rempe, *Observation of Molecules Produced from a Bose-Einstein Condensate*, Phys. Rev. Lett. **92**, 020406 (2004).

[Ess98] T. Esslinger, I. Bloch, and T. W. Hänsch, *Bose-Einstein condensation in a quadrupole-Ioffe-configuration trap*, Phys. Rev. A **58**, R2664 (1998).

[Fat00] F. K. Fatemi, K. M. Jones, and P. D. Lett, *Observation of Optically Induced Feshbach Resonances in Collisions of Cold Atoms*, Phys. Rev. Lett. **85**, 4462 (2000).

[Fed96a] P. O. Fedichev, Y. Kagan, G. V. Shlyapnikov, and J. T. M. Walraven, *Influence of Nearly Resonant Light on the Scattering Length in Low-Temperature Atomic Gases*, Phys. Rev. Lett. **77**, 2913 (1996).

[Fed96b] P. O. Fedichev, M. W. Reynolds, and G. V. Shlyapnikov, *Three-Body Recombination of Ultracold Atoms to a Weakly Bound s Level*, Phys. Rev. Lett. **77**, 2921 (1996).

[Fes58] H. Feshbach, *A Unified Theory of Nuclear Reactions*, Ann. Phys. **5**, 337 (1958).

[Fes62] H. Feshbach, *A Unified Theory of Nuclear Reactions. II*, Ann. Phys. **19**, 287 (1962).

[Fio01] A. Fioretti, C. Amiot, C. M. Dion, O. Dulieu, M. Mazzoni, G. Smirne, and C. Gabbanini, *Cold rubidium molecule fromation through photoassociation: A spectroscopic study of the* 0_g^- *long-range state of* $^{87}Rb_2$, Eur. Phys. J. D **15**, 189 (2001).

[Geh98] M. E. Gehm, K. M. O'Hara, T. A. Savard, and J. E. Thomas, *Dynamics of noise-induced heating in atom traps*, Phys. Rev. A **58**, 3914 (1998).

[Ger00] J. M. Gerton, D. Strekalov, I. Prodan, and R. G. Hulet, *Direct observation of growth and collapse of a Bose-Einstein condensate with attractive interactions*, Nature **408**, 692 (2000).

[Ger01] J. M. Gerton, B. J. Frew, and R. G. Hulet, *Photoassociative frequency shift in a quantum degenerate gas*, Phys. Rev. A **64**, 053410 (2001).

[Got62] Y. V. Gott, M. S. Ioffe, and V. G. Tel'kovskii, *Some new results on confinement in magnetic traps*, Nucl. Fusion **Suppl. 3**, 1045 (1962).

[Gre01] M. Greiner, I. Bloch, T. W. Hänsch, and T. Esslinger, *Magnetic transport of trapped cold atoms over a large distance*, Phys. Rev. A **63**, 031401(R) (2001).

[Gre02] M. Greiner, O. Mandel, T. Esslinger, T. W. Hänsch, and I. Bloch, *Quantum phase transition from a superfluid to a Mott insulator in a gas of ultracold atoms*, Nature **415**, 39 (2002).

[Gre03] M. Greiner, C. A. Regal, and D. S. Jin, *Emergence of a molecular Bose-Einstein condensate from a Fermi gas*, Nature **426**, 540 (2003), doi:10.1038/nature02199; Published online 26 November 2003.

[Gri93] G. F. Gribakin and V. V. Flambaum, *Calculation of the scattering length in atomic collisions using the semiclassical approximation*, Phys. Rev. A **48**, 546 (1993).

[Gro61] E. P. Gross, *Structure of a Quantized Vortex in Boson Systems*, Il Nuovo Cimento **20**, 454 (1961).

[Hak98] H. Haken and H. C. Wolf, *Molekülphysik und Quantenchemie*, vol. 3rd edition, Springer-Verlag, Berlin, Heidelberg, New York, 1998.

[Hak00] H. Haken and C. Wolf, *Atom- und Quantenphysik*, Springer-Verlag, Berlin, Heidelberg, New York, 2000, 7th ed.

[Hän01] W. Hänsel, P. Hommelhoff, T. W. Hänsch, and J. Reichel, *Bose-Einstein condensation on a microelectronic chip*, Nature **413**, 498 (2001).

[Hau98] L. V. Hau, B. D. Busch, C. Liu, Z. Dutton, M. M. Burns, and J. A. Golovchenko, *Near-resonant spatial images of confined Bose-Einstein condensates in a 4-Dee magnetic bottle*, Phys. Rev. A **58**, R54 (1998).

[Hel05] M. Hellwig, Master's thesis, University of Innsbruck (2005), in preparation.

[Her03] J. Herbig, T. Kraemer, M. Mark, T. Weber, C. Chin, H.-C. Nägerl, and R. Grimm, *Preparation of a Pure Molecular Quantum Gas*, Science **301**, 1510 (2003), published online 21 August 2003; 10.1126/science.1088876.

[Hes86] H. F. Hess, *Evaporative cooling of magnetically trapped and compressed spin-polarized hydrogen*, Phys. Rev. B **34**, 3476 (1986).

[Hol96] M. Holland and J. Cooper, *Expansion of a Bose-Einstein condensate in a harmonic potential*, Phys. Rev. A **53**, R1954 (1996).

[Hua87] K. Huang, *Statistical Mechanics*, Wiley, New York, 1987, 2nd ed.

[Ino98] S. Inouye, M. R. Andrews, J. Stenger, H.-J. Miesner, D. M. Stamper-Kurn, and W. Ketterle, *Observation of Feshbach resonances in a Bose-Einstein condensate*, Nature **392**, 151 (1998).

[Ino04] S. Inouye, J. Goldwin, M. L. Olsen, C. Ticknor, J. L. Bohn, and D. S. Jin, *Observation of Heteronuclear Feshbach Resonances in a Bose-Fermi Mixture*, Phys. Rev. Lett. **93**, 183201 (2004).

[Jak98] D. Jaksch, C. Bruder, J. I. Cirac, C. W. Gardiner, and P. Zoller, *Cold Bosonic Atoms in Optical Lattices*, Phys. Rev. Lett. **81**, 3108 (1998).

[Jak02] D. Jaksch, V. Venturi, J. I. Cirac, C. J. Williams, and P. Zoller, *Creation of a Molecular Condensate by Dynamically Melting a Mott Insulator*, Phys. Rev. Lett. **89**, 040402 (2002).

[Joa75] C. J. Joachain, *Quantum Collision Theory*, North Holland, Amsterdam, 1975.

[Joc00] S. Jochim, *Aufbau einer Apparatur zum magnetooptischen Einfang von fermionischen Lithiumatomen*, Master's thesis, Universität Heidelberg (2000).

[Joc03] S. Jochim, M. Bartenstein, A. Altmeyer, G. Hendl, S. Riedl, C. Chin, J. Hecker Denschlag, and R. Grimm, *Bose-Einstein Condensation of Molecules*, Science **301**, 2101 (2003), published online 13 November 2003; 10.1126/science.1093280.

[Jul89] P. S. Julienne and F. H. Mies, *Collisions of Ultracold Trapped Atoms*, J. Opt. Soc. Am. B **6**, 2257 (1989).

[Jul92] P. Julienne, A. Smith, and K. Burnett, *Theory of collisions between laser cooled atoms*, Advances in Atomic, Molecular, and Optical Physics **30**, 141 (1992).

[Jul97] P. S. Julienne, F. H. Mies, E. Tiesinga, and C. J. Williams, *Collisional Stability of Double Bose Condensates*, Phys. Rev. Lett. **78**, 1880 (1997).

[Jul01] P. S. Julienne, *Ultra-Cold Collisions of Atoms and Molecules*, in: E. R. Pike and P. Sabatier (Eds.), *Scattering*, Academic Press, 2001.

[Jul04a] P. S. Julienne (2004), private communication.

[Jul04b] P. S. Julienne and E. Tiesinga (2004), private communication.

[Jul04c] P. S. Julienne, E. Tiesinga, and T. Köhler, *Making Cold Molecules by Time-dependent Feshbach Resonances*, J. Mod. Opt. **51**, 1787 (2004).

[Kag85] Y. Kagan, B. V. Svistunov, and G. V. Shlyapnikov, *Effect of Bose condensation on inelastic processes in gases*, Sov. Phys. JETP Lett. **42**, 209 (1985).

[Kag96] Y. Kagan, E. L. Surkov, and G. V. Shlyapnikov, *Evolution of a Bose-condensed gas under variations of the confining potential*, Phys. Rev. A **54**, R1753 (1996).

[Ket96] W. Ketterle and N. J. van Druten, *Evaporative Cooling of Trapped Atoms*, Adv. At. Mol. Opt. Phys. **37**, 181 (1996).

[Ket97] W. Ketterle and H.-J. Miesner, *Coherence properties of Bose-Einstein condensates and atom lasers*, Phys. Rev. A **56**, 3291 (1997).

[Ket99] W. Ketterle, D. S. Durfee, and D. M. Stamper-Kurn, *Making, probing and understanding Bose-Einstein condensates*, in: M. Inguscio, S. Stringari, and C. E. Wieman (Eds.), *Proceedings of the International School of Physics - Enrico Fermi*, 67, IOS Press, 1999.

[Kha02] L. Khaykovich, F. Schreck, G. Ferrari, T. Bourdel, J. Cubizolles, L. D. Carr, Y. Castin, and C. Salomon, *Formation of a Matter-Wave Bright Soliton*, Science **296**, 1290 (2002).

[Kin04] J. Kinast, S. L. Hemmer, M. E. Gehm, A. Turlapov, and J. E. Thomas, *Evidence for Superfluidity in a Resonatly Interacting Fermi Gas*, Phys. Rev. Lett. **92**, 150402 (2004).

[Lan77] L. D. Landau and E. M. Lifshitz, *Quantum Mechanics: Non-Relativistic Theory*, Pergamon Press, Oxford, 1977, 3rd ed.

[Lev49] N. Levinson, K Danske Vidensk. Selsk. Mat. Fys. Medd. **25** (1949).

[Lid00] D. R. Lide (Ed.), *CRC Handbook of Chemistry and Physics*, CRC Press, Boca Raton, 2000, 81st ed.

[Lin92] K. Lindquist, M. Stephens, and C. Wieman, *Experimental and theoretical study of the vapor-cell Zeeman optical trap*, Phys. Rev. A **46**, 4082 (1992).

[Lui96] O. J. Luiten, M. W. Reynolds, and J. T. M. Walraven, *Kinetic theory of the evaporative cooling of a trapped gas*, Phys. Rev. A **53**, 381 (1996).

[Mac04] M. Mackie, K. Härkönen, A. Collin, K.-A. Suominen, and J. Javanainen, *Improved efficiency of stimulated Raman adiabatic passage in photoassociation in a Bose-Einstein condensate*, Phys. Rev. A **70**, 013614 (2004), and references therein.

[Maj33] E. Majorana, *Atomi Orientati in Campo Magnetico Variabile.*, Nouvo Cimento **9**, 43 (1933).

[Mar98] M. Marinescu and L. You, *Controlling Atom-Atom Interaction at Ultralow Temperatures by dc Electric Fields*, Phys. Rev. Lett. **81**, 4596 (1998).

[Mar02] A. Marte, T. Volz, J. Schuster, S. Dürr, , G. Rempe, E. G. M. van Kempen, and B. J. Verhaar, *Feshbach Resonances in Rudidium 87: Precision Measurement and Analysis*, Phys. Rev. Lett. **89**, 283202 (2002).

[Mar03] A. Marte, *Feshbach-Resonanzen bei Stößen ultrakalter Rubidiumatome*, Ph.D. thesis, Technische Universität München (2003).

[McK02] C. McKenzie, J. H. Denschlag, E. Tiesinga, P. S. Julienne, K. Helmerson, P. D. Lett, S. L. Rolston, W. D. Phillips, and Others, *Photoassociation of Sodium in a Bose-Einstein Condensate*, Phys. Rev. Lett. **88**, 120403 (2002).

[Met99] H. J. Metcalf and P. van der Straten, *Laser Cooling and Trapping*, Springer-Verlag, New York, Berlin, Heidelberg, 1999.

[Mew96] M.-O. Mewes, M. R. Andrews, N. J. van Druten, D. M. Kurn, D. S. Durfee, and W. Ketterle, *Bose-Einstein Condensation in a Tightly Confining dc Magnetic Trap*, Phys. Rev. Lett. **77**, 416 (1996).

[Mig85] A. L. Migdall, J. V. Prodan, W. D. Phillips, T. H. Bergeman, and H. J. Metcalf, *First Observation of Magnetically Trapped Neutral Atoms*, Phys. Rev. Lett. **54**, 2596 (1985).

[Moe95] A. J. Moerdijk, B. J. Verhaar, and A. Axelsson, *Resonances in ultracold collisions of ^6Li, ^7Li and ^{23}Na*, Phys. Rev. A **51**, 4852 (1995).

[Moe96] A. J. Moerdijk, B. J. Verhaar, and T. M. Nagtegaal, *Collisions of dressed ground-state atoms*, Phys. Rev. A **53**, 4343 (1996).

[Moh99] P. J. Mohr and B. N. Taylor, *CODATA Recommended Values of the Fundamental Physical Constants: 1998*, J. Phys. Chem. Ref. Data **28** (1999).

[Mon90] C. Monroe, W. Swann, H. Robinson, and C. Wieman, *Very Cold Trapped Atoms in a Vapor Cell*, Phys. Rev. Lett. **65**, 1571 (1990).

[Moo89] J. H. Moore, C. C. Davis, and M. A. Coplan, *Building Scientific Apparatus*, Addison Wesley, 1989.

[Mot65] N. F. Mott and H. S. W. Massey, *The Theroy of Atomic Collisions*, Clarendon, Oxford, 1965.

[Mya97] C. J. Myatt, E. A. Burt, R. W. Ghrist, E. A. Cornell, and C. E. Wieman, *Production of Two Overlapping Bose-Einstein Condensates by Sympathetic Cooling*, Phys. Rev. Lett. **78**, 586 (1997).

[Nar98] M. Naraschewski and D. M. Stamper-Kurn, *Analytical description of a trapped semi-ideal Bose gas at finite temperature*, Phys. Rev. A **58**, 2423 (1998).

[Nes63] A. N. Nesmeyanov, *Vapor Pressure of the Chemical Elements*, Elsevier, Amsterdam, 1963.

[O'H89] J. F. O'Hanlon, *A User's Guide to Vacuum Technology*, Wiley, 1989, 2nd ed.

[Ott01] H. Ott, J. Fortagh, G. Schlotterbeck, A. Grossmann, and C. Zimmermann, *Bose-Einstein Condensation in a Surface Microtrap*, Phys. Rev. Lett. **87**, 230401 (2001).

[Pet02] C. J. Pethik and H. Smith, *Bose-Einstein Condensation in Dilute Gases*, Cambridge University Press, 2002.

[Phi98] W. D. Phillips, *Laser cooling and trapping of neutral atoms*, Rev. Mod. Phys. **70**, 721 (1998).

[Pit61] L. P. Pitaevskii, *Vortex lines in an imperfect Bose gas*, Sov. Phys. JETP **13**, 451 (1961).

[Pit03] L. Pitaevskii and S. Stringari, *Bose-Einstein Condensation*, Oxford University Press, 2003.

[Pri83] D. E. Pritchard, *Cooling Neutral Atoms in a Magnetic Trap for Precision Spectroscopy*, Phys. Rev. Lett. **51**, 1336 (1983).

[Raa87] E. L. Raab, M. Prentiss, A. Cable, S. Chu, and D. E. Pritchard, *Trapping of Neutral Sodium Atoms with Radiation Pressure*, Phys. Rev. Lett. **59**, 2631 (1987).

[Raj79] R. K. Raj, D. Bloch, J. J. Sydner, G. Camy, and M. Ducloy, *High-Frequency Optically Heterodyned Saturation Spectroscopy Via Resonant Degenerate Four-Wave Mixing*, Phys. Rev. Lett. **32**, 145 (1979).

[Reg03] C. A. Regal, C. Ticknor, J. L. Bohn, and D. S. Jin, *Creation of ultracold molecules from a Fermi gas of atoms*, Nature **424**, 47 (2003).

[Reg04] C. A. Regal, M. Greiner, and D. S. Jin, *Observation of Resonance Condensation of Fermionic Atom Pairs*, Phys. Rev. Lett. **92**, 040403 (2004).

[Ric94] L. Ricci, M. Weidemüller, T. Esslinger, A. Hemmerich, C. Zimmermann, V. Vuletic, W. König, and T. Hänsch, *A compact grating-stabilized diode laser system for atomic physics*, Opt. Comm. 541 (1994).

[Rob98] J. L. Roberts, N. R. Claussen, J. P. Burke, Jr., C. H. Greene, E. A. Cornell, and C. E. Wieman, *Resonant Magnetic Field Control of Elastic Scattering of Cold ^{85}Rb*, Phys. Rev. Lett. **81**, 5109 (1998).

[Rob00] J. L. Roberts, N. R. Claussen, S. L. Cornish, and C. E. Wieman, *Magnetic Field Dependence of Ultracold Inelastic Collisions near a Feshbach Resonance*, Phys. Rev. Lett. **85**, 728 (2000).

[Rom04] T. Rom, T. Best, O. Mandel, A. Widera, M. Greiner, T. W. Hänsch, and I. Bloch, *State Selective Production of Molecules in Optical Lattices*, Phys. Rev. Lett. **93**, 073002 (2004).

[Sak94] J. J. Sakurai, *Modern Quantum Mechanics*, Addison-Wesley, 1994, revised ed.

[Sch99] U. Schünemann, H. Engler, R. Grimm, M. Weidemüller, and M. Zielonkowski, *Simple scheme for tunable frequency offset locking of two lasers*, Rev. Sci. Instr. **70**, 242 (1999).

[Sch02] J. Schuster, *Stoßlawinen in einem Bose-Einstein-Kondensat*, Ph.D. thesis, Universität Konstanz (2002).

[Shi82] J. H. Shirley, *Modulation transfer processes in optical heterodyne saturation*, Optics Letters **7**, 537 (1982).

[Sim02] A. Simoni, P. S. Julienne, E. Tiesinga, and C. J. Williams, *Intensity effects in ultracold photoassociation line shapes*, Phys. Rev. A **66**, 063406 (2002).

[SK99] D. M. Stamper-Kurn, A. P. Chikkatur, A. Görlitz, S. Inouye, S. Gupta, D. E. Pritchard, and W. Ketterle, *Excitation of Phonons in a Bose-Einstein Condensate by Light Scattering*, Phys. Rev. Lett. **83**, 2876 (1999).

[Söd99] J. Söding, D. Guèry-Odelin, P. Desbiolles, F. Chevy, H. Inamori, and J. Dalibard, *Three-body decay of a rubidium Bose-Einstein condensate*, Appl. Phys. B **69**, 257 (1999).

[Sta04] C. A. Stan, M. W. Zwierlein, C. H. Schunck, S. M. F. Raupach, and W. Ketterle, *Observation of Feshbach Resonances between Two Different Atomic Species*, Phys. Rev. Lett. **93**, 143001 (2004).

[Ste99a] J. Stenger, S. Inouye, M. R. Andrews, H.-J. Miesner, D. M. Stamper-Kurn, and W. Ketterle, *Strongly Enhanced Inelastic Collisions in a Bose-Einstein Condensate near Feshbach Resonances*, Phys. Rev. Lett. **82**, 2422 (1999).

[Ste99b] J. Stenger, S. Inouye, A. P. Chikkatur, D. M. Stamper-Kurn, D. E. Pritchard, and W. Ketterle, *Bragg Spectroscopy of a Bose-Einstein Condensate*, Phys. Rev. Lett. **82**, 4569 (1999).

[Ste02] D. A. Steck, *Rubidium 87 D Line Data* (2002), http://steck.us/alkalidata, revision 0.5.

[Str02] K. E. Strecker, G. B. Partridge, A. G. Truscott, and R. G. Hulet, *Formation and propagation of matter-wave soliton trains*, Nature **417**, 150 (2002).

[Str03] K. E. Strecker, G. B. Partridge, and R. G. Hulet, *Conversion of an Atomic Fermi Gas to a Long-Lived Molecular Bose Gas*, Phys. Rev. Lett. **91**, 080406 (2003).

[Tha05a] G. Thalhammer, Ph.D. thesis, University of Innsbruck (2005), in preparation.

[Tha05b] G. Thalhammer, M. Theis, K. Winkler, R. Grimm, and J. Hecker Denschlag, *Inducing an Optical Feshbach Resonance via Stimulated Raman Coupling*, Phys. Rev. A **71**, 033403 (2005).

[The04] M. Theis, G. Thalhammer, K. Winkler, M. Hellwig, G. Ruff, R. Grimm, and J. Hecker Denschlag, *Tuning the Scattering Length with an Optically Induced Feshbach Resonance*, Phys. Rev. Lett. **93**, 123001 (2004).

[Tie92] E. Tiesinga, A. Moerdijk, B. J. Verhaar, and H. T. C. Stoof, *Conditions for Bose-Einstein condensation in magnetically trapped atomic cesium*, Phys. Rev. A **46**, R1167 (1992).

[Tie93] E. Tiesinga, B. J. Verhaar, and H. T. C. Stoof, *Threshold and resonance phenomena in ultracold ground-state collisions*, Phys. Rev. A **47**, 4114 (1993).

[Tie04a] E. Tiemann (2004), private communication.

[Tie04b] E. Tiesinga (2004), private communication.

[Tim99] E. Timmermans, P. Tommasini, M. Hussein, and A. Kerman, *Feshbach resonances in atomic Bose-Einstein condensates*, Phys. Rep. **315**, 199 (1999).

[Vog97] J. M. Vogels, C. C. Tsai, R. S. Freeland, S. J. J. M. F. Kokkelmans, B. J. Verhaar, and D. J. Heinzen, *Prediction of Feshbach resonances in collisions of ultracold rubidium atoms*, Phys. Rev. A **56**, R1067 (1997).

[Web03] T. Weber, J. Herbig, M. Mark, H.-C. Nägerl, and R. Grimm, *Bose-Einstein Condensation of Cesium*, Science **299**, 232 (2003).

[Wei99] J. Weiner, V. S. Bagnato, S. Zilio, and P. S. Julienne, *Experiments and theory in cold and ultracold collisions*, Rev. Mod. Phys. **71**, 1 (1999).

[Wei03] J. Weiner, *Quantum Collisions*, in: M. Weidemüller and C. Zimmermann (Eds.), *Interactions in Ultracold Gases: From Atoms to Molecules*, Wiley-VHC, Weinheim, 2003.

[Wie91] C. E. Wieman and L. Hollberg, *Using diode lasers for atomic physics*, Rev. Sci. Instrum. **61**, 1 (1991).

[Win84] W. H. Wing, *On Neutral Particle Trapping in Quasistatic Electromagentic Fields*, Prog. Quant. Elect. **8**, 181 (1984).

[Win02] K. Winkler, *Aufbau einer magnetischen Transportapparatur für ultrakalte Atome*, Master's thesis, Universität Innsbruck (2002).

[Win05] K. Winkler, G. Thalhammer, M. Theis, H. Ritsch, R. Grimm, and J. H. Denschlag (2005), in preparation.

[Wut89] M. Wutz, H. Adam, and W. Walcher, *Theory and Practice of Vacuum Technology*, Vieweg, 1989.

[Wyn00a] R. Wynar, R. S. Freeland, D. J. Han, C. Ryu, and D. J. Heinzen, *Molecules in a Bose-Einstein Condensate*, Science **287**, 1016 (2000).

[Wyn00b] R. H. Wynar, *Ultra-cold Molecules in an Atomic Bose-Einstein Condensate*, Ph.D. thesis, University of Texas, Austin (2000).

[Xu03] K. Xu, T. Mukaiyama, J. R. Abo-Shaeer, J. K. Chin, D. E. Miller, and W. Ketterle, *Formation of Quantum-Degenerate Sodium Molecules*, Phys. Rev. Lett. **91**, 210402 (2003).

[Ye96] J. Ye, S. Schwartz, P. Jungner, and J. L. Hall, *Hyperfine structure and absolute frequency of the ^{87}Rb 5 $P_{3/2}$ state*, Opt. Lett. **21**, 1280 (1996).

[Zwi03] M. W. Zwierlein, C. A. Stan, C. H. Schunck, S. M. F. Raupach, S. Gupta, Z. Hadzibabic, and W. Ketterle, *Observation of Bose-Einstein Condensation of Molecules*, Phys. Rev. Lett. **91**, 250401 (2003).

[Zwi04] M. Zwierlein, C. A. Stan, C. H. Schunck, S. M. F. Raupach, A. J. Kerman, and W. Ketterle, *Condensation of Pairs of Fermionic Atoms near a Feshbach Resonance*, Phys. Rev. Lett. **92**, 120403 (2004).

Vielen Dank

Hier möchte ich mich bei allen herzlich bedanken, die mit ihrer Unterstützung zum Gelingen dieser Arbeit beigetragen haben.

Ein großes Dankeschön an ...

Rudi für die Betreuung dieser Arbeit als Doktorvater, für seine stetige Unterstützung und viele hilfreiche Diskussionen, sowie für die äußerst lehrreiche und interessante Zeit in dieser Gruppe.

Johannes, dem Leiter des Rubidium Projekts und meinem direkten Betreuer bei dieser Arbeit. Er war immer bereit anfallende Fragen gründlich zu diskutieren und hat alle denkbare Hilfe gegeben.

Die anderen Mitstreiter am Rubidium Experiment, allen voran Klaus und Gregor, die fast von Anfang an dabei waren und mit denen ich viele Laborstunden geteilt habe. Neben den beiden haben auch Michael H., George, Ina, Stefan und Florian L. in unserem Team gearbeitet und zum Erfolg des Experiments beigetragen.

Meine Bürokollegen Jens und Stefan, für ihre Hilfsbereitschaft, viele hilfreiche Diskussionen und die äußerst nette Atmosphäre.

Alle derzeitigen und ehemaligen Kollegen an den Nachbarexperimenten: Markus H., David, Bastian, Charly, Antti, Almar, Hanns-Christoph, Tino, Jens, Michael M., Tobias, Philipp, Cheng, Selim, Markus B., Gerhard, Alexander, Stefan, Reece, Mattias, Peter, Toni, Florian S., Eric und Gabriel für vielfältige gegenseitige Hilfe und ein wirklich angenehmes Arbeitsklima.

Toni, Stefan, Joseph, Helmuth und Manuel aus unseren Werkstätten. Nur mit deren Arbeit sowie den exzellenten Vakuumkammern und Spulenkörpern von Toni konnte unser Experiment gebaut werden.

Christine, Frau Moser und Frau Köhle für unzählige Formen von organisatorischer Unterstützung.

Noch einmal an viele der bereits genannten für nette Mittagspausen, bergige Wochenenden und einige unterhaltsame Abende.

Meine Eltern und meine Schwester, die mich all die Jahre in jeder Form unterstützt haben.